Maneuvering and Platooning of Automated Vehicles via Comprehensive Predictive Control

A Numerical Analysis

Anand Sie

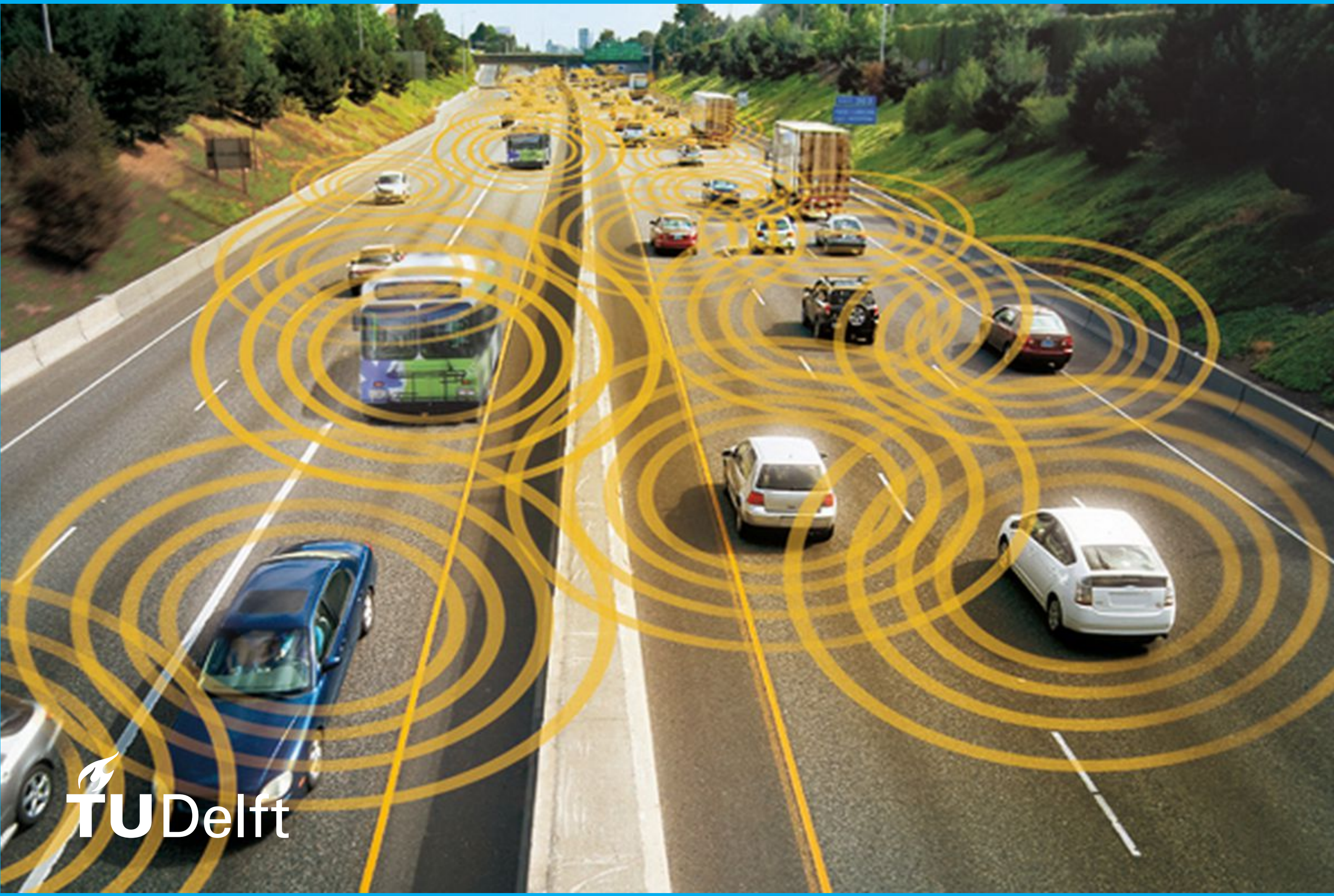

TU Delft

Maneuvering and Platooning of Automated Vehicles via Comprehensive Predictive Control

A Numerical Analysis

by

Anand Sie

to obtain the degree of Master of Science
at the Delft University of Technology,
to be defended publicly on Tuesday October 24, 2022 at 10:00 AM.

Student number:	4367456	
Project duration:	September 1, 2021 – October 24, 2022	
Thesis committee:	Dr S. Grammatico,	TU Delft, supervisor
	Dr W. Ananduta,	TU Delft, daily supervisor

Preface

After completing my Mechanical Engineering bachelor, I continued exploring my interest in control, robotics and automation during the master Systems & Control. Next to my studies, I also worked on a physical flight simulator and the software for a walking hexapod. During this thesis project, I combined these different experiences and interests. In addition, as a *Delftenaar*, I enjoy working on futuristic ideas. That is why researching autonomous vehicles was a perfect fit for me. This concept promises improved safety on the road, reduced congestion and a more enjoyable commuting experience: watching your favourite movie in the car would be possible. This thesis is mainly meant for researchers interested in autonomous vehicles, particularly autonomous vehicles in a platoon setting. However, as the autonomous vehicles is a concept not too abstract to grasp, a curious reader is also able to follow along.

Looking back, this project has been the biggest challenge of my academic journey: I am proud to see how far I have come. Of course, this project would not have been possible on my one. Especially, I want to sincerely thank Dr Wicak Ananduta, which was generous to spend so much time with me. Our discussions were extensive and in-depth. Without his active contribution, this project would not have turned out the way it did. Furthermore, I'm grateful that Dr Sergio Grammatico allowed me to work with him. Initially, I was matched with another supervisor. This way, I could work on autonomous vehicles. In addition, I want to thank my friends and family that always were willing to listen and assist where possible. Especially, Lisa was the best supporter and motivator I needed. And lastly, Rik was the best *Rubber Duck* I could have wished for.

Anand Sie
Delft, October 2022

Abstract

Ongoing research in autonomous driving currently focuses on creating new applications for autonomous vehicles (AV) and connected autonomous vehicles (CAV). Specifically, motion planning and control solutions are being developed based on the combination of Artificial Potential Functions (APF) with economic Model Predictive Control (eMPC). These two methods are integrated into a new Comprehensive Predictive Control (CPC) strategy. Although preliminary research shows promising results, a performance analysis of this approach, both for AV and CAV, has not yet been published. Therefore this thesis studies the capabilities of this novel APF-eMPC framework by carrying out numerical simulations. Multiple manoeuvres and varying amounts of white noise are utilized to test the controller's limitations. For the AV part, multiple basic driving manoeuvres are simulated: lane-keeping, car-following and lane-changing. The results show that an AV based on this framework can execute these different manoeuvres without precise measurements. The CAV concept is simulated using a platoon scenario. The gap-closing behaviour of the multiple CAVs in a platoon is examined. The state-of-the-art gap-closing APF is compared with an APF based on inter-molecular dynamics and fitted on actual traffic. Various experiments are carried out using a constant time-headway in combination with different time gaps between the vehicles. The results show that the resulting behaviour by the inter-molecular APF better matches human driving behaviour and results in less dangerous gap-closing behaviour than the quadratic platoon APF. The latter has a more considerable change of lateral instability occurring. Therefore the APF based on inter-molecular dynamics and fitted on actual traffic data outperforms the APF based on a quadratic function. Lastly, it was found that the coupling between the longitudinal and lateral dynamics, often neglected in literature, cannot be ignored during platoon stability analysis.

Contents

List of Figures

List of Tables

List of Algorithms

Nomenclature

APF	artificial potential function
AV	autonomous vehicle
CAV	connected autonomous vehicle
CPC	comprehensive predictive control
CV	connected vehicle
$eMPC$	economic model predictive control
MPC	model predictive control
$V2V$	vehicle to vehicle

1

Introduction

This chapter introduces the concept of autonomous driving and the state-of-art. First, Section 1.1 discusses the motivation behind self-driving cars. Following that, Section 1.2 elaborates on the state-of-the-art. Section 1.3 provides the research question for this thesis based on gaps in the literature. The research topic is broken down into several sub-questions. Finally, Section 1.4 ends this chapter by explaining the thesis structure and what the reader can expect.

1.1. Motivation

The Autonomous Vehicle (AV) is a futuristic concept where the vehicle uses sensors to perceive its surroundings, as illustrated in Figure 1.2 and Figure 1.1. Based on this information the AV autonomously makes decisions. Multiple levels of autonomy exist. The SAE J3016 standard [1] introduces a scale from 0 to 5 for different level of vehicle automation, where level 0 represents no automation and level 5 represents full driving automation. Cruise control, for example, is a level 1 type of autonomy. This thesis focuses on the higher levels of autonomy.

Autonomous driving has many benefits compared to manual driving. To start, every year, numerous traffic accidents occur [2], where the primary cause for these traffic accidents is by far because of human error [3]. Humans often participate in traffic while tired, stressed, angered or under influence, or possessing various driving abilities [4], [5]. By replacing the human by an AV, a more predictable and safer environment on the road can be ensured. Furthermore, a person is less likely to make decisions that benefit all road users yet reduce their personal travel time. Working together, a group of automobiles can face fewer traffic congestion [6], [7], reducing traffic pollution emissions [8], [9]. This positive impact on climate change can be significant if we as a society would like to reach the goals of the Paris Climate Accords [10], where the goal is to limit global warming to below temperature levels compared to pre-industrial levels. The last benefit has to do with comfort and mental wellbeing. Commuting to work every day is time-consuming [11]. So when humans are not required to drive the car, they can focus their attention elsewhere as participating in traffic is a stressful activity [12], [13]. These benefits are appealing and explain the rise of interest in AVs.

Currently, there are already AVs driving around in the form of autonomous busses that transport passengers [16], [17], [18]. These vehicles have been a mere part of experiments. Some operate in a closed and predictable environment, whereas the surroundings of an ordinary car is unpredictable. Designing an AV that can operate in such an environment is complex. These observations lead to an interesting paradox. In an ideal scenario, solely AVs would be allowed on the road. However, not everyone will buy an AV overnight. Because of this slow transition, the produced AVs should handle the current chaotic and dangerous environment. Eventually, traffic will become more predictable when enough AVs are driving around. This change would allow for simpler AV designs. Before reaching that state, more research on AVs is still necessary.

Another trend which could accelerate the integration of autonomous driving in society is the Connected Vehicle (CV). With this approach, a CV communicates with different parts of its surroundings, increasing the amount of usable information and making decision-making easier. By sharing motion states with different vehicles on the road via vehicle-to-vehicle (V2V) connectivity, for example, vehi-

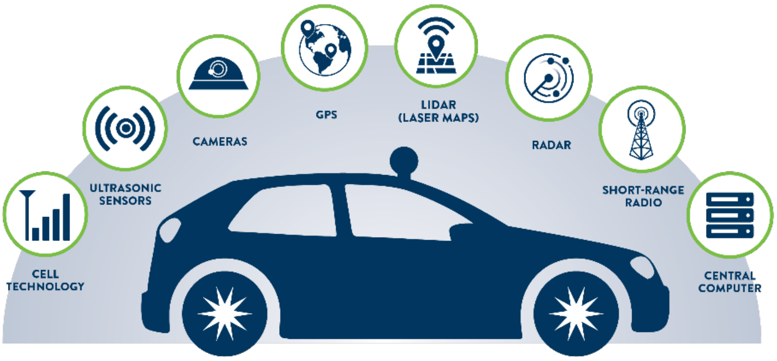

Figure 1.1: An AV uses different sensors to estimate its own position, change of position and its surroundings [14].

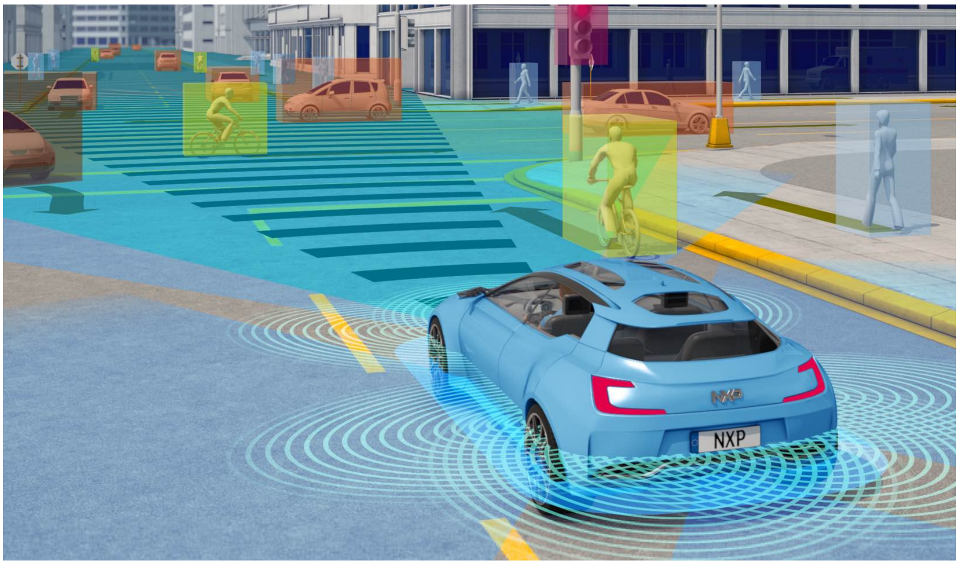

Figure 1.2: An artist impression how an AV perceives its surroundings using different sensors and categorizes them [15].

cles could approach each other much closer [19]. Predicting or guessing the future paths of other road users would be no longer required. Other types of connectivity, illustrated in Figure 1.3, are Vehicle-to-infrastructure (V2I) [20] or even vehicle-to-everything (V2X) [21], [22], which could allow for an even more efficient road or city use.

The Connected Autonomous Vehicle (CAV) is another type of autonomous driving that combines the concepts of the AV and the CV. New concepts have emerged as a result of this new sort of vehicle. While adaptive cruise control (ACC) is gradually replacing cruise control , research is focusing on new sorts of cooperative driving. Rather of measuring the location of the preceding vehicle, the vehicle in front will exchange information via V2V communication. Hereby allowing for use of cooperative adaptive cruise control (CACC), such that such that automobiles can drive even closer together [23], [24], [25]. One step further, vehicles would not only communicate with one another, but would also collaborate. Such a collaboration is also referred to as a platoon [21], [26], [27]. With this concept, the vehicles strive to stay in a formation with a specific spacing between them. These enhancements would make self-driving vehicles even safer and more efficient, traffic congestion will reduce, driving will be more pleasurable, and the environmental impact will reduce [28].

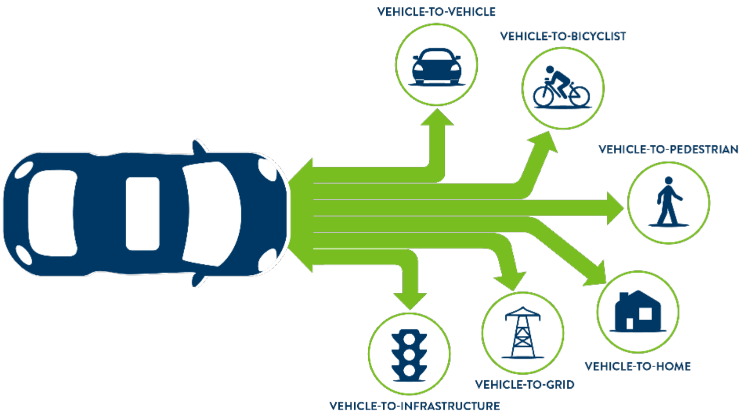

Figure 1.3: A CV can be connected to multiple parts of its surroundings and exchange information with it [14].

1.2. State of the Art

As the motivation of self-driving vehicles is now clear, this section outlines the research development and current gaps for AVs and CAVs. Prior to writing this thesis, a literature review was conducted, which served as the foundation for this thesis [29]. For a more theoretical and in-depth explanation, the reader is directed to this survey.

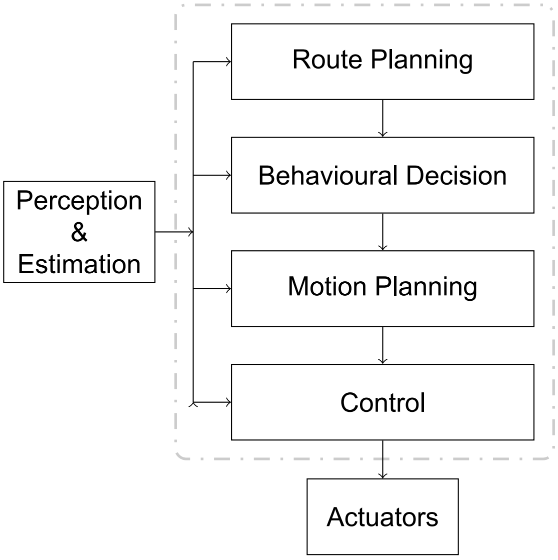

Figure 1.4: Classic architecture for an AV [30]. Here the *Perception & Estimation* module forms the input for the PDM modules, which consist out of four sub-modules. The output from the PDM module serves as the input for the car's actuators.

Because of the complexity of a fully autonomous vehicle's design, it is usually divided into multiple hierarchical subproblems. A schematic overview of the corresponding architecture can be helpful for a better understanding; one example can be seen in Figure 1.4 [30]. The methods inside the dotted box are also known as *Planning & Decision Making* (PDM) [31]. Multiple solutions for these modules are explained in [29]. In this survey, two methods specifically are highlighted; the Artificial Potential Function (APF) as a motion planner and the economic Model Predictive Control (eMPC) as a control strategy.

Due to their characteristics, they can be combined into a single algorithm [30] [32], [33]. This combination is referred to as the APF-eMPC framework. This single solution serves as a (local)

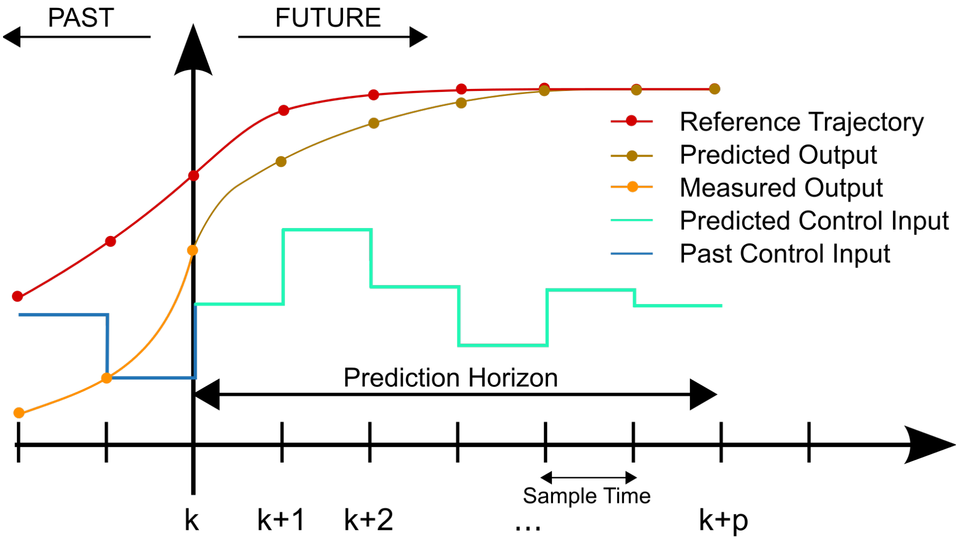

Figure 1.5: A discrete scheme visualization of principles of MPC [36]. The dotted lines represent the system's reference, predicted and measured states. The step lines represent the predicted and actual injected control input. The finite prediction horizon (in this figure $k + p$) can be observed as the graphs are also finite.

behavioral-decision maker, motion planner and controller at the same time. A traditional path planner or a behavioural-decision maker is no longer required. This approach is also known as the Comprehensive Control Strategy (CPC) because off the architectural simplification.

The remainder of this section will first discuss the state-of-the-art of the APF and eMPC approaches individually, followed by an explanation of the APF-eMPC. Finally, the CAV is explored in more detail, and how the CPC can be used for CAV applications as well [34], [35].

1.2.1. Economic Model Predictive Control

First, the original Model Predictive Control (MPC) is discussed, followed by the eMPC extension.

Standard Model Predictive Control

Research on this topic started in the 1960s [37]. Compared to traditional controllers, such as the Proportional Integral Derivative (PID) controller, chemical processes are relatively slow compared to automotive or aerial applications. Therefore, chemical plants were the ideal testbeds for this hardware demanding controller. Because computational power has increased in the last decades, it has become possible to use MPC in real-time for other domains; for instance, aerospace [38], automotive [39], [40], water networks [41], or even drones [42].

MPC, in its most basic form, is a regulation controller where it tries to steer the system to its origin. The necessary input needed to do so is calculated through an optimization problem. In contrast to the well-known PID controller [43], the current state is not only evaluated; MPC keeps in mind where the system will be in the future ensuring better control input. The MPC makes use of a cost function V_N, which traditionally is a sum of stage costs ,

$$V_N\left(x_0, u\right) = \sum_{k=0}^{N-1} \ell(x_k, u_k), \tag{1.1}$$

where k is the timestep, $x \in \mathbb{R}^n$ the system state-space vector, $u \in \mathbb{R}^m$ the system input and l is the stage cost. The latter, often has the following quadratic form,

$$\ell(x_k, u_k) = \frac{1}{2} x_k^T Q x_k + \frac{1}{2} u_k^T R u_k, \tag{1.2}$$

where $Q \in \mathbb{R}^{n \times n}$ and $R \in \mathbb{R}^{m \times m}$ are positive definite matrices that weight the state and input respectively. An optimal control problem can then be formulated as following,

$$\underset{\mathcal{U}_u}{\arg\min} \quad \mathbb{P}_N(x_0) : V_N = \sum_{k=0}^{N-1} \ell(x_k, u_k) \tag{1.3a}$$

$$\text{subject to} \quad x_{k+1} = f(x_k, u_k), \;\; k = 0, 1, \dots, N-1, \tag{1.3b}$$

$$x_k \in \mathbb{X}, \;\; k = 0, 1, \dots, N-1, \tag{1.3c}$$

$$u_k \in \mathbb{U}, \;\; k = 0, 1, \dots, N-1, \tag{1.3d}$$

$$x_0 = x(t), \tag{1.3e}$$

where f represents the systems dynamics in the form of a linear time-invariant system $x_{k+1} = Ax_k + Bu_k$. The matrix $A \in \mathbb{R}^{n \times n}$ and $B \in \mathbb{R}^{n \times m}$ are the corresponding discrete time state-space matrices. Furthermore, $\mathcal{U}_u = \left[u_0^{\mathrm{T}}, u_1^{\mathrm{T}}, \dots, u_{N-1}^{\mathrm{T}}\right]^{\mathrm{T}}$, x_0 is the initial initial state of optimization problem and is set equal to the most recent measurement $x(t)$. Lastly, $\mathbb{X}$ and $\mathbb{U}$ are the admissible state and input sets respectively.

The MPC predicts the future states of a system by using its equations of motion, which are derived from a system model. Because of this advantage, MPC is more sophisticated compared to PID. The idea of predicting future states based on a model is also used by the Linear Quadratic Regulator (LQR). However, the optimization for LQR is done offline, whereas the MPC controller executes the optimization every timestep and is thus called online. For each timestep, new measurements are collected, such that every new optimization problem depends on the system's current state. Because of this online approach, the MPC controller is considered more flexible than LQR. After an input sequence is found that minimizes a specific cost function over N steps, the first element of this sequence is inserted into the system. These steps are combined together in Algorithm 1 [44]. Carrying out this strategy every timestep is also known as the *Receding Horizon* principle. In Figure 1.5, these main principles of MPC can be observed; the finite prediction horizon, the prediction of where the system will be in the future, and the system are steered to a reference trajectory.

Algorithm 1 MPC Algorithm

```
Measure current state $x(t)$
Set $x_o := x(t)$
Calculate $\mathbb{X}$ and $\mathbb{U}$
Solve $\mathbb{P}_N$ (1.3) for $x_0$
Select first element of calculated input sequence $\mathcal{U}_u$
Inject this control input $u_0^{\mathrm{T}}$ into the plant
```

Several MPC papers for AV applications have been presented in the literature. A handful of them will be covered briefly to demonstrate the broad capabilities of MPC. In [39], an MPC based on the Bicycle model is used to control an AV. In contrast with other references, the road in this research is considered slippery, making the tire-road interactions extra relevant. In [45], an MPC tracks a path while avoiding obstacles. Next to the steering angle of the front wheels, the individual wheel torques are controlled by the MPC controller, introducing more degrees of freedom. With the improvements in hardware, more advanced optimizations are possible. In [46], a non-linear MPC problem is solved by using an iterative linearization approach. When a simplified vehicle model is used, performance limitations could arise due to these assumptions. In [47], this problem is tackled by incorporating the actuator dynamics of the steering system into the MPC control design. Usually, control designs are based on LTI systems. However, in practice, linear time-varying systems could be considered for a more accurate representation [48]. Eventually, theoretical proposals should be tested on practical testbeds to investigate their practical feasibility. In [49], an MPC controller for AVs is designed where simplified algorithms are applied such that a control strategy is implemented in a 16-bit microcontroller. In practice, an AV will face difficult situations. Therefore, a robust MPC controller was designed to cope with additive disturbances, such as varying wind and road friction while driving at high speed or on a low friction road [50]. Finally, for a more detailed overview of the different applications with MPC, the reader is referred to a recent review [51].

Economic Model Predictive Control

A recent extension of standard MPC is eMPC [52]. With standard MPC, the controller tries to steer the system to a predetermined set-point. A real-time optimization (RTO) algorithm, in the form of a motion planner, determines this goal. The RTO optimization runs at a slower rate than standard MPC [53], such that the standard MPCs convex optimization problem can be solved at a higher rate. Generally, one would like to optimize a system for *economic* goals (e.g. profits, cost reduction, input usage reduction) [54]. Climate control in a building is a logical application [55], [56], as the goal is to heat a building while minimizing the amount of money spent. So with standard MPC, a reference is calculated by the RTO.

With the improvements of computational power, it is not always required to let the control layer solely solve a convex problem. The concept of eMPC is to eliminate this extra step and directly optimise over these economic goals by modifying (1.2) to

$$\ell(x_k, u_k) = g_{\text{economic}}(x, u), \tag{1.4}$$

where $g_{\text{economic}}(x, u)$ represents the underlying economic goals. Furthermore, the model on which the RTO is based is not always consistent with the one MPC uses, preventing loss of information [57]. For standard MPC with a convex state cost, theoretical stability can be guaranteed [58]. With (1.4), however, convexity is not always the case. For eMPC, theoretical stability can be proved by making use of dissipativity [52].

The term *economic* is an abstract definition. In [59], a heavy truck is forced to make smooth turns, which is vital due to heavy stresses on the axles. This target, represented by curvature functions, could be interpreted as the *economic* goal of the system. The specific trajectory that the truck drove does not matter, as long as its corresponding curvatures are limited. Furthermore, another straightforward eMPC application is to influence the car-following behaviour of groups of vehicles, as this improvement could improve fuel usage. This goal is a logical application of eMPC [60], [8].

Another AV application integrates the motion planner in the cost function of the eMPC [30], [32], [34], [61], [62]. The authors do not specifically address eMPC, but they do state that their control technique renders the RTO layer unnecessary. Without the need of an intermediary reference, the AV is controlled directly. This architectural simplification is accomplished by optimizing over a cost function that includes APFs, which are explained next.

1.2.2. Artificial Potential Functions

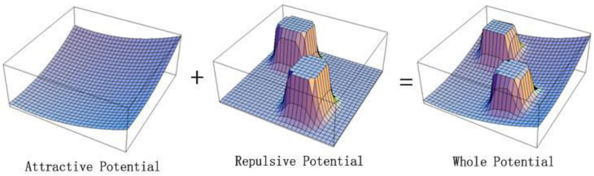

Figure 1.6: An example of an environment represented by potential functions [63]. The goal is represented by slopes (left), two obstacles are represented by two steep hills (middle), and together they are combined (right). If a ball were placed on the slope, it would roll down while avoiding the two local peaks, representing the obstacles.

The APF method is a motion planner that finds a path for a robot to track from one configuration to another. The APF method was first introduced in the 1980s [64], [65], [66]. The concept of the APF is based on the idea that the environment of a robot, in which one tries to find a path, is modelled by so-called potential functions, which can be split into two categories. The first are attractive potential functions representing the robot's goal(s). The second contains repulsive potential functions that represent the obstacles to avoid. The *attractive potential* $U_{\text{attractive}}(x)$ and *repulsive potential* $U_{\text{repulsive}}(x)$ are combined together,

$$U(x) = U_{attractive}(x) + U_{repulsive}(x), \tag{1.5}$$

where x is the state of the system. The following thought experiment explains how a path is found from these combined APFs. In Figure 1.6, (1.5) is illustrated by a 2D system. Plotting the calculated potential results in a 3D shape, resembling a mountainous area. If one would imagine placing a ball on this hill, gravity would cause the ball to roll toward the valley. When the ball encounters the two pillars, the ball rolls around them, avoiding the obstacles represented by these pillars. This comparison with gravity is line with the way the APF method traditionally finds a path by using gradient descent [67]. This path, hereafter can then be tracked by a feedback controller.

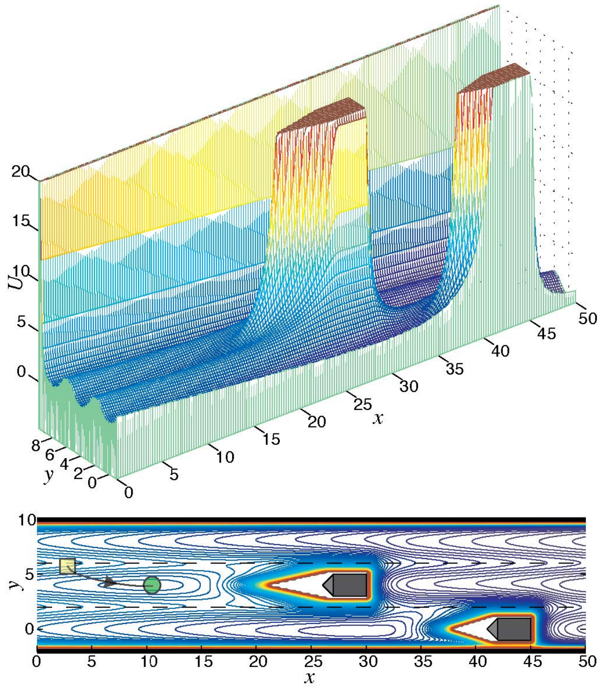

Figure 1.7: An example of four different APFs together [67]. Three lanes and two obstacle vehicles can be seen. In the bottom part, the resulting path can be seen. The path starts at $(x = 3, y = 6)$ and ends at $(x = 10, y = 4)$, due to a local minimum.

In Figure 1.7, an example can be seen where the different APFs are used together as a motion planner. Multiple APFs, representing two obstacle vehicles, two-lane markers (i.e. three lanes) and one road boundary can be observed. Furthermore, it can be noticed that the obstacle vehicle and road boundary have a different maximum potential value than the lane markers. This is because the AV is allowed to cross a lane marker (e.g. lane changing). However, coming close to the road boundary or another vehicle can result in a crash that should be avoided. By combining these APFs, an appropriate path for the AV can be calculated.

Applications

APFs are often used as a motion planner for AVs. Mainly, three types of APFs are used to represent the AVs surroundings; road boundaries, lane markers and obstacle vehicle. In [67], these classic APFs are used to present a full-fledged motion planner. Because not every obstacle vehicle is equally important, the obstacle APF can be extended. A vehicle heading towards the ego vehicle is more dangerous than one driving away. Obstacle APFs can be improved by taking the heading, velocity or acceleration into account as well [68], [69], [70]. Furthermore, crashing into a heavy truck has a more significant impact than crashing into a small city car. In [71], the obstacle APFs depends on the mass of the vehicle as well. Next to the motion and size of the car, the driver influences the amount of risk. Staying farther away from an aggressive road user is enforced by the obstacle APF in [72], [73]. In practise, more objects than road boundaries, lane markers, or obstacle vehicles present problems. The shifting light conditions in a tunnel, for example, might be difficult. A tunnel APF is therefore created [74]. Furthermore, an AV could face an scenario where a collision is unavoidable. APFs can then be used as well to handle these unavoidable situations [75], [76]. Real-world tests are required to verify computer simulations. In [77], [78] it was found that the APF method is a powerful method for real-world use as well. Because APFs contain different parameters that can significantly change the shape, and, thus the function of the APF, it is crucial to choose them wisely. So far, most of the research presented has used custom-tuned APFs. Another approach is to base these parameters on actual human driving behaviour by fitting APFs on traffic data [79], [80], [81], [82], [83].

1.2.3. Comprehensive Predictive Control

Traditionally, APF and (e)MPC are used separately in the AV design as solutions for motion planning and control [45], [68], [84]. This part explains how these two methods are integrated into one solution.

Integration

Both eMPC and APF rely on mathematical objective functions for optimization. Because of this structural commonality, the APF-eMPC framework can be formed. The APF term U (1.5) can be integrated into the original stage cost function of the eMPC (1.2),

$$\ell(x_k, u_k) = K_U U(x_k) + \frac{1}{2}(x_k - x_{\mathrm{r}})^T Q (x_k - x_{\mathrm{r}}) + \frac{1}{2} u_k^T R u_k, \tag{1.6}$$

where $K_U \in \mathbb{R}$ is a gain parameter and x_{r} a predetermined reference. This objective function still has the same goal of tracking a reference trajectory while minimizing input. With this extension, however, the reference trajectory can be simplified; obstacle avoidance is done due to the addition of the obstacle APF in the objective function. The motion planner does not have to handle obstacle avoidance anymore. This part is thus done by the MPC itself [68], [76], [85], [86], [87], [88]. These studies have demonstrated that the AV can perform lane keeping, lane changing and overtaking other vehicles while avoiding obstacle vehicles. Figure 1.9 shows an example where the ego AV tracks a reference while avoiding other vehicles. The controller does receive a basic reference, which does not avoids the obstacle vehicles. However, because U contains information about these obstacles, the controller is able to avoid these vehicle.

Basic decision-making is thus carried out without a any decision making module, as explained by [87]. This architectural simplification is visualized in Figure 1.8, where the original PDM architecture from Figure 1.4, is adjusted.

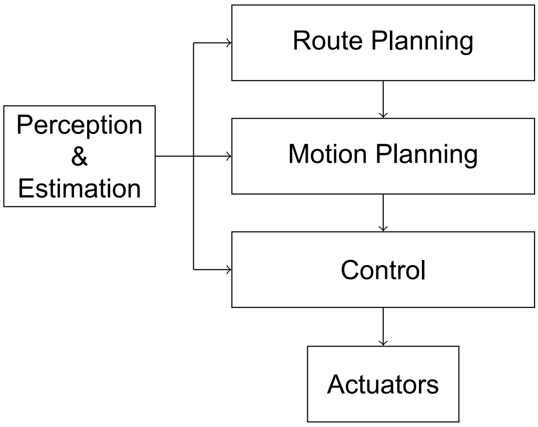

Figure 1.8: Overview of the AV architecture, where *Behavioural-Decision Making* is incorporated into the control layer, adapted from [30]

Comprehensive Predictive Control

One step further is omitting the reference $\frac{1}{2}(x_k - x_{\mathrm{r}})^T Q (x_k - x_{\mathrm{r}})$ from the stage cost (1.6), as a whole [30], [35], [32], [34], [61], [62]. Again, the APF U is added to the objective function. The optimization then contains all the required information to maintain a safe and desirable position on the road,

$$\ell(x_k, u_k) = K_U U(x_k) + \frac{1}{2} u_k^T R u_k. \tag{1.7}$$

These studies also demonstrate that the AV can perform lane keeping, lane changing and overtaking other vehicles while avoiding these obstacles. In Figure 1.11, an overtaking manoeuvre using this method is executed. As no reference is provided, the ego AV does not have to change back to its original lane. However, because another (stationary) vehicle is ahead, a lane change is executed again, and the first obstacle vehicle is also overtaken. Thus a complicated driving manoeuvre is possible *” without any driving decision-making and trajectory planning ”* [30]. The new architectural simplification

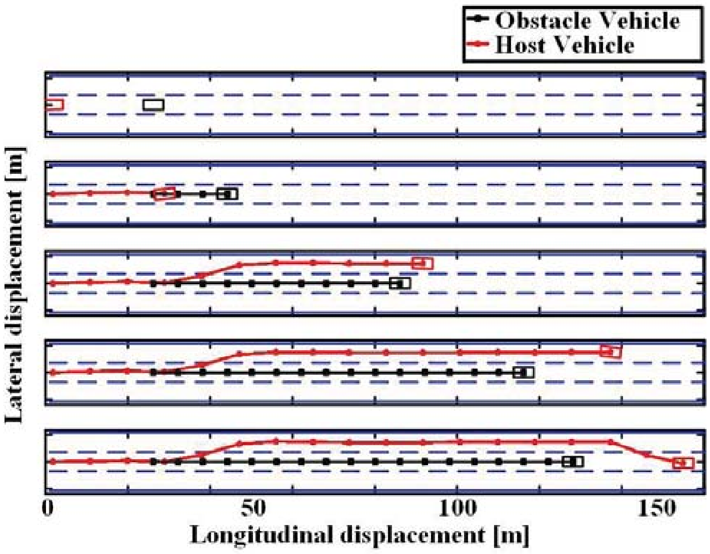

Figure 1.9: An ego AV tracks a predetermined reference, which does not take other vehicles into account [30]. Because the cost function is set up as (1.6), the ego AV tracks the reference while avoiding obstacle vehicles [87].

of this new strategy is visualized in Figure 1.10. The motion planner and behavioural decision-maker modules are now both omitted.

The authors from [30], have named this approach *Comprehensive Predictive Control* (CPC) because three modules are merged into one. They clearly explain the benefits of this new framework: "*The decisions [that were made] are neither given by other parts of the automated driving system nor specifically made by our comprehensive predictive control method itself. The automated vehicles do not have the knowledge of the [manoeuvres] and bear the capability to predict them in advance; it just simply executes the commands generated by this method*." Next to simplifying the AVs architecture, this approach would also allow for more realistic and improved research results [30], [34]. The latter research explains that traditionally the different AV tasks are decomposed into subproblems. These corresponding solutions, however, do not always work well together [57]. With this CPC approach, separate solutions for decision making and motion planning are no longer required as all the information is contained in optimizations cost function of controller. This CPC strategy is thus a fundamentally different approach compared to the classic architecture from Figure 1.4: the AV can navigate itself on the road while avoiding obstacles without the need of a RTO.

These studies have thus demonstrated that the CPC control strategy, based on the APF-eMPC framework, is capable of autonomous driving [35], [32], [34], [61], [62]. However, as the objective function is non-linear and non-convex, no theoretical guarantees are yet discovered. Furthermore, these studies have only shown demonstrations. A more extensive (numerical) analysis can reveal more about the possibilities and limits of this approach.

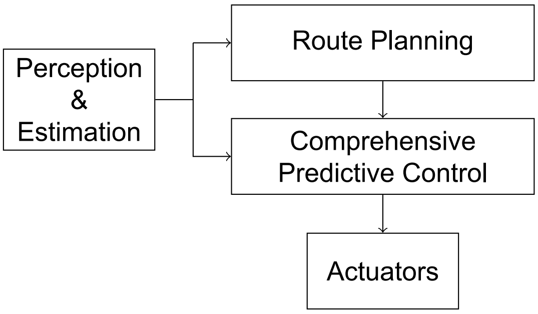

Figure 1.10: Overview of the AV architecture, where the *Behavioural-Decision Making* and the *Motion Planning* layers are incorporated into the control layer; this approach is called *Comprehensive Predictive Control*, adapted from [30]

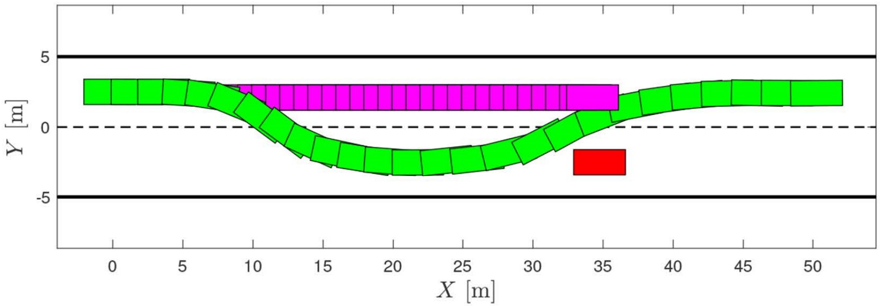

Figure 1.11: The green ego AV avoids two obstacle vehicles by making two lane changes; the purple vehicle drives slower than the ego AV, and the red vehicle is stationary. No reference path was provided to the ego AV, and because the cost function is set up as (1.7), the AV still manages to find a trajectory.

1.2.4. Connected Autonomous Vehicles

Research on the Connected Autonomous Vehicle (CAV) started in the 2000s [89]. The promise of the CAV ensures that road use will become even more efficient and safer than the AV. The CAVs fundamental requirement is that it is able to share information with its surroundings. Improper connectivity, however, can have significant impact on the performance. The following sources could serve as a starting point if the reader is interested [6],[90], [91], [92]. The rest of this thesis does not explicitly discuss solutions for this problem. Furthermore, solely V2V is discussed. Other types of connectivity, V2I for instance, can be found in [6], [22]. The progression of cruise control to CACC is covered first, followed by a discussion on stability. Following that, the platoon application is explored, followed by an discussion on the state-of-art for platoons based on the CPC approach. Finally, APFs that enforce platoon behaviour are addressed.

Cruise Control Evolution

The well-known cruise control functionality is one of the first (semi)autonomous driving features. With the newer (ACC) variant, the driver is no longer required to constantly turn the cruise control on or off when another vehicle is to close. Next to the fact that this feature facilitates the driver's comfort, traffic flow, in general, can improve as well. When humans do not brake unnecessary, phantom traffic jams will reduce [92]. Preventing this problem will lead to enhanced traffic flow, increased road capacity and thus reduced fuel consumption [93], [60], [8], [94]. With CACC, the CAVs no longer need to measure and estimate the motion states of the obstacle vehicles. The problems of measurement inaccuracies and computational delays reduces. By extending ACC to CACC, these advantages increase even more [24], [28], [95].

Platoon

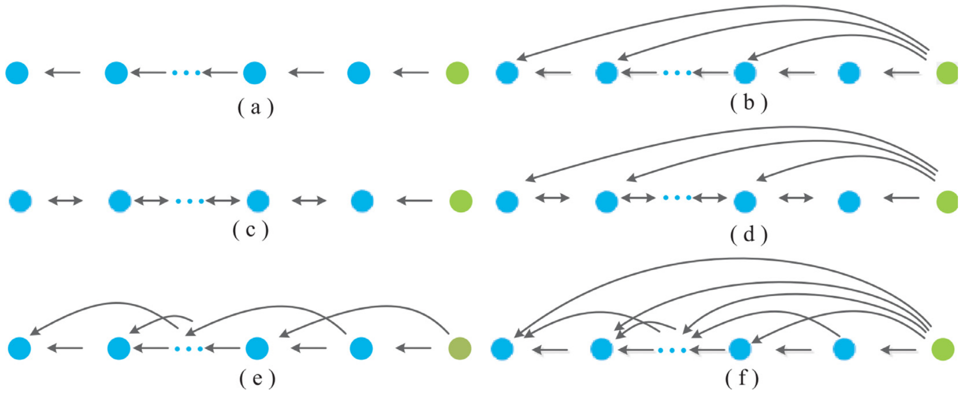

Figure 1.12: Different ways of information sharing in a platoon exist. Here six different information flow topologies are shown. The green node represents the leader vehicle and the blue ones the followers [96].

If multiple CAVs were using CACC at the same time, more information is faster available which has the potential to improve cooperative behaviour even further. For example, instead informing that something has happened at the front of the group via braking vehicle by vehicle, the group could be informed via V2V connectivity. The concept of CAVs working together as a group is referred to as a platoon. Different options for information sharing exist and are visualized in Figure 1.12 [96]. Here each CAV calculates his own set of actions, so this setup is referred to as decentralized control [97] [98], [96]. Before a platoon is formed, the CAVs first navigate themselves to the correct position on the road to creating the required formation [99], [100], [101], [102]. Furthermore, platoons are not limited to using one lane. In [103], [104] solutions are discussed where multi-lane platoons are formed. Platoons merging from two lanes into one lane is studied in [105]. Just as regular driving, a platoon could decide to make a lane change. However, because of the size of the platoon, extra challenges occur. Solutions for safe operation during a platoon lane change are explored in [106]. Finally, a single CAV entering the highway via an onramp and merging into the platoon is discussed in [107], [108]. If the reader would like to read on the topic of platoons, the following surveys are a good starting point [20], [21], [109], [110], [27], [28], [111]. All these studies ensure that a group of vehicles in the form of a platoon can form a tight group.

When vehicles drive closer, safety becomes a more significant concern. Therefore, the stability of a platoon is also vital. A group of vehicles is often modelled and simulated as a strain of nodes interacting with each other; the general behaviour can be compared to a group of nodes moving back and forth with strings in-between [96]. In literature, the problem of phantom traffic jams is therefore referred to as string instability. In literature, multiple kinds of string stability definitions can be found. One of the earliest definitions was discussed in [112]. In [113], an extensive overview can be found, which explains how these different definitions also compare and connect. The idea of string stability implies that disturbances in position, speed or acceleration do not accentuate while propagating backwards along the string of vehicles [114]. However, when string instability occurs, phantom traffic jams can result.

Because the improvement of string stability mainly improves longitudinal control, stability research often neglects lateral control [60], [8], [94], [115], [93], [116], [117], [118], [119], [120], [121]. However, vehicles must still steer during car-following to follow the road's curvature and adjust for noise and disturbances. Because the longitudinal and lateral dynamics are coupled, lateral dynamics should also be looked into during string stability analysis [122], [123], [99].

Comprehensive Predictive Control for a Platoon

The APF-eMPC framework has been applied for platoon research as well [34]. This implementation is similar to the original study of CPC for AVs introduced in Subsection 1.2.3. In [34], no reference is provided, and the APF is integrated into the eMPC cost function. An APF enforces platooning in the form of a quadratic function. This APF ensures that the ego vehicle mains a certain distance behind the vehicle in front. The main focus of this research is the concept of *Hybrid Automata*; a CAV is allowed to follow another CAV when it has a direct line of sight and receives V2V information simultaneously. Because CAVs will not always drive in a platoon, the vehicles switch between solo and combined driving. However, the paper merely demonstrates the workings of the forming and splitting of the platoon based on this *Hybrid Automata*. An extensive numerical analysis of the platoon's stability, just as with its AV counterpart, still lacks; it could be interesting to explore the limits of this specific CPC solution based on the quadratic car-following APF.

Car-Following with Artificial Potential Functions

Safety is of utmost importance while attracting vehicles closer to each other. One of the main goals of platoon research is to reduce inter-vehicle distances by improving car-following behaviour. In literature, two styles of APFs that actively enforce car-following can be found. The first APF is based on a quadratic function; the convex shape attracts the ego vehicle towards the global minimum of this function [34], [121], [115]. However, this specific type of APF could be undesirable as it is symmetrical. Coming too close to the preceding vehicle is a more significant problem, due to a collision, than staying too far away. Therefore, gap closing does not have to happen as fast as collision avoidance.

The second style is an asymmetrical APF containing a repulsive and attractive part [95], [122], [25], [124], [83], [82]. The attractive part is not as strong as the quadratic function, which could ensure that the ego vehicle closes the gap more gradually than the quadratic APF [34].

In [19], a similar solution, as the asymmetrical APF, is created for the problem that traditional approaches would close the gap between vehicles too fast such that this quick gap-closing results in uncomfortable responses and negatively influences string stability.

The amount of research on CAVs in a car-following platoon setting using the APF-eMPC framework is little, as only demonstrations have been shown so far. A more extensive (numerical) analysis is desired. Lastly, these studies have used straightforward solutions that do not mimic realistic driving behaviours.

1.3. Research Question

The following research question is formulated based on the found gaps in the state-of-the-art.

Main Thesis Research Question

How can the Artificial Potential Function - economic Model Predictive Control framework be used more effectively for a Connected Autonomous Vehicle application?

To answer this research question, the following sub-questions are answered first,

Sub Research Questions

I What APFs can achieve platoon-specific behaviour?

II Is there a performance guarantee for the APF-eMPC framework?

III What metrics can be used to measure the performance of the APF-eMPC framework?

IV For which kind of CAV-specific scenarios can the APF-eMPC framework be used?

1.4. In This Thesis

This chapters has explained how the APF-eMPC framework can be an effective solution for AV and CAV applications. However, no thorough performance analysis has been carried out. That is why this thesis conducts a numerical analysis to explore the limits for both the AV and CAV.

The work of [30] served as the foundation for the design of an AV based on the APF-eMPC framework. The APF-eMPC controller is formulated in Chapter 2. Furthermore, this chapter covers the method for the numerical analysis: four different basic driving maneuvers are used to test the controller. Hereafter, Chapter 3 discusses the the CAV part. Based on [32], the AV controller is expanded to a CAV. This chapter compares two APFs meant for platooning. Finally, this thesis concludes in Chapter 4 and discusses recommendations for future work.

2

Autonomous Vehicle

This chapter examines an AV based on the APF-eMPC framework. First, Section 2.1 introduces the dynamical vehicle model that serves as the controller's foundation. Hereafter, Section 2.2 discusses the different APFs which are used by the controller. Hereafter, the designed controller is presented in Section 2.3. Recent studies on the APF-eMPC framework are case studies that only demonstrate single simulations. This chapter goes one step further by examining the control strategy more thoroughly. Multiple experiments are conducted with a linear and non-linear plant, and with different amounts of white noise. Three types of essential manoeuvres are used to test the capabilities of the AV. In Section 2.4, these different experiments and more specific details regarding the numerical experiments are discussed. The results from these thorough experiments are presented in Section 2.5 and finally the key-points are summarized and discussed in Section 2.6.

2.1. Vehicle model

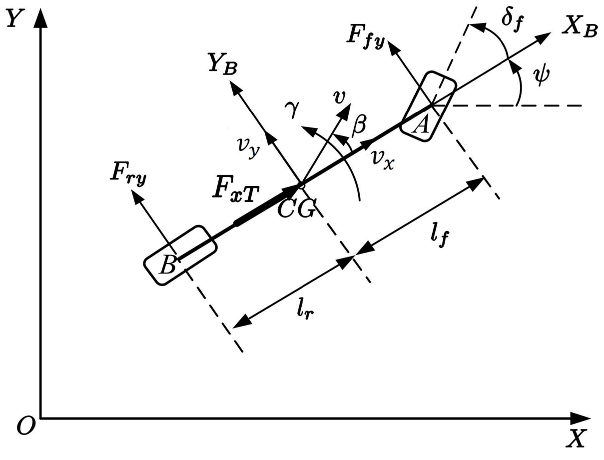

Figure 2.1: Bicycle model schematic, adapted from [30], where forces due to the road-wheel interaction are part of the system. It is assumed that these forces act on just two wheels instead of four, which explains the model's name.

The dynamical model which forms the basis for the controller is the *Bicycle Model*. This vehicle model was first introduced in 1950s [125]. A visualization is shown in Figure 2.1. The differential equations are as following [30], [68],

$$
\begin{aligned}
m\dot{v}_x &= F_{x_T} + m v_y \gamma \\
m\dot{v}_y &= F_{f_y} + F_{r_y} - m v_x \gamma \\
I_z \dot{\gamma} &= F_{f_y} l_f - F_{r_y} l_r \\
\dot{\psi} &= \gamma \\
\dot{X} &= v_x \cos\psi - v_y \sin\psi \\
\dot{Y} &= v_x \sin\psi + v_y \cos\psi,
\end{aligned}
\tag{2.1}
$$

where ψ is the heading of the car, γ is the yaw rate, X and Y are the longitudinal and lateral position in the global frame. Furthermore, v_y and v_x represent the velocities in the local longitudinal and lateral direction. The variable I_z represents the moment of inertia about the z-axis, which is perpendicular to the $X - Y$ plane and has the opposite positive direction to gravity. Furthermore, m is the mass of the car, l_f and l_r are the distances from the front and rear wheel to the centre of gravity of the vehicle respectively,δ_F is the steering angle of the car. The outer width and length of the car are referred to as w_{AV}, l_{AV} respectively.

This vehicle model merges the right and left wheels into one wheel. By doing this, it is assumed that the forces due to the road-wheel interaction, F_{ry}, F_{fy}, act on just two wheels instead of four which explains the name of the model: *Bicycle Model*. The third external force, F_{x_T}, is the acceleration of the car. In this model, only lateral forces on the front and rear tires are considered. Herefor, a linear tire model by Pacjeka is used [126],

$$
\begin{aligned}
F_{fy} &= C_f \left(\delta_f - \frac{v_y + l_f \gamma}{v_x} \right) \\
F_{ry} &= C_r \left(-\frac{v_y - l_r \gamma}{v_x} \right),
\end{aligned}
\tag{2.2}
$$

where C_f and C_r are the cornering stiffness coefficients for the front and rear wheel respectively. The vehicle is controlled via the following dimensionless control inputs, $\left[\delta_f, F_{xT}\right]^{\mathrm{T}} = \left[C_\delta u_\delta, C_F u_F\right]^{\mathrm{T}}$, where C_δ and C_F are normalizing constants that ensure that u_δ and $u_f \in [-1, 1]$ are dimensionless variables that take the mechanical constraints of the steering and the engine into account. The corresponding continuous state-space matrices are formulated as following,

$$
\begin{aligned}
\dot{x} &= A_c x + B_c u \\
x &= \begin{bmatrix} u_x & u_y & \gamma & \psi & X & Y \end{bmatrix}^{\mathrm{T}} \\
u &= \begin{bmatrix} u_\delta & u_F \end{bmatrix}^{\mathrm{T}},
\end{aligned}
\tag{2.3}
$$

where

$$
A_c = \begin{bmatrix}
0 & x_{op_3} & x_{op_2} & 0 & 0 & 0 \\
a_{21} & a_{22} & a_{23} & 0 & 0 & 0 \\
a_{31} & a_{32} & a_{33} & 0 & 0 & 0 \\
0 & 0 & 1 & 0 & 0 & 0 \\
a_{51} & a_{52} & 0 & a_{54} & 0 & 0 \\
a_{61} & a_{62} & 0 & a_{64} & 0 & 0
\end{bmatrix},
\tag{2.4}
$$

$$
\begin{aligned}
a_{21} &= C_f \frac{x_{op_2} + l_f x_{op_3}}{m x_{op_1}^2} + C_r \frac{x_{op_2} - l_r x_{op_3}}{x_{op_1}^2} - x_{op_3}, \\
a_{22} &= -\frac{C_f + C_r}{m x_{op_1}}, \\
a_{23} &= -\frac{l_f C_f - l_r C_r}{m x_{op_1}} - x_{op_1}, \\
a_{31} &= \frac{(C_f x_{op_2} + C_f l_f^2 x_{op_3}) - (l_r C_r x_{op_2} - l_r^2 C_r x_{op_3})}{x_{op_1}^2 I_z}, \\
a_{32} &= -\frac{l_f C_f - l_r C_r}{I_z x_{op_1}}, \\
a_{33} &= -\frac{(l_f^2 C_f + l_r^2 C_r}{I_z x_{op_1}}, \\
a_{51} &= \cos(x_{op_4}), \\
a_{52} &= -\sin(x_{op_4}), \\
a_{54} &= -x_{op_1} \sin(x_{op_4}) - x_{op_2} \cos(x_{op_4}), \\
a_{61} &= \sin(x_{op_4}), \\
a_{62} &= \cos(x_{op_4}), \\
a_{64} &= x_{op_1} \cos(x_{op_4}) - x_{op_2} \sin(x_{op_4}),
\end{aligned}
\tag{2.5}
$$

$$
B_c = \begin{bmatrix} 0 & \frac{c_F}{m} \\ \frac{c_f c_\delta}{m} & 0 \\ \frac{c_f c_\delta l_f}{I_z} & 0 \\ 0 & 0 \\ 0 & 0 \\ 0 & 0 \end{bmatrix}. \tag{2.6}
$$

These state space matrices are calculated by linearizing the equations of motions Equation 2.1 around an operating point,

$$
x_{\mathrm{op}} = \begin{bmatrix} v_{\mathrm{ref}} & 0 & 0 & 0 & 0 & 0 \end{bmatrix}^{\mathrm{T}}. \tag{2.7}
$$

This operating points implies that the AV drives straight at a constant longitudinal speed of $v_x = v_{\mathrm{ref}}$, and $v_y = \gamma = \psi = X = Y = 0$. Here v_{ref} is the AVs reference velocity. Based on the continuous state-space matrices (2.4), (2.6), the discrete state-space matrices A, B are created using the zero-order-hold method from the SciPy library which is based on [127]; these matrices are calculated as following,

$$
\begin{bmatrix} A & B \\ 0 & I \end{bmatrix} = e^{\begin{bmatrix} A_c & B_c \\ 0 & 0 \end{bmatrix} T}, \tag{2.8}
$$

where T is the time-step. The discrete difference equation is as then following,

$$
x_{k+1} = A x_k + B u_k, \tag{2.9}
$$

where k is the k-th time segment. Furthermore, full measurability is assumed, and lastly the numerical values used for these parameters can be found in Table A.3 [30].

2.2. Artificial Potential Functions

This section discusses the different APFs used. During the design process of this thesis, the work of [30] formed the main inspiration. Changes that were made to original APFs of this research, will briefly be explained. All numerical values used for the APF parameters can be found in Table A.5.

2.2.1. Road

The main goal of the road APF is to steer the AV away from the road boundary while not interfering to much when the AV is distanced far enough. The widely used multiplicative inverse function was selected because it best meets these characteristics. Two changes were made to the original version[30]. First, a safety distance was added to account for the width of the AV. Secondly, the multiplicative inverse is constrained between the road boundaries; beyond the road boundaries the APF returns infinity. Because the multiplicative is symmetric around the road boundary, without this change, the AV can be attracted beyond the road boundary due to the discrete nature of the system. Finally, the road APF is constructed as following,

Artificial Potential Function: Road

$$U_{\text{Road}} = \begin{cases} k_{\text{Road}} \left(\frac{1}{(Y-(Y_{r,r}+S+r))^2} + \frac{1}{((Y_{r,l}-S+r)-Y)^2} \right) & \text{if } Y_{r,r} + S + r \leq Y \leq Y_{r,l} - S + r, \\ \infty & \text{otherwise,} \end{cases} \tag{2.10}$$

where k_{Road} is a gain, the safety distance $S = 0.5w_{\text{AV}}$. Furthermore, $Y_{r,l}$ and $Y_{r,r}$ are the right and left road boundaries respectively, and r represents measurement noise which will be discussed later. The function is convex and continuous for $Y_{r,r} + S \leq Y \leq Y_{r,l} - S$. In Figure 2.2, the road APF is visualized.

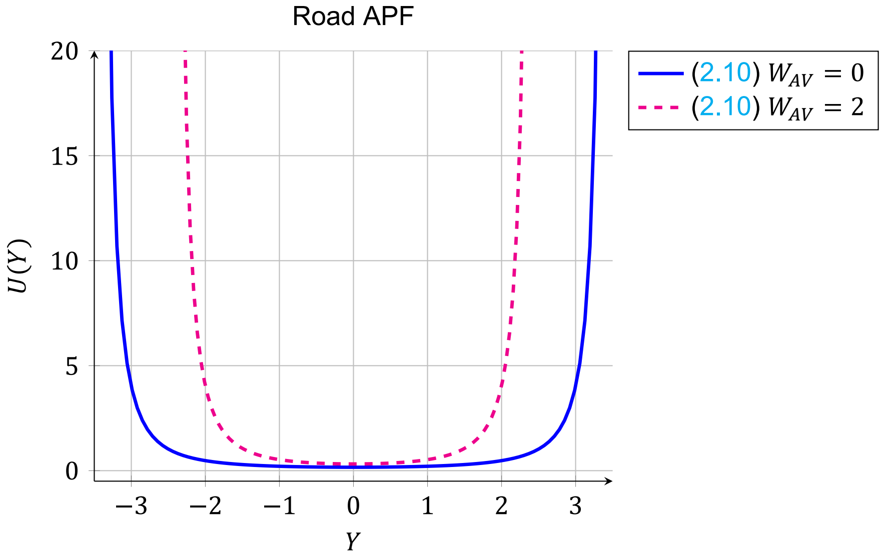

Figure 2.2: For this example, the left road boundary $Y_{r,l} = 3.5$, the right road boundary $Y_{r,r} = -3.5$, $k = 1$.

2.2.2. Lane

The goal of the lane APF is to repulse the AV away from the lane marker. In contrast with the road APF, the maximum value should be finite and relatively small allowing the AV still to change lanes when necessary. During the design process, it was concluded that the original lane APF [30], in the form of the non-convex Gaussian function was sufficient. No changes were made to the lane APF itself, other than different numerical values due to tuning of other new parts. All lane markers are represented by the following APF,

Artificial Potential Function: Lane

$$U_{\text{Lane}}(Y) = \sum_{i=1}^{n_L} k_{\text{Lane}} e^{-\frac{\left(Y-(Y_{l,i}+r)\right)^2}{2\sigma_{\text{Lane}}^2}}, \tag{2.11}$$

where $Y_{l,i}$ is the lateral position of the i-th lane, for a total of n_L lanes. Furthermore, σ_{Lane} is a parameter that determines the width of the APF and k_{Lane} is a gain parameter. Lastly, this function is continuous for $Y \in \mathbb{R}$. This lane APF can be seen in Figure 2.3 and in Figure 2.4 the combination of the lane and road APF can be seen.

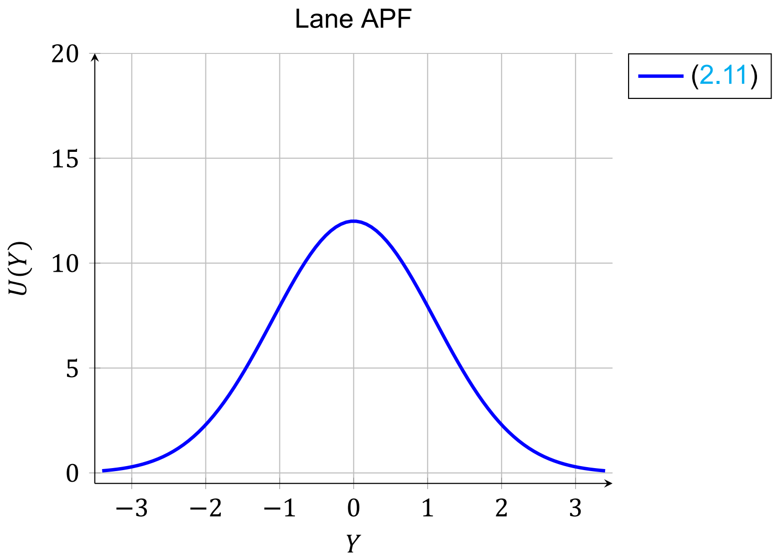

Figure 2.3: For this example, the lane marker is located at $Y_l = 0$, $k = 12$, $\sigma = 1.2$ and $w_{\text{AV}} = 2$.

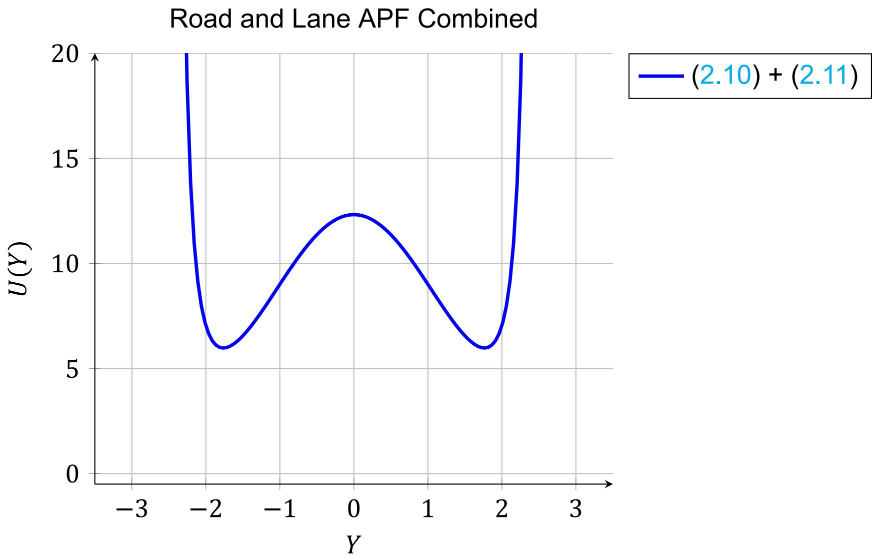

Figure 2.4: For this example, the left road boundary $Y_{r,l} = 3.5$, the right road boundary $Y_{r,r} = -3.5$, the lane marker $Y_l = 0$, $k_{\text{Road}} = 1$, $k_{\text{Lane}} = 12$, $\sigma = 1.1$ and $w_{\text{AV}} = 2$.

2.2.3. Obstacle Vehicle

To make sure the ego AV stays far enough away from each obstacle vehicle, the widely-used Yukawa function is used [65], [128]. This APF consists out of two parts; a multiplicative inverse and an exponential function, forming a non-convex function. Similar to the road APF, the multiplicative part ensures that the ego AV is repulsed away from the APF. The exponential part ensures the APF decreases quickly when the relative distance increases. This addition ensures that the obstacle APF does not interfere when there is enough space between the vehicles. In literature, the body of the obstacle vehicle is often represented by a rectangle set. The Euclidean distance K between the ego AV and this set of

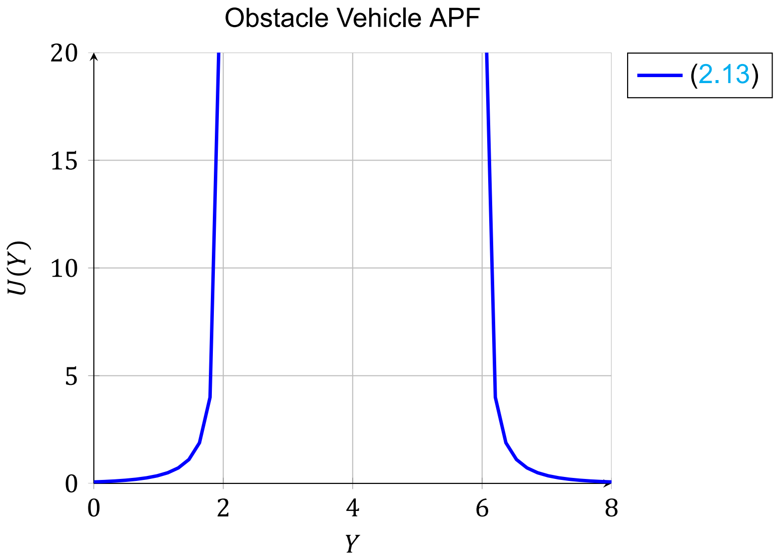

Figure 2.5: Visualization of the obstacle vehicle APF, where only the lateral axis is visualized. Here the enlarged set representing the obstacle vehicle is $B = \{Y | 2 \leq Y \leq 8\}$ and thus $w_{\text{AV}} = 2$. Lastly, $k_{\text{Obstacle}} = 1.5$, and $\alpha = 1$.

points B is calculated as following,

$$K = \min_{b \in B} \sqrt{(X - (b_X + r))^2 + (Y - (b_Y + r))^2}. \tag{2.12}$$

Similar to the addition with the road APF, this rectangle set is enlarged to account for the width and length of the ego AV. This APF is visualized in Figure 2.5. However, during the design process it was found that this rectangle shape was not sufficient. Inspired by [62], [67], an triangle was added behind the rectangle set. As explained by the latter reference; the triangle works like an wedge allowing for an easier lane change. The height of the triangle represents a one second time gap. These changes lead to the following obstacle APF,

Artificial Potential Function: Obstacle Vehicle

$$U_{\text{Obstacle}} = k_{\text{Obstacle}} \frac{e^{-\alpha K}}{K}, \tag{2.13}$$

where k_{Obstacle} is a gain parameter, and α is an parameters that determines the steepness of the function. In Figure 2.6, an example showcasing the obstacle APF and the resulted wedge can be seen.

2.2.4. Velocity

In literature, the ego AV is often enforced to drive forward by either velocity constraints [30] or a quadratic penalty term [34]. With the latter approach, the AV is still able to brake if an emergency situation would occur. To ensure, braking is also possible with the constraints approach, slack variables are introduced [30]. However, with both implementations, braking hard is penalized significantly. In an emergency situation, the AV should not be penalized as harsh to allow the AV to drive slower. Therefore, this thesis uses a Gaussian function is used for slower driving than the desired velocity. This implementations still penalizes the velocity around the desired velocity, similar to a quadratic penalty. However, if a special situation requires the AV to brake quickly, this movement is not penalized extra. For faster driving, the same quadratic function is used. The APF has the following form,

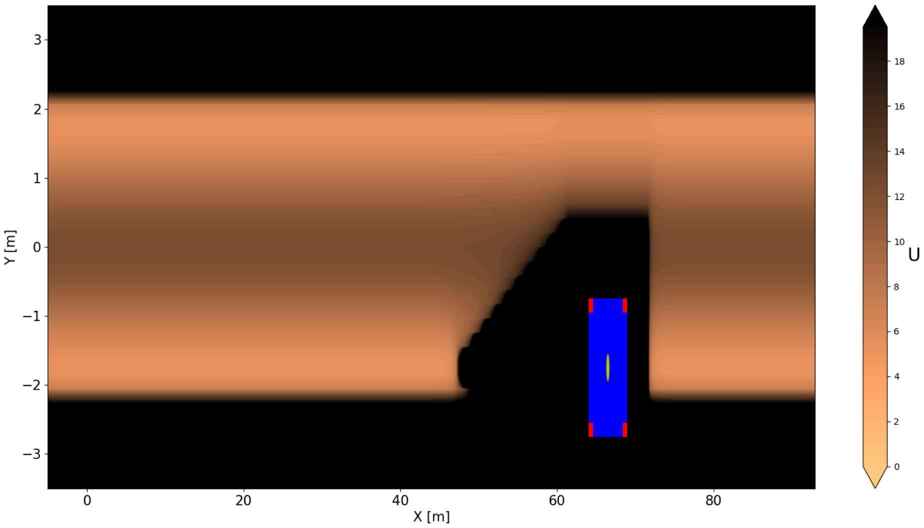

Figure 2.6: An example, where the triangle shape behind the obstacle vehicle creates an wedge, allowing for easier lane changing.

Artificial Potential Function: Velocity

$$U_{\text{Velocity}} = \begin{cases} k_{\text{Velocity}} - k_{\text{Velocity}} e^{-\frac{(v_x - v_{\text{ref}})^2}{2\sigma_{\text{Velocity}}^2}} & \text{if } v_x \leq v_{\text{ref}}, \ , \\ k_{\text{Velocity},2}\,(v_x - v_{\text{ref}})^2 & \text{otherwise,} \end{cases} \tag{2.14}$$

where k_{Velocity}, $k_{\text{Velocity},2}$ are a gain parameters, v_{ref} the reference velocity and σ_{Velocity} is a parameter that determines the width of the APF. Furthermore, the function is continuous but non-convex. An example is visualized in Figure 2.7.

2.2.5. Combined

The overall potential U is then defined as,

Artificial Potential Function: Total

$$U = U_{\text{Road}} + U_{\text{Lane}} + U_{\text{Obstacle}} + U_{\text{Velocity}}, \tag{2.15}$$

and an example of this combined function is visualized in Figure 2.8.

2.3. Controller Formulation

Based on the vehicle model, introduced in Section 2.1, and the different APFs, discussed in Section 2.2, the optimization problem can be formulated. First, the stage cost is defined as $l : \mathbb{X} \times \mathbb{U} \to \mathbb{R}$,

$$\ell(x_k, u_k) = K_u U(x_k) + u_k^{\intercal} R u_k, \tag{2.16}$$

where k represents the time step, K_u is a scalar constant, $R \in \mathbb{R}^{m \times m}$ is a positive definite matrix, N is the horizon, $\mathbb{X}$ is the set of admissible states, $\mathbb{U}$ is the set of admissible inputs and $\mathbb{N}$ is the set of the predicting horizon. From Equation 2.3 the size of the state $n = 6$ and input $m = 2$. The optimization problem can then be formulated where the objective function $V_N : \mathbb{N} \times \mathbb{X} \times \mathbb{U} \to \mathbb{R}$ is defined as a sum of stage costs,

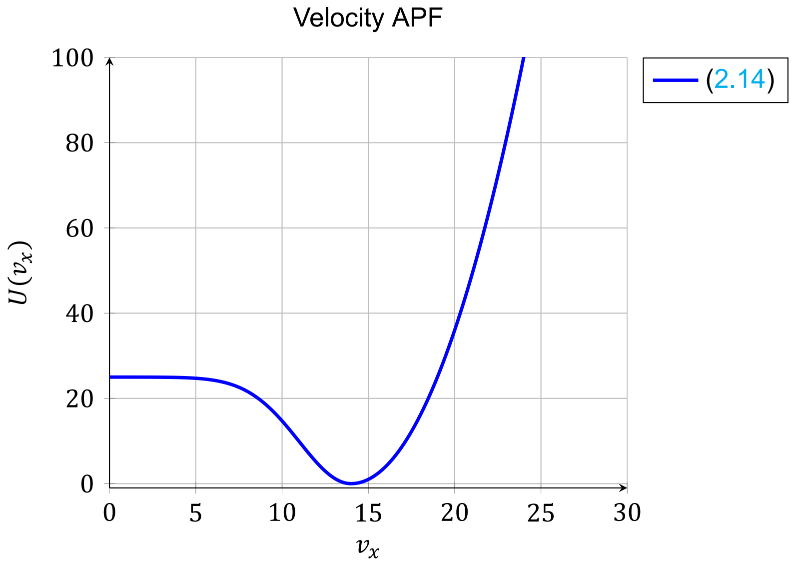

Figure 2.7: For this example, $k_{\text{Velocity}} = 25$, $k_{\text{Velocity},2} = 2$ $\sigma = 3$ and the desired velocity $v_{\text{ref}} = 14\ [m/s]$.

Optimization Problem: AV

$$\begin{aligned}
\underset{\mathcal{U}_u}{\arg\min} \quad & \mathbb{P}_N(x_0) : V_N = \sum_{k=0}^{N-1} \ell(x_k, u_k) && \text{(2.17a)}\\
\text{subject to} \quad & x_{k+1} = f(x_k, u_k),\ k = 0, 1, \dots, N-1, && \text{(2.17b)}\\
& u_{\min} \le u_k \le u_{\max},\ k = 0, 1, \dots, N-1, && \text{(2.17c)}\\
& \Delta u_{\min} \le u_{k+1} - u_k \le \Delta u_{\max},\ k = 0, 1, \dots, N-2, && \text{(2.17d)}\\
& \Delta u_{\min} \le u_0 - u(t-1) \le \Delta u_{\max}\ , && \text{(2.17e)}\\
& v_{x,\min} \le v_{x,k} \le v_{x,\max},\ k = 1, 2, \dots, N, && \text{(2.17f)}\\
& \gamma_{\min} \le \gamma_{x,k} \le \gamma_{\max},\ k = 1, 2, \dots, N, && \text{(2.17g)}\\
& x_0 = x(t) + r, && \text{(2.17h)}
\end{aligned}$$

where $\mathcal{U}_u = \left[u_0^{\mathrm{T}}, u_1^{\mathrm{T}}, \dots, u_{N-1}^{\mathrm{T}}\right]^{\mathrm{T}}$. The system dynamics $f : \mathbb{X} \times \mathbb{U} \rightarrow \mathbb{X}$ (2.17b) are represented by the linear time-invariant version $x_{k+1} = Ax_k + Bu_k$ from (2.9). The input is constrained by $u_{\min} \in \mathbb{R}^m$ and $u_{\max} \in \mathbb{R}^m$ defined in (2.17c). Comparable, the rate of change of the input is constrained by $\Delta u_{\min} \in \mathbb{R}^m$ and $\Delta u_{\max} \in \mathbb{R}^m$ defined in (2.17d) and (2.17e). Even-tough, the velocity APF (2.14) is used to make sure the AV drives with the desired velocity, (2.17f) ensures that the AV does not drive backwards ($v_{x,\min}$) and to represent the fact that the velocity of the AV cannot increase indefinitely ($v_{x,\max}$). Furthermore, (2.17g) limits the AVs yaw rate to prevent too violent movements. The limits $\gamma_{\min}$ and $\gamma_{\max}$ are set to the maximum yaw rate experienced during intense maneuvers [129]. The variable $x(t)$ is the current state of the vehicle which is determined through measurements. Lastly, these measurements are not perfect; r is measurement noise, which Subsection 2.4.6 discusses in more detail.

In Table A.4 and Table A.6 the values used for this optimization problem can be found. Appendix D explains how (2.17) is reformulated into a compact equivalent used in the numerical implementation.

2.4. Experiment Setup

This section explains how this APF-eMPC controller is tested under different circumstances. One of the main goals of this thesis is to carry out a more extensive analysis than currently can be found in literature. For each experiment, multiple simulations are carried out. Lastly, for each individual

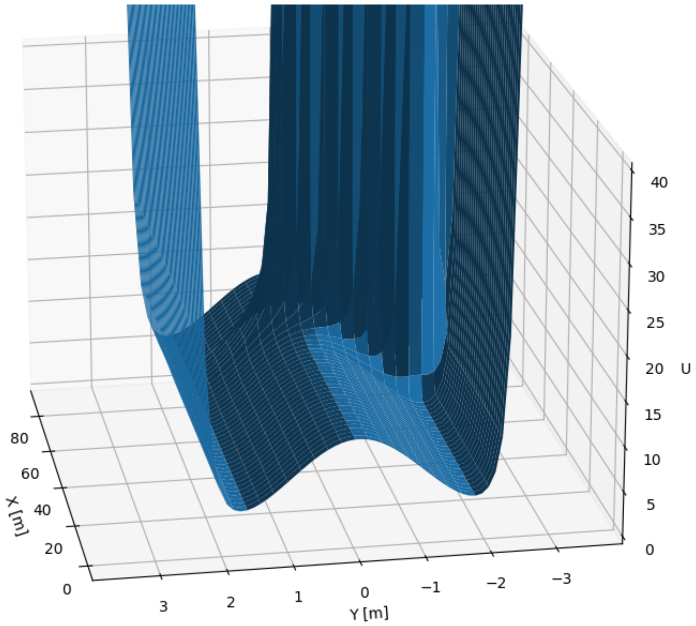

Figure 2.8: A visualization of the road, lane and obstacle APF. The road APF creates a larger canyon with a small hill in the middle due to the lane APF. The obstacle APF creates a larger pillar in the middle of the right lane.

simulation the AVs initial state is varied. This approach gives an insight of the capabilities and limits of the controller. All numerical values, used in a simulation, can be found in Table A.1.

First, Subsection 2.4.1 explains which performance metrics are used to measure the performance of the AV based on the APF-eMPC framework. Hereafter, the different scenarios are introduced in Subsection 2.4.5. Followed by an explanation how measurement noise is used to challenge the controller Subsection 2.4.6. In Subsection 2.4.7 the two different plants are discussed. Lastly, some more details regarding the simulation itself are given in Subsection 2.4.8

2.4.1. Performance Metrics

The general goal of the CPC strategy is to stabilize the AV while dealing with obstacles that the vehicle encounters during driving. As this optimization problem is non-convex, a numerical analysis is carried out. The lateral position is the state which is the most important. The corresponding transient response of the lateral position will be used to gain an understanding how the different obstacles are handled under the different circumstances.

Transient Response

For each scenario, a certain maneuver is expected. The parameters of the road and lane APF are tuned in such a way, that resulted local minima represent the middle line of each lane. From this information, the expected lane, and thus lateral position to which the AV should converge is known. The transient response with respect to the expected lateral position Y_{ss} is analyzed and not the final value. The lateral trajectory is normalized $Y_k = (Y_k - Y_0)/(Y_{ss} - Y_0)$, where Y_0 is the initial state of the simulation. Based on this normalized transient response, the following performance metrics are calculated.

The settling time, is defined as the first time that the error $|Y_k - Y_{ss}| \leq \epsilon_{st} |Y_{ss} - Y_0|$ and stays in this settling time band. The parameter ϵ_{st} is the settling time threshold and is equal to 2% [130] [131]. The rise time is defined as the time it takes the AV to rise from 10% to 90% of the way from Y_0 to Y_{ss}. Overshoot is calculated as $\max(Y_k) - Y_{ss}$.

2.4.2. Position Prediction Of Obstacle Vehicle

Because the APF-eMPC uses a prediction horizon, the future location of the obstacle vehicle ideally is known. This requirement, however, is not achievable without extensive V2V communication. As a consequence, the AV should either consider only the measured location or estimate the future position of the obstacle vehicle for the whole horizon. The second option is a problem of itself in literature [85],

[132], [133], [134], [135]. Therefore it is a stretch to presume that the AV can reliably compute the obstacle future motion states.

However, the first choice of assuming each vehicle to be static is also not acceptable. When the AV is behind an obstacle vehicle, it will behave conservatively; because the obstacle vehicle is perceived to be static, the ego AV will stay further away from the obstacle vehicle than necessary. Furthermore, presuming that the obstacle vehicles behind the ego AV are static is dangerous. If an AV wants to overtake a slower obstacle vehicle, it must change lanes. However, if an obstacle car in the adjacent lane moves faster than the ego AV, an accident may occur since the AV feels there is enough leeway for a lane change.

Following this reasoning, it would be illogical to design an AV that is incapable of predicting. Similarly to [30], the obstacle future position is predicted assuming constant velocity and heading during the optimization horizon.

Lastly, in [30] only the obstacles in front of the AV were considered in the optimization. However, for obstacles vehicles approaching the AV from behind, dangerous lane changes would still be the result. Therefore, this thesis also takes vehicles behind the AV into account as well. Assuming that the sensors are limited, only obstacle vehicles that are in a range of $L_{\text{min}} = 50[m] \leq X_{AV} \leq L_{\text{max}} = -25[m]$ are considered.

2.4.3. Horizon

Generally, a longer horizon is preferred such that obstacles can be anticipated earlier, for example. In [30] a horizon of $N = 20$ is used. During the different design iterations, computational time was a limiting factor that hindered the research progress. A larger horizon increases the computational time non-linear. Herefor it was decided to lower the horizon to $N = 15$. In combination with a time step of 0.1 seconds, the AV is able to look 1.5 seconds ahead. Computational time became bearable and the AVs control capability was still satisfactory.

2.4.4. Dimensions

Road

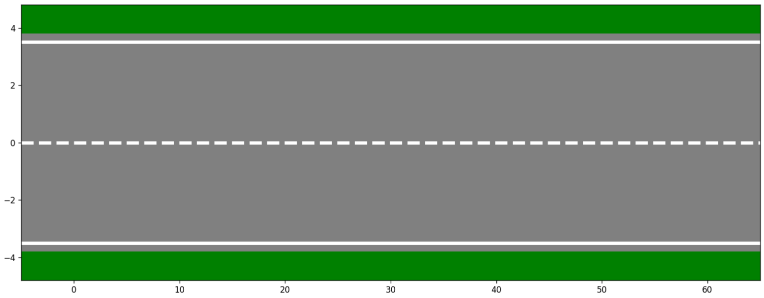

Figure 2.9: The grey road containing two lanes.

Fro the simulations from the original inspiration [30], a lane width of $5m$ was used. However, in Europe and especially the Netherlands, $3.5m$ is a more common lane width. Herefor, the road width was changed to $3.5m$ to ensure more realistic scenarios.

Furthermore, the road boundary is usually not the actual physical edge of the road. Often, there is an extra buffer, named a *redresseerstrook* in dutch. For these simulations an extra width of $0.3m$ is added to the road [136]. In Figure 2.9, both features are visualized.

Car

In [30], no outer car dimensions were shared. Based on [30, Fig. 2] and the other known parameters, it was estimated that the authors used an average city car for simulations. For the simulations carried out in this thesis, the outer dimensions of the car were set to $5m$ and $2m$ which approximates the dimensions of such an average city car [137].

2.4.5. Scenarios

There are different kinds of maneuvers possible on a road. In general, these can be split up into three basic maneuvers; lane keeping, car-following and lane changing. If an AV is able to execute these, the AV is capable to drive on a road. Inspired by the simulations from [30], three scenarios are formulated such that these three basic driving maneuvers can be tested. Finally, one extra scenario is used where everything comes together. Because these scenarios are relatively simple, an expected steady state Y_{ss} of the AV can be formulated.

Lane Keeping

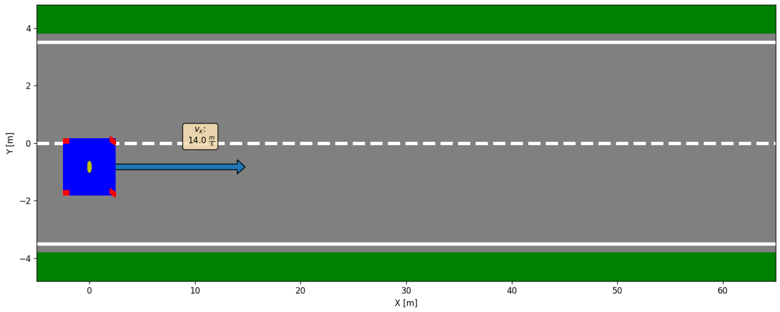

Figure 2.10: With the *lane keeping* scenario, the AV is initialized close to the middle lane marker with a longitudinal velocity of $14m/s$.

The AV is initialized at the side of the lane with no other obstacle vehicles around, visualized in Figure 2.10. Influenced by the road and lane APF, the AV should be able to drive back to the middle of the lane.

Car-Following

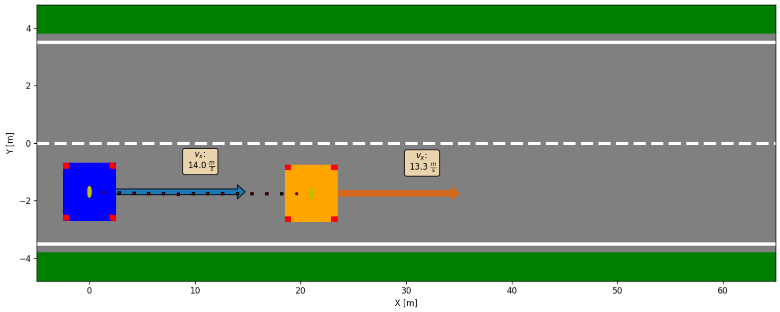

Figure 2.11: With the *car-following* scenario, the AV is initialized in the middle of lane with a longitudinal velocity of $14m/s$. In front of the AV, a yellow obstacle vehicle is ahead with a longitudinal velocity of $13.3m/s$.

The AV is initialized in the middle of the right lane, visualized in Figure 2.11. In the same lane, an obstacle vehicle is initialized in front of the AV. The obstacle vehicle drives 5% slower than the AV such that it will catch up. Is the AV capable of staying behind another obstacle vehicle without any unnecessary wild maneuvers?

Lane Changing

The AV is initialized in the middle of the right lane. In the same lane, a static obstacle vehicle is present, visualized in Figure 2.12. The AV is expected to make a lane change such that the obstacle vehicle is avoided and the AV can continue driving.

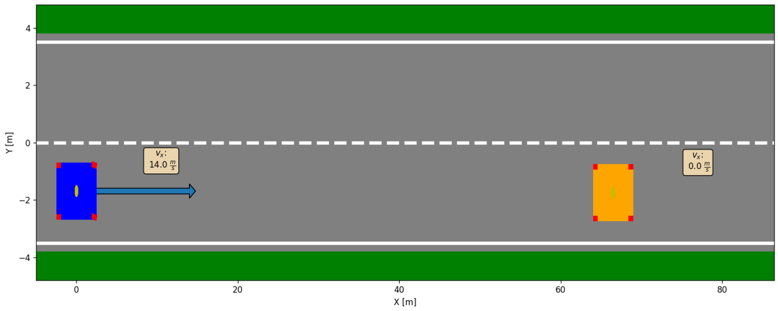

Figure 2.12: With the *lane change* scenario, the AV is initialized in the middle of lane with a longitudinal velocity of $14m/s$. In front of the AV, a static yellow obstacle vehicle is present.

Emergency Stop

This scenario a combination of the other three scenarios. The obstacle vehicle is initialized behind a moving obstacle vehicle. Suddenly, the obstacle vehicle performs an emergency brake with a deceleration of $8m/s^2$, which a modern vehicle with good brakes and tyres, is capable of [138]. To avoid crashing with the obstacle vehicle, the AV is thus expected to make a lane change. Will the prediction of the obstacles future position, explained in Subsection 2.4.2, be sufficient to anticipate the emergency stop: braking is not taking into account in this calculation.

2.4.6. Measurement Noise

The AV relies on measurements to make decisions. In practice, these measurements are not perfect. As the measurements become more inaccurate, the controller will have a harder time navigating the road. By simulating measurements noise as well, the limits of the controller will be found. During the simulations, noise is calculated as following,

$$r = r_i * W(0,1), \tag{2.18}$$

where W is a Gaussian function with mean zero and a standard deviation of one. Multiple numerical values for gain r_i are used in this thesis, which can be found in Table 2.1.

Parameter	Value	Unit	Explanation
r_0	0	-	No Noise
r_1	$1e^{-6}$	-	Noise level 1
r_2	$1e^{-5}$	-	Noise level 2
r_3	$1e^{-4}$	-	Noise level 3
r_4	$1e^{-3}$	-	Noise level 4

Table 2.1: Numerical values to imitate different amount of measurement noise

2.4.7. Plant

After an control input is found, it gets injected into a plant, which is a simplified model representing the AV. Two types of plants are used. The first is the same linearized model which the eMPC uses (2.9). The plant is thus updated by a linear algebra operation. The second plant is the non-linear Bicycle Model Equation 2.1. With this implementation, the plant is updated by solving a initial value problem for the equations of motions from the Bicycle Model (2.1) using the SciPy library. For both plants, it is assumed that the calculation of the control input happens instantly. As the second plant is more realistic, it is interesting to see under what circumstances the performance differs.

2.4.8. Simulation Details

The rest of this subsection will discuss some important details which are important for the simulation.

Optimization Method

To simulated the different experiments, the Python programming language is used. To solve the optimization the Constrained Optimization BY Linear Approximation (COBYLA) algorithm from the SciPy library is used. This derivative-free numerical optimization method was invented by Powell [139], [140]. As explained in the original work, no global properties or conditions can be given. As the acronym suggest, the objective function and constrains are linearly approximated by (N+1) points, which form the vertices of a simplex. Based on these approximations, a solution is found using trust regions. When the solution can no longer improve, the radius of the trust region is reduced similar to the way Nelder-Mead works [141]. When the radius of the trust region, tol, has become sufficiently small, the algorithm stops. The relevant numerical values can be found in Table A.6.

Orientation of Axis

The AVs local coordinate system is oriented following the right-hand rule [31]. The forward direction of the AV is along the local positive X axis. The local positive Y axis is in the direction when looking to the left from inside the car. The global axis are aligned in the same manner. The global X axis is parallel to the forward driving direction on the road. The global Y axis is perpendicular to this axis.

Auto Stop

During the simulations two checks are performed to see if the AV has either crossed the *redresseerstrook* or collided with another vehicle. If one of these events happen, the simulation is labeled as a fail and is aborted. To simplify these collision checks, it is assumed that the dynamical COG is the middle of the outer dimensions of the car.

Initial State

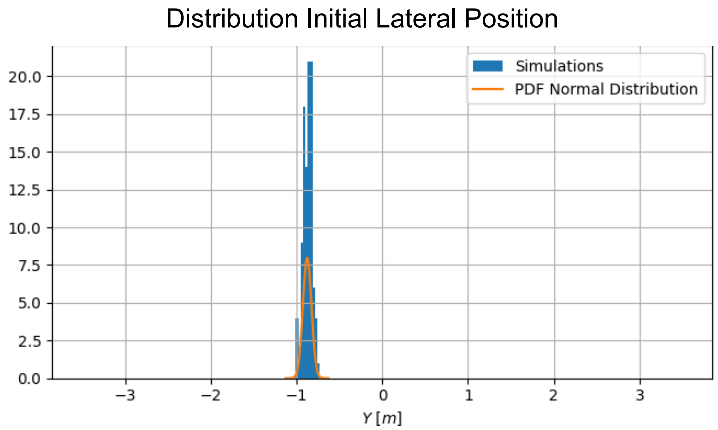

Figure 2.13: Distribution of the initial lateral positions off an lane keeping experiment for 100 simulations. The orange line represents the Gaussian function.

To explore the limits of the framework multiple simulations are carried out with different initial states. For each discussed scenario there is a specific base lateral position, which is perturbed using a Gaussian distribution, with a zero mean and standard deviation of $0.05m$. An example for the lane keeping scenario can be seen in Figure 2.13.

The initial longitudinal velocity is set to $14m/s, 50km/h$, which resembles a city road and is thus more realistic than [30]. The remaining states are set to zero.

Warm-start

To give each optimization a head start, a so-called warm-start is provided. The previous found input sequence is reused; the first time step (as it was just injected into plant) is deleted and the last time step is repeated. For the first optimization, a warmstart is not possible. That is why a zero vector is provided, which resembles driving with a constant heading and velocity.

2.4.9. Algorithms

Based on everything discussed so far, the original standard MPC algorithm, Algorithm 1, is updated to Algorithm 2. Furthermore, Algorithm 3 contains all the steps how each simulation is carried out.

Algorithm 2 APF-eMPC

```
Measure AVs current state $x(t)$ and surroundings
Predict future positions of all obstacle vehicles assuming constant velocity and heading
Set $x_o := x(t)$
Set min and max limits (2.17c) - (2.17g)
Create warm-start based on previous time-step $u(t-1)$
Solve $\mathbb{P}_N$ (2.17) for $x_0$
Select $u_0$ of calculated input sequence,
Inject this control input $u_0$ into the plant using (2.1) or (2.9)
```

Algorithm 3 Autonomous Vehicle Simulation

```
Initialize $\mathrm{AV}$
Perturb $Y$
Create list of $\mathrm{Obstacles}$ according to scenario
$T_{\mathrm{sim}}$ := Length Simulation
for $k \leftarrow 1$ to $T_{\mathrm{sim}}$ do
    Add noise to measurements
    Move $\mathrm{AV}$ using Algorithm 2
    for $\mathrm{Obstacle}$ in $\mathrm{Obstacles}$ do
        Move $\mathrm{Obstacle}$
    end for
    if $\mathrm{AV}$ Crossed Redresseerstrook then
        break
    else if $\mathrm{AV}$ crashed with a $\mathrm{Obstacle}$ then
        break
    end if
end for
```

2.5. Results

For each scenario, the expected steady state Y_{ss} for the lateral position is known, such that the normalized transient response can be calculated from the initial and the expected lateral position. If a simulation does not manage to settle in the settling time band, it is labelled as a fail. Only the simulations that were considered to be a success, are further analyzed. For each experiment, 100 simulations were carried out. The plots that are deemed relevant for the analysis are shown in this section. However, all data can also be found in Appendix B.

2.5.1. Lane keeping

Lateral Position

Firstly, Figure 2.14 shows that the AV is able to converge to the middle of a lane. The simulations that were influenced by noise, oscillate more, depicted in Figure 2.15. From Figure 2.16a, it becomes clear that for simulations with the most noise levels, around 55-60 % of the simulations, manage to settle in the settling band. Between the two plants there is little difference. For more noise, the AV operates further from the linearization point, making it more difficult to stabilize the AV.

However, even for the simulations without noise, there a few trajectories that converge to the adjacent lane. In Figure 2.16a, it can be seen that this only happened for a few simulations, as these were labelled as not a success. Even tough the middle of a lane was reached, it was not the lane which was expected. This observation can be explained as following; as the AV is initialized slightly next to the local maximum of the lane APF, it was expected that the AV would follow the gradient towards the middle of the lane. However, because the optimization is based on a discrete sum of stage costs, only

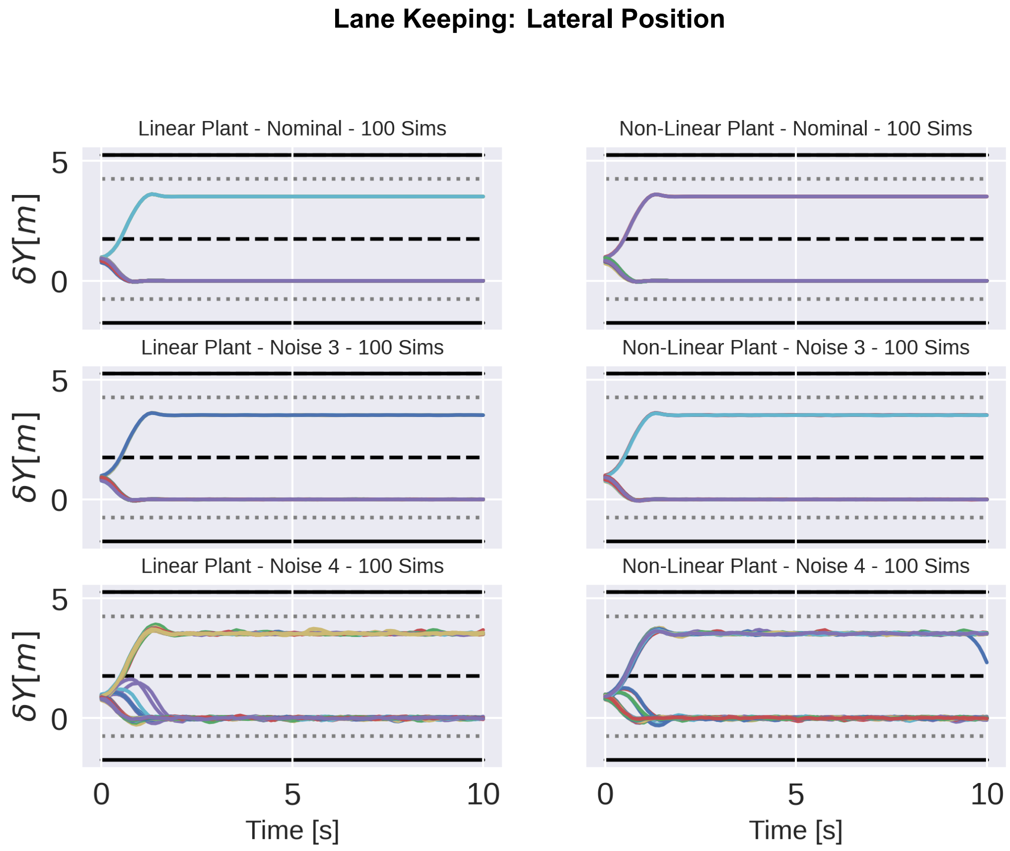

Figure 2.14: The lateral position for the scenario lane keeping. If the trajectory converges to $\delta Y = 0$, this result implies that the AV is driving in the middle of the expected lane. The black lines represent the road boundaries, the grey dotted line road boundary including the width of the vehicle, the black dashed line represents the lane marker. The rows represent different noise levels, where the first rows has no noise and the last one the most noise. The left column represents the linear plant and the right column the non-linear plant.

part of the lane APF was *sampled* and this setup can thus result in the AV *skipping* the peak of the lane APF.

Due to the noise, the AV can interpret its own position closer to the lane marker than it actually is, which can result that the *skipping* behaviour happens even faster. For the maximum noise, it can also be observed in the lower right subplot, that one trajectory suddenly started to move back to the other lane. Because there is nothing in the vicinity that should be avoided, this behaviour is highly undesirable.

Lastly, there seems to be hardly any difference between the linear and non-linear plant, which is interesting as Figure 2.18 shows that the yaw rate relatively far from the linearization point of zero. However, only two turns are carried out which could explain the similarities.

So the AV is able to find the minimum of a lane. However, for a certain size time-step in combination with a high enough velocity, the optimization does not sample the lane APF sufficiently which can result unexpected behaviours. With a higher velocity, this *skipping* can occur even faster as the discrete points lie further from each other.

Transient Response

The success percentages for the higher noise levels can be deceptive. Figure 2.16b shows that the settling time for the simulations with noise level four is almost equal to the length of the simulation (i.e. ten seconds). If the simulations would have continued for longer, the trajectories most likely would have moved out of the settling band which becomes more clear from Figure 2.17.

Another essential point to note is that the settling time band depends on the difference between the initial state and the expected final state. Because the AV is expected only to move slightly, the settling time band is smaller compared to the other scenarios.

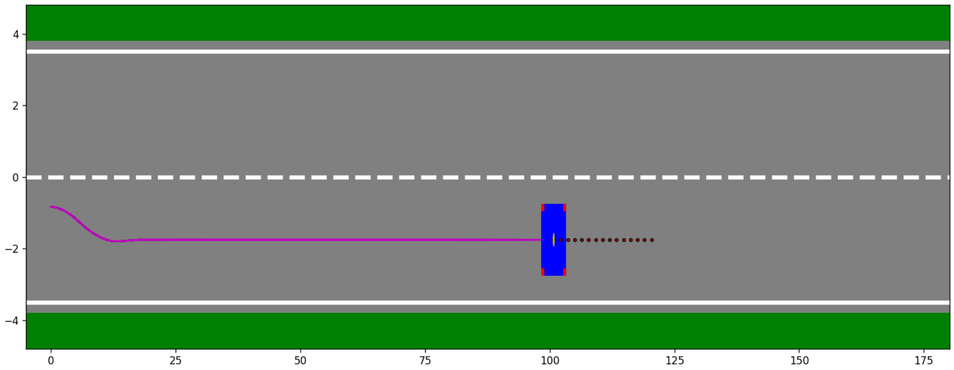

(a) Without Noise

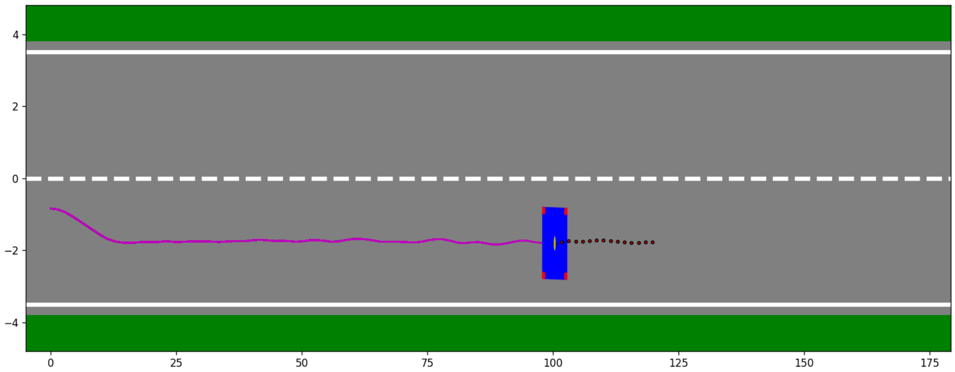

(b) With Noise

Figure 2.15: Two animations showcasing lane keeping with noise in Figure 2.15b and without noise in Figure 2.15a.

The rise-times, visualized in Figure 2.16c, are grouped at $0.4s$ or $0.5s$ which generally is the same for all noise levels, except for a few outliers with the highest noise level. This observation is because the measurements are carried out at each time step as explained in Subsection 2.4.7. The spread between $0.4s$ and $0.5s$ is almost identical, indicating that the actual rise-time is highly similar. Lastly, due to the noise the highest noise level has a larger overshoot, depicted in Figure 2.16d.

Yaw Rate

Figure 2.18 shows that the AVs yaw rate. It clearly can be seen that during the initial maneuver the controller steers the AV to the middle of the lane with the maximum allowed yaw rate. This behaviour ensures that the AV converges as fast as possible to the minimum of the combined road and lane APF, illustrated in Figure 2.4. Figure 2.18 also shows that the yaw rate during the maneuver is a lot higher than is considered to be comfortable [142]. For the simulations with a lot of noise this problems is even worse, as the yaw rate does not settle between this comfortable band.

Optimization Iterations

Figure 2.19 shows that the warmstart ensures that less iterations are required after the AV has converged to the middle of the lane. However, when there is a lot of measurement noise, the warm start is not sufficient and each optimization requires the same amount of iterations. Lastly, the top row shows that during the first part of the simulation, less iterations were required for the experiment with the linear plant than with the non-linear plant, indicating that the warm start is more effective for the linear plant.

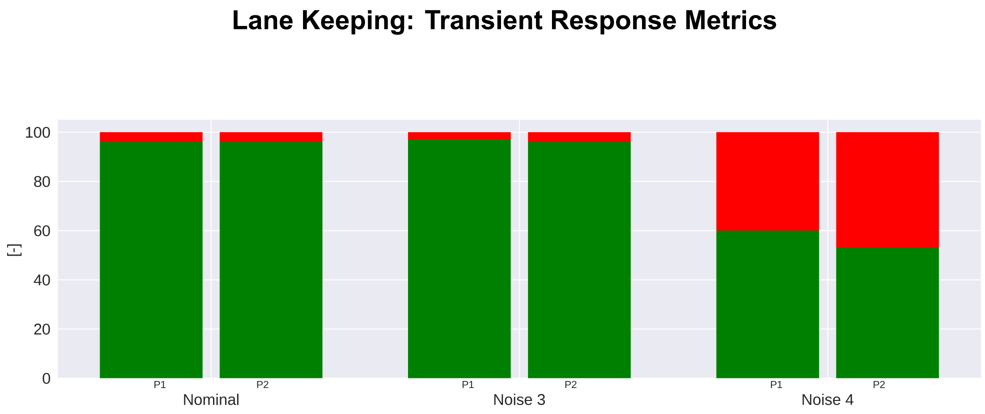

(a) Success Ratio

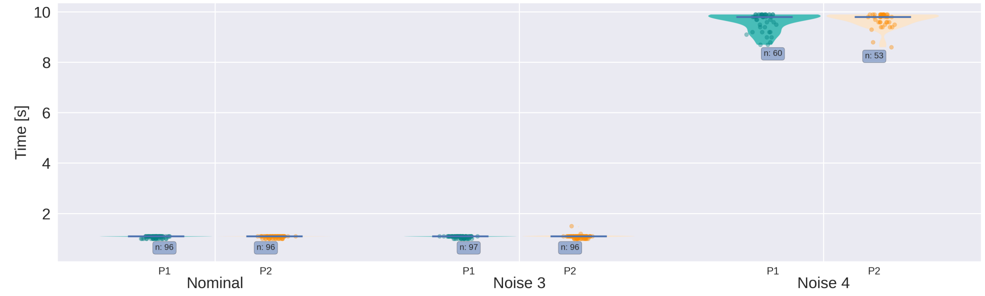

(b) Settling Time

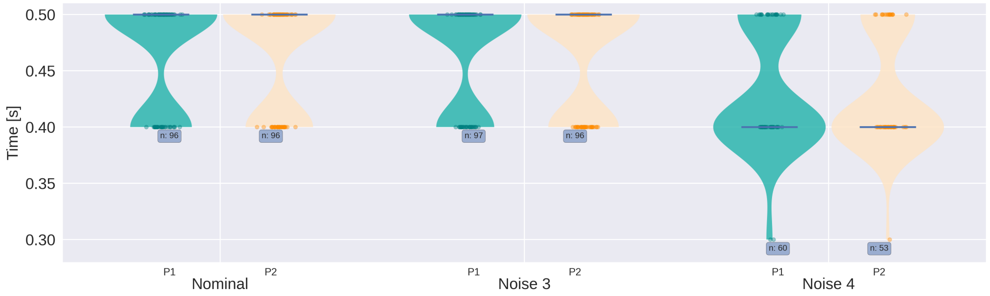

(c) Rise Time

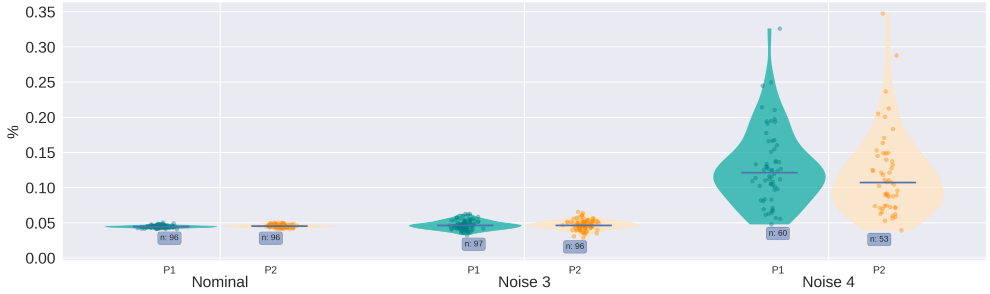

(d) Overshoot

Figure 2.16: Transient response metrics for the scenario lane keeping. The small numbers in the blue boxes in the subplots Figure 2.16c, Figure 2.16b, Figure 2.16d, indicates how many simulations were able to reach the settling band before the simulations ended. The overshoot, rise-time and settling-time is thus only calculated for the simulations that were labelled as a *success*. The success ratios are plotted in Figure 2.16a as well, where the red areas indicate fail and the green success. Lastly, $P1$ implies the linear plant and $P2$ the non-linear plant.

Figure 2.17: When the trajectories converge from zero to one, the AV manage to converge to the expected lane. Furthermore, the left column represents the simulations carried out with the linear plant and the right with non-linear plant. Each row represents a different amount of white noise used during the simulations. The upper row had no noise and the lower row had the most noise.

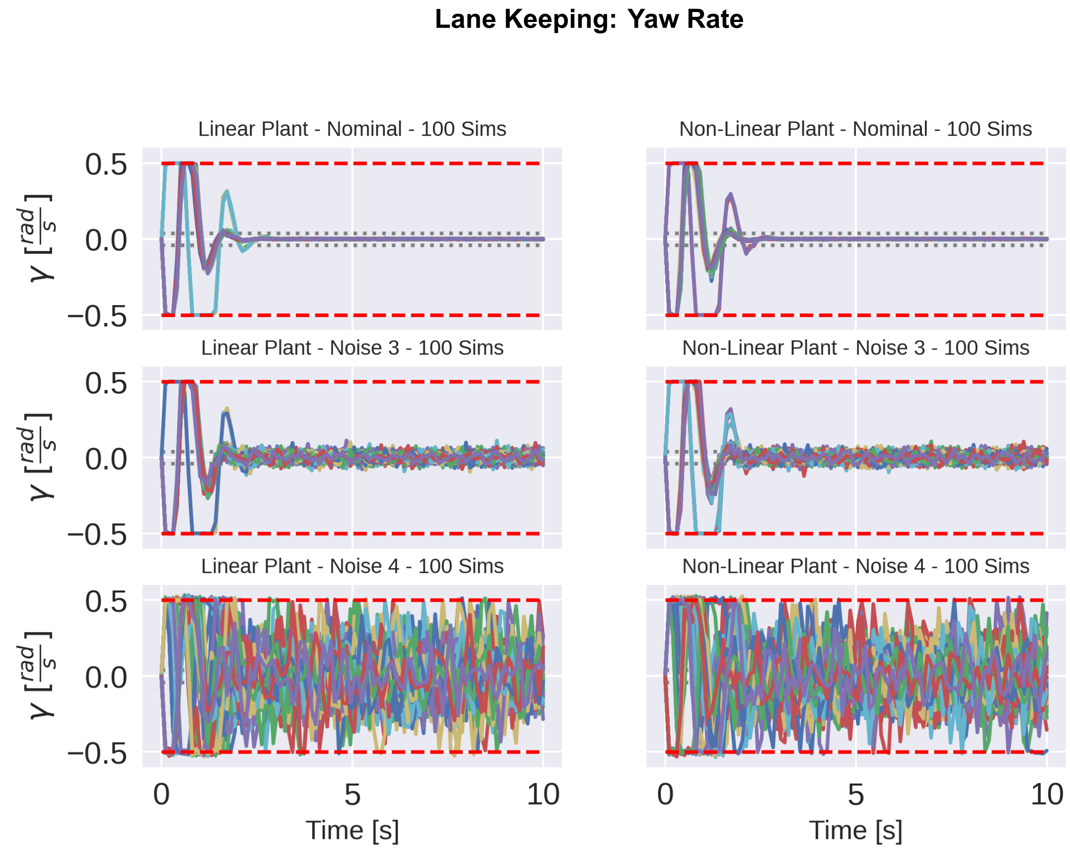

Figure 2.18: The dashed red lines represents the yaw rate constraints (2.17g) and the dotted grey lines represent the comfortable yaw rate for the reference velocity v_{ref}, as defined by [142]. Furthermore, the rows represent different noise levels, where the first rows has no noise and the last one the most noise. The left column represents the linear plant and the right column the non-linear plant.

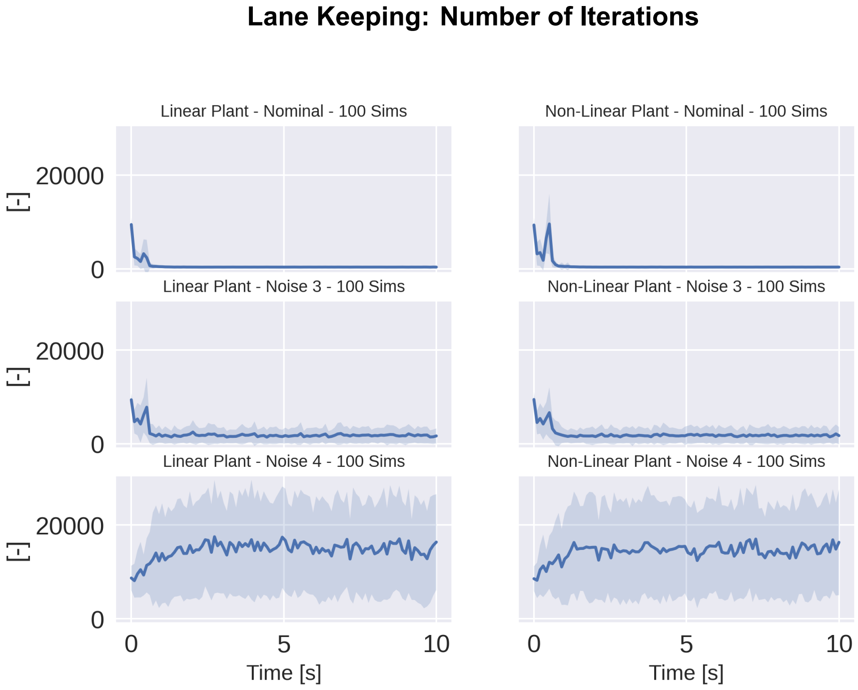

Figure 2.19: The average and the corresponding standard deviation for the amount of iterations is visualized in this figure. The left column represents the linear plant and the right column the non-linear plant. The upper row had no noise and the lower row had the most noise. The plots with less noise do not converge to zeros, as might appear, but have an average around 350-400 iterations.

2.5.2. Car-Following

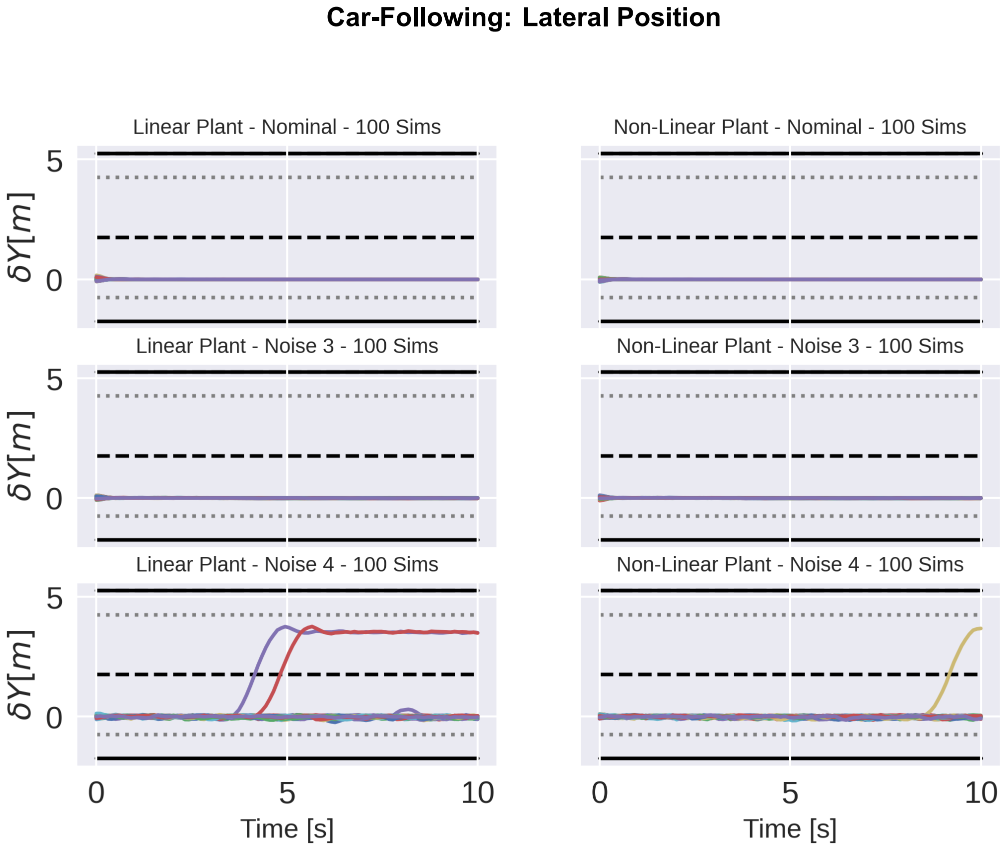

Figure 2.20: The lateral position for the scenario car-following; $\delta Y = 0$ implies that the AV is driving in the middle of the expected lane. The black lines represent the road boundaries, the grey dotted line road boundary including the width of the vehicle, the black dashed line represents the lane marker. The rows represent different noise levels, where the first rows has no noise and the last one the most noise. The left column represents the linear plant and the right column the non-linear plant.

Figure 2.20 shows that for the lower noise levels all trajectories stay in the same lane as where they started. The AV lowers its velocity to match it with the obstacle vehicle, as can be seen in Figure 2.21. This action allows the AV to follow a car that drives slightly slower than the AVs reference velocity, without changing lanes. Both figures, show that for more noise, there a few trajectories that change lane and the car-following behaviour is undesirable aborted.

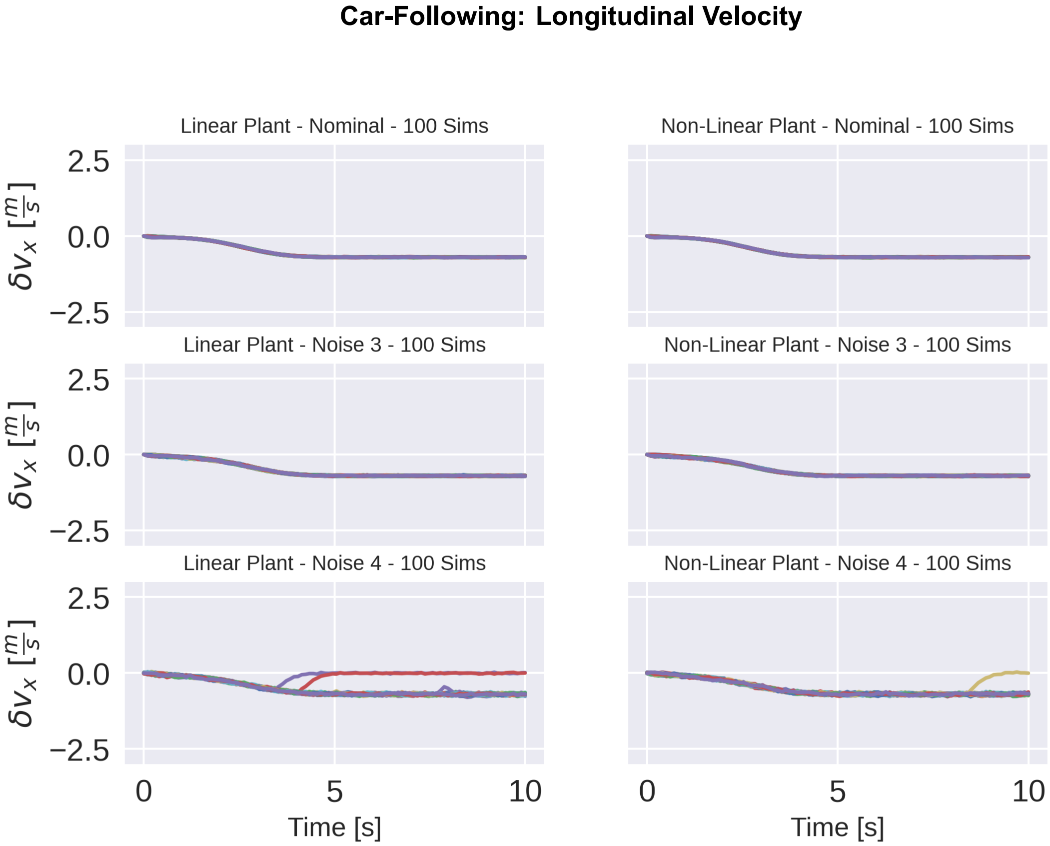

Figure 2.21: When the AV drives with $\delta v_x = 0$, the vehicle drives with the desired reference speed v_{ref}. The rows represent different noise levels, where the first rows has no noise and the last one the most noise. The left column represents the linear plant and the right column the non-linear plant.

2.5.3. Lane Changing

Lateral Position

Figure 2.22 illustrates that the trajectories with less noise are almost identical. All simulations manage to change lane and avoid the obstacle vehicle. When more noise gets added, the trajectories start to differ. Some converge back to the original starting lane instead of the adjacent lane. Unnecessary changing lane, like with lane keeping, is not observed before the obstacle vehicle is encountered. The skipping problem, due to the discrete nature of the system, does thus not occur when initiated around the middle of the lane. Even tough it was not what was expected that some trajectories would converge back to the original lane beforehand, the AV still manages to avoid the obstacle and converge back to the middle of a lane.

Transient Response

The amount of success, as shown in Figure 2.23a, is a lot higher than with the lane keeping scenario because the settling-time band is larger. So now there are simulations, influenced by the highest noise level, that manage to stay in this broader settling-time band. The rise time, visualized in, Figure 2.23c, is similar for all experiments. There is a bit more spread for the highest noise level. Similarly, the overshoot is a lot higher for the this amount of noise Figure 2.23d. Again, the differences between the two plants is negligible.

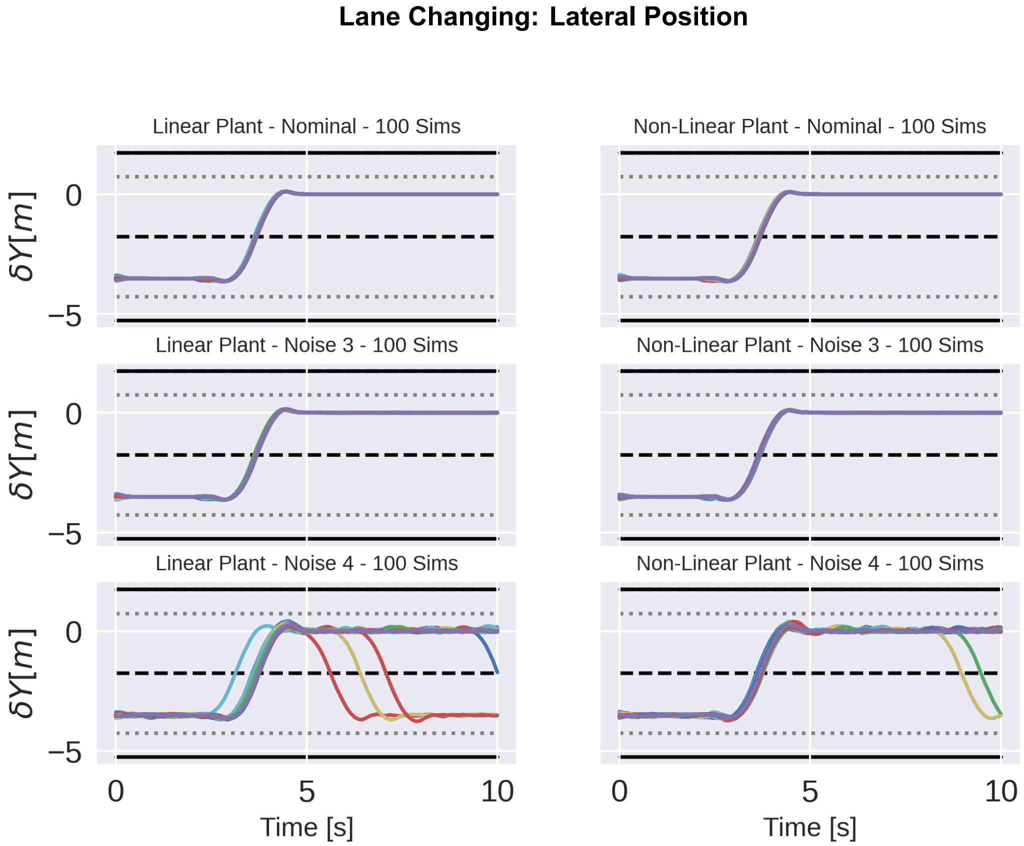

Figure 2.22: The lateral position for the scenario lane changing. If the trajectory converges to $\delta Y = 0$, this result implies that the AV is driving in the middle of the expected lane. The black lines represent the road boundaries, the grey dotted line road boundary including the width of the vehicle, the black dashed line represents the lane marker. The rows represent different noise levels, where the first rows has no noise and the last one the most noise. The left column represents the linear plant and the right column the non-linear plant.

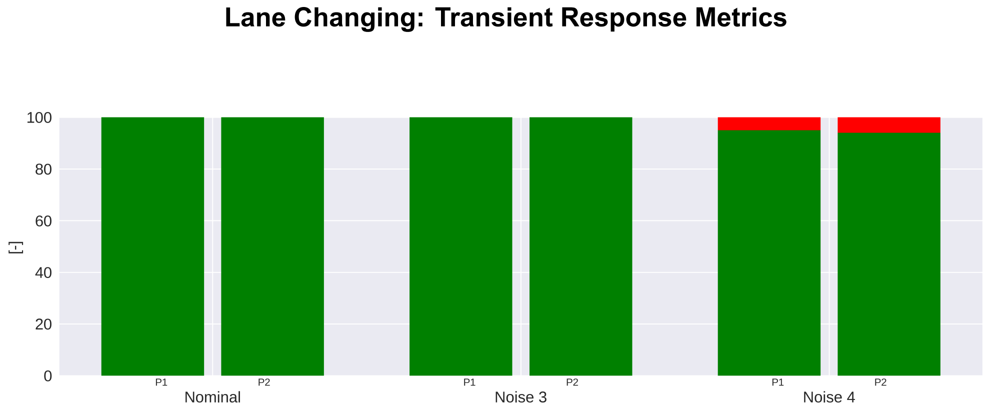

(a) Success Ratio

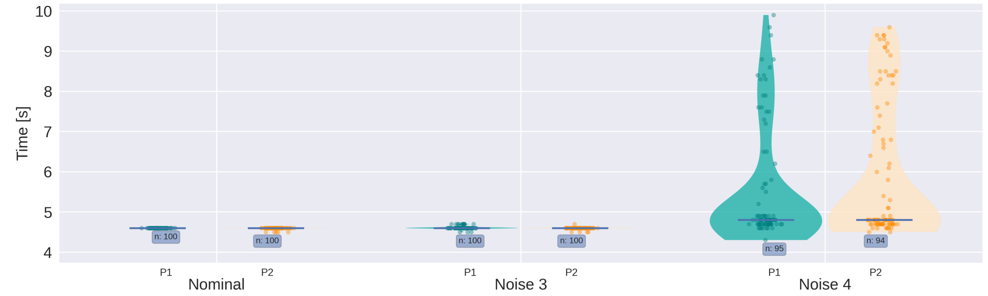

(b) Settling Time

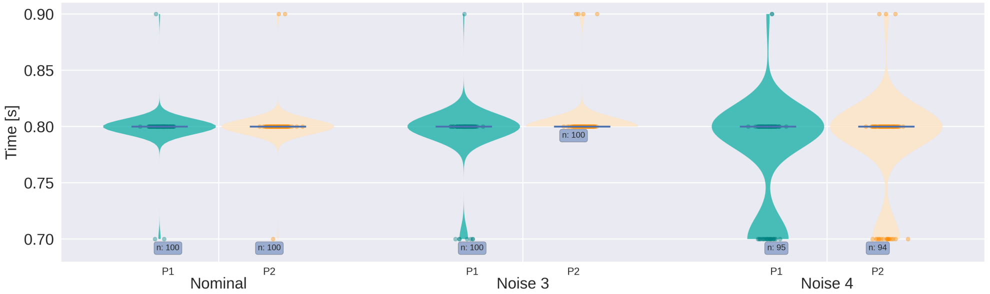

(c) Rise Time

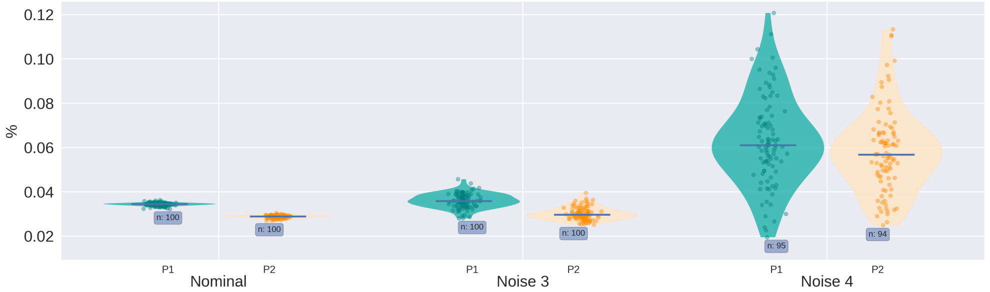

(d) Overshoot

Figure 2.23: Transient response metrics for the scenario lane changing. The small numbers in the blue boxes in the subplots Figure 2.23c, Figure 2.23b, Figure 2.23d, indicates how many simulations were able to reach the settling band before the simulations ended. The overshoot, rise-time and settling-time is thus only calculated for the simulations that were labelled as a *success*. The success ratios are plotted in Figure 2.23a as well, where the red areas indicate fail and the green success. Lastly, $P1$ implies the linear plant and $P2$ the non-linear plant.

2.5.4. Emergency Stop

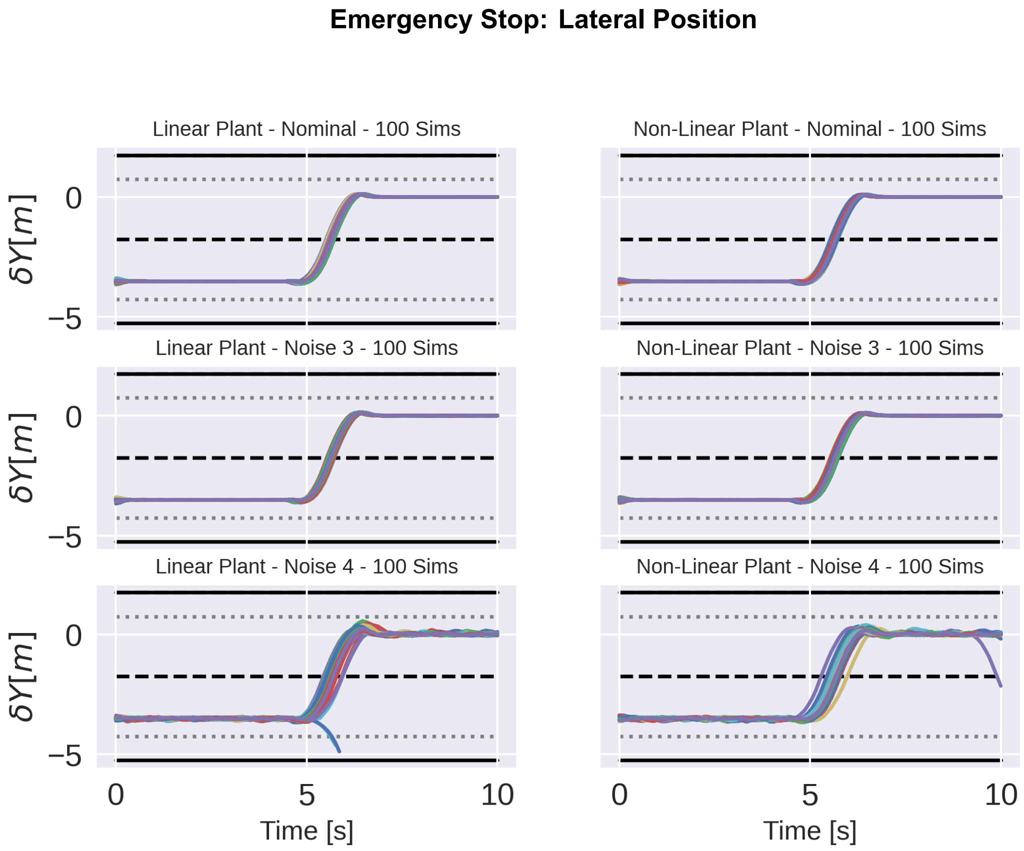

Figure 2.24: The lateral position for the scenario emergency stop. If the trajectory converges to $\delta Y = 0$, this result implies that the AV is driving in the middle of the expected lane. The black lines represent the road boundaries, the grey dotted line road boundary including the width of the vehicle, the black dashed line represents the lane marker. The rows represent different noise levels, where the first rows has no noise and the last one the most noise. The left column represents the linear plant and the right column the non-linear plant.

Generally, the same observations as with the prior three scenarios can be made. Most trajectories were able to avoid the obstacle safely. Furthermore, in comparison with the lane lane changing scenario, there are hardly any trajectories that converge back to the original starting lane after the lane changing maneuver. Avoiding a vehicle at maximum breaking speed, with this specific horizon, is less challenging than a static vehicle. The prediction of the future position of the obstacle vehicle appears to be adequate.

However, in lower subplots off Figure 2.24 two outliers can be observed. These trajectories attempt to make a lane change by steering to the right instead to the left. However, because of this the AV crosses the road boundary. Even tough, this approach does not happen on a regular basis, the AV should still be able to handle this situation.

2.6. Discussion

The first half of this thesis attempted to provide a better understanding of the limitations of an AV based on the APF-eMPC framework as yet no stability analysis has yet been found in literature. Several experiments were carried out, where the most important types of driving manoeuvres were simulated. A linear and non-linear plant were used in combination with different levels of white noise were used to test the controller's capabilities.

The results demonstrate that the AV can manage the three most important forms of driving: lane keeping, car-following, and lane changing. For lower noise levels, the AV can carry out these basic manoeuvres. However, with increasing noise levels, the AV sometimes misinterprets the level of risk, resulting in a larger spread of trajectories, increased oscillation, and in some simulations, a crash. As a result, safety cannot be assured when noise level four, defined in Subsection 2.4.6, influences AV measurements.

Additionally, the results demonstrate clearly that the AV executes these maneuvers relatively violently as the yaw rate exceeds the values which are considered to be comfortable. This observation makes sense as only the yaw rate was hard constrained and thus the AV tries to converge to the minimum of the road and lane APF with the largest allowed yaw rate.

Furthermore, small but negligible differences between the linear and non-linear plant was observed, implying that deviating from the linearization point is not a concern for these types of manoeuvres while driving at $14m/s, 50km/h$ and executing two turns. What would happen if the AV would make more turns in one maneuver while driving at a higher velocity?

These simulations also show that, for this specific setup, the basic prediction of an obstacle vehicle's future position is adequate to avoid a collision with an obstacle vehicle performing an emergency stop.

Additionally, the results demonstrated that, for this particular setup, the size of the timestep can impact the AVs behaviour. Due to the discrete nature of the optimization, the APFs are only partially sampled, and the peak of the lane APF may be *skipped* and resulting in the unexpected lane-changing with the lane-keeping scenario. With a higher velocity, this effect will be more significant as the distance between the predicted positions increases. A steeper lane APF could prevent this behaviour, but decreasing the timestep will probably be more beneficial as the gaps between the predicted positions become smaller.

In general, the AV based on the APF-eMPC framework can steer the vehicle around without needing a positional trajectory reference and handle a certain noise level. Safety cannot be assured from the highest noise level, and additional procedures are required to mitigate this amount of noise.

3

Connected Autonomous Vehicles

This chapter extends the framework to a CAV, such that cooperative driving is possible. This chapter discusses only the steps required to create the CAV controller, based on the AV from Chapter 2. The goal is to compare two different APFs that enforce car-following. First, these two APFs are introduced in Section 3.1. Hereafter, the controller optimization is updated in Section 3.2. Furthermore, Section 3.3, discusses the details of the three scenarios, which test the controllers, and what performance metrics are used. The CAVs are required to close different size gaps between them such that a tighter platoon formation is created. The results from these experiments are presented in Section 3.4 and finally the key points are summarized and discussed in Section 3.5.

3.1. Artificial Potential Functions

The control of an individual CAV inside a platoon can be split up in longitudinal control and lateral control. As explained in Section 1.2, longitudinal control is mostly studied in literature, as it affects the performance of the platoons the most. However, because the dynamics are coupled, lateral control still is relevant. This section introduces and briefly discusses the two longitudinal APFs found in literature, followed by the lateral APF. All numerical values used for the APFs parameters can be found in Table A.5.

3.1.1. Longitudinal Control

In Chapter 2, it was shown that the AV is capable of maintaining a safe distance from the vehicle ahead. However, within a platoon, the CAV should actively maintain a specific relative distance from the preceding vehicle and not only a safe enough distance. So the car-following behaviour in this context can be split up in two separate actions. First, the CAV is attracted towards the desired position if its to far away. Secondly, to minimize the risk of collision, the CAV should maintain a large enough distance from the preceding vehicle.

The first APF is an asymmetric function [82], [83], based on the Lennard-Jones function which imitates inter-molecular interactions, such that the repulsive part and the attractive part are different. The idea of the asymmetrical property is that when the distance between the preceding vehicle is too small, braking hard is required to minimize the risk of collision. Whereas gap closing can happen more gradually. This APF is constructed as following,

Artificial Potential Function: Platoon Longitudinal Control - I - Inter-Molecular

$$U_{\text{Platoon},1} = \begin{cases} k_{\text{Platoon},X1} + \frac{k_{\text{Platoon},X1}}{a-b}\left(b\left(\frac{X_r}{\Delta X+r}\right)^a - a\left(\frac{X_r}{\Delta X+r}\right)^b\right) & \text{if } \Delta X + r \leq 0, \\ \infty & \text{otherwise,} \end{cases} \quad , \tag{3.1}$$

where $\Delta X = X_o - X$ and X_o is the longitudinal position of preceding CAV, which the ego CAV is following. The variable ΔX thus represents the relative longitudinal distance, and X_r is the required safety distance between the two vehicles. Furthermore, $k_{\text{Platoon},X1}$ is a gain, and the parameters a and b shape this function. The latter two were fitted to traffic data [83]: this APF thus represents actual human driving. Lastly, to avoid dividing by zero, the APF is updated such that it returns ∞ for $\Delta X + r \leq 0$. The second APF that enables platooning is a symmetric quadratic function [34],

Artificial Potential Function: Platoon Longitudinal Control - II - Quadratic

$$U_{\text{Platoon},2} = k_{\text{Platoon},X2}\left((\Delta X + r) - X_r\right)^2, \tag{3.2}$$

where $k_{\text{Platoon},X2}$ is a gain. For comparison, these two functions are visualized in Figure 3.1, where different time-gaps are represented by vertical lines. For the repulsion part, $\Delta X < X_r$, it can be observed that inter-molecular APF (3.1) is stronger than (3.2), because the inter-molecular APF increases faster for $\Delta X \rightarrow 0 \forall \Delta X \leq X_r$.

The differences for the attraction part reversed. First, both functions are comparable when $\Delta X - X_r$ is small for $X > X_r$. However, for a larger time-gaps, it can be observed that (3.1) is smaller than (3.2) and this difference keeps growing for even larger inter-vehicle distance. Figure 3.1 shows that the gradient of the quadratic APF keeps increasing while the gradient of the inter-molecular APF decreases for $\Delta X \rightarrow \infty \forall \Delta X >> X_r$. So the quadratic APF (3.2) keeps getting larger than the inter-molecular APF (3.1) when inter-vehicle distance increases. Lastly, Figure 3.1 shows that inter-molecular APF (3.1) is non-convex, whereas (3.2) is convex.

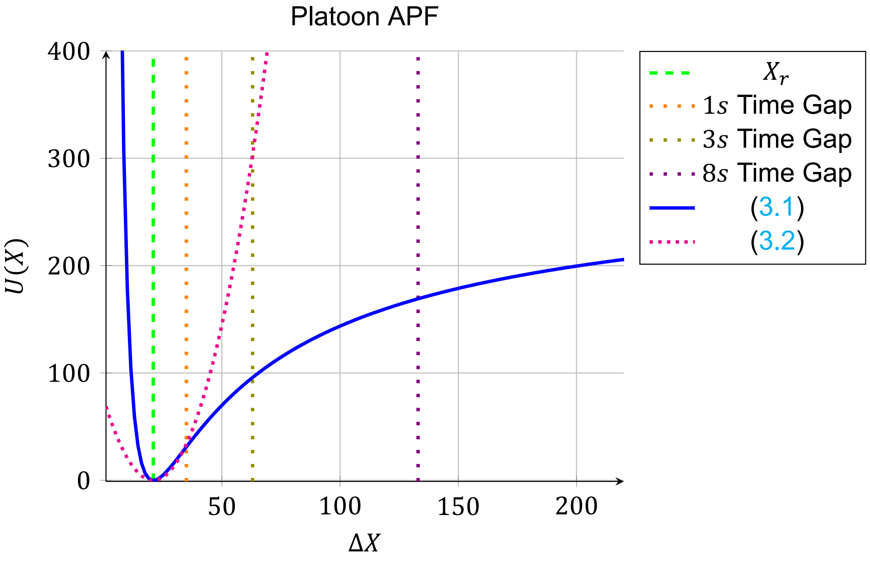

Figure 3.1: Visualization of the two platoon APFs for longitudinal control, where $k_{\text{Platoon},X1} = 1$, $k_{\text{Platoon},X2} = 1400$, $a = 1.648$, $b = 0.713$ and $X_r = 21[m]$. When driving with $v_x = 14[m/s]$, $\Delta X = 63[m]$ and $\Delta X = 133[m]$ represent a three and eight second time gap respectively from the desired required safety distance X_r.

Required Safety Distance

There this thesis uses a constant time gap (CTH) to calculated X_r,

Required Safety Distances:Constant Distance Headway (CDH)

$$X_r = t_0 v_x \tag{3.3}$$

where t_0 represents the required time-gap between vehicles. Thus the longitudinal platoon APF does not only depend on the (relative) longitudinal distance, but also on the longitudinal velocity. In Figure 3.2, this extra dimension is visualized. For a larger v_x, the local minimum in the X_r axis increases. The red trajectories represent possible trajectories during gap closing. When the relative distance

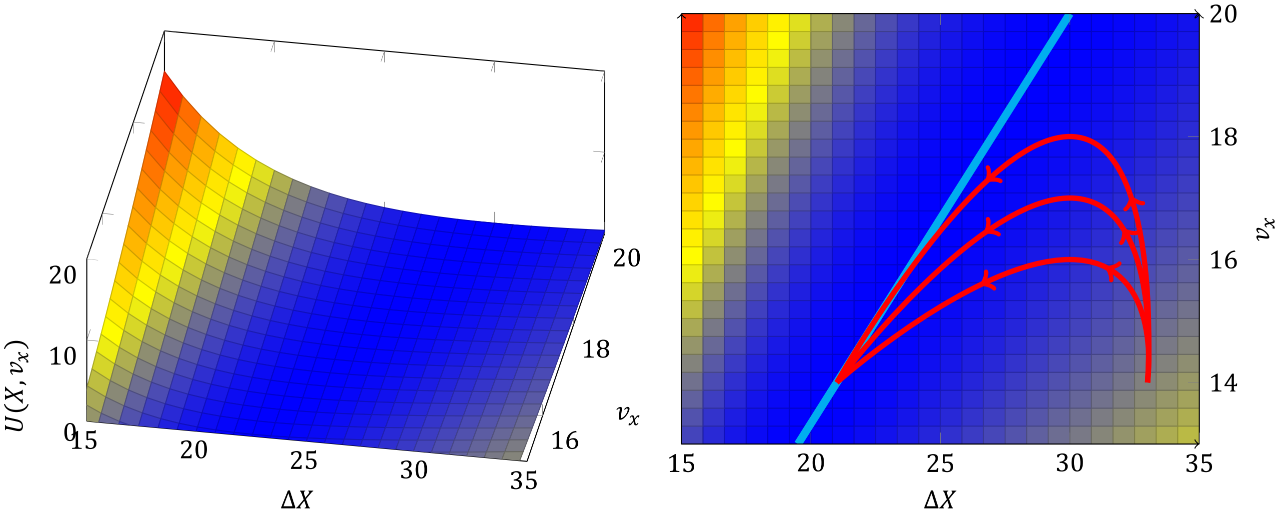

(a) Inter-Molecular Platoon APF (3.1) with CTH (3.3)

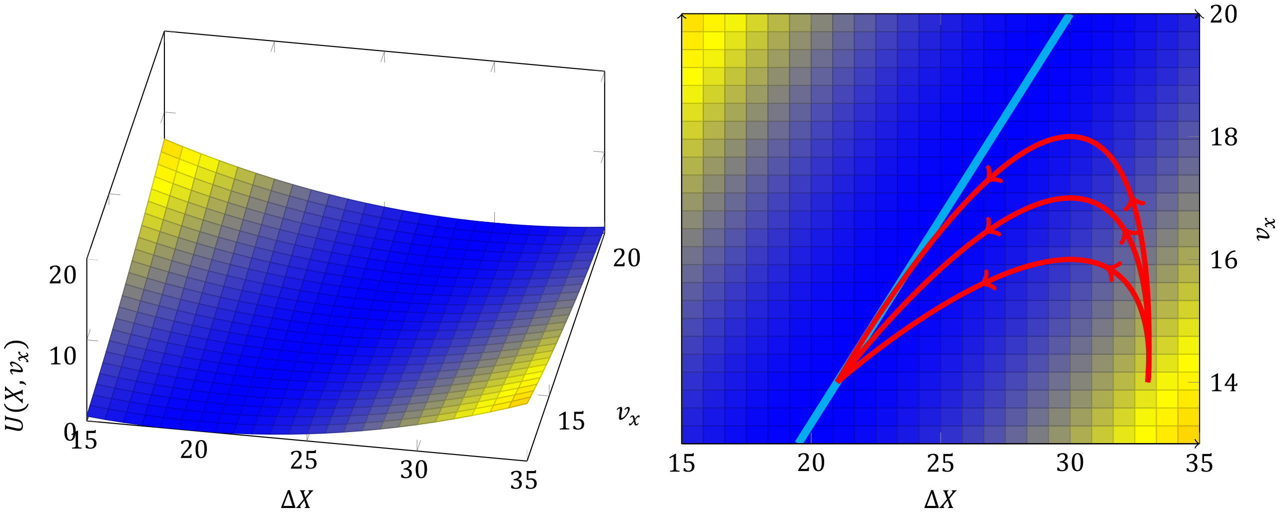

(b) Quadratic Platoon APF (3.2) with CTH (3.3)

Figure 3.2: The two longitudinal platoon APFs, (3.1) and (3.2) are shown using a surf plot. The CTH (3.3) is represented by the cyan lines. The red lines demonstrate possible trajectories if the CAV would be distanced further away than the required X_r. To close this gap, the CAV would first need to increase its v_x and afterwards slow down when the CAV approaches the correct ΔX.

between ego CAV and the preceding CAV is too large, the ego CAV first needs to increase v_x. Hereafter, the velocity needs to decrease again such that the ego CAV can drive at the same speed as the preceding vehicle at the correct X_r.

3.1.2. Lateral Control

Because research mainly focuses on on longitudinal control for platoon, only one lateral APF is currently found [34]. This APF is a quadratic function,

Artificial Potential Function: Platoon Lateral Control

$$U_{\text{Lateral}} = k_{\text{Platoon},Y} \left(Y_o - Y\right)^2, \tag{3.4}$$

where Y_o is the lateral position of preceding vehicle which the ego CAV is following and $k_{\text{Platoon},Y}$ is a gain. This quadratic function is convex and symmetric.

3.1.3. Combined

The two longitudinal APFs, (3.2) and (3.1) are combined with the lateral version (3.4) to create the two platoon APFs,

$$U_{\text{Platoon},1} = \begin{cases} k_{\text{Platoon},Y} \left(Y_o - Y\right)^2 + k_{\text{Platoon},X1} \left(\frac{1}{a-b} \left(b \left(\frac{X_r}{\Delta X + r} \right)^a - a \left(\frac{X_r}{\Delta X + r} \right)^b \right) + 1 \right) & \text{if } \Delta X + r \leq 0, \\ \infty & \text{otherwise}, \end{cases} \tag{3.5}$$

$$U_{\text{Platoon},2} = k_{\text{Platoon},Y} \left(Y_o - Y\right)^2 + k_{\text{Platoon},X2} \left(\left(\Delta X + r\right) - X_r\right)^2. \tag{3.6}$$

3.2. Controller Formulation

Each CAV in the platoon solves its own optimization, making the whole platoon control scheme a decentralized setup. The optimization behind eMPC, as defined in Section 2.3, stays the same for the leader vehicle. For each the follower, the combined potential term (2.15) is updated as following,

Artificial Potential Function: Combined - Follower

$$U_{\text{Follower},i} = U_{\text{Road}} + U_{\text{Lane}} + U_{\text{Obstacle}} + U_{\text{Velocity}} + U_{\text{Platoon},i}, \tag{3.7}$$

where i is either 1 or 2. So for each follower the platoon APF is added. Similarly, the stage cost (2.16) is updated,

$$\ell_{\text{Follower},i}(x_k, u_k) = K_u U_{\text{Follower},i}(x_k) + u_k^{\intercal} R u_k, \tag{3.8}$$

where i is either 1 or 2. The two different optimization problems for each CAV follower is formulated as following,

Optimization Problem: CAV - Follower - I - Inter-Molecular Platoon APF

$$\underset{\mathcal{U}_u}{\arg\min} \quad \mathbb{P}_{N,\text{Follower},1}(x_0) : V_N = \sum_{k=0}^{N-1} \ell_{\text{Follower},1}(x_k, u_k) \tag{3.9a}$$

$$\text{subject to} \quad \text{(2.17b), (2.17c), (2.17d), (2.17e), (2.17f), (2.17g), (2.17h)}, \tag{3.9b}$$

Optimization Problem: CAV - Follower - II - Quadratic Platoon APF

$$\underset{\mathcal{U}_u}{\arg\min} \quad \mathbb{P}_{N,\text{Follower},2}(x_0) : V_N = \sum_{k=0}^{N-1} \ell_{\text{Follower},2}(x_k, u_k) \tag{3.10a}$$

$$\text{subject to} \quad (2.17b), (2.17c), (2.17d), (2.17e), (2.17f), (2.17g), (2.17h). \tag{3.10b}$$

3.3. Experiment Setup

This section discusses how the two controllers based on the two platoon APFs (3.10) and (3.10) are simulated. First, Subsection 3.3.1 discusses what performance metrics are used to compare the controllers. Hereafter, the V2V implementation is explained in Subsection 3.3.2. Followed by Subsection 3.3.3 which introduces the different scenarios which are used to test the different capabilities. Subsection 3.3.4 briefly discusses how the different gains for the platoon APFs were chosen. Subsection 3.3.5 explains how the multiple simulations are initialized. Finally, all the steps are summarized in an algorithm formulation in Subsection 3.3.6.

3.3.1. Performance Metrics

Similar to Subsection 2.4.1, the settling time, the rise time and the overshoot of a transient response are analyzed to quantify the performance. However, instead of the lateral dynamics, the longitudinal dynamics are now considered. More specifically, the sum of all relative distances between the vehicles is used to study performance of the group as a whole. In literature, this goal is also referred to as string stability and is formulated in Definition 3.3.1.

String Stability

Definition 3.3.1. (SS) A string of vehicles is stable if, for any set of bounded initial disturbances to all the vehicles, the longitudinal position fluctuations of all the vehicles remain bounded, and these fluctuations approach zeros as t → ∞ [113].

In addition, the authors of [113] also explain that string stability implies that *"the [platoon] disturbances are not amplified when propagating along the vehicle string"*. Furthermore, for *longitudinal position fluctuations*, the following variable is formulated,

$$\Delta X_{\text{tot}} = \frac{\sum_{i=2}^{n_p} X_{i-1} - X_i}{X_r(n_p - 1)} \tag{3.11}$$

where n_p is the amount of vehicles in a platoon, i is the i-th vehicle, and X_r is the required relative longitudinal distance. Similarly to the experiments with the AV, explained in Subsection 2.4.1, a normalized transient response is calculated for ΔX_{tot}. Furthermore, the authors of [113] have defined the following platoon disturbances;

Platoon Disturbances

- Type I: Initial condition perturbations for the leading vehicle
- Type II: Initial condition perturbations for all vehicles

Because SS implies longitudinal dynamics, these types of disturbances are assumed to refer to longitudinal perturbations and disturbances. With a type I disturbance, only the gap with the leader vehicle and the first follower is incorrect. The gaps between all other vehicles are correct. An example off this type of disturbance is a platoon which is already formed attempts to attach itself to another vehicle in front or another platoon, merging these two platoons.

3.3.2. Vehicle to Vehicle Connectivity

During simulations, each CAV gathers information about the surrounding vehicles. Via V2V each CAV receives the current motion states of the vehicle in front. This type of information flow topology is visualized in Figure 1.12. This setup implies that each CAV should predict the future states of the other vehicles.

3.3.3. Scenarios

To compare the two different controllers, (3.10), (3.9), three different scenarios are created. These different scenarios will give insight of the limits of the controllers. The type I and II platoon disturbances are used in combination with a small and larger initial time gap. Lastly, the platoon contains five vehicles including the leader vehicle and $t_0 = 1.5s$.

Scenario Platoon 1: Disturbance Type I - One Second Time Gap

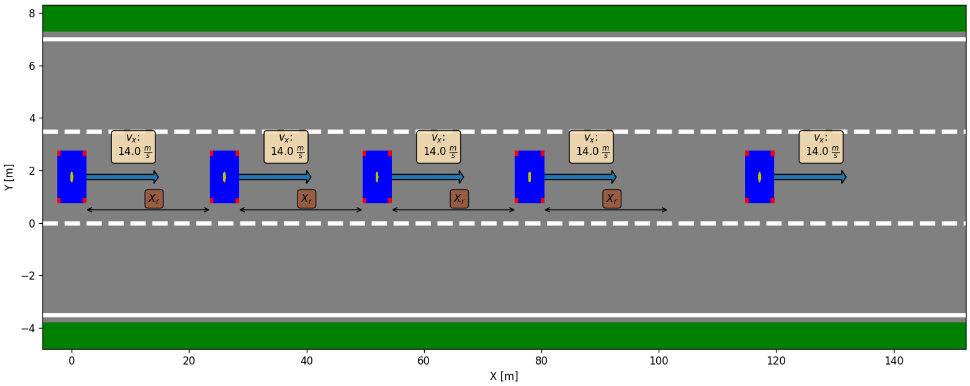

Figure 3.3: Initial position of the platoon, where the inter-vehicle distance between the front vehicle and the second vehicle is one second larger than required.

For the first scenario, the platoon is initialized such that the initial gap away from the preceding vehicle is one second larger than the required safety distance. This calculation is based on the velocity reference v_{ref}. This setup is visualized in Figure 3.3. This scenario could resemble a platoon attaching itself to another vehicle or even another platoon.

Scenario Platoon 2: Disturbance Type I - Three Second Time Gap

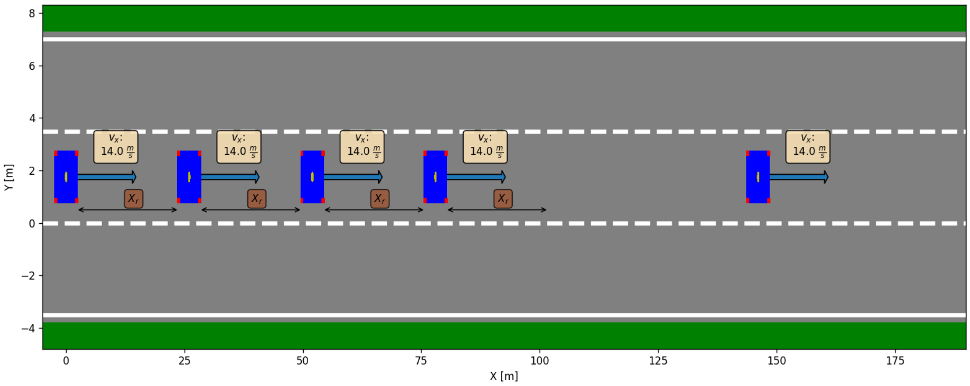

Figure 3.4: Initial position of the platoon, where the inter-vehicle distance between the front vehicle and the second vehicle is three seconds larger than required.

This scenario investigates how a three second time gap is handled instead of one. This setup is visualized in Figure 3.4.

Scenario Platoon 3: Disturbance Type II - Three Second Time Gap

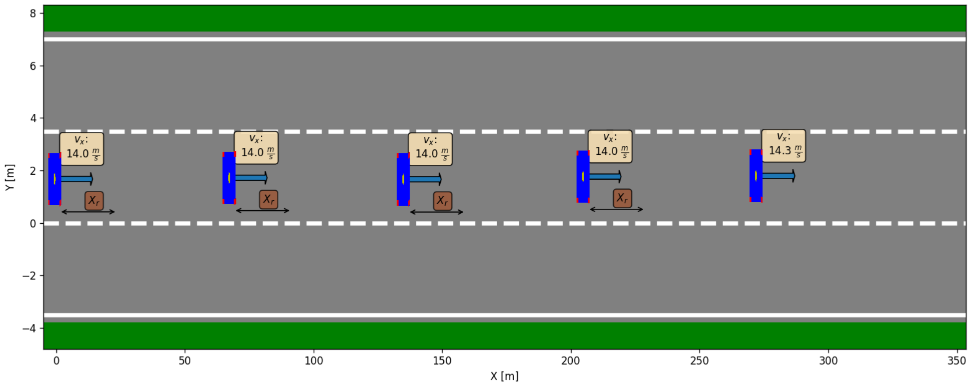

Figure 3.5: Initial position of the platoon, where the inter-vehicle distance between the all vehicles is three seconds larger than required.

With the last scenario, the platoon is disturbed by a disturbance of type II. This scenario is the most challenging. All vehicles start three second behind the required safety distance X_r. This setup is visualized in Figure 3.5. This scenario could resemble the start of a platoon; multiple CAVs approach each other to form a compact platoon formation.

3.3.4. Tuning

The gains of both APFs (3.1), (3.2) are tuned based the first platoon scenario. First, the gain of (3.1) was increased such that acceleration of the first follower did not saturate and the longitudinal velocity did not increase more than approximately $5\ m/s$, such that the gap closing maneuver did not happen too fast and with too much acceleration. Hereafter (3.2) was tuned such that the attraction part of the APF was similar to (3.1). The result is visualized in Figure 3.1.

The gain for the lateral control (3.4), was increased until the platoon was able to make a lane change instead of staying in one lane due to the lane APF (2.11) overpowering the lateral platoon APF.

3.3.5. Initial State

The initial states of the various simulations are changed to ensure that the numerical analysis captures adequate information. The states of the CAVs are varied from the basic scenario specified in the preceding part, using a Gaussian distribution with mean zero and standard deviation; these numerical values used can be found in Table A.2.

Because the main point of interest is the longitudinal interactions, the relative longitudinal position for all simulations is varied. For the scenarios influenced by the platoon disturbance of type I, this perturbing is only done for the inter-vehicle distance between the first two vehicles. For the last scenario, influenced by the platoon disturbance of Type II, the relative positions is varied for all vehicles. Lastly, the longitudinal velocity of the leader vehicle, and the lateral position of each vehicle are perturbed to stimulate the platoon even more.

3.3.6. Algorithms

The algorithm from the AV, Algorithm 2, is updated accordingly to the CAV application Algorithm 4. Similarly, Algorithm 3 is altered to Algorithm 5, which contains all the required information how each simulation is executed.

Algorithm 4 APF-eMPC:CAV

```
Measure CAVs current state $x(t)$ and surroundings
Receive current motion states of other CAVs
Predict future positions of all (obstacle) vehicles assuming constant velocity and heading
Set $x_o := x(t)$
Set min and max limits (2.17c) - (2.17g)
Create warm-start based on previous time-step $u(t-1)$
Solve $\mathbb{P}_{N,\text{Follower},1}$ (3.10) or $\mathbb{P}_{N,\text{Follower},2}$ (3.10) for $x_0$
Select $u_0$ of calculated input sequence,
Inject this control input $u_0$ into the plant using (2.1) or (2.9)
```

Algorithm 5 Connected Autonomous Vehicle Simulation

```
Initialize $n_p$ CAVs
Perturb states according to scenario
$T_{\text{sim}}$ := Length Simulation
for $k \leftarrow 1$ to $T_{\text{sim}}$ do
    Add noise to measurements
    Move Leader CAV using Algorithm 2
    for Follower CAV in Platoon do
        Move Follower CAV using Algorithm 4
    end for
    for CAV in Platoon do
        if CAV Crossed Redresseerstrook then
            break
        else if CAV crashed with another CAV then
            break
        end if
    end for
end for
```

3.4. Results

The results for the three different scenarios are discussed in Subsection 3.4.1, Subsection 3.4.2 and Subsection 3.4.3. For each experiment, multiple simulations were carried out. The relevant plots are shared in this section. In Appendix C, more data can be found if the reader is interested. Furthermore, for ease of writing, the controller (3.9), based on the inter-molecular longitudinal platoon APF (3.1), is referred to as *the inter-molecular controller* (3.9). Similarly, the controller (3.10) based on the quadratic platoon APF (3.2) is referred to as *the quadratic controller* (3.2).

3.4.1. Scenario Platoon 1: Disturbance Type I - One Second Time Gap

First, Figure 3.6 visualizes the normalized transient responses for ΔX_{tot} (3.11) and that all simulations achieve the desired lateral formation indicating that string stability is achieved. Between the two plants, no sizable difference can be observed. Similarly, the shape of the responses is comparable between the two controllers. However, slight differences in the transient response metrics can be observed. This observation is in line with the differences between the two platoon APFs, which were visualized in Figure 3.1. The APFs are similar but not identical for this one-second time gap.

To start, the rise-time depicted in Figure 3.7b is faster for the inter-molecular controller (3.9). Because the overshoot is practically zero, it is logical that the settling-time, as shown in Figure 3.7a, is faster for the inter-molecular controller (3.9).

From the velocity graph of two examples in Figure 3.8, this difference in rise-time and settling time can be explained when looking at the peak's area and width. Although the first follower for the quadratic controller (3.10) has a higher velocity peak, it also decreases faster, which is indicated by the arrows overlapping the subplots. This difference ensures that the settling-time and rise-time are faster for the inter-molecular controller (3.9).

These differences are directly related to the difference between the APFs, visualized in Figure 3.1. Here the quadratic platoon APF (3.2) has a larger potential value at the one second time gap ($\Delta X = X_r + v_{\text{ref}} * 1$), but also decreases quicker than the inter-molecular platoon APF (3.1) for $\Delta X \rightarrow X_r \forall \Delta X \geq X_r$.

Finally, Figure 3.9 shows that the Type I disturbance propagates through the platoon. Both controllers manage to dampen the disturbance similarly, as the maximum value of inter-vehicle distance decreases along the string of vehicles.

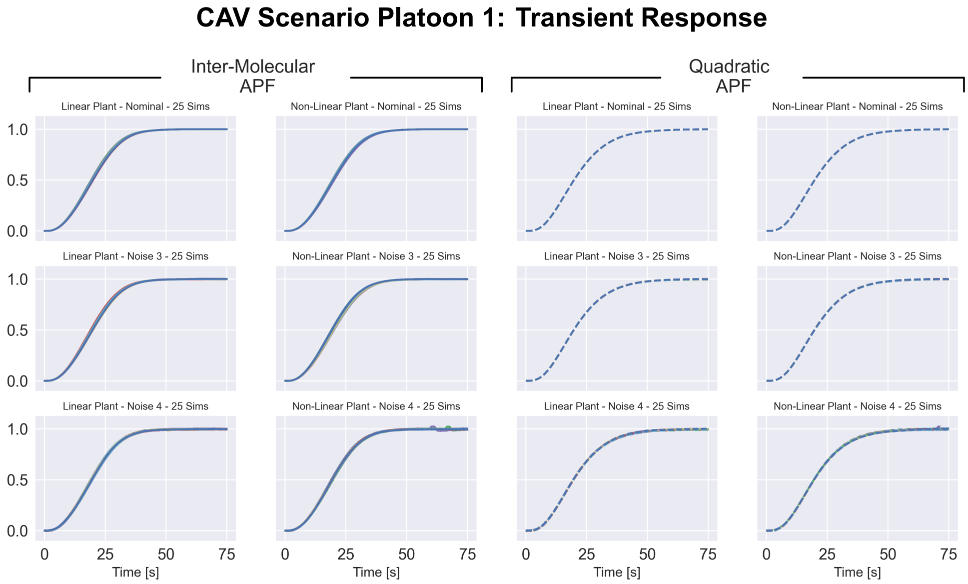

Figure 3.6: Transient response for the platoon 1 scenario, introduced in Subsection 3.3.3. The two left columns represent the simulations carried out with the inter-molecular controller (3.9). The two right columns, with the quadratic controller (3.10), are also indicated by the dashed lines. Each row represents a different noise level, where the first row contains no noise and the lower row represents the most. Lastly, columns one and three were simulated using the linear plant and columns two and four with the non-linear plant.

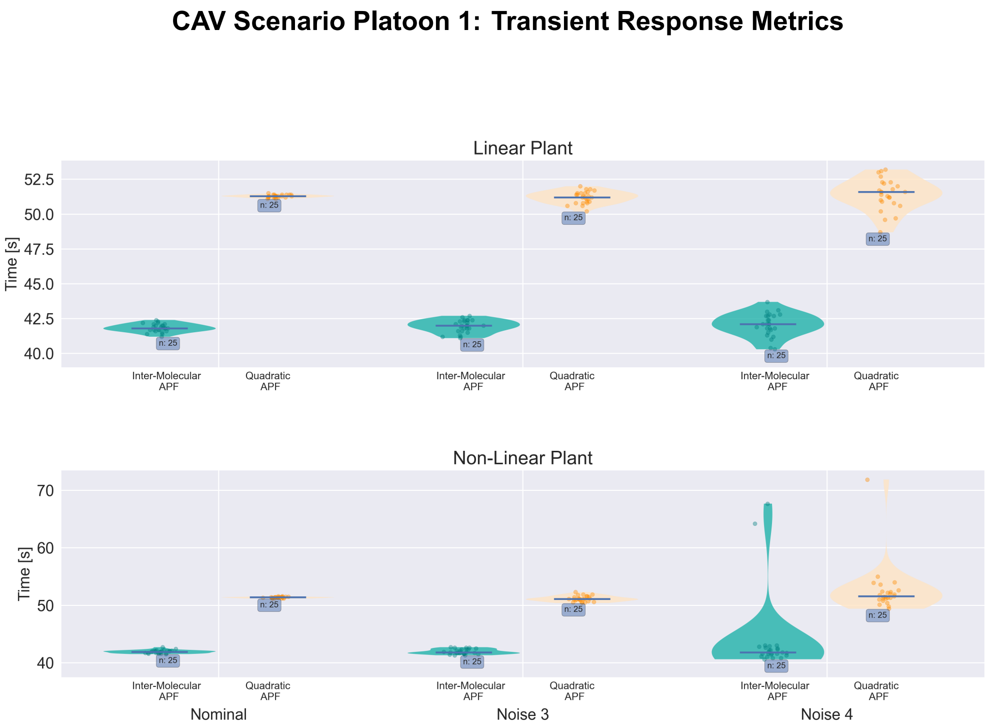

(a) Settling-Time

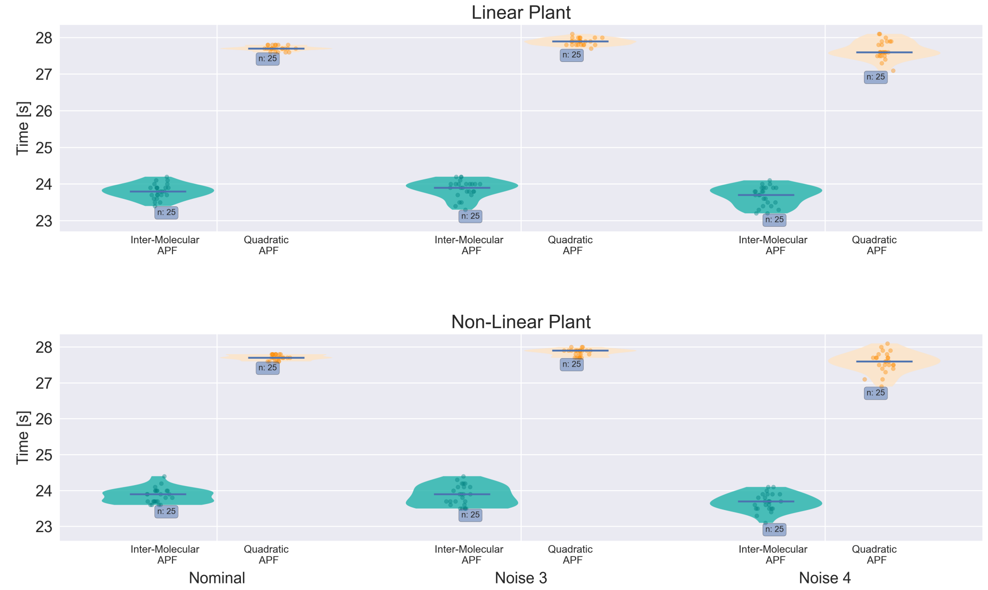

(b) Rise-Time

Figure 3.7: Based on the transient response from Figure 3.6, are the settling-time is shown in Figure 3.7a, and the rise-time in Figure 3.7b. Multiple groups can be seen in the subplot, where each group represents a different amount of measurement noise. The leftmost group represents simulations without noise, and the rightmost group represents the most noise. Furthermore, the left violinplot of each group contains the results from the inter-molecular controller (3.9), and the right with the quadratic controller (3.10). Lastly, the upper subplot represents the simulations with the linear plant and the lower subplot with the non-linear plant.

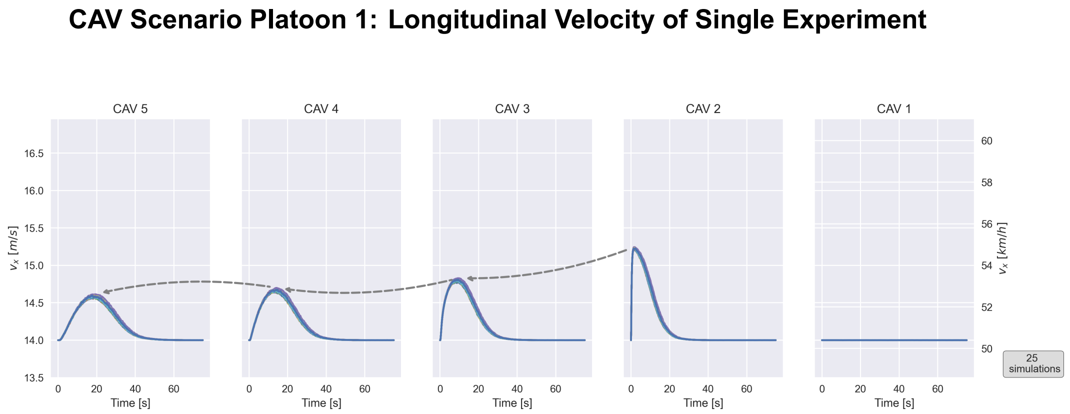

(a) Inter-molecular APF (3.9)

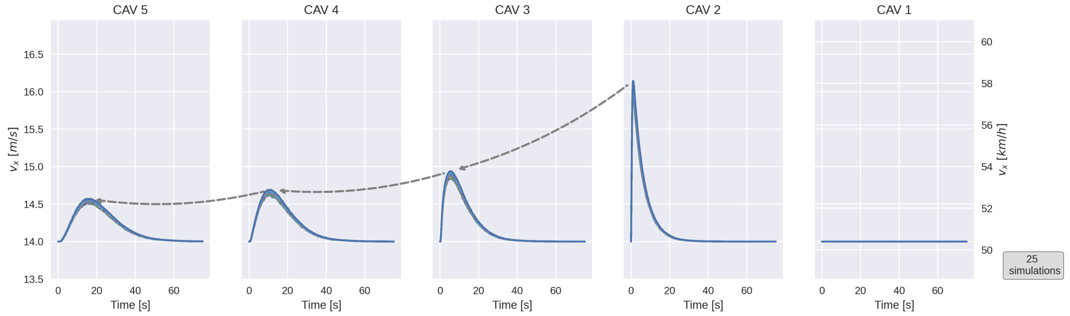

(b) Quadratic APF (3.10)

Figure 3.8: The longitudinal velocities for platoon scenario 1 of a single experiment is visualized. The rightmost plot represents the leader vehicle, and the leftmost plot represents the last follower. Figure 3.8a is the result of the simulation carried out by the inter-molecular controller(3.9) and Figure 3.8b by quadratic controller (3.10). The arrows overlapping the subplots indicate the amount of dampening along the string of vehicles. These two experiments were simulated using the non-linear plant. Furthermore, no measurement noise was used.

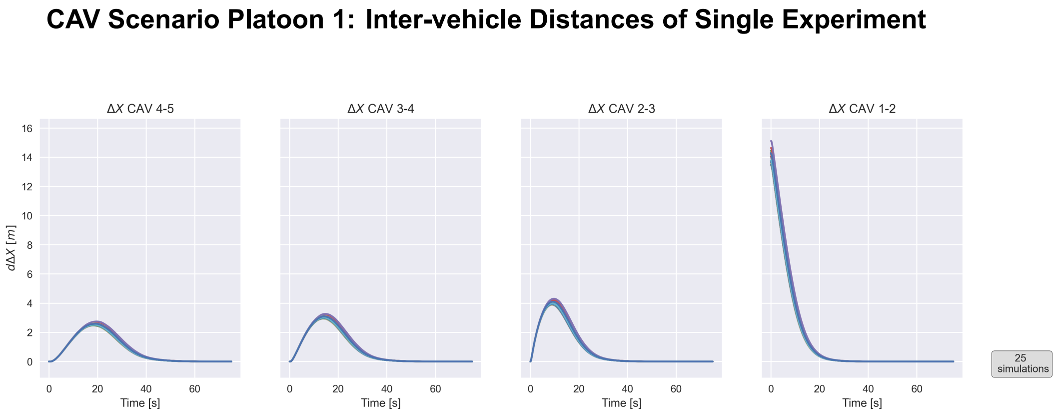

(a) Inter-molecular APF (3.9)

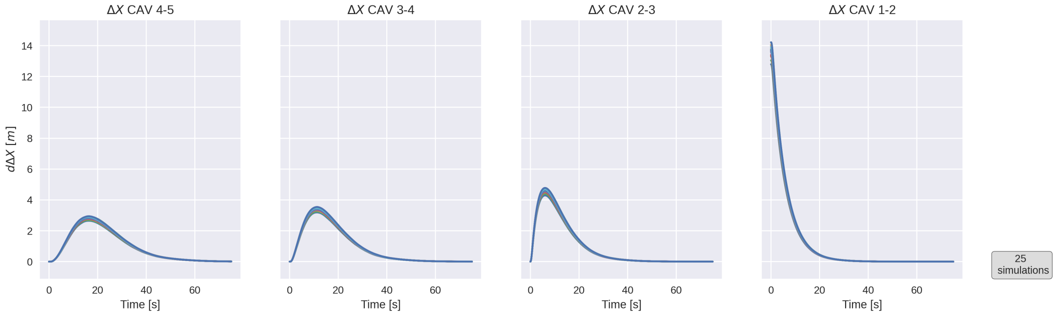

(b) Quadratic APF (3.10)

Figure 3.9: The inter-vehicle distance for platoon scenario 1 of a single experiment is visualized. The rightmost plot represents the inter-vehicle distance between the leader vehicle and the first follower, and the leftmost plot represents the distance between the last two followers. When the trajectories converge to $\delta\Delta X = 0$, this result implies that $\Delta X = X_r$ and the desired safety distance is reached for the corresponding v_{ref}. Figure 3.9a is the result of the simulations carried out by the inter-molecular controller (3.9) and Figure 3.9b by the quadratic controller (3.10). These two experiments were simulated using the non-linear plant. Furthermore, no measurement noise was used.

3.4.2. Scenario Platoon 2: Disturbance Type I - Three-Second Time Gap

First, Figure 3.10 shows that all trajectories manage to reach string stability, and all simulations were labelled a success. Secondly, the general shape of the transient responses for both controllers is similar, even though the difference between the APF is now more apparent, as demonstrated in Figure 3.1.

However, when examining the transient response metrics, differences become apparent. Figure 3.11a shows that the inter-molecular controller (3.9) has a slightly slower settling time than the quadratic controller (3.10). Similarly, the rise-time is also longer for the inter-molecular controller (3.9), as seen in Figure 3.11b. However, the difference in the rise-time is more significant than in settling-time. The example in Figure 3.12 shows where these differences come from. Again, the longitudinal velocity increases faster and to a higher maximum for the quadratic controller (3.10).

Figure 3.13 shows that the maximum value of the vehicles' inter-vehicle distance decreases throughout the platoon; the type I disturbance is dampened along the string of vehicles. For the inter-molecular controller (3.9), the maximum values off all inter-vehicle distances are smaller. This observation implies that the dampening of the type I disturbance by the inter-molecular controller (3.9) is more significant than by the quadratic controller (3.10). Lastly, this figure also shows the direct result of the faster accelerations by the quadratic controller (3.10); the second inter-vehicle distance increases more rapid than for the inter-molecular controller (3.9): thus resulting in the quicker rise-time.

Figure 3.14 illustrates the delay inside the platoon. In this scenario, only the gap between the first two vehicles has to be closed. The other cars start at the correct distance from each other. However, as the second vehicle begins to accelerate to close the gap, the other vehicles must also do so. The blue line in Figure 3.14 represents the desired inter-vehicle spacing, defined by (3.3), for a given longitudinal speed. When increasing speed, each CAVs trajectory should ideally match this blue line. However, these CAVs must first detect or receive that the preceding vehicle is accelerating before they can begin accelerating themselves, resulting in a delayed response. As a result, the trajectories do not match the blue line.

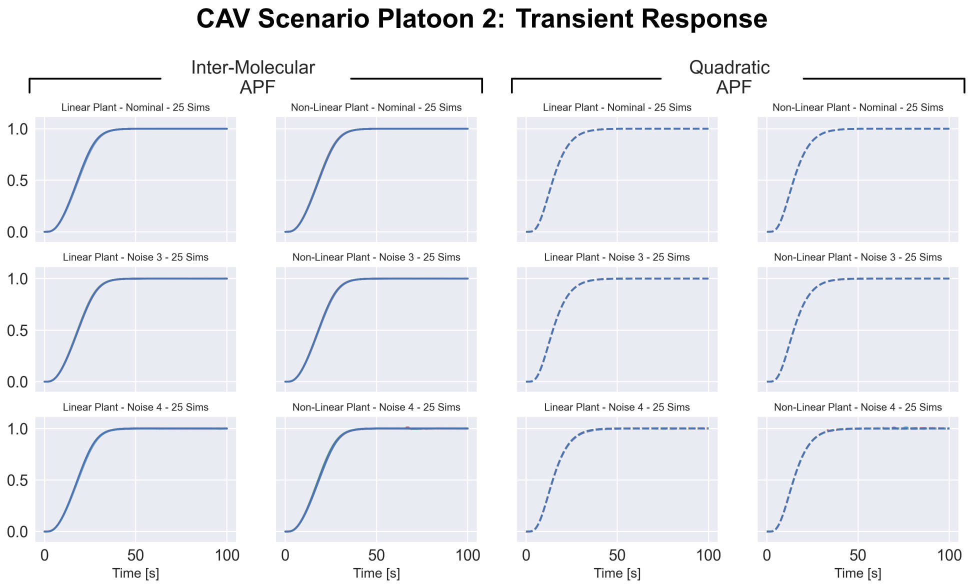

Figure 3.10: Transient response for the Platoon 2 scenario, introduced inSubsection 3.3.3. The two left columns represent the simulations carried out with the inter-molecular controller (3.9). The two right columns, with the quadratic controller (3.10), are also indicated by the dashed lines. Each row represents a different noise level, where the first row contains no noise and the lower row represents the most. Lastly, columns one and three were simulated using the linear plant and columns two and four with the non-linear plant.

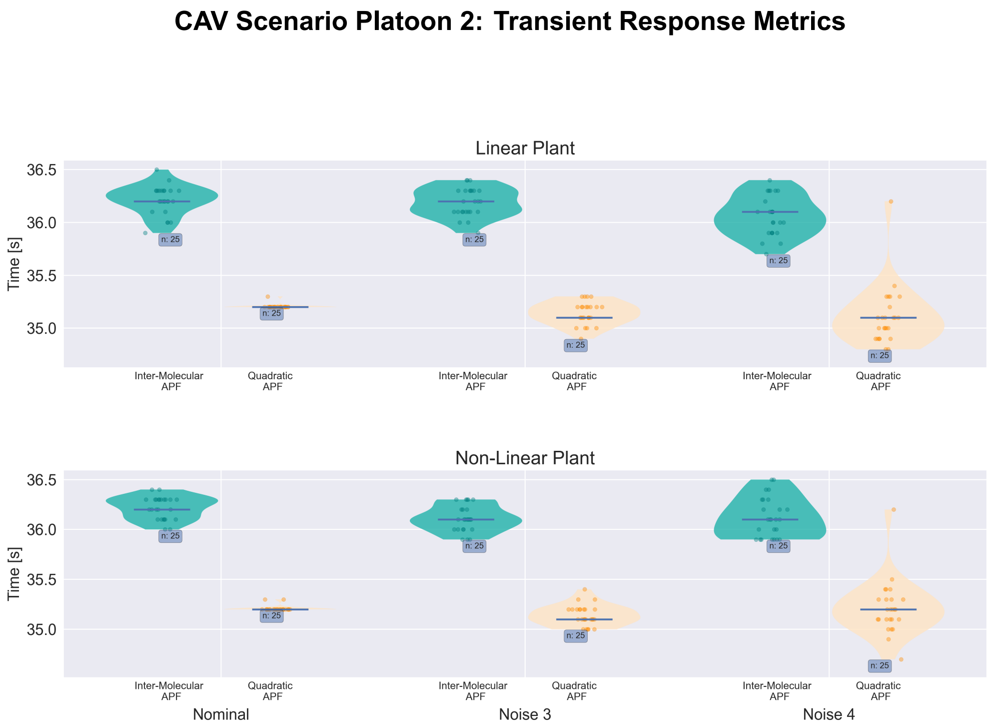

(a) Settling-Time

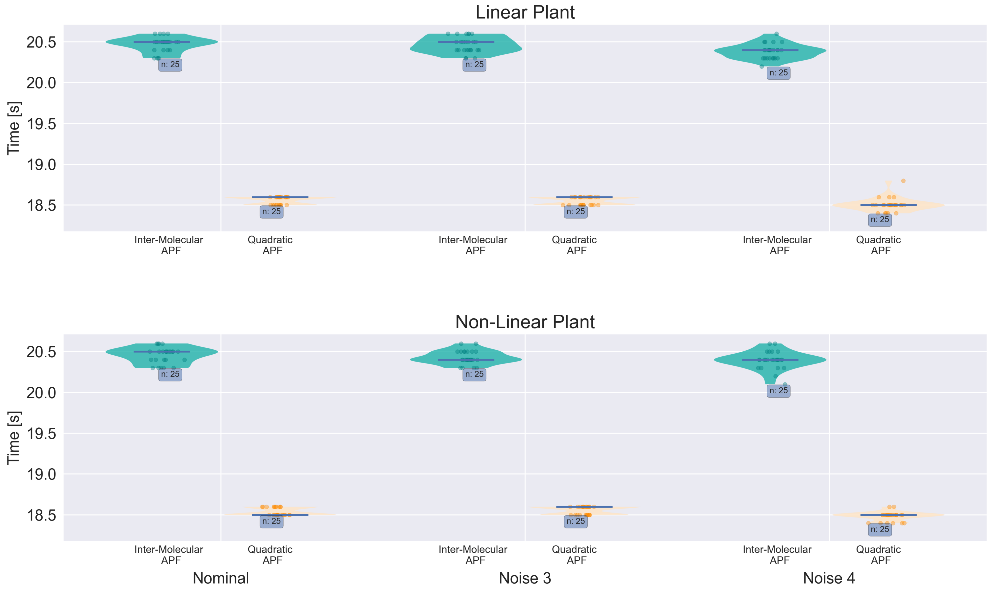

(b) Rise-Time

Figure 3.11: Based on the transient response from Figure 3.10, are the settling-time is shown in Figure 3.11a, and the rise-time in Figure 3.11b. Multiple groups can be seen in the subplot, where each group represents a different amount of measurement noise. The leftmost group represents simulations without noise, and the rightmost group represents the most noise. Furthermore, the left violinplot of each group contains the results from the inter-molecular controller (3.9), and the right with the quadratic controller (3.10). Lastly, the upper subplot represents the simulations with the linear plant and the lower subplot with the non-linear plant.

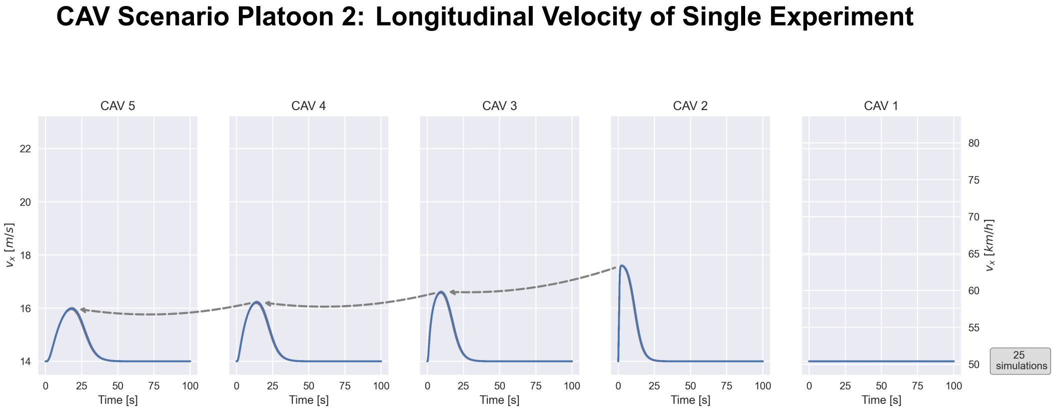
CAV Scenario Platoon 2: Longitudinal Velocity of Single Experiment

(a) Inter-molecular APF (3.9)

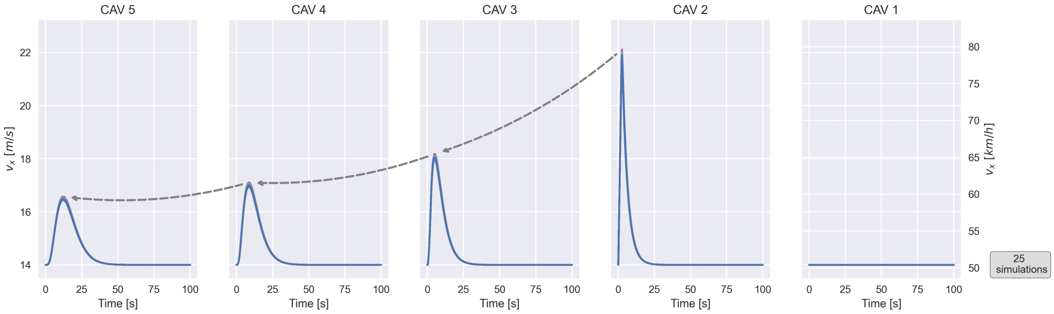

(b) Quadratic APF (3.10)

Figure 3.12: The longitudinal velocities for platoon scenario 1 of a single experiment is visualized. The rightmost plot represents the leader vehicle, and the leftmost plot represents the last follower. Figure 3.12a is the result of the simulation carried out by the inter-molecular controller (3.9) and Figure 3.12b by the quadratic controller (3.10). The arrows overlapping the subplots indicate the amount of dampening along the string of vehicles. These two experiments were simulated using the non-linear plant. Furthermore, no measurement noise was used.

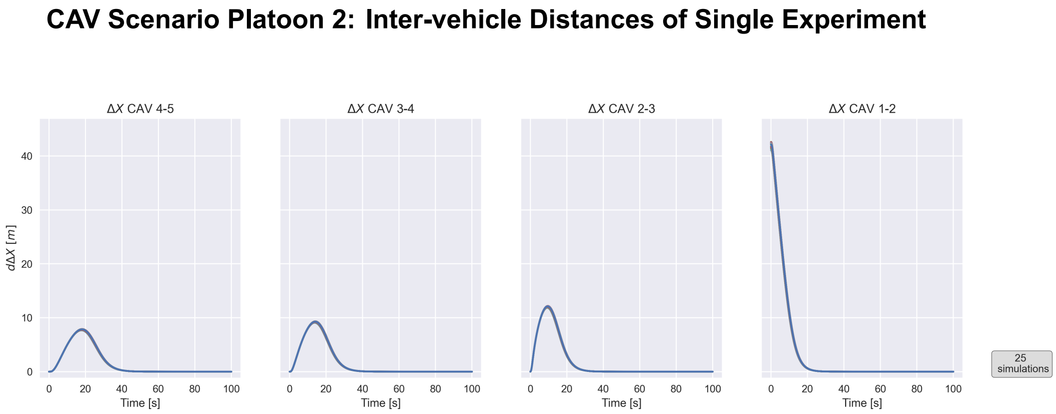

(a) Inter-molecular APF (3.9)

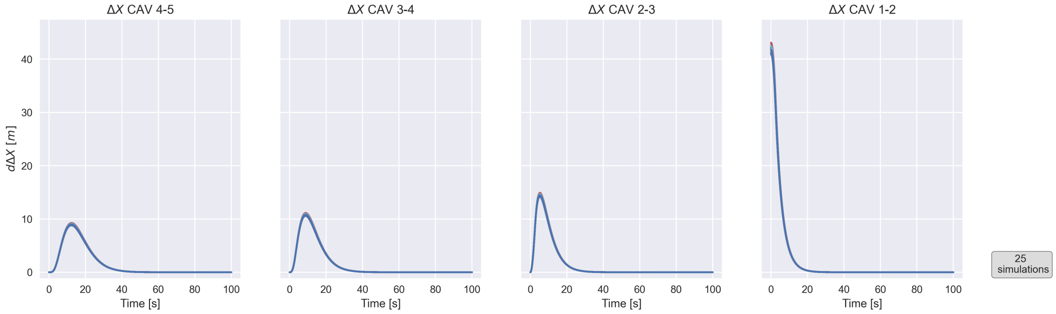

(b) Quadratic APF (3.10)

Figure 3.13: The inter-vehicle distance for platoon scenario 2 of a single experiment is visualized. The rightmost plot represents the inter-vehicle distance between the leader vehicle and the first follower, and the leftmost plot represents the distance between the last two followers. When the trajectories converge to $\delta\Delta X = 0$, this result implies that $\Delta X = X_r$ and the desired safety distance is reached for the corresponding v_{ref}. Figure 3.9a is the result of the simulations carried out by the controller with the inter-molecular controller (3.9) and Figure 3.9b the quadratic controller (3.10). These two experiments were simulated using the non-linear plant. Furthermore, no measurement noise was used.

CAV Scenario Platoon 2: Longitudinal Velocity & Relative Longitudinal Position

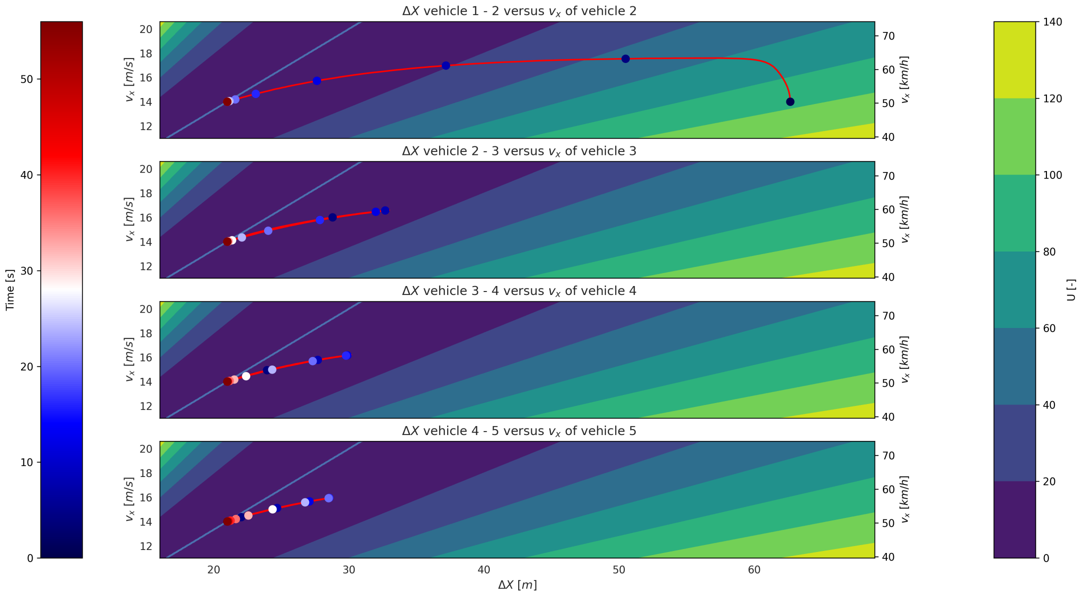

(a) Inter-molecular Platoon APF (3.9)

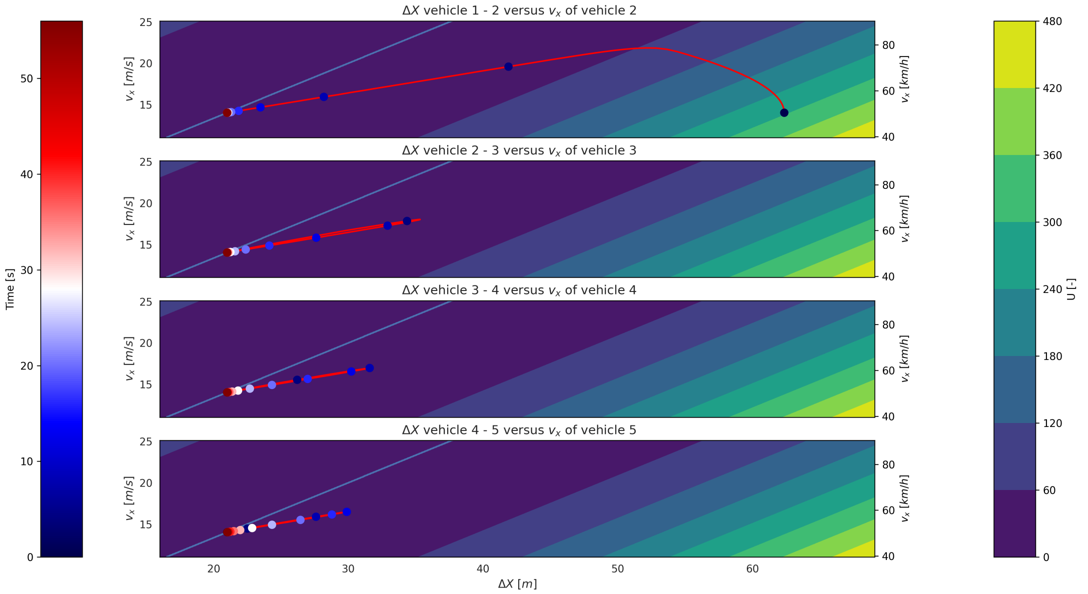

(b) Quadratic Platoon APF (3.10)

Figure 3.14: The progress of the different inter-vehicle distances ΔX is visualized against the longitudinal velocity of the corresponding following vehicle. The contour plot represents the longitudinal platoon APF, supported by the right colour bar. The dots on each red trajectory is the progress throughout time. For the lower three subplots, it should be noticed that the trajectory goes back and forth on the plotted right line, whereas for the upper subplot, the trajectory starts at the right and ends at the left. Furthermore, the light blue is the CTH (3.3); if each vehicle had perfect knowledge of the situation, its trajectory would lie on top of this line. However, in this case, the trajectories overlay this blue line indicating that there are delays inside the platoon. Figure 3.14a is the result of the simulation carried out by the controller with the inter-molecular controller (3.9) and Figure 3.14b the quadratic controller (3.10). These two experiments were simulated using the non-linear plant and the vehicles according to platoon scenario 2. Lastly, no measurement noise was used.

3.4.3. Scenario Platoon 3: Disturbance Type II - Three-Second Time Gap

The transient responses in Figure 3.15 differ in shape from those in scenario two: for the inter-molecular controller (3.9) the plots rise linearly-like, whereas the shape of the transient responses for (3.10) is comparable to the other scenarios. Furthermore, Figure 3.16 shows even more differences compared to the last two scenarios. For the simulations with the linear plant, all simulations achieve string stability. However, for the non-plant, with the highest noise level, only a few simulations by inter-molecular controller (3.9) manage to achieve string stability. Whereas for the quadratic controller (3.10), no simulations manage to reach string stability with the non-linear plant in combination with the highest noise level.

Analyzing the velocities in Figure 3.18 reveals the difference in the shape of the transient responses between the two controllers. Again, the quadratic controller (3.10) increases the CAVs velocity much more than the inter-molecular controller (3.9). For the latter controller, the velocity remains constant for a few seconds because the velocity APF (2.14) prevents the velocity from growing further; when ΔX increases, the derivative of (3.1) decreases (while the derivative of (3.2) increases). As a result, ΔX does not decrease for the first part of the simulation for the last few followers, as seen in Figure 3.19. This reason explains why the transient reaction in Figure 3.15 has a linear-like form. However, for the quadratic controller (3.10), the velocity does not saturate but rises along the string of vehicles; the peak velocity keeps increasing through the platoon, which does not indicate dampening as introduced in Subsection 3.3.1.

Furthermore, when CAVs drive at a higher speed, other aspects next to lateral control become more challenging. Figure 3.20 shows that for the simulations with the quadratic controller (3.10) the rear CAVs have a sizeable lateral deviation even without noise. The vehicles in this scenario were perturbed from the centre of the lane at the start of the simulation. Consequently, the vehicles must return to the centre of the lane while following the preceding vehicle's lateral position. This task appears to be conflicting and thus challenging for some simulations: the last two cars cross the lane markers, as seen in Figure 3.21.

This problem emerges when each CAV predicts the future position of the other vehicles for the eMPC horizon based on their current motion states. When a preceding vehicle starts moving to the middle of the lane, it is headed to the adjacent lane. At this moment, the following CAV expects the preceding CAV to make a lane change and begins to follow it. With multiple CAVs after each other, this problem can lead to large lateral manoeuvres and the CAVs crossing the lane markers.

For some simulations, the platoon still manages to reach the desired platoon configuration after such an undesired evasive manoeuvre. From a longitudinal perspective, the platoon thus managed to reach string stability, and one could argue that the lateral control was insufficient. However, even though the lateral control could have been inadequate, the quadratic controller (3.10) controller increased the longitudinal velocity to the point where the coupling between the longitudinal and lateral dynamics became an issue. With the inter-molecular controller (3.9), this problem did not arise. As no saturation of the longitudinal velocity has been observed for the quadratic controller (3.10), a larger maximum velocity can be expected for an even larger initial time gap. Therefore, the coupling of longitudinal and lateral dynamics is a larger source of concern when using the quadratic controller (3.10) based on quadratic platoon APF (3.2) compared to the inter-molecular controller (3.9) based on the inter-molecular platoon APF (3.1).

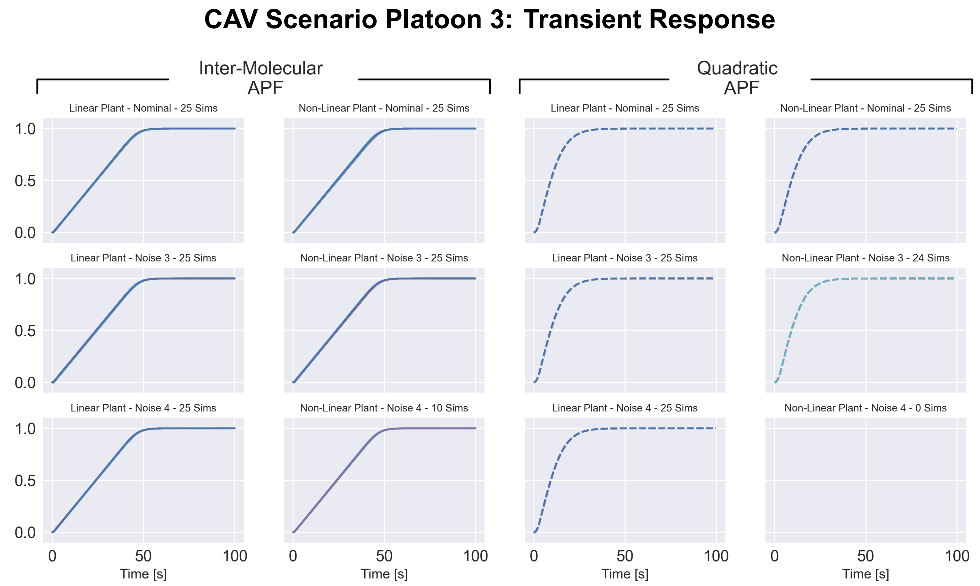

Figure 3.15: Transient response for the Platoon 3 scenario, introduced inSubsection 3.3.3. The two left columns represent the simulations carried out with the inter-molecular controller (3.9). The two right columns with the quadratic controller (3.10), are also indicated by the dashed lines. Each row represents a different noise level, where the first row contains no noise and the lower row represents the most. Columns one and three were simulated using the linear plant, and columns two and four with the non-linear plant. Lastly, the lower right subplot has no trajectories because not a single trajectory was able to converge to string stability. Thus no normalized transient response was calculated.

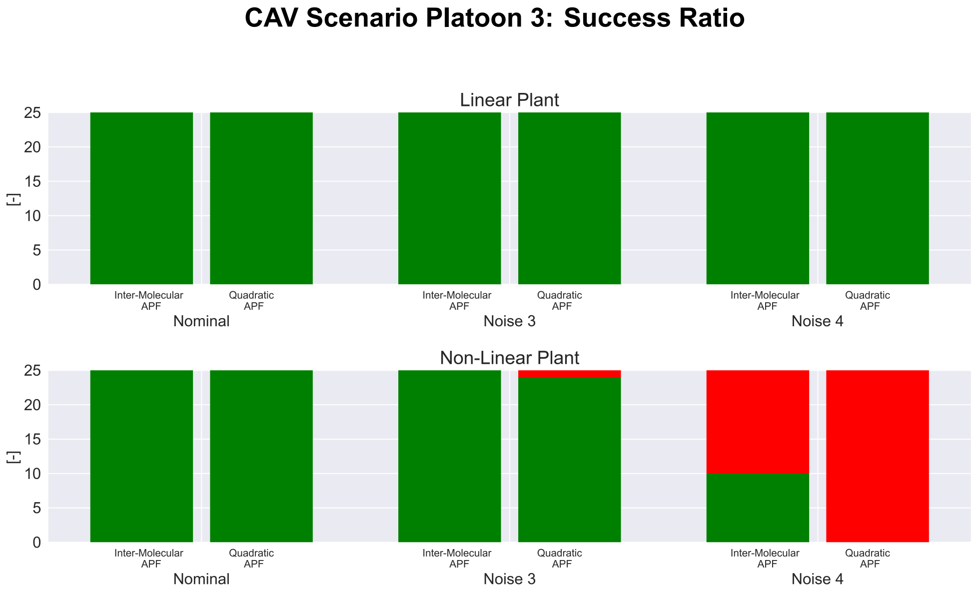

Figure 3.16: Visualization of the amount of success for the Platoon 3 scenario, introduced inSubsection 3.3.3. Each group represents a different noise level; the leftmost group represents no noise, and the rightmost group the most noise. The results in the upper subplot were gathered using a linear plant and the lower subplot with the non-linear plant. Lastly, the left column from each group represents the simulations carried out with the inter-molecular controller (3.9), and the right two columns with the quadratic controller (3.10). Lastly, the red areas indicate failure and the green success.

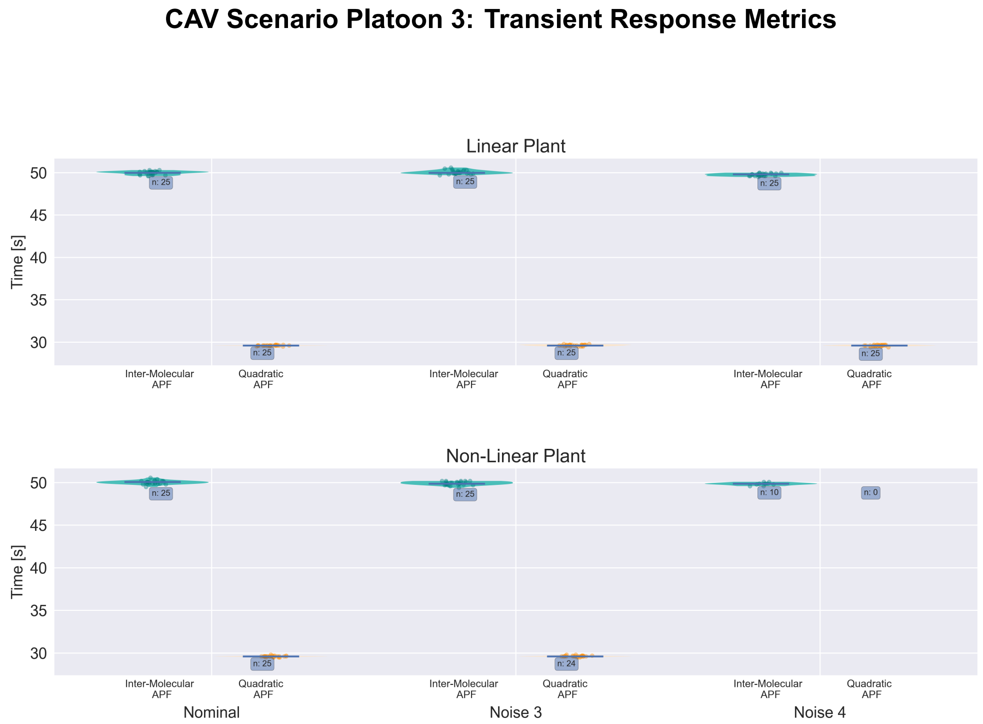

(a) Settling-Time

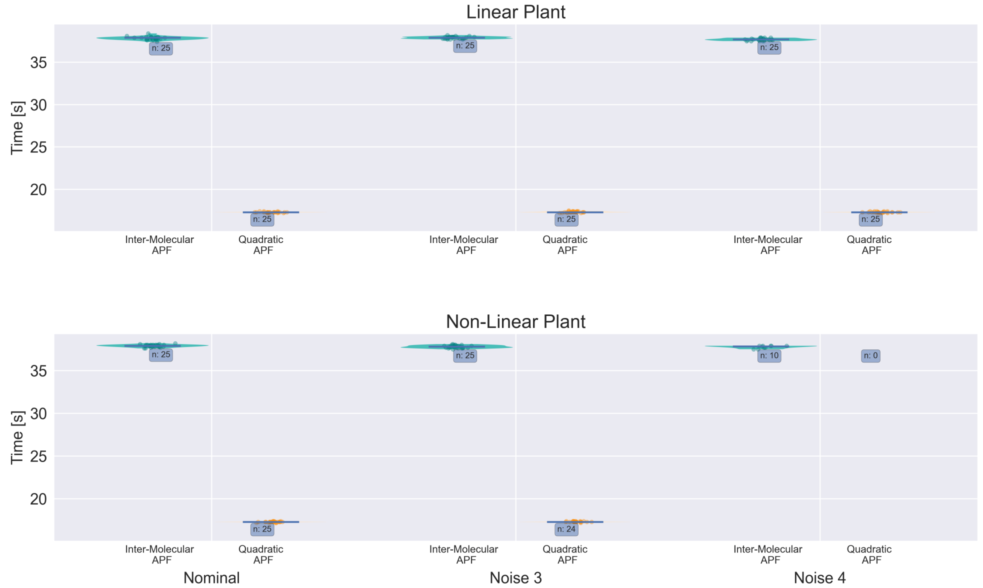

(b) Rise-Time

Figure 3.17: Based on the transient response from Figure 3.15, are the settling-time is shown in Figure 3.17a, and the rise-time in Figure 3.17b. Multiple groups can be seen in the subplot, where each group represents a different amount of measurement noise. The leftmost group represents simulations without noise, and the rightmost group represents the most noise. Furthermore, the left violinplot of each group contains the results from the controller with the inter-molecular controller (3.9), and the right with the quadratic controller (3.10). The upper subplot represents the simulations with the linear plant, and the lower subplot with the non-linear plant.

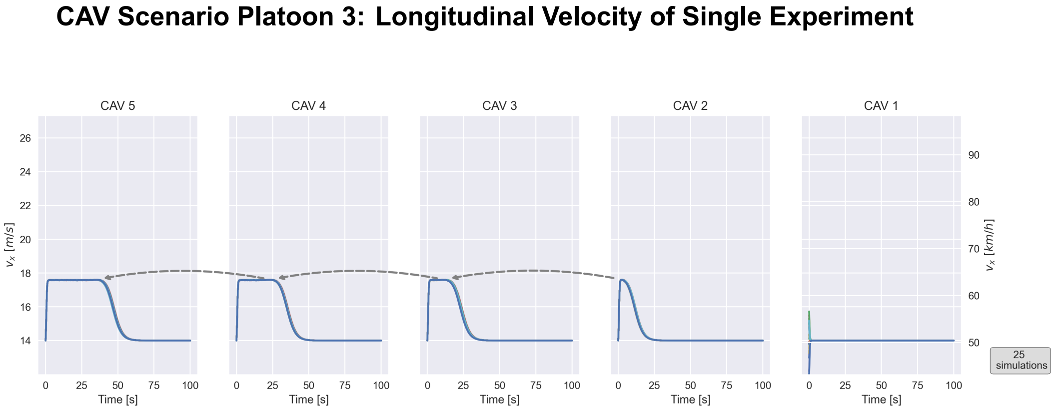

(a) Inter-molecular APF (3.9)

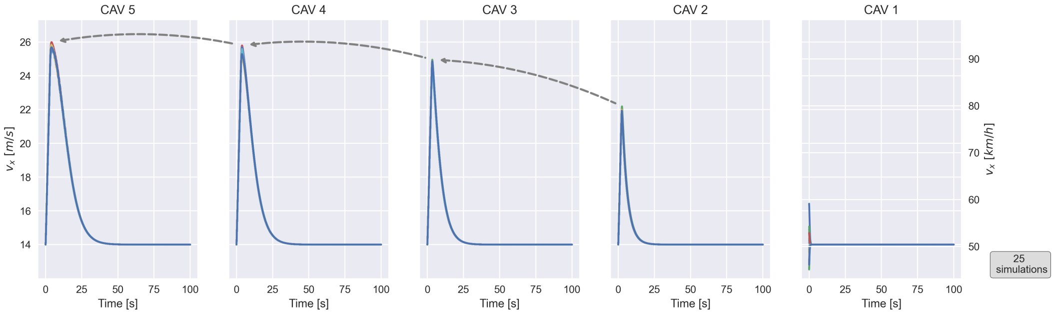

(b) Quadratic APF (3.10)

Figure 3.18: The longitudinal velocities for platoon scenario 3 of a single experiment is visualized. The rightmost plot represents the leader vehicle, and the leftmost plot represents the last follower. Figure 3.18a is the result of the simulation carried out by the controller with the inter-molecular controller (3.9) and Figure 3.18b the quadratic controller (3.10). The arrows overlapping the subplots indicate the amount of dampening taking place along the string of vehicles. These two experiments were simulated using the non-linear plant. Furthermore, no measurement noise was used.

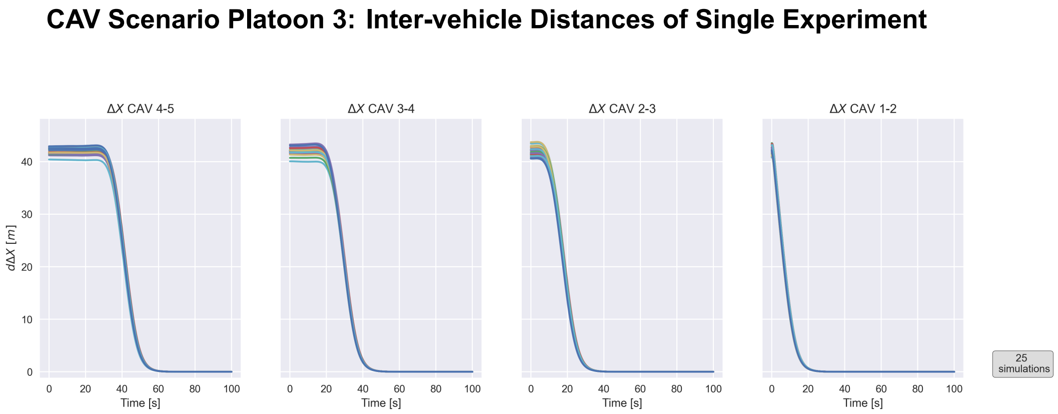

CAV Scenario Platoon 3: Inter-vehicle Distances of Single Experiment

(a) Inter-molecular APF (3.9)

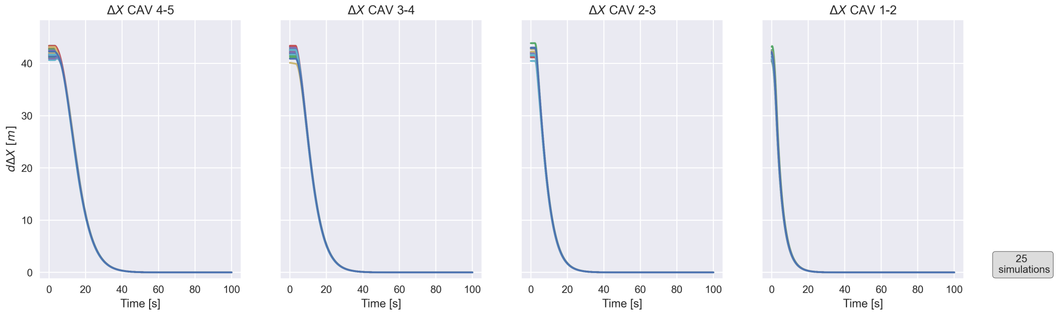

(b) Quadratic APF (3.10)

Figure 3.19: The inter-vehicle distance for platoon scenario 3 of a single experiment is visualized. The rightmost plot represents the inter-vehicle distance between the leader vehicle and the first follower, and the leftmost plot represents the distance between the last two followers. When the trajectories converge to $\delta \Delta X = 0$, this result implies that $\Delta X = X_r$ and the desired safety distance is reached for the corresponding v_{ref}. Figure 3.19a is the result of the simulation carried out by the controller with the inter-molecular controller (3.9) and Figure 3.19b the quadratic controller (3.10). Lastly, these two experiments were simulated using the non-linear plant without measurement noise.

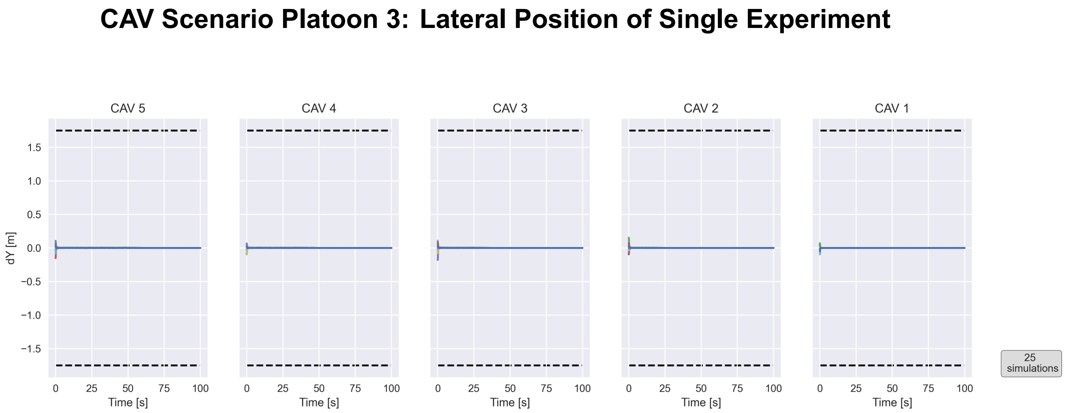

(a) Inter-molecular APF (3.9)

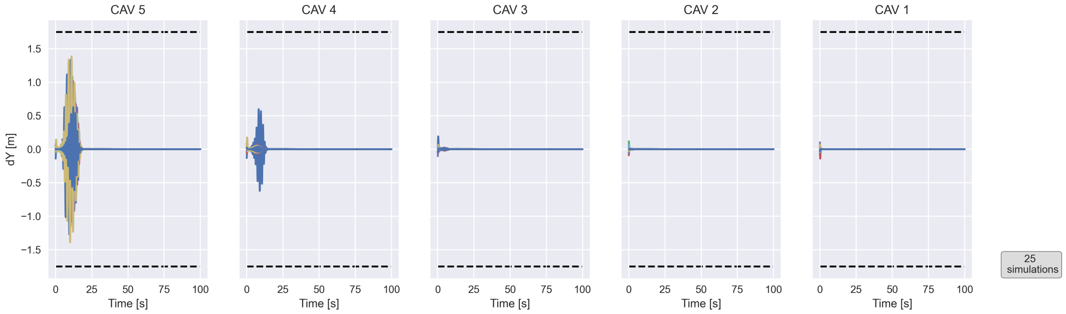

(b) Quadratic APF (3.10)

Figure 3.20: The lateral position for platoon scenario 3 of a single experiment is visualized. The rightmost plot represents the leader vehicle, and the leftmost plot represents the last follower. Figure 3.20a is the result of the simulations carried out by the controller with the inter-molecular controller (3.9) and Figure 3.20b the quadratic controller (3.10). These two experiments were simulated using the non-linear plant. Furthermore, no measurement noise was used.

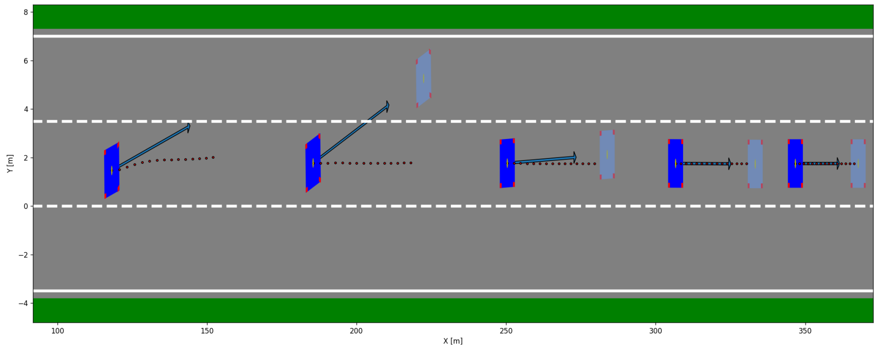

(a) Last CAV predicts second-last CAV to make a lane change, but due to lane APF, it plans to stay in the current lane.

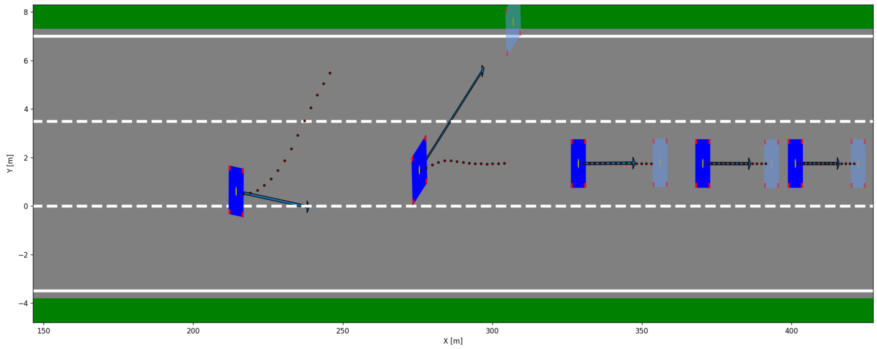

(b) Last CAV predicts second-last CAV to make a big lane change, and plans to make lane change as well.

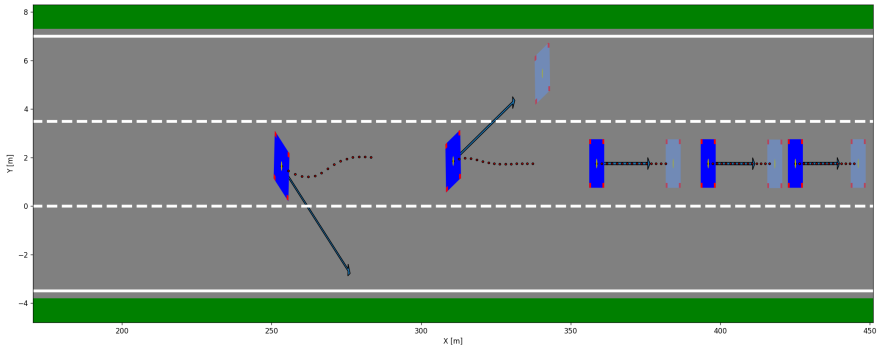

(c) Last CAV predicts second-last CAV to make a lane change, but due to lane APF, it plans to stay in the current lane.

Figure 3.21: The last two vehicles of the platoon move too much to the side of the lane resulting in an unnecessary, dangerous manoeuvre. Each sub-figure represents a moment in time. The light blue vehicles represent the predicted position of each preceding vehicle at the end of the prediction horizon. The red dots represent the discrete steps during this horizon. Lastly, the blue arrows indicate the local longitudinal velocity and the heading of each CAV.

3.5. Discussion

Two platoon controllers were compared based on two different longitudinal platoons APFs (3.2) and (3.1). Three different scenarios were used to examine the platoon stabilizing capabilities. Even though the main focus was longitudinal control, it was also found that the lateral control was influenced by these longitudinal APFs as well when the velocity was increased too much. Furthermore, it was observed that the platoon could not match the desired safety distance (3.3) while rejecting the platoon disturbance. This section will discuss these parts in more detail and summarise the key points.

Longitudinal Control

Both controllers can reach string stability for the lower noise levels for the three scenarios. The transient responses of ΔX_{tot} have negligible overshoot, which is desirable for collision avoidance. Both controllers can handle the situation in the first scenario similarly. In the second scenario, both controllers still reached string stability but with a different approach.

However, with the third scenario, the results of the quadratic controller (3.10), were not satisfactory. Although the platoon reached the desired formation, the approach was undesirable. The maximum velocity of each individual CAV kept increasing along the string of vehicles. Next to reaching the desired relative longitudinal position, string stability also implies that the platoon disturbances are not increased along the string of vehicles. On the contrary, the inter-molecular controller reached the desired longitudinal position while the maximum velocity did not increase through the platoon.

Furthermore, controllers handle the last two scenarios differently for a larger time-gap. Gap-closing happens much faster for the quadratic controller (3.10) than the inter-molecular controller (3.9). This difference could be seen as either more efficient or less comfortable.

This difference in velocity can be explained when one looks at the gradient from the quadratic longitudinal platoon APF (3.2) in Figure 3.1: when ΔX increases, the gradient keeps increasing. On the contrary, the gradient of the inter-molecular platoon APF(3.1) decreases when ΔX increases. This characteristic is the reason that the quadratic controller (3.10) kept increasing the maximum velocity along the string of vehicles, whereas the inter-molecular controller (3.5) was able to ensure the platoon disturbance was not amplified.

Lateral Control

Even though both controllers could reach the desired longitudinal formation, the lateral response was insufficient because lane markers were crossed. When analyzing platoon stability, focusing solely on longitudinal control is inadequate.

Additionally, this observation raises the question of whether the quadratic APF for lateral control is sufficient, as minor movements of the preceding CAV should have little impact on the following vehicles. The objective of this lateral APF is to attract the CAV to a specific spot in the lane. When a CAV is not in the centre of the lane, the lateral platoon APF (3.4) attracts the following CAV to an exact lateral position in the lane. However, there is enough room in the lane for the CAV to manoeuvre around. The following CAV should not be forced to the same lateral position because the lane is wide enough to allow for manoeuvring around.

Alternatively, one could argue that predicting the CAVs future position based on the current velocity and direction is overly simplistic and that a more advanced approach or ideal V2V should be utilized. Perfect position prediction, or V2V, on the other hand, would not enable the following CAV to use extra lane space; instead, it would merely improve the handling of these high demands.

With the current framework, the high demand by the quadratic lateral platoon APF, along with the simplistic prediction, leads to this unwanted unstable behaviour. This issue becomes more severe when driving at a higher velocity. In the AV chapter, hardly any differences between the two plants were observed. However, due to this increase in velocity, the CAVs operated further away from the operating point, and this lateral control problem became a more significant issue for the non-linear plant.

Delay

The desired relative distance for different velocities was defined by (3.3). In Figure 3.14, this safety distance was visualized. The results showed that the actual trajectories did not match this line. This difference arises because each CAV must first detect that the preceding vehicle is accelerating before it can start accelerating itself. This fact results in a delayed response and a more considerable inter-vehicle distance than needed. Could extra information or more extensive V2V enhance this response and ensure that the CAVs trajectory comes closer to this desired inter-vehicle distance (3.3)?

4

Conclusion

After discussing the AV results in Section 2.6 and the CAV results in Section 3.5, the following section will first answer the thesis sub-questions introduced in Section 1.3. Based on these answers, the main thesis research question is answered hereafter. Finally, this chapter will end with some recommendations for future research.

4.1. Sub Research Question

Sub Research Question I

What metrics can be used to measure the performance of this Artificial Potential Function - economic Model Predictive Control framework?

Analyzing the transient response of the AVs lateral position gave sufficient insights into the capabilities of the AV. For the CAV, the sum of the inter-vehicle distance is a reasonable parameter to analyze if the whole group of vehicles is able to form and maintain a platoon formation. By looking at the longitudinal velocity of the individual vehicles, the platoon's ability to dampen platoon disturbances along the vehicle string is revealed. Lastly, the lateral position of the rear vehicle(s) indicates if the platoon is able to stay in the desired lane.

Sub Research Question II

What Artificial Potential Functions can achieve platoon-specific behaviour?

For lateral control, the quadratic lateral platoon APF (3.4) can keep the following CAVs in the correct lane. However, during more complex manoeuvres, this APF is not sufficient. Due to the shape of the function, the CAV is prevented from using the whole width of the lane.
For the longitudinal part, the quadratic controller (3.10), based on the quadratic platoon APF (3.2), can maintain a platoons formation. However, when a platoon is being formed, platoon disturbances are amplified instead of dampened and more importantly, safe manoeuvring can not be guaranteed.
On the contrary, the inter-molecular controller (3.9) based on the inter-molecular platoon APF (3.9) was able to reject the platoon disturbances while maintaining safe lateral manoeuvres.
So the state-of-the-art controller (3.10) is sufficient for maintaining a platoon's formation, while the inter-molecular controller (3.9) is more appropriate when creating a platoon.

Sub Research Question III

Is there a performance guarantee for this Artificial Potential Function - economic Model Predictive Control framework?

From the different simulations performed with the AV and CAV, it can be concluded that the AV and CAV are both capable of reaching the desired goals till noise level three. For the AV specifically, this conclusion applies in the same manner both for linear and non-linear plants. However, for the CAV part, this general statement is still correct, but there are more apparent differences between them.

Sub Research Question IV

For which kind of CAV-specific scenarios can the Artificial Potential Function - economic Model Predictive Control be used?

Based on the multiple simulations, it can be concluded that the APF-eMPC, in combination with the inter-molecular APF, can safely handle the various platoon disturbances and can be used for gap-closing manoeuvres to form a platoon.

4.2. Research Question

Finally, the main research question of this thesis is answered.

Main Thesis Research Question

How can the Artificial Potential Function - economic Model Predictive Control framework be used more effectively for a Connected Autonomous Vehicle application?

Based on the inter-molecular platoon APF (3.1), this improved APF-eMPC framework is better capable of forming platoons without jeopardizing individual vehicle safety than the state-of-the-art.

4.3. Recommendations

Multiple opportunities for future research arose during the design process and the result analysis. These recommendations will briefly be discussed. First, specific improvements to an AV based on the APF-eMPC framework will be shared. Furthermore, as APFs form the backbone of this framework, some precise details and improvements regarding these will also be shared. Additionally, there are various ways to extend and improve the numerical analysis. Finally, specific improvements are addressed to ensure that the framework may be used in a physical case study.

4.3.1. Extending the Framework

One of the CPC strategy's main goals is to create a more complete framework that is a solution for multiple problems instead of one [30]. The following extensions will ensure that the APF-eMPC framework comes closer to such a complete solution. To start, eMPC has also been applied to improve fuel usage of platoons [94]. As this thesis uses eMPC already, it could be interesting to see how this framework could be extended to improve a platoon's fuel usage. This thesis used a yaw rate constraint (2.17g) to avoid undesirable hard turning. The numerical value represents the maximum experienced yaw rate during an extreme manoeuvre [129]. The results demonstrated to converge as fast as possible to the middle of the lane; the AV operates at this maximum allowed yaw rate. However, in any normal situation, it would be more comfortable if the vehicle would be stimulated to use a lower yaw rate if the situation allows for it [142]. Again, this additional requirement could be added to the eMPC stage cost.

It could be interesting to see how different methods could improve the AVs and CAVs performance. The resulting behaviour was not always as expected and desired for the highest used noise level. Incorporating solutions that deal with the noise, like a Kalman filter, could improve the performance further. Furthermore, the main benefit of the CAV is the ability to share information via V2V connectivity. In the simulations of this thesis, only the current motion state of each vehicle was shared. Next to the current state, the future planned states of each CAV can be shared. With this extra information, will each CAV be better able to stay closer to the blue line, depicted in Figure 3.14, representing the CTH (3.3)?

In practice, however, not all vehicles will be able to share information. The future position of some obstacle vehicles will still have to be predicted. In Subsection 3.4.3, it was shown that this current approach is not always ideal. A more advanced method could improve the framework. For instance, [85] combines APFs with velocity obstacles.

4.3.2. Artificial Potential Functions

The lateral platoon APF based on a square function was found inadequate; the APF attracted the vehicle to a specific position in the lane while there was sufficient room to move around. A so-called *bump* function could be used in future research [143]. The region around the minima is broad and less steep compared to the quadratic function, allowing more freedom.

More generally, [30] and [34] claim that this APF-eMPC framework omits motion-planning and even behavioural-decision-making. However, this effect is limited to local planning and control. For example, the current APFs cannot enforce these manoeuvres if a vehicle wants to exit the highway. Global autonomous driving is currently impossible with the CPC strategy, and extra APFs must be designed.

The inter-molecular platoon APF (3.5) was fitted on actual traffic data [83]. However, instead of trying to recreate the way humans drive, different parameters might outperform the human style of driving: the parameters of this APF could be tuned using machine learning, for example.

4.3.3. Numerical Stability Analysis

This thesis has performed a numerical stability analysis to showcase the possibilities and limits of the framework for autonomous driving. This analysis can be expanded even further by using the following suggestions. Firstly, the framework has been shown to work to a certain noise level. However, this additive white Gaussian noise may not represent the actual noise of a sensor. Looking into real sensors to determine these noise patterns would result in more realistic simulations.

Next to noise, disturbances due to wind, for example, could make the simulations more realistic. The simulations could be varied more by perturbing other states of the AV. Even though some state combinations may not be so likely, they will reveal more about the controller. Furthermore, the vehicle interactions could be altered by changing the obstacle and (C)AVs dynamics from homogeneous to heterogeneous. Similarly, the obstacle vehicles could be varied by using different driving styles (e.g. slower and aggressive road users).

The AV was allowed to operate near its linearization point during the simulations. It was found that offline linearization was adequate. However, letting the vehicle operate farther away from this state makes it possible to determine when online linearization would be required. For this thesis, the non-linear bicycle model served as the most realistic simulator. However, using a more realistic simulator, like CarSim [144], could result in even more improved simulations. Lastly, it would be interesting to see how a larger platoon would influence the controller's ability to reach string stability.

4.3.4. Numerical Implementation

The current codebase optimization uses the Constrained Optimization BY Linear Approximation (COBYLA) algorithm from the SciPy library, invented by Powell [139]. This algorithm was developed for problems where the gradient was not known. However, for most APFs, the gradient and Hessian are straightforward to calculate. If the gradient and Hessian of each APF could be calculated, an optimization method from the SciPy library that uses the gradient and the Hessian could improve the computation time.

However, finding the gradient and the Hessian of the distance function for the obstacle APF, (2.12), is nontrivial. From the APF plots depicted in Figure 2.6, it becomes clear that it is continuous but non-smooth. However, from the same figure, it can also be observed that the gradient of the APF always points away from the obstacle set and never towards the subdomains of the obstacle set, which could ease the derivation.

Lastly, converting the code base to a c++ equivalent would result in much quicker run times, further improving the computation time. Hereafter, a more extensive parameter sweep could be performed to optimize the framework further, and an actual physical implementation could be attempted.

A

Numerical Values

Parameter	Value	Unit	Explanation
w_{road}	3.5	m	road width
L_{min}	-25	m	sensor reach forward
L_{max}	50	m	sensor reach backward
v_{ref}	14	m/s	velocity reference
ϵ	2	$\%$	settling-time threshold
n_p	5	$-$	amount of vehicles in platoon

Table A.1: Numerical values which are simulation specific

Parameter	Value	Unit	Explanation
σ_{v_x}	1	m/s	perturbing longitudinal velocity
σ_X	0.5	m	perturbing longitudinal position
σ_Y	0.05	m	perturbing lateral position

Table A.2: Numerical values for the standard deviation to vary initial state based on Gaussian function with zero mean

Parameter	Value	Unit	Explanation
m	1450	kg	mass vehicle
I_z	2740	$kg \cdot m^2$	moment of inertia around z-axis
l_f	1.1	m	distance from COG to front axle
l_r	1.6	m	distance from COG to rear axle
C_f	65000	N/rad	front wheel cornering stiffness coefficient
C_r	65000	N/rad	rear wheel cornering stiffness coefficient
C_δ	0.8	rad	limits of steering wheel
C_F	5000	N	limits of engine
w_{AV}	5	m	outer width of AV
l_{AV}	2	m	outer length of AV
T	0.1	s	time-step

Table A.3: Numerical values for Bicycle Model [30]

Parameter	Value	Unit	Explanation
u_{min}	$[-1,-1]^\intercal$	-	input constraints min
u_{max}	$[1,1]^\intercal$	-	input constraints max
Δu_{min}	$[-0.3,-0.5]^\intercal$	-	input rate constraints min
Δu_{max}	$[0.3,0.5]^\intercal$	-	input rate constraints max
$v_{x,\text{min}}$	0	m/s	longitudinal velocity constraint min
$v_{x,\text{max}}$	30	m/s	longitudinal velocity constraint max
$\gamma_{x,\text{min}}$	-0.5	m/s	yaw rate constraint min
$\gamma_{x,\text{max}}$	0.5	m/s	yaw rate constraint max

Table A.4: Numerical values for constraints

Parameter	Value	Unit
k_{Road}	1	-
k_{Lane}	12	-
σ_{Lane}	1.2	-
k_{Obstacle}	1.5	-
α	1	-
k_{Velocity}	25	-
$k_{\text{Velocity,2}}$	1	-
σ_{Velocity}	3	-
$k_{\text{Platoon,X1}}$	300	-
$k_{\text{Platoon,X2}}$	0.172	-
$k_{\text{Platoon,Y}}$	0.35	-
a [83]	1.648	-
b [83]	0.713	

Table A.5: Numerical values for the parameters of the APFs

Parameter	Value	Unit	Explanation
K_u	1	-	weight APF
R	I_2	-	weight Input
N	15	-	horizon
tol	$1e^{-4}$	-	final accuracy COBYLA
maxiter	$1e^{6}$	-	max iterations allowed

Table A.6: Numerical values for optimization problem

B

Results Autonomous Vehicle

B.1. Lane Keeping

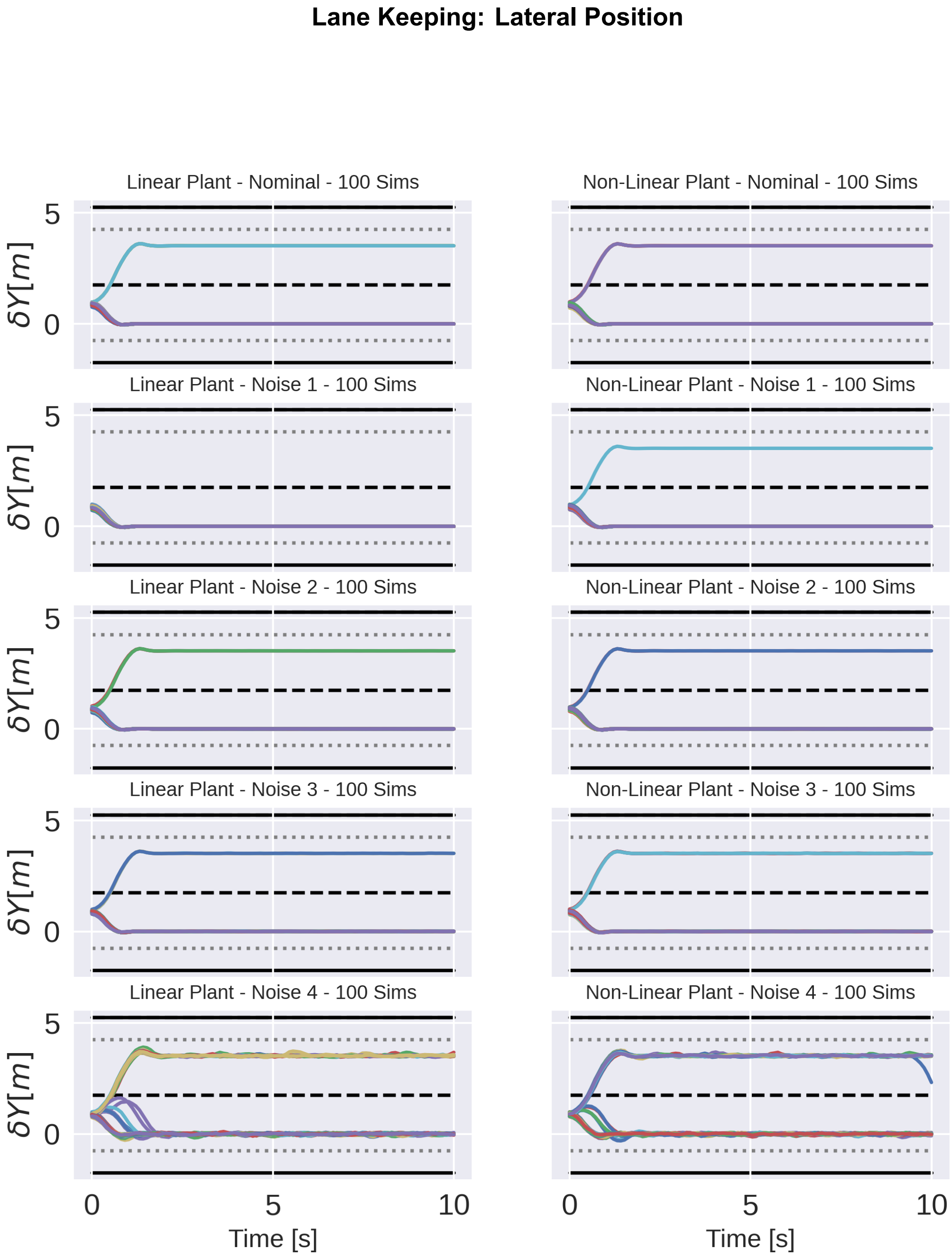

Figure B.1: When the trajectories converge to $\delta Y = 0$, the AV manage to converge to the expected lane. Furthermore, the left column represents the simulations carried out with the linear plant and the right with non-linear plant. Each row represents a different amount of white noise used during the simulations. The upper row had no noise and the lower row had the most noise.

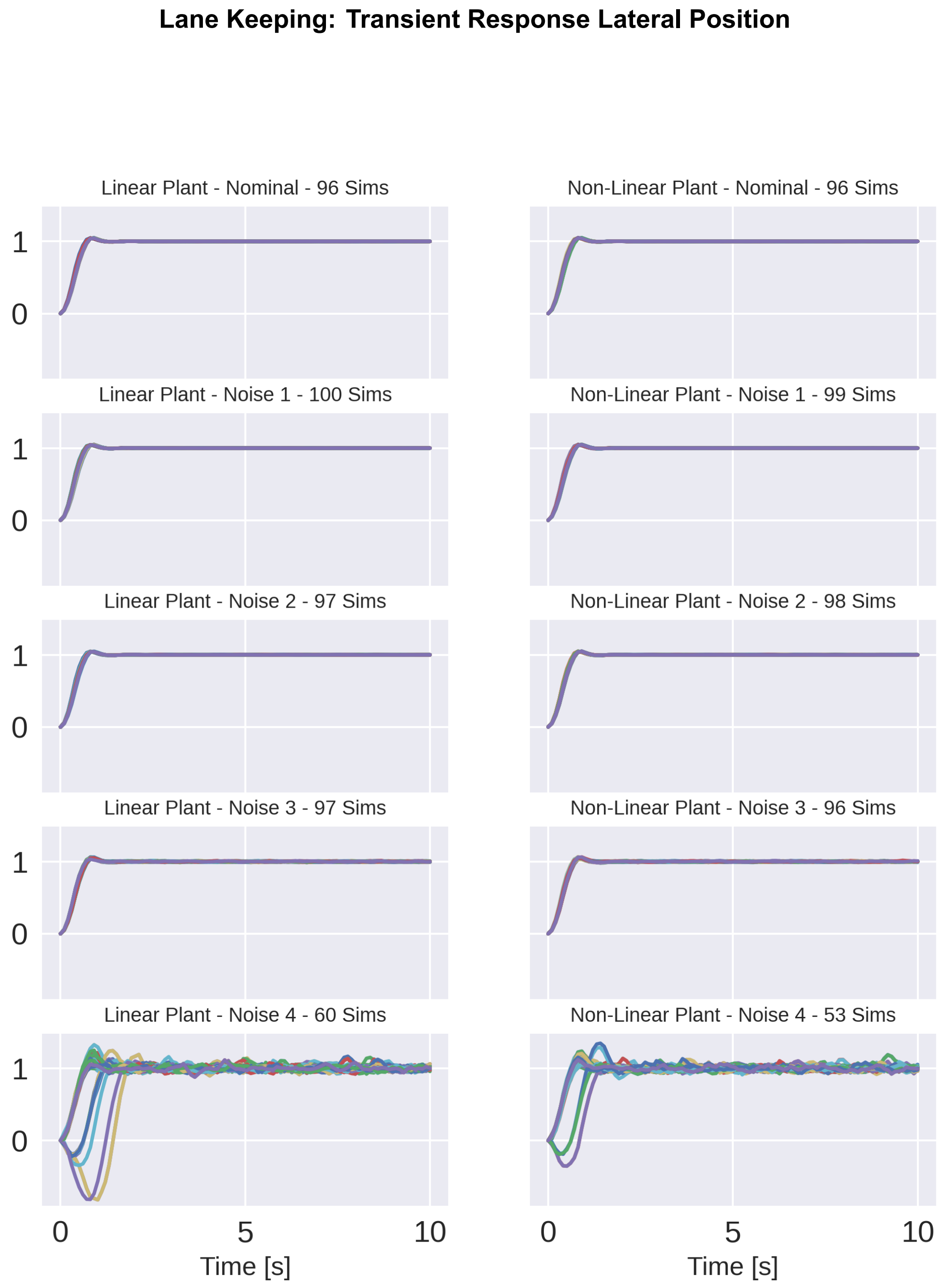

Figure B.2: When the trajectories converge from zero to one, the AV manage to converge to the expected lane. Furthermore, the left column represents the simulations carried out with the linear plant and the right with non-linear plant. Each row represents a different amount of white noise used during the simulations. The upper row had no noise and the lower row had the most noise.

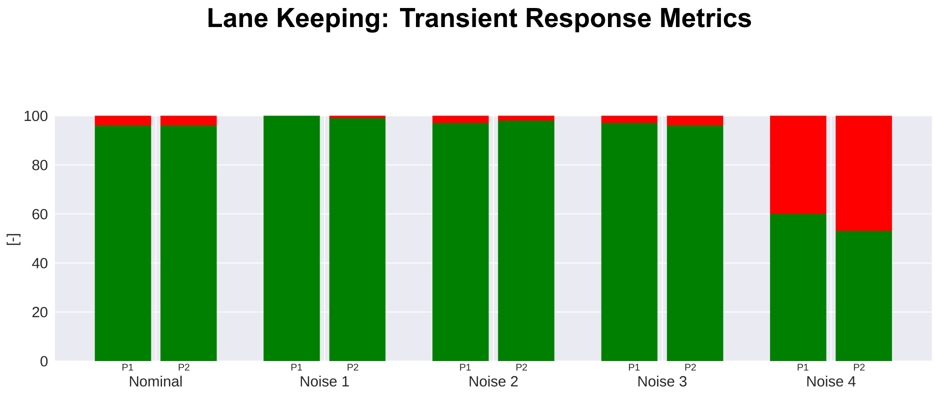

(a) Success Ratio

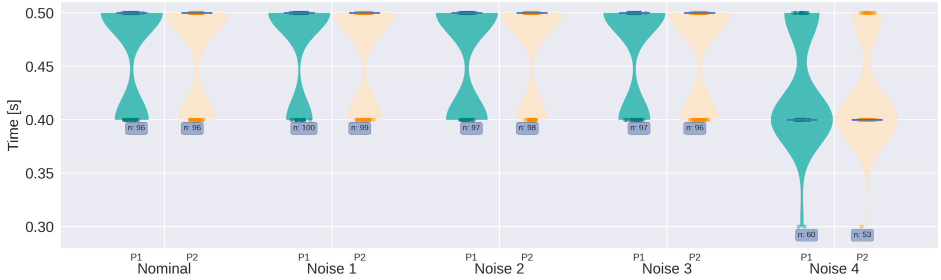

(b) Rise Time

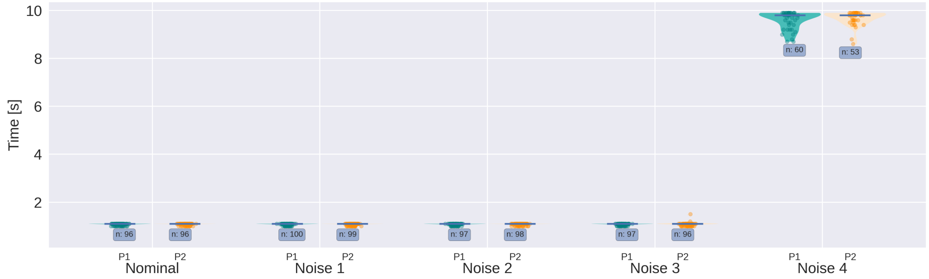

(c) Settling Time

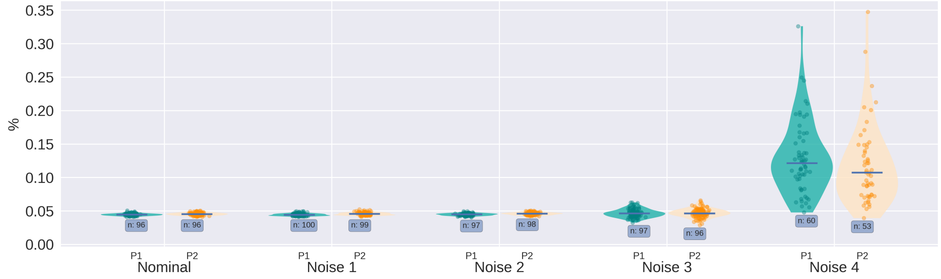

(d) Overshoot

Figure B.3: Transient response metrics for the scenario Lane Keeping. The blue text box indicates how many simulations were labelled as an *success*, which is also visualized in Figure B.3a.

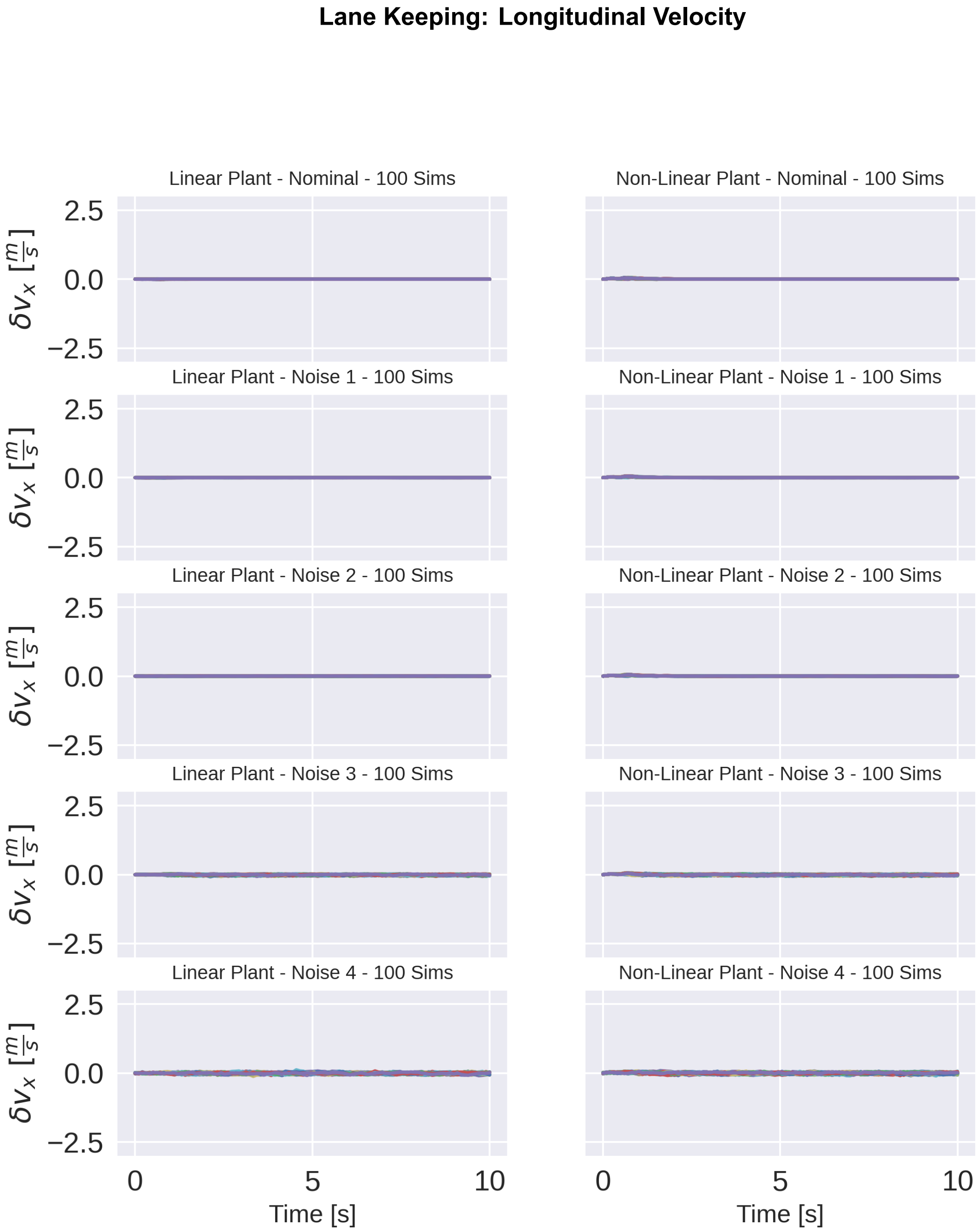

Figure B.4: $\delta v_x = 0$ implies that AV is driving with the desired referenced velocity. Furthermore, the left column represents the simulations carried out with the linear plant and the right with non-linear plant. Each row represents a different amount of white noise used during the simulations. The upper row had no noise and the lower row had the most noise.

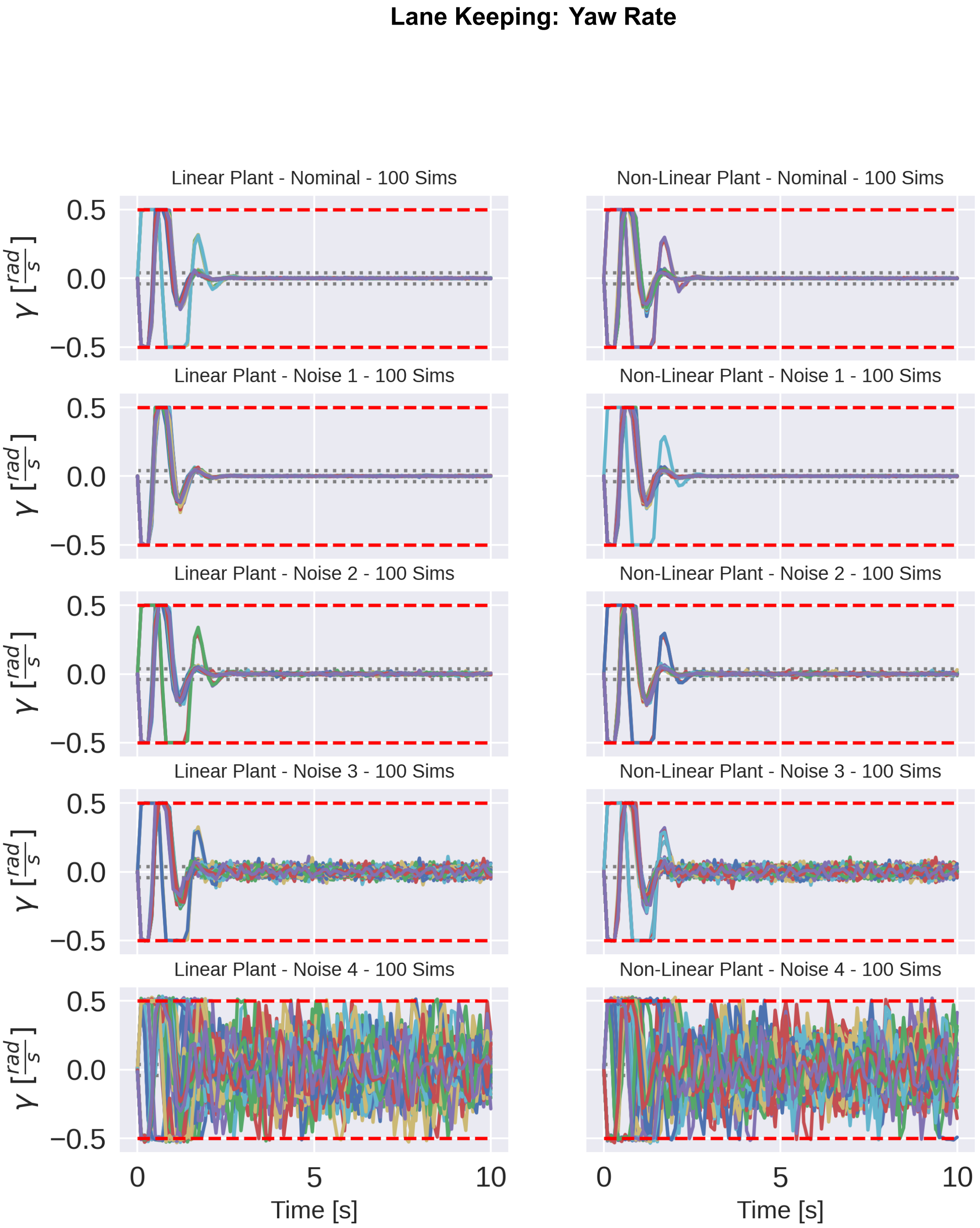

Figure B.5: The left column represents the simulations carried out with the linear plant and the right with non-linear plant. Each row represents a different amount of white noise used during the simulations. The upper row had no noise and the lower row had the most noise.

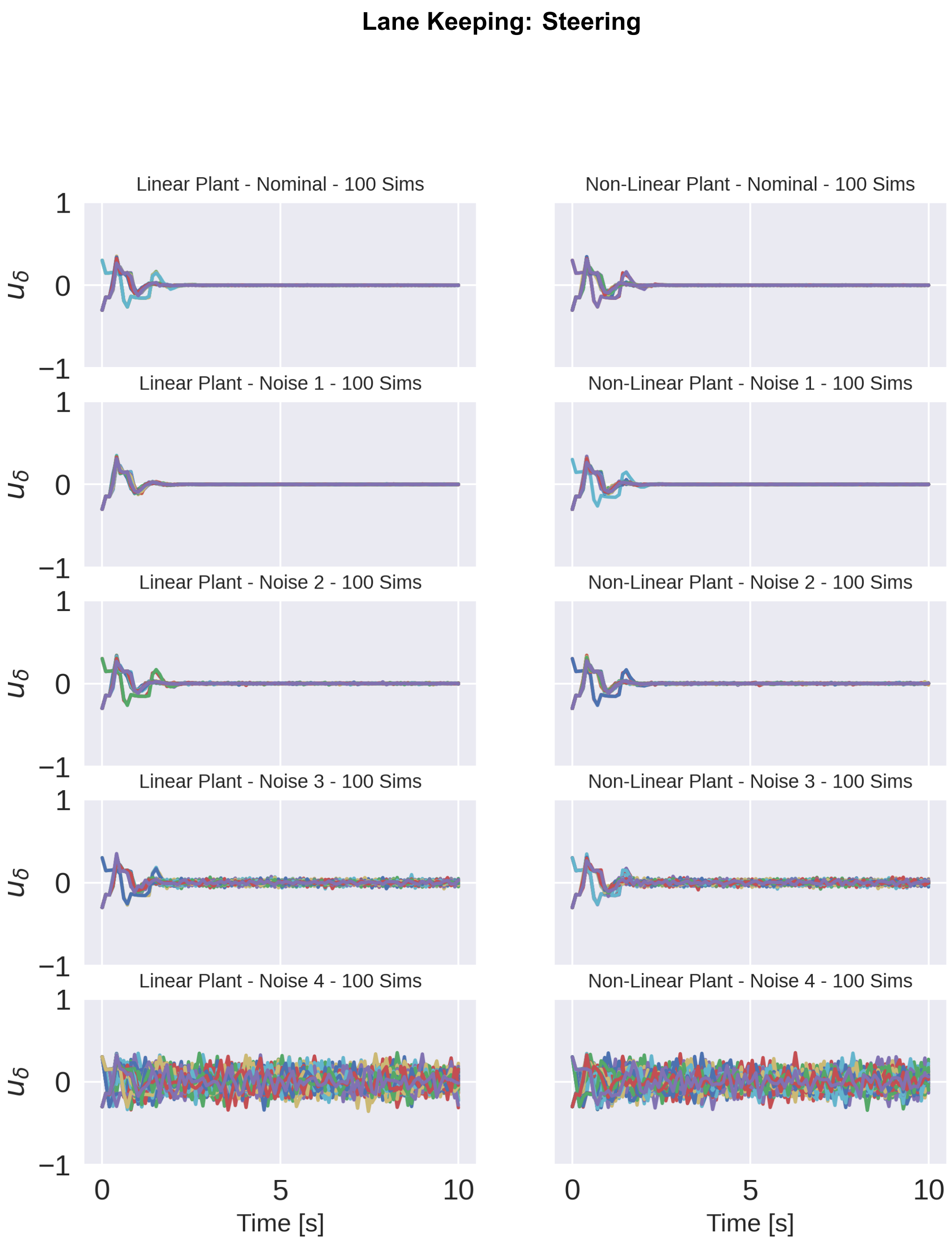

Figure B.6: The left column represents the simulations carried out with the linear plant and the right with non-linear plant. Each row represents a different amount of white noise used during the simulations. The upper row had no noise and the lower row had the most noise.

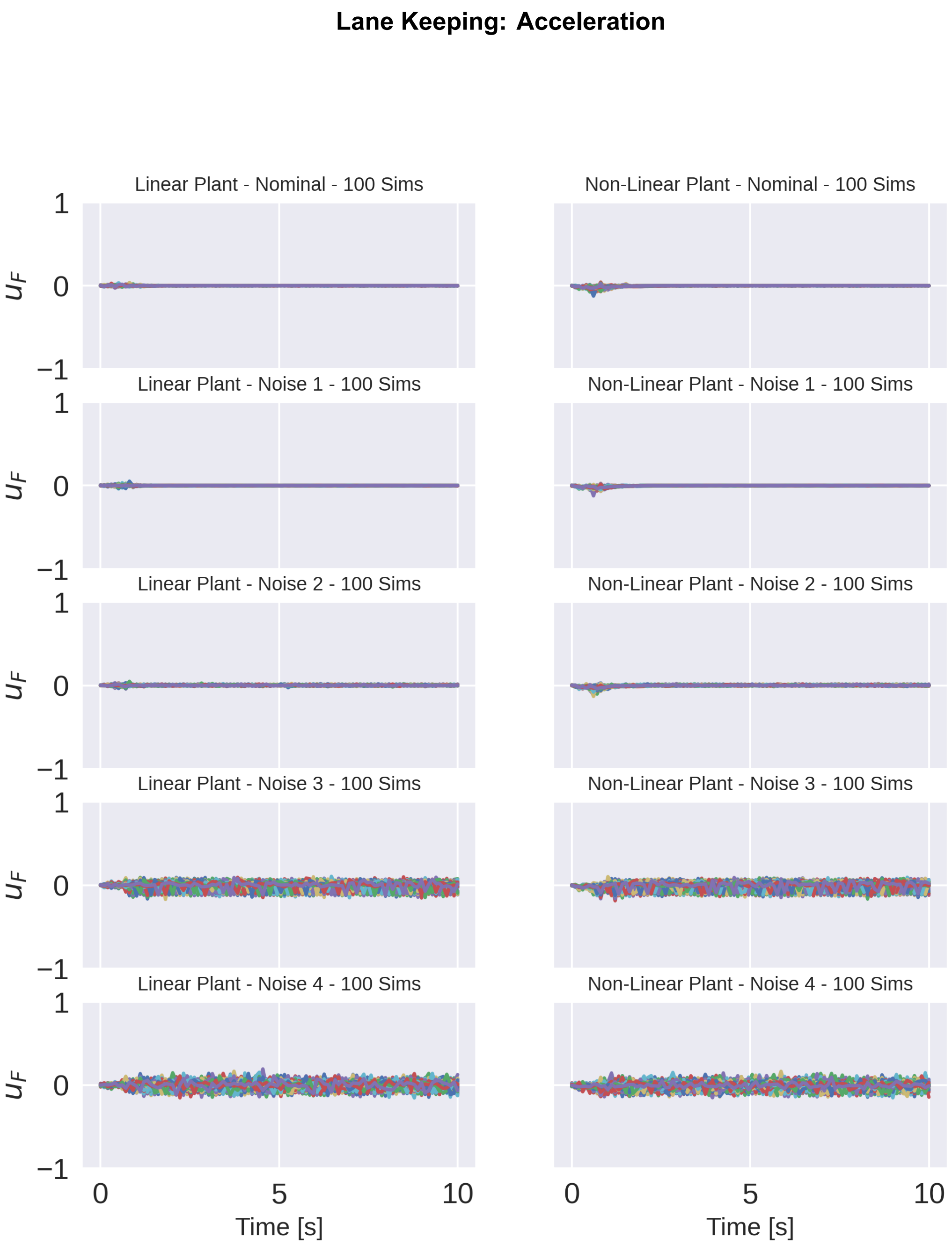

Figure B.7: The left column represents the simulations carried out with the linear plant and the right with non-linear plant. Each row represents a different amount of white noise used during the simulations. The upper row had no noise and the lower row had the most noise.

B.2. Car-Following

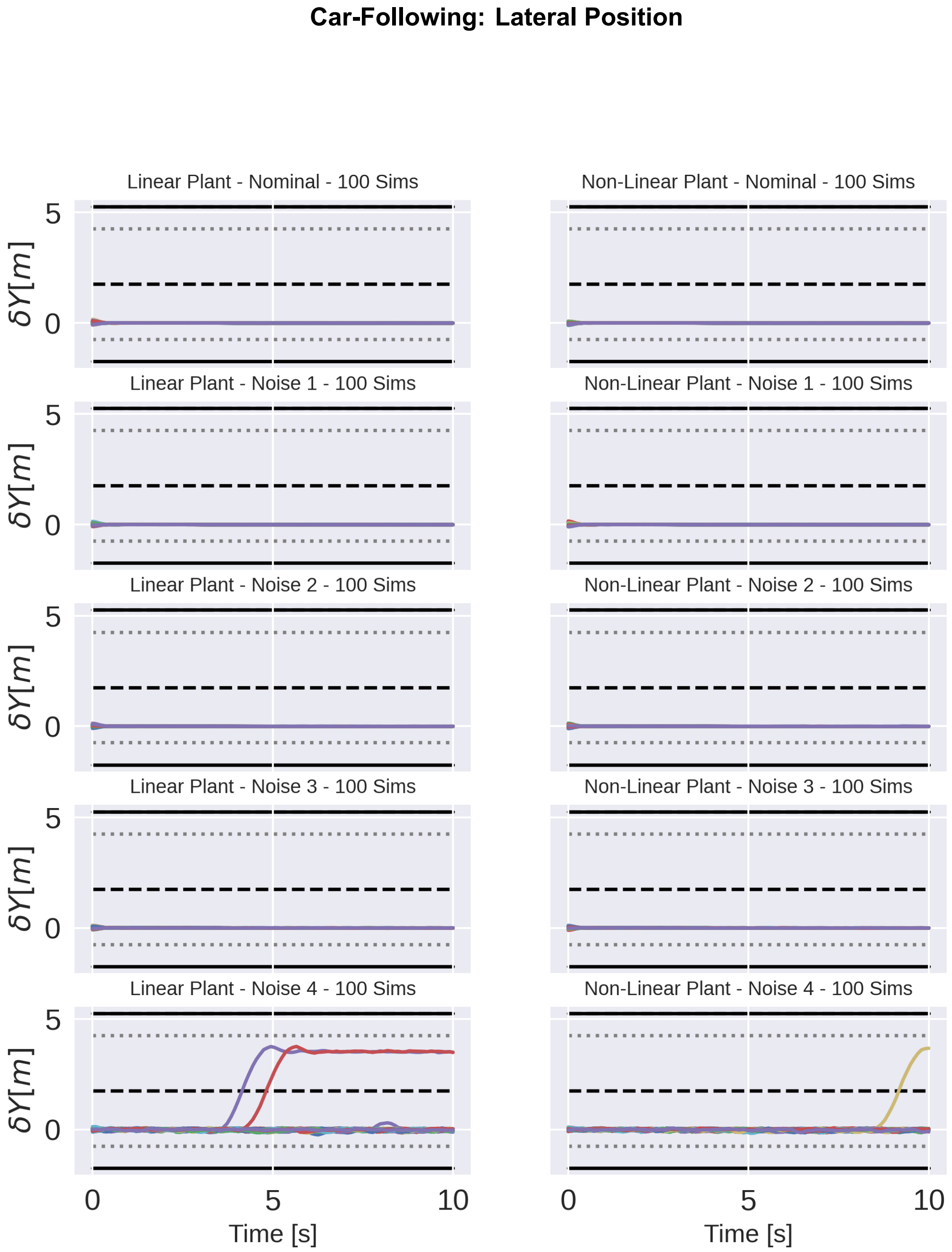

Figure B.8: When the trajectories converge to $\delta Y = 0$, the AV manage to converge to the expected lane. Furthermore, the left column represents the simulations carried out with the linear plant and the right with non-linear plant. Each row represents a different amount of white noise used during the simulations. The upper row had no noise and the lower row had the most noise.

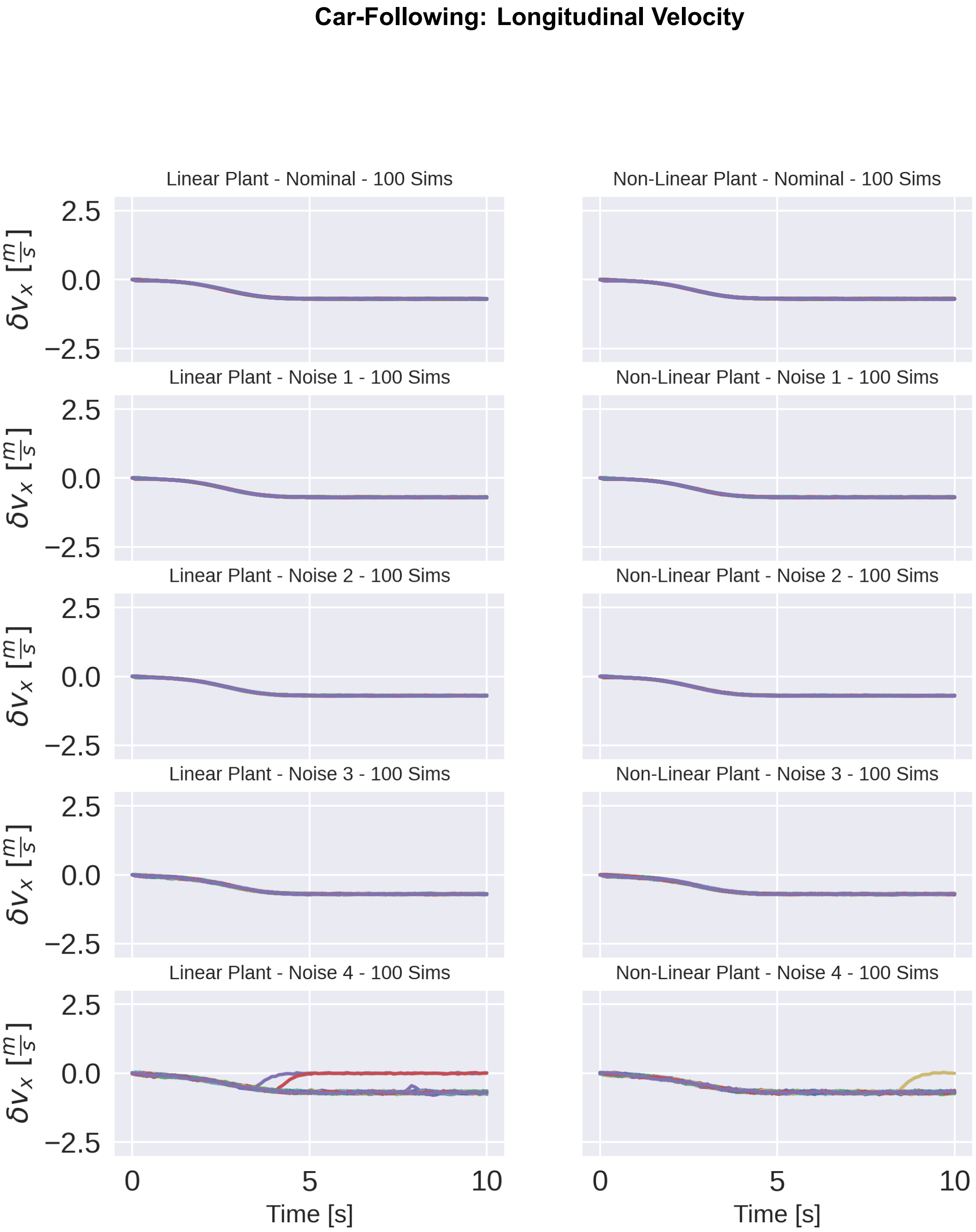

Figure B.9: $\delta v_x = 0$ implies that AV is driving with the desired referenced velocity. Furthermore, the left column represents the simulations carried out with the linear plant and the right with non-linear plant. Each row represents a different amount of white noise used during the simulations. The upper row had no noise and the lower row had the most noise.

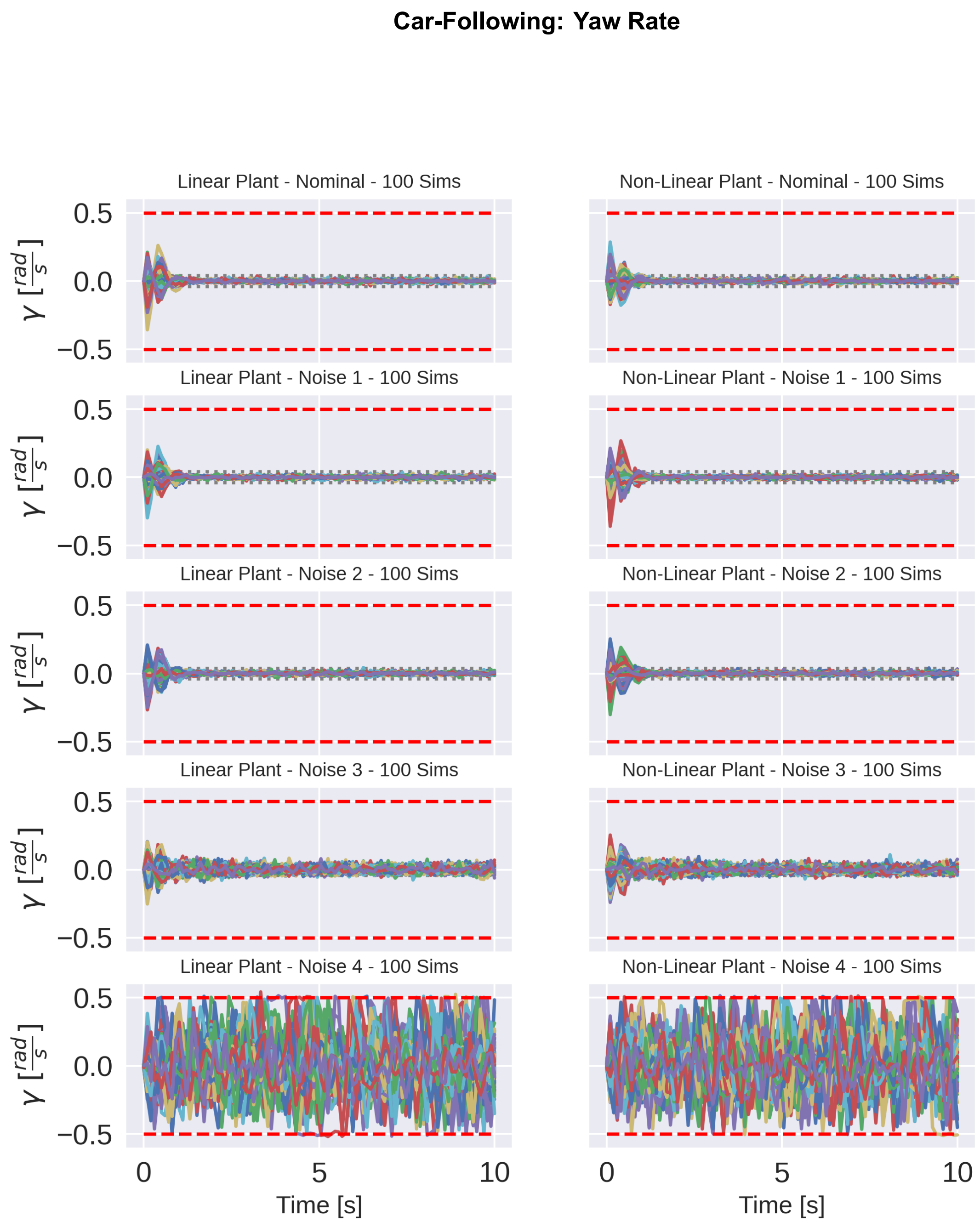

Figure B.10: The left column represents the simulations carried out with the linear plant and the right with non-linear plant. Each row represents a different amount of white noise used during the simulations. The upper row had no noise and the lower row had the most noise.

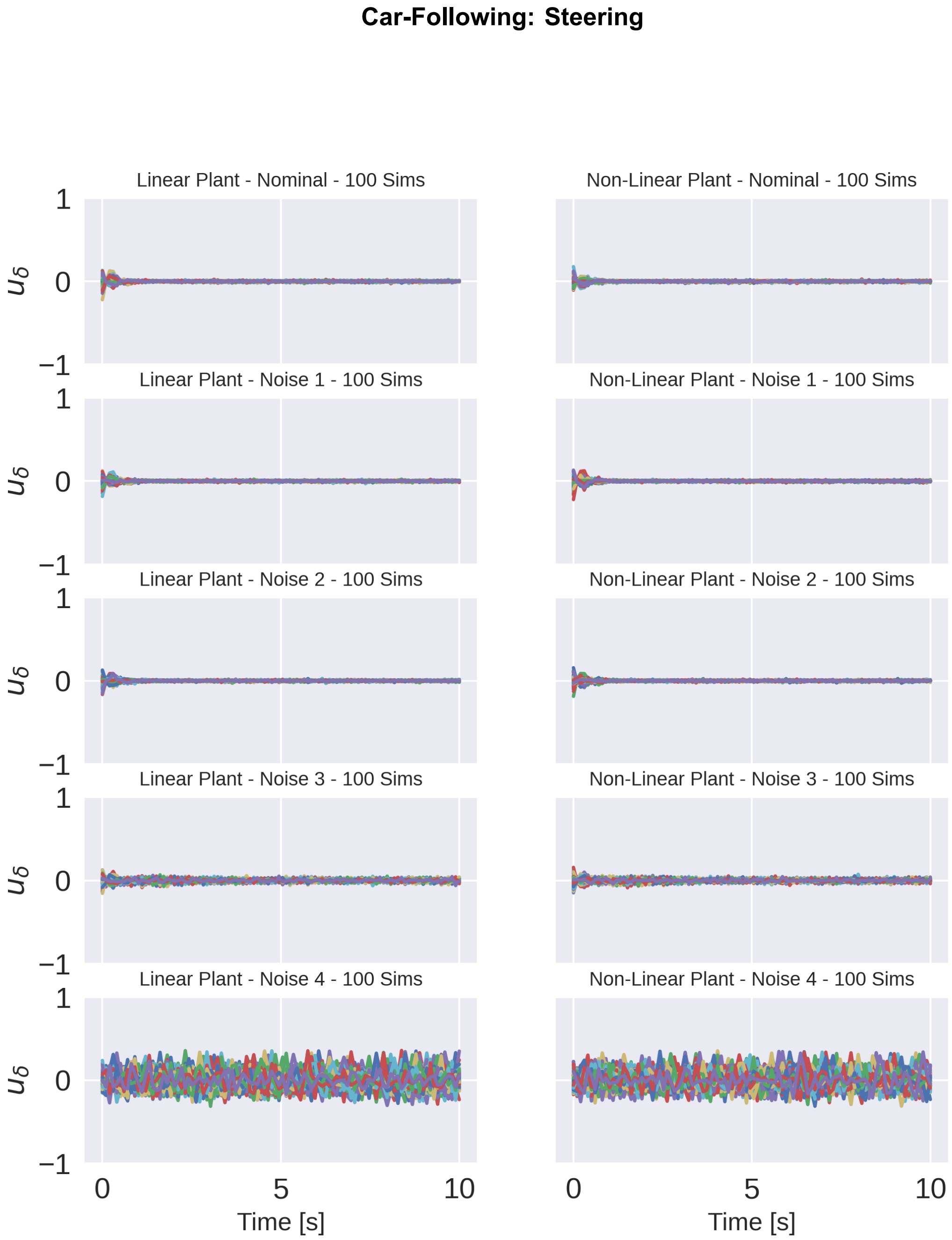

Figure B.11: The left column represents the simulations carried out with the linear plant and the right with non-linear plant. Each row represents a different amount of white noise used during the simulations. The upper row had no noise and the lower row had the most noise.

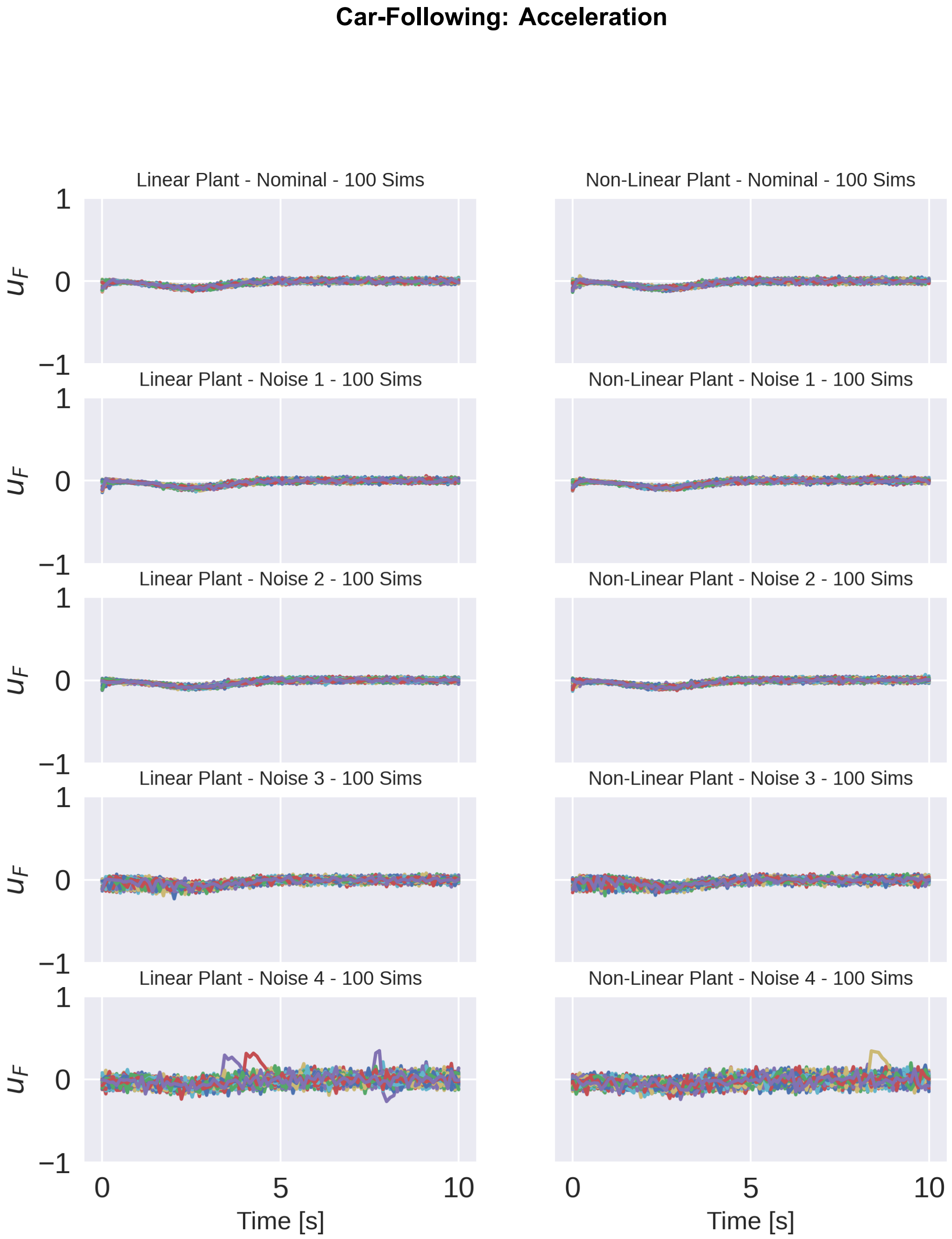

Figure B.12: The left column represents the simulations carried out with the linear plant and the right with non-linear plant. Each row represents a different amount of white noise used during the simulations. The upper row had no noise and the lower row had the most noise.

B.3. Lane Changing

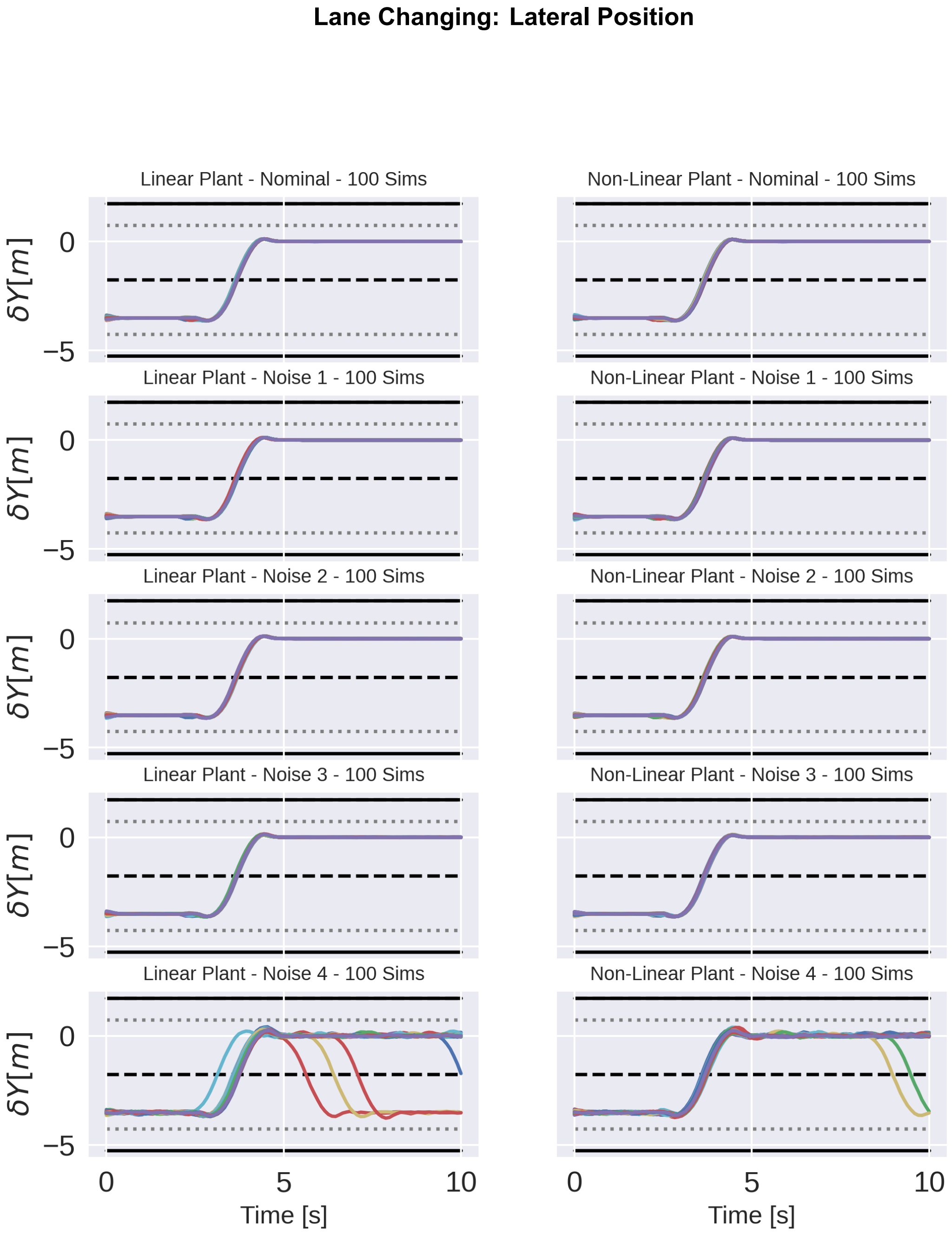

Figure B.13: When the trajectories converge to $\delta Y = 0$, the AV manage to converge to the expected lane. Furthermore, the left column represents the simulations carried out with the linear plant and the right with non-linear plant. Each row represents a different amount of white noise used during the simulations. The upper row had no noise and the lower row had the most noise.

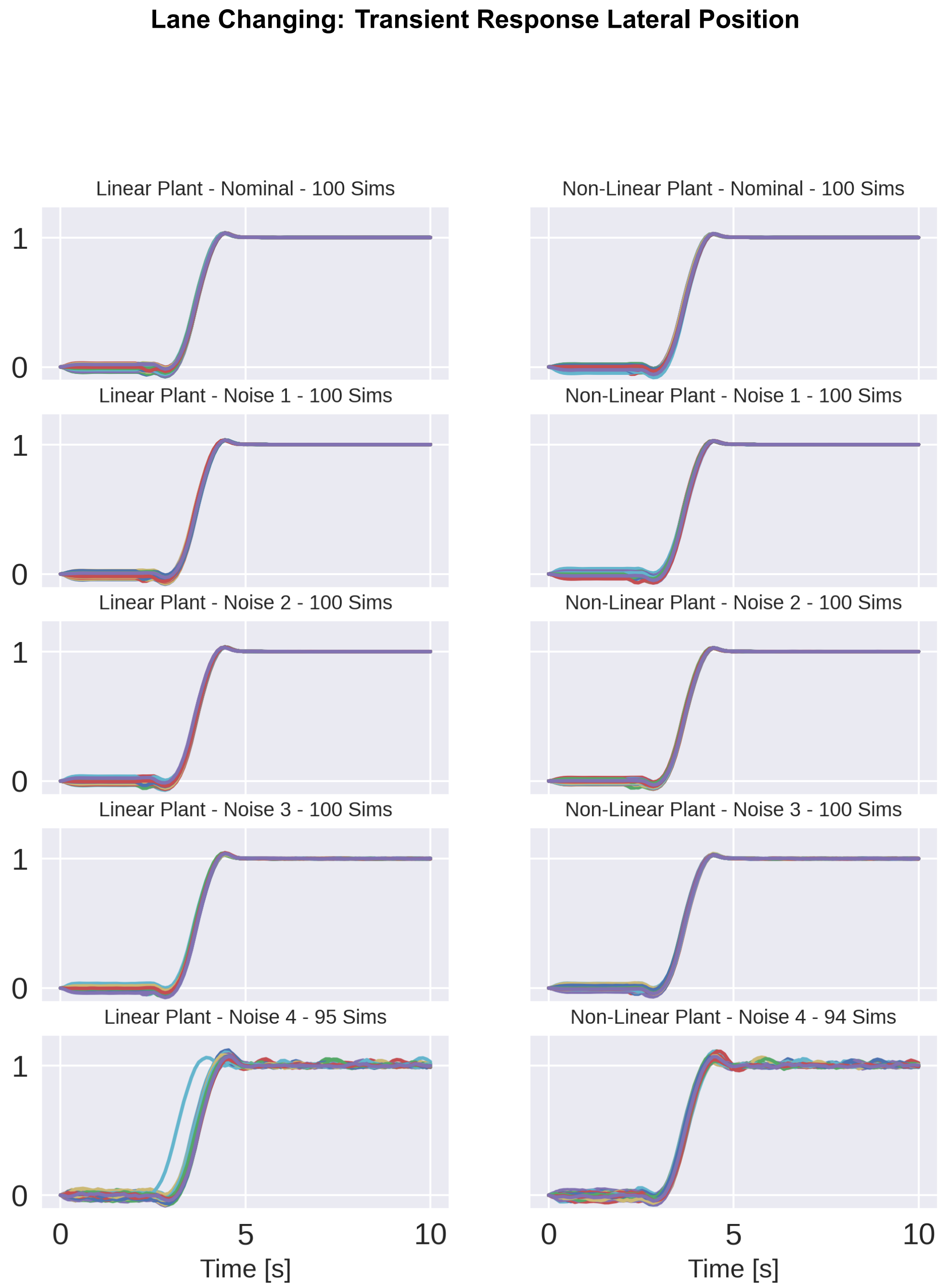

Figure B.14: When the trajectories converge from zero to one, the AV manage to converge to the expected lane. Furthermore, the left column represents the simulations carried out with the linear plant and the right with non-linear plant. Each row represents a different amount of white noise used during the simulations. The upper row had no noise and the lower row had the most noise.

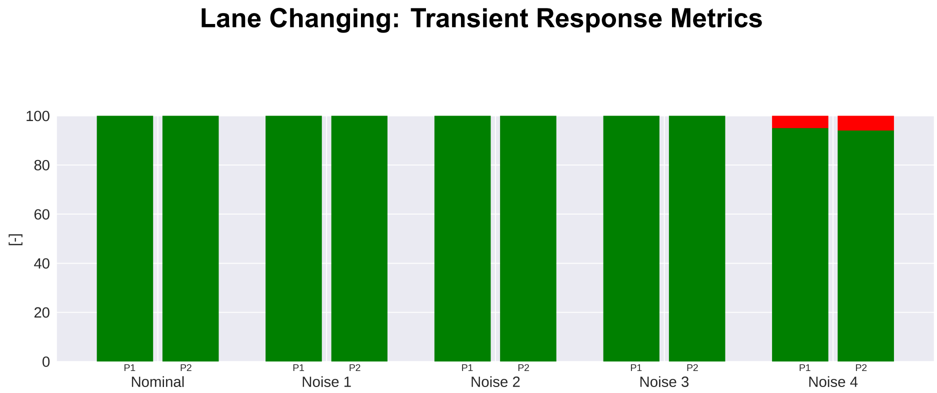

(a) Success Ratio

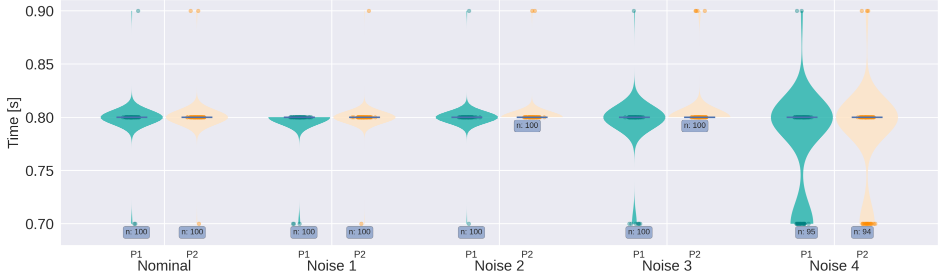

(b) Rise Time

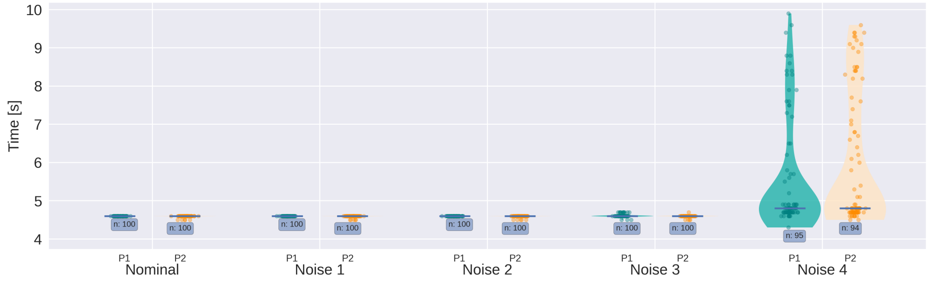

(c) Settling Time

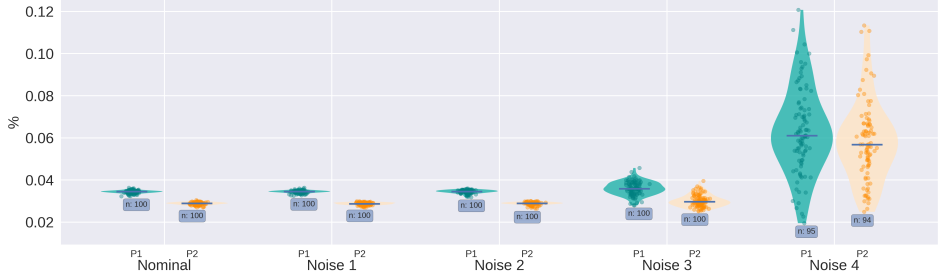

(d) Overshoot

Figure B.15: Transient response metrics for the scenario Lane Changing. The blue text box indicates how many simulations were labelled as an *success*, which is also visualized in Figure B.15a.

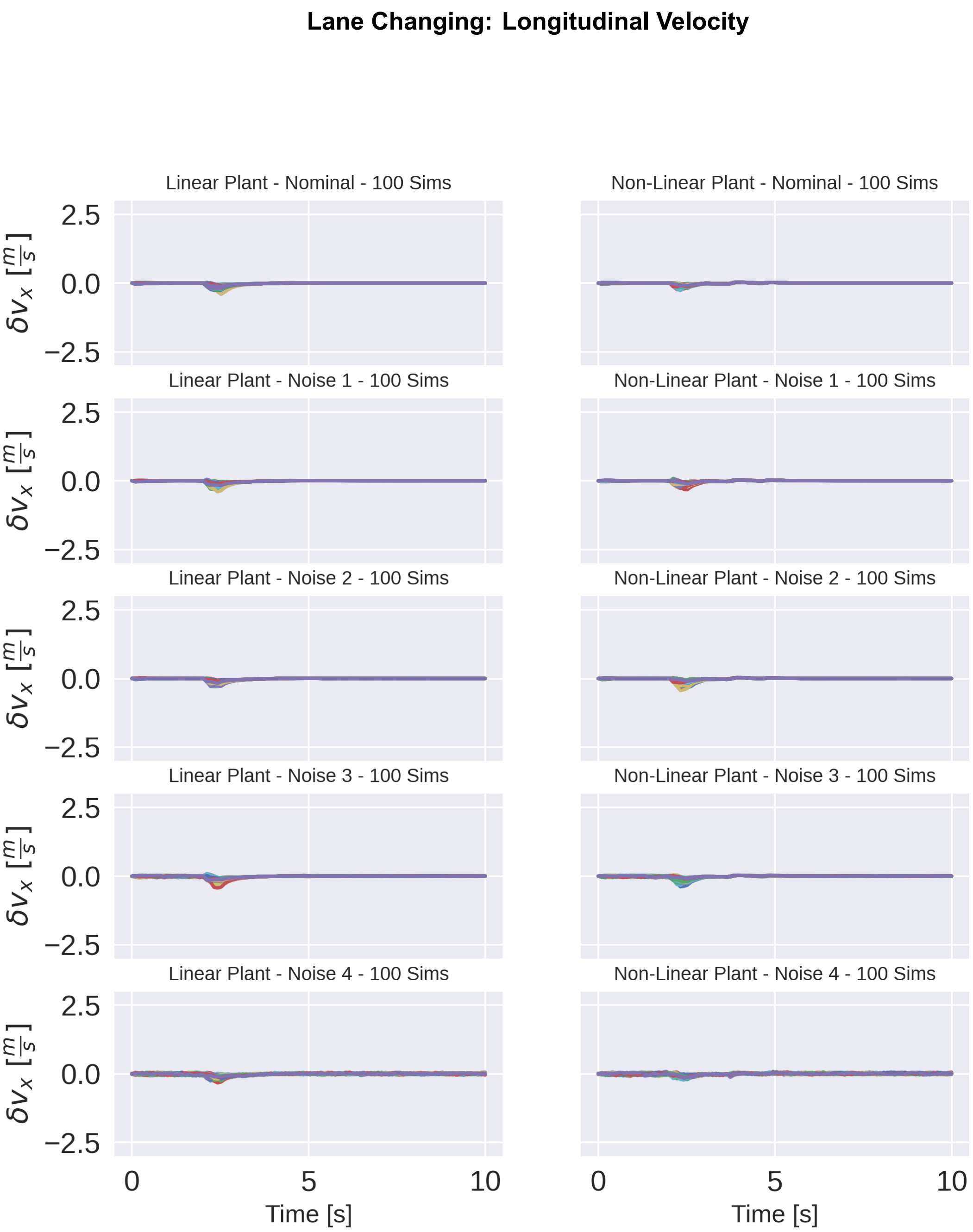

Figure B.16: $\delta v_x = 0$ implies that AV is driving with the desired referenced velocity. Furthermore, the left column represents the simulations carried out with the linear plant and the right with non-linear plant. Each row represents a different amount of white noise used during the simulations. The upper row had no noise and the lower row had the most noise.

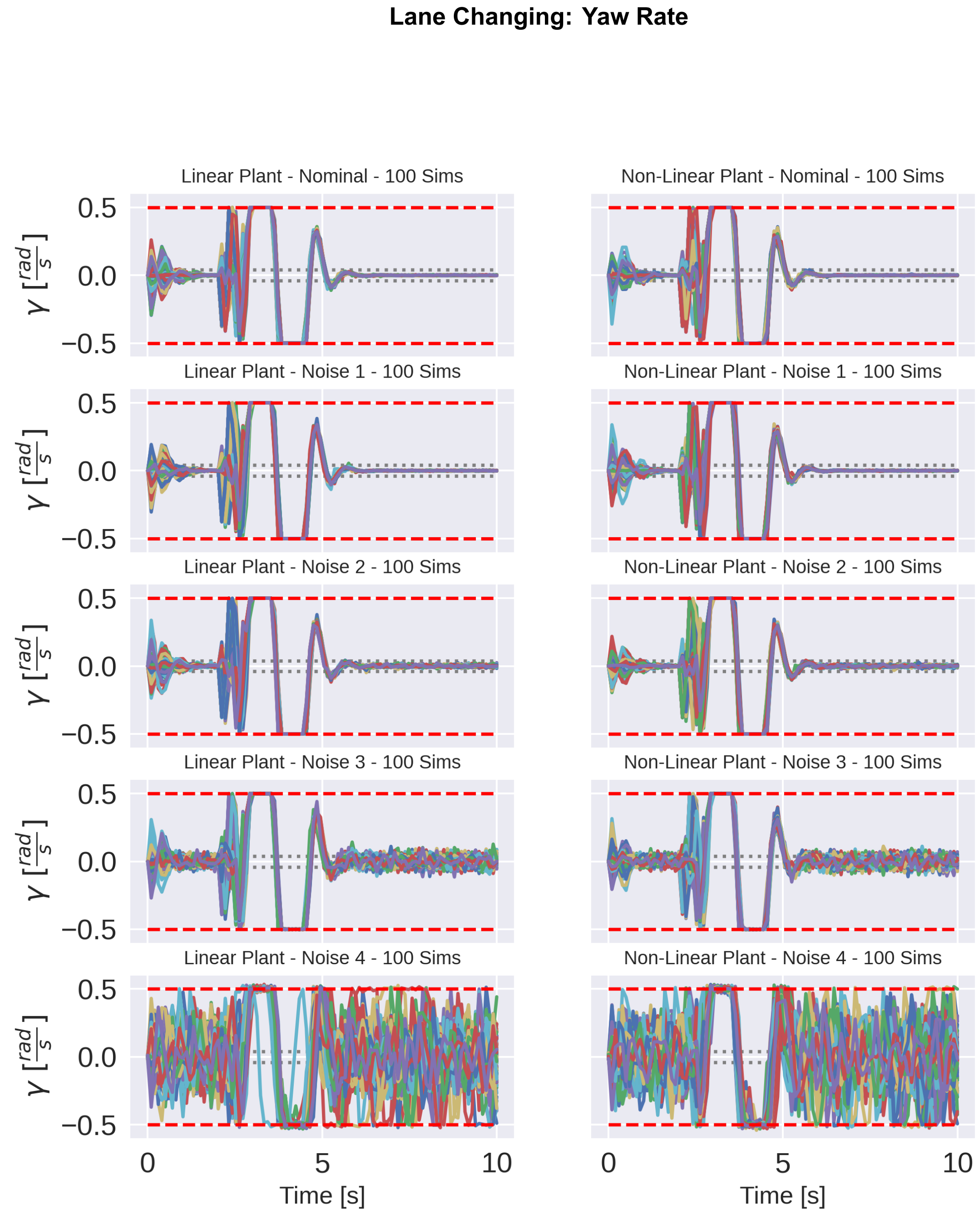

Figure B.17: The left column represents the simulations carried out with the linear plant and the right with non-linear plant. Each row represents a different amount of white noise used during the simulations. The upper row had no noise and the lower row had the most noise.

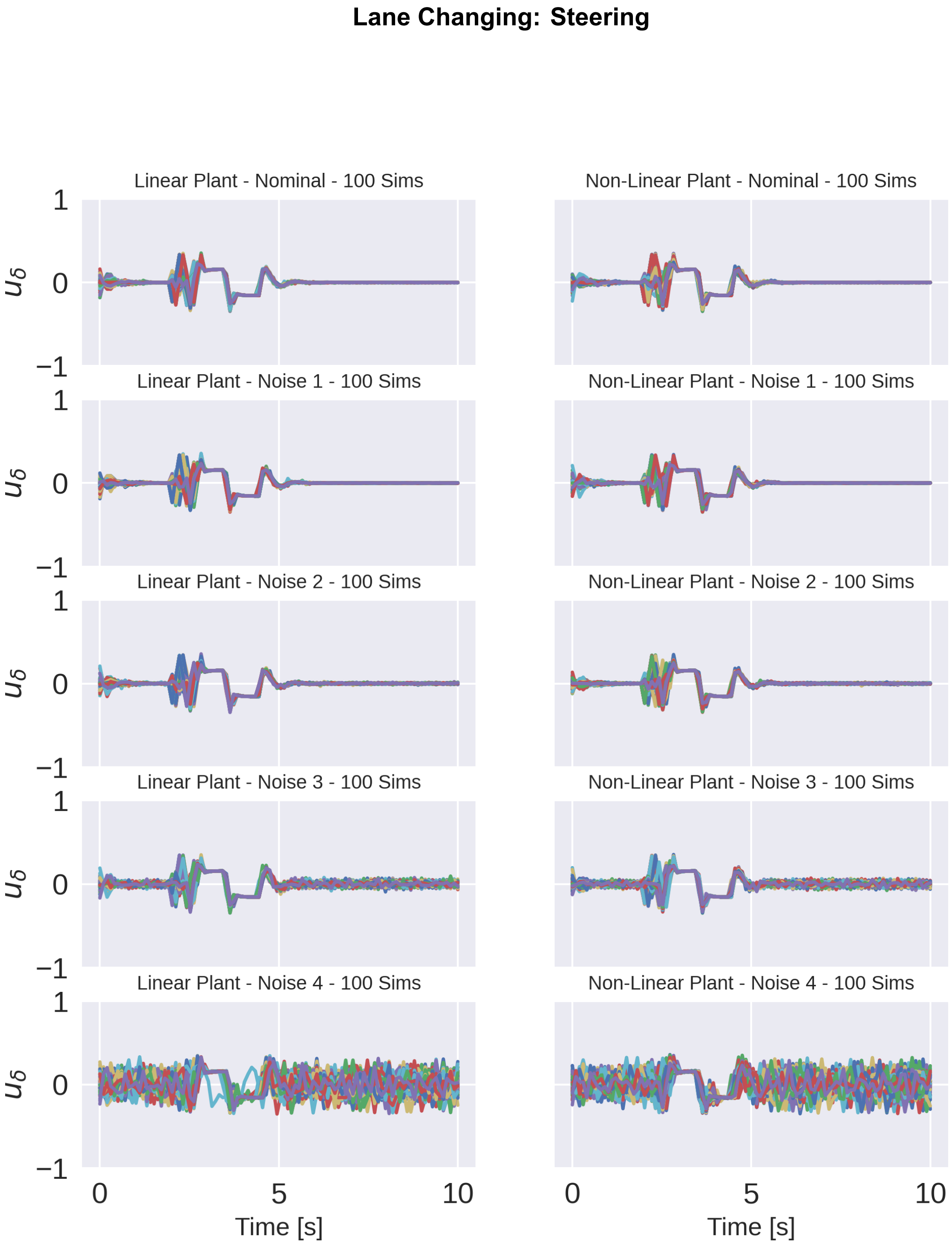

Figure B.18: The left column represents the simulations carried out with the linear plant and the right with non-linear plant. Each row represents a different amount of white noise used during the simulations. The upper row had no noise and the lower row had the most noise.

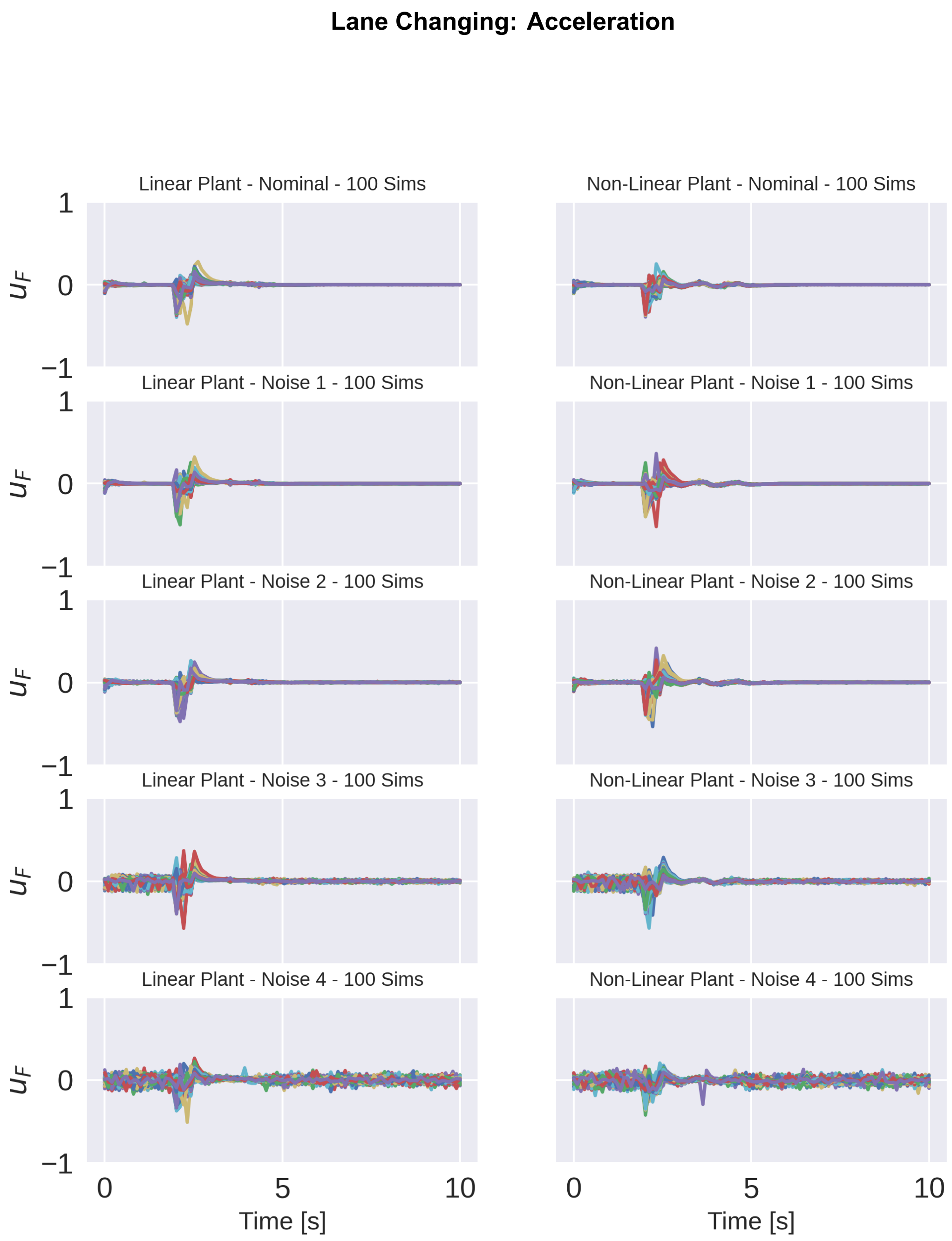

Figure B.19: The left column represents the simulations carried out with the linear plant and the right with non-linear plant. Each row represents a different amount of white noise used during the simulations. The upper row had no noise and the lower row had the most noise.

B.4. Emergency Stop

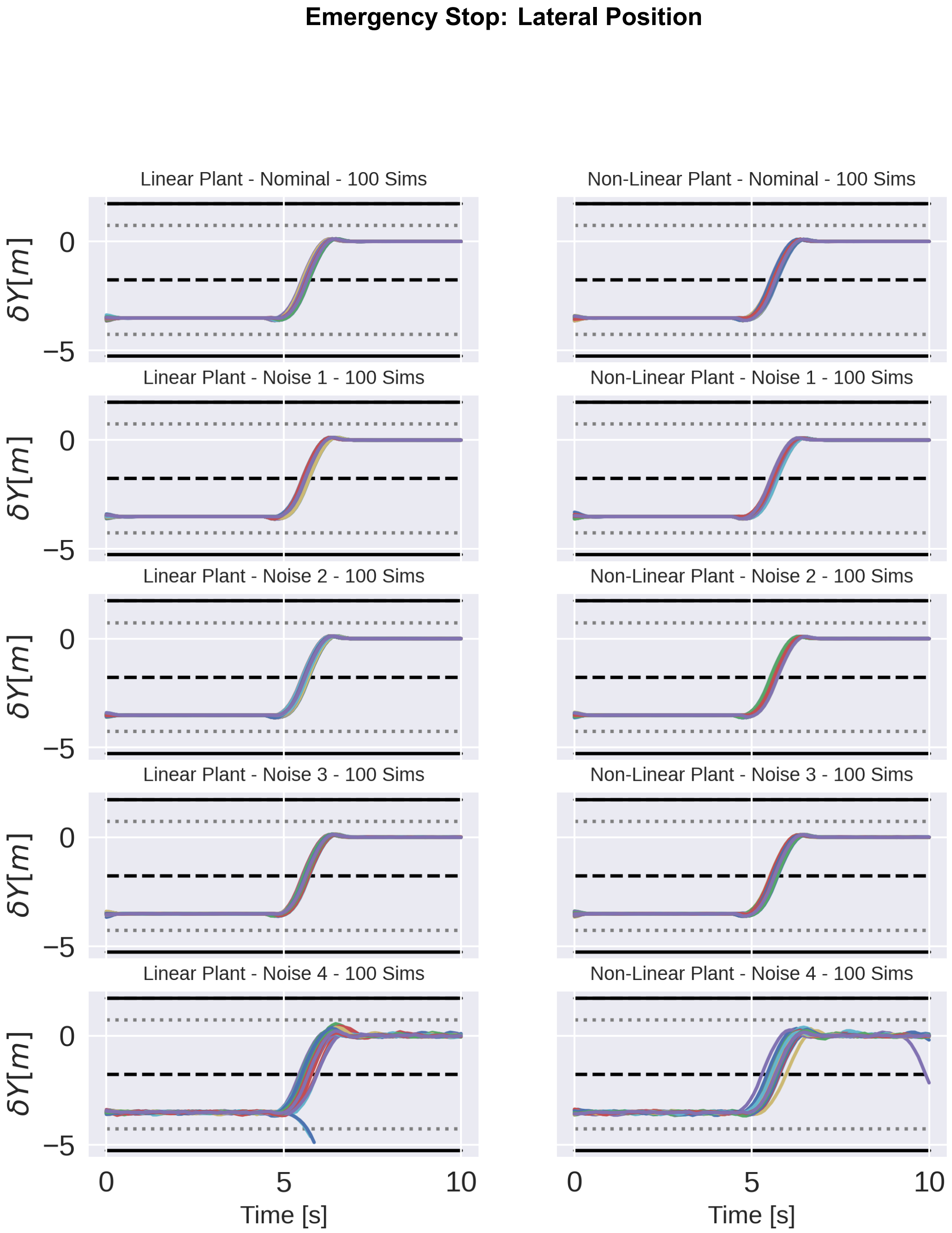

Figure B.20: When the trajectories converge to $\delta Y = 0$, the AV manage to converge to the expected lane. Furthermore, the left column represents the simulations carried out with the linear plant and the right with non-linear plant. Each row represents a different amount of white noise used during the simulations. The upper row had no noise and the lower row had the most noise.

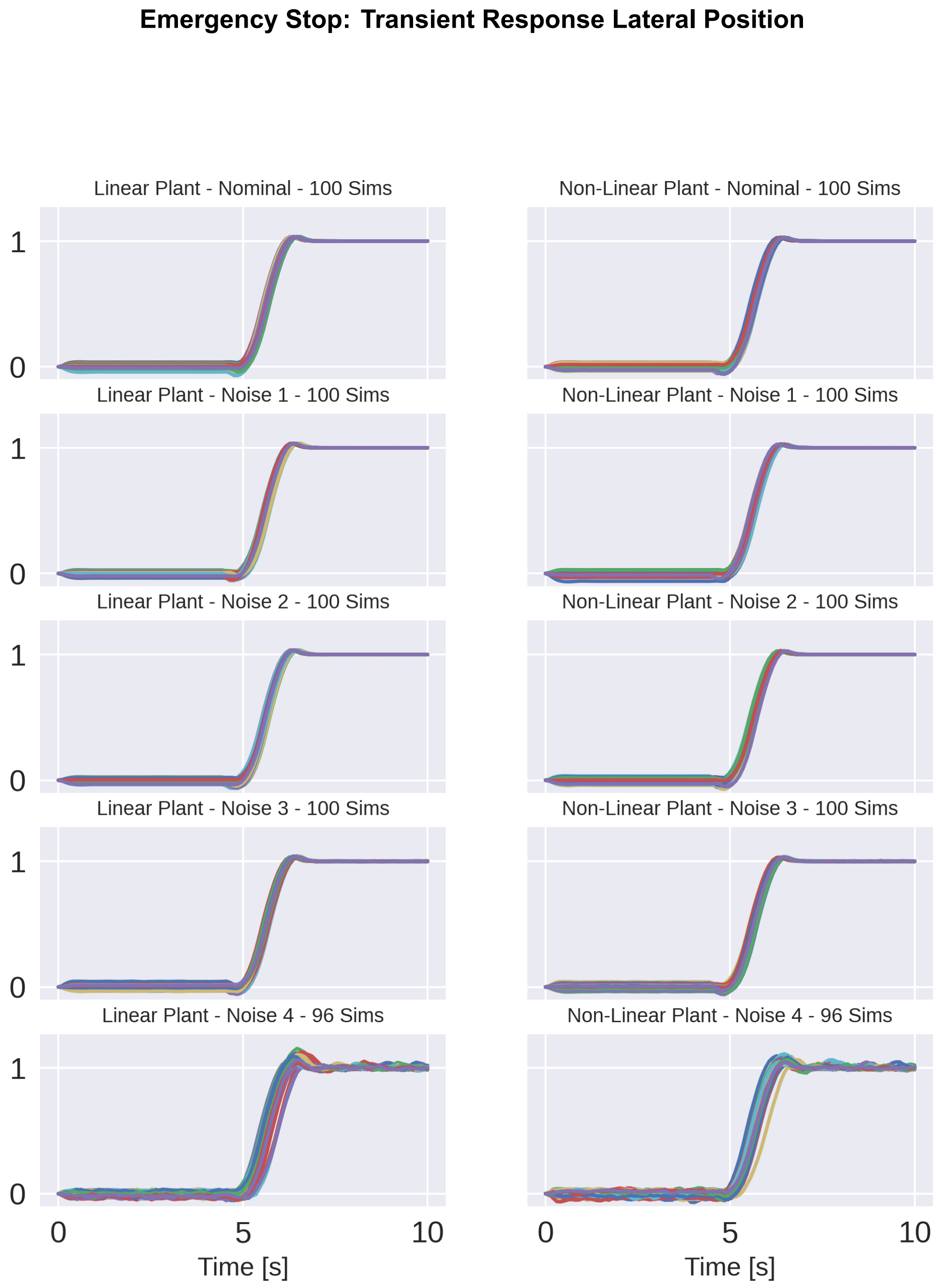

Figure B.21: When the trajectories converge from zero to one, the AV manage to converge to the expected lane. Furthermore, the left column represents the simulations carried out with the linear plant and the right with non-linear plant. Each row represents a different amount of white noise used during the simulations. The upper row had no noise and the lower row had the most noise.

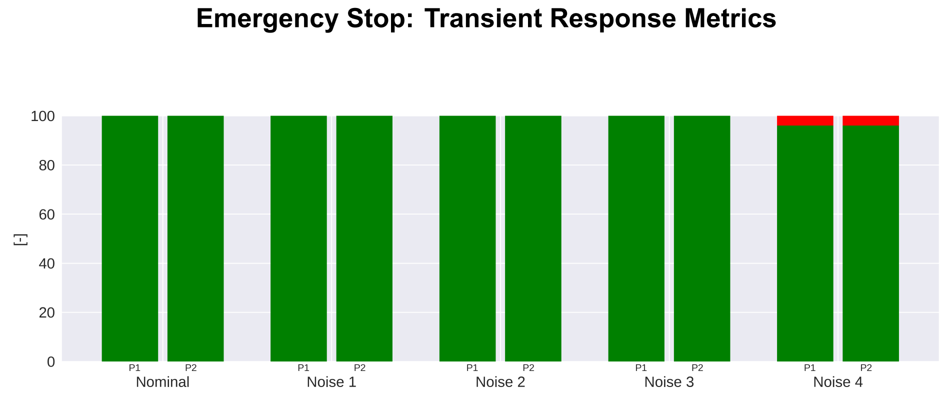

(a) Success Ratio

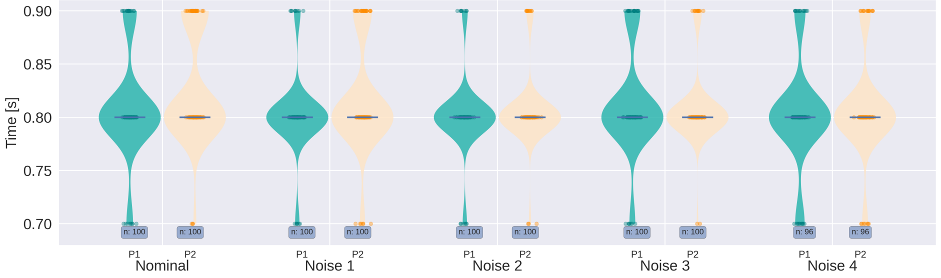

(b) Rise Time

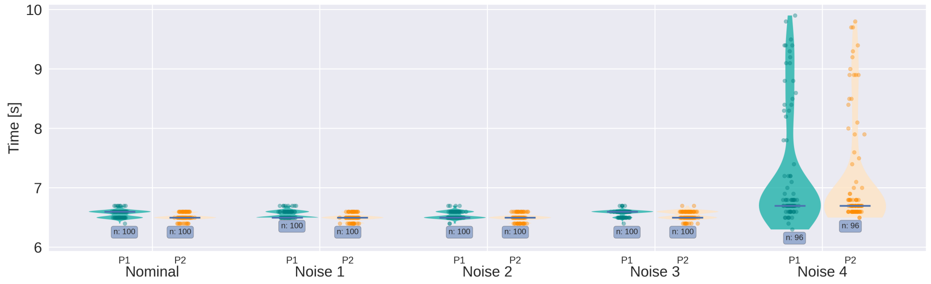

(c) Settling Time

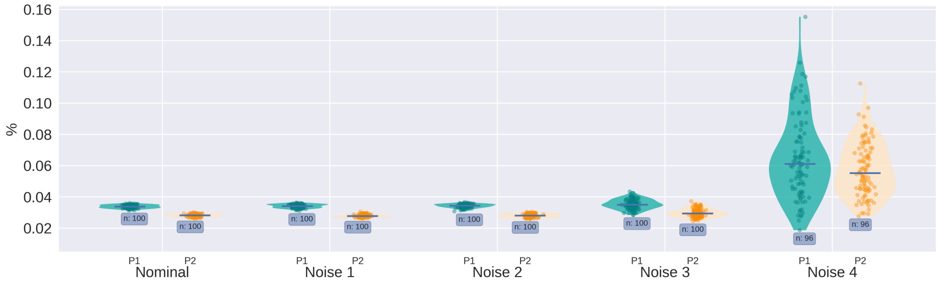

(d) Overshoot

Figure B.22: Transient response metrics for the scenario Emergency Stop. The blue text box indicates how many simulations were labelled as an *success*, which is also visualized in Figure B.22a.

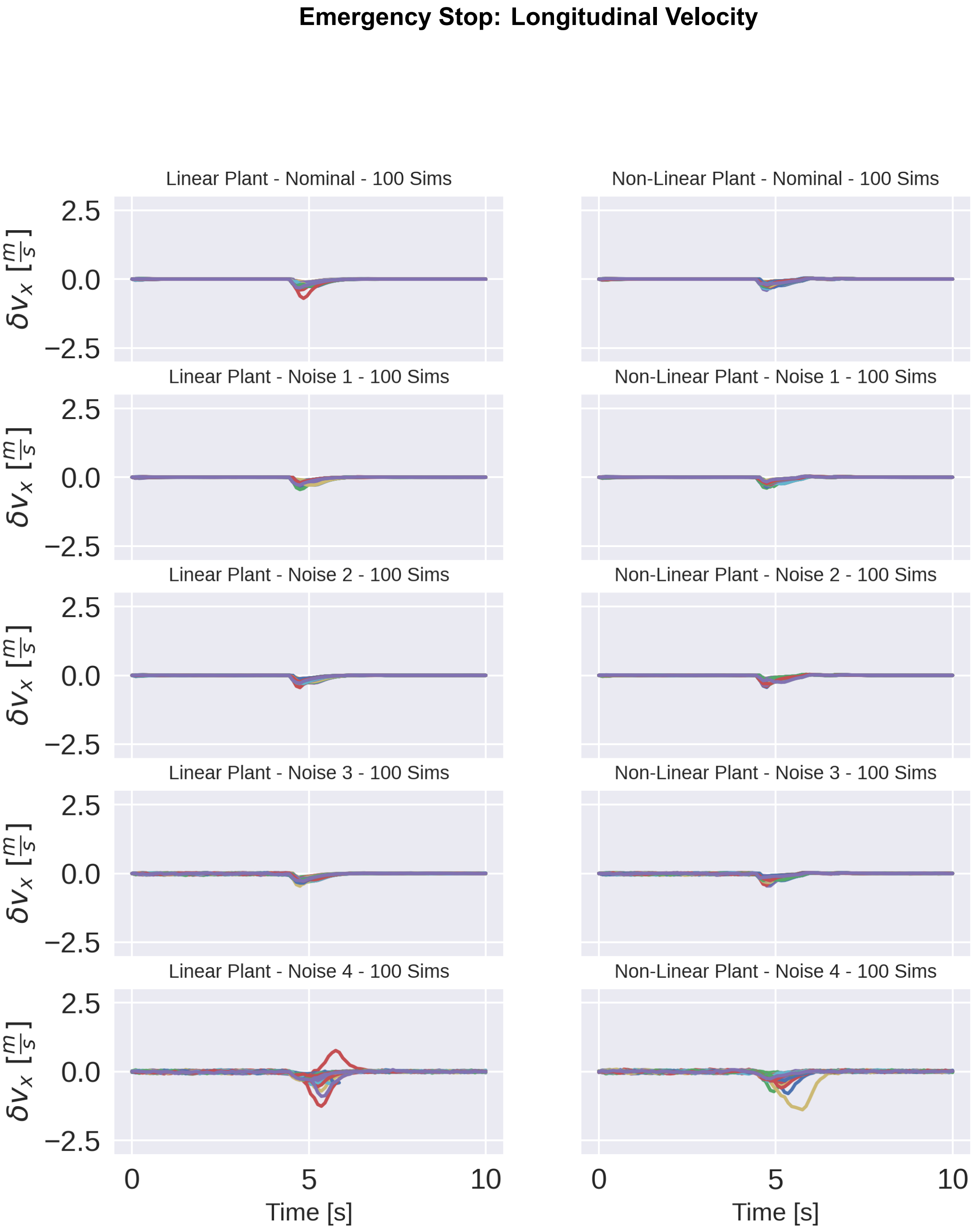

Figure B.23: $\delta v_x = 0$ implies that AV is driving with the desired referenced velocity. Furthermore, the left column represents the simulations carried out with the linear plant and the right with non-linear plant. Each row represents a different amount of white noise used during the simulations. The upper row had no noise and the lower row had the most noise.

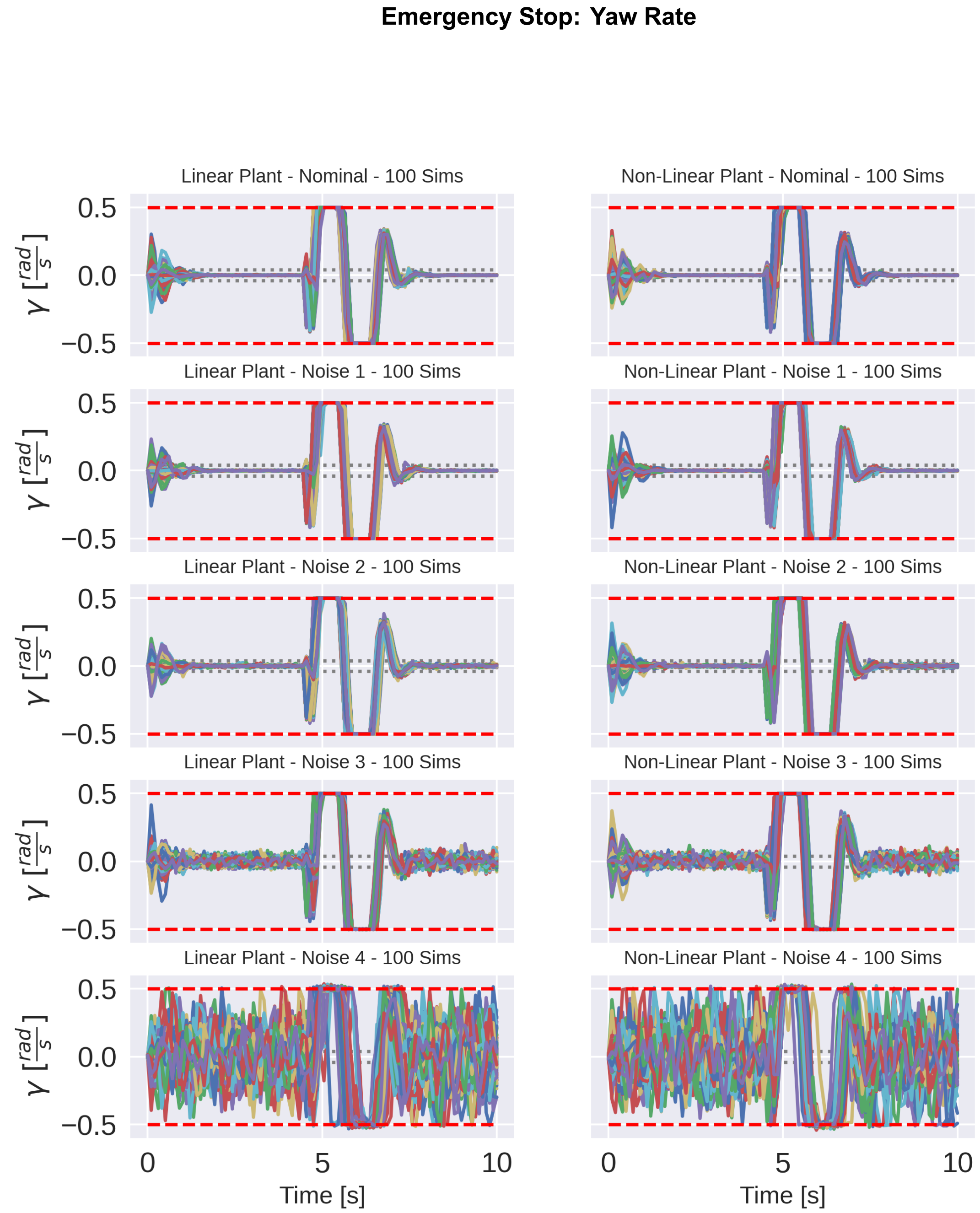

Figure B.24: The left column represents the simulations carried out with the linear plant and the right with non-linear plant. Each row represents a different amount of white noise used during the simulations. The upper row had no noise and the lower row had the most noise.

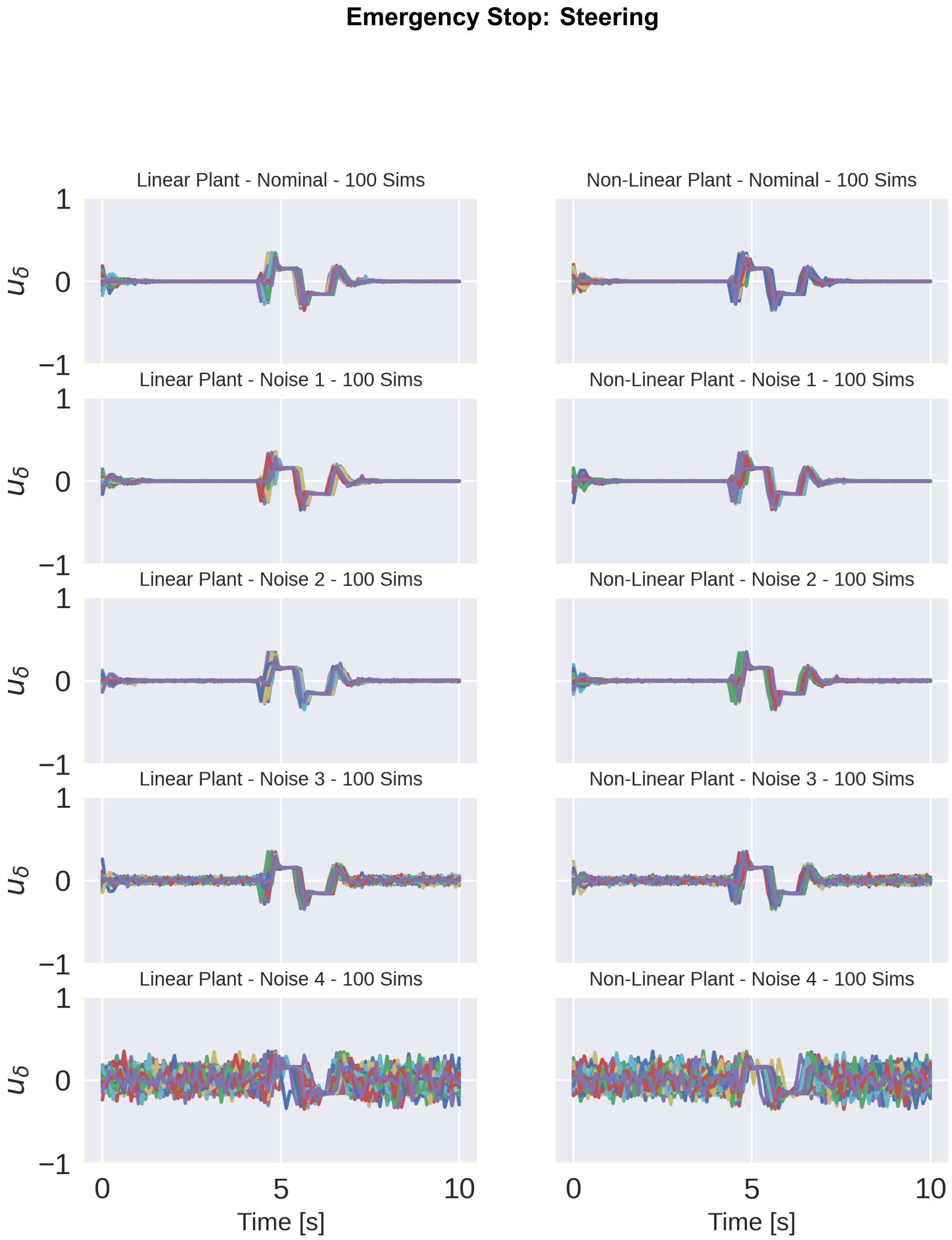

Figure B.25: The left column represents the simulations carried out with the linear plant and the right with non-linear plant. Each row represents a different amount of white noise used during the simulations. The upper row had no noise and the lower row had the most noise.

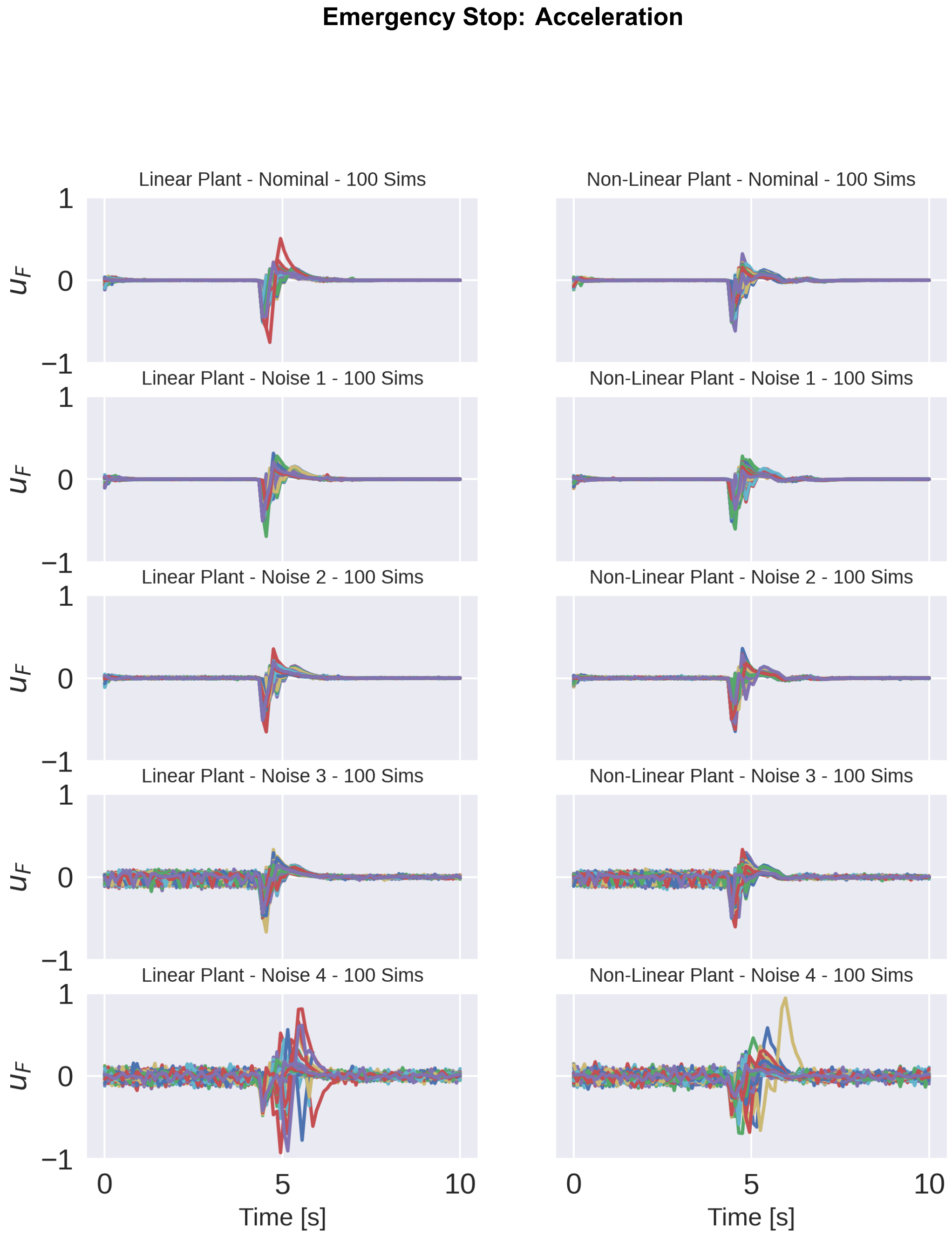

Figure B.26: The left column represents the simulations carried out with the linear plant and the right with non-linear plant. Each row represents a different amount of white noise used during the simulations. The upper row had no noise and the lower row had the most noise.

C

Results Connected Autonomous Vehicle

C.1. Scenario Platoon 1: Disturbance Type I - One Second Time Gap

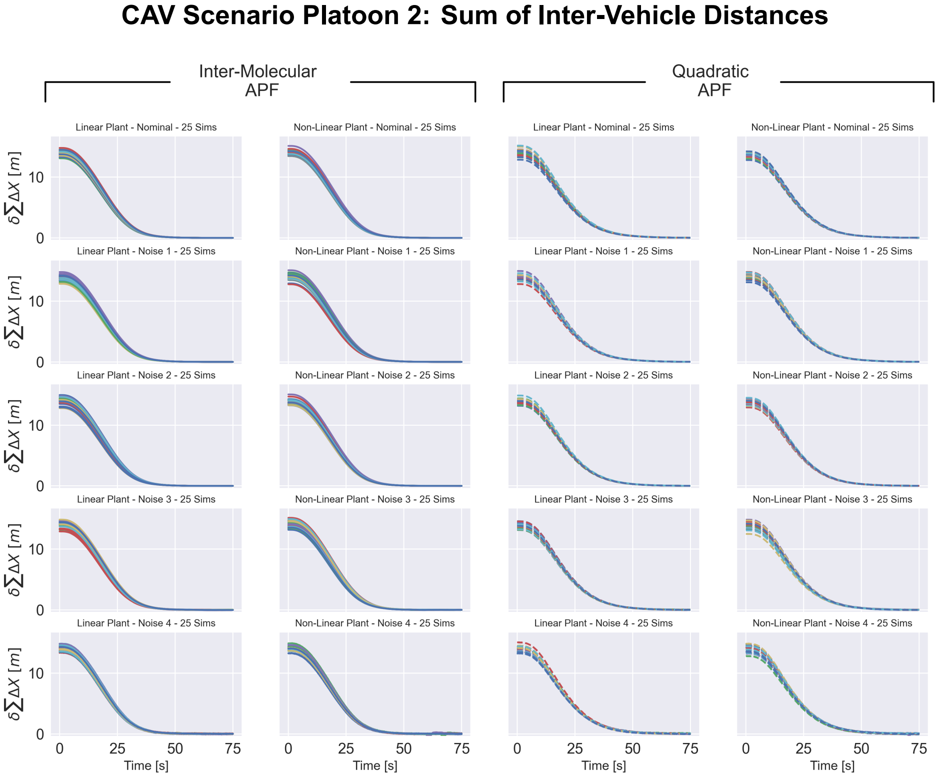

Figure C.1: Sum of the inter-vehicle distance for the platoon 1 scenario. The two left columns represent the simulations carried out with the the inter-molecular controller (3.9), and the right two columns with the quadratic controller (3.10), also indicated by the dashed lines. Each row represents a different noise level, where the first row contains no noise and the lower row represents the most. Lastly, columns one and three were simulated using the linear plant and columns two and four with the non-linear plant.

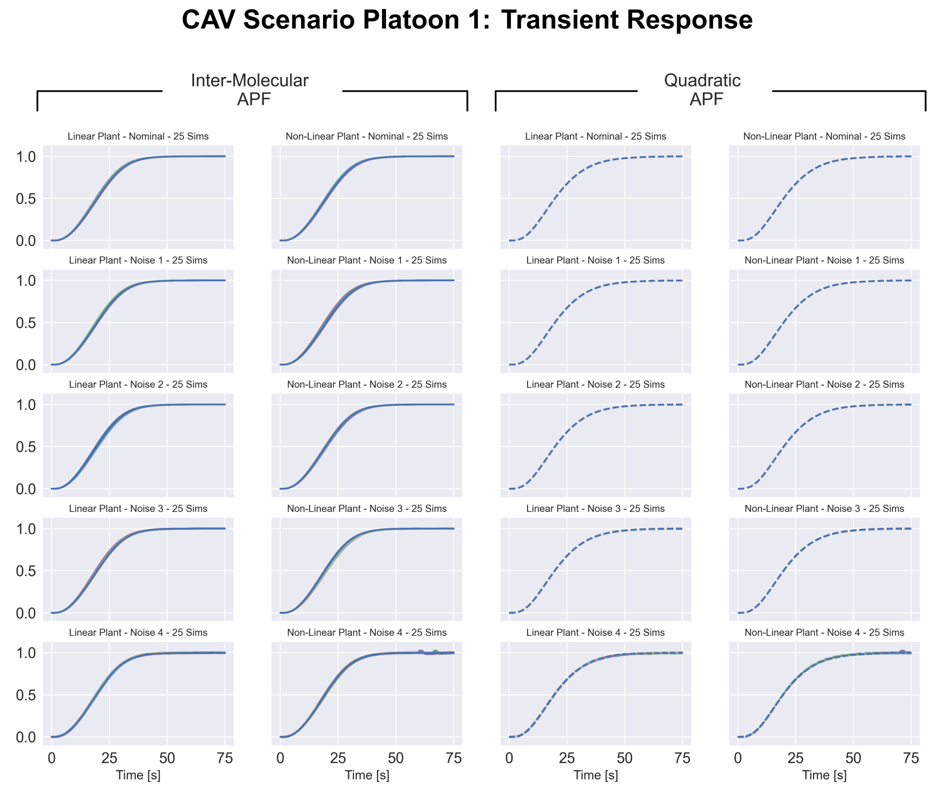

Figure C.2: Transient response of the sum of the inter-vehicle distance for the platoon 1 scenario. The two left columns represent the simulations carried out with the the inter-molecular controller (3.9), and the right two columns with the quadratic controller (3.10), also indicated by the dashed lines. Each row represents a different noise level, where the first row contains no noise and the lower row represents the most. Lastly, columns one and three were simulated using the linear plant and columns two and four with the non-linear plant.

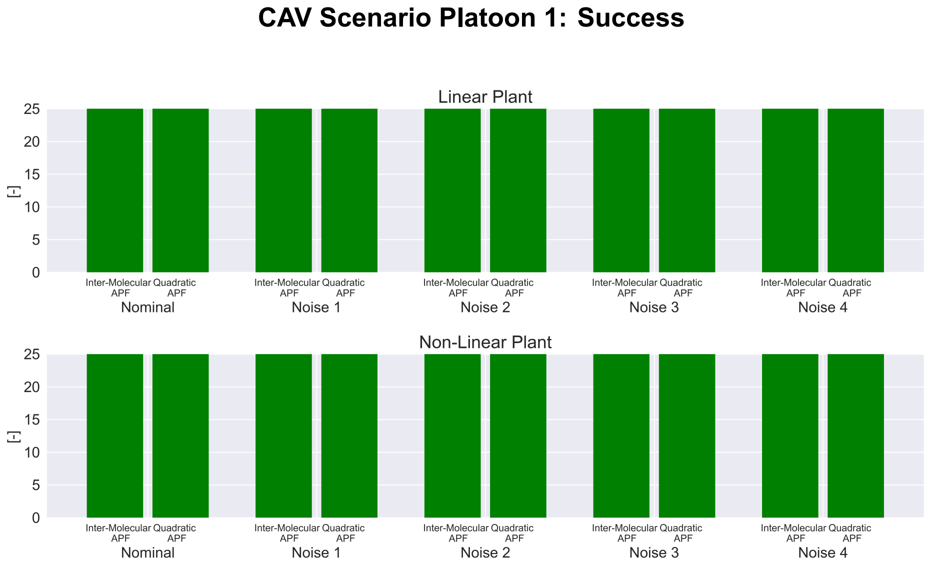

Figure C.3: Visualization of the amount of success for the Platoon 1 scenario. Each group represents a different noise level; the left-most group represents no noise, and the rightmost group the most noise. The results in the upper subplot were gathered using a linear plant and the lower subplot with the non-linear plant. Lastly, the left column from each group represents the simulations carried out with the inter-molecular controller (3.9), and the right two columns with the quadratic controller (3.10). Lastly, the red areas indicate fail and the green success.

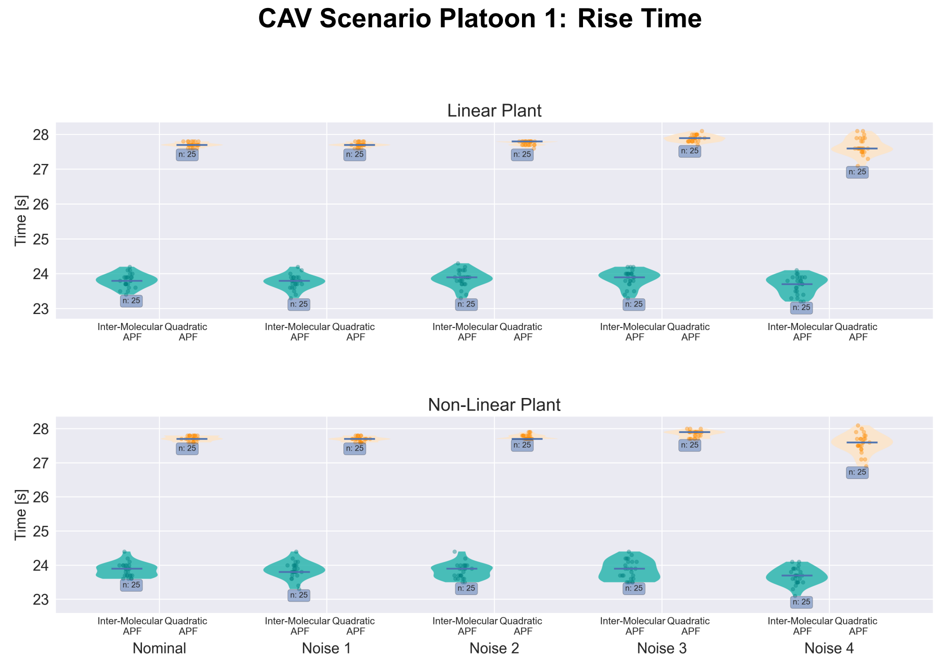

Figure C.4: Based on the transient response the Rise Time displayed. Multiple groups can be seen in subplot, where each group represents a different amount of measurement noise. The left-most group represents simulations without noise, and the rightmost group represents the most noise. Furthermore, the left violinplot of each group contains the results from the controller with the inter-molecular controller (3.9), and the right with the quadratic controller (3.10). The upper subplot represents the simulations with the linear plant and the lower subplot with the non-linear plant.

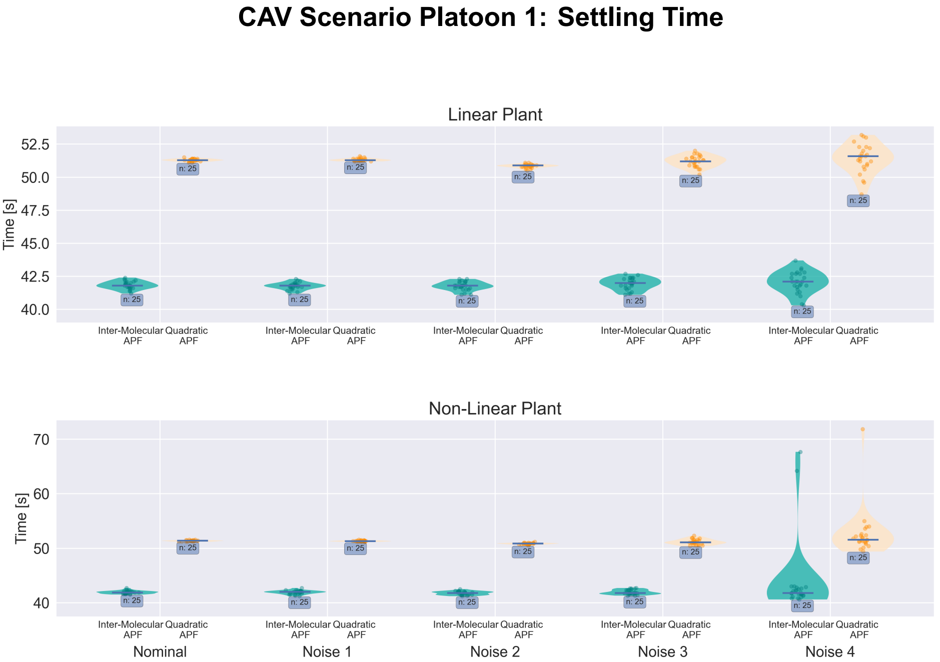

Figure C.5: Based on the transient response the Settling Time displayed. Multiple groups can be seen in subplot, where each group represents a different amount of measurement noise. The left-most group represents simulations without noise, and the rightmost group represents the most noise. Furthermore, the left violinplot of each group contains the results from the controller with the inter-molecular controller (3.9), and the right with the quadratic controller (3.10). The upper subplot represents the simulations with the linear plant and the lower subplot with the non-linear plant.

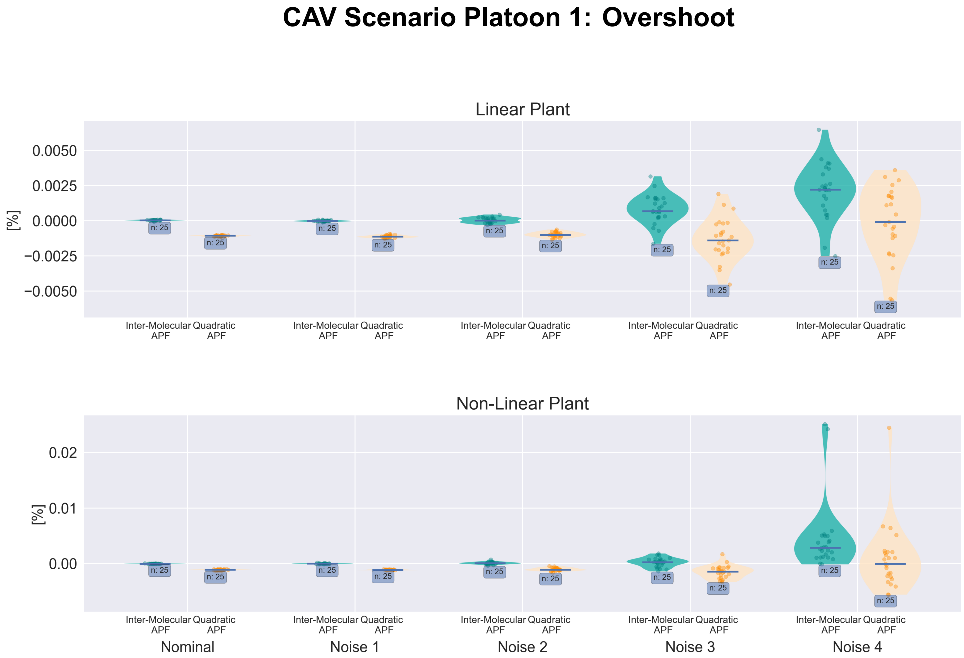

Figure C.6: Based on the transient response the overshoot displayed. Multiple groups can be seen in subplot, where each group represents a different amount of measurement noise. The left-most group represents simulations without noise, and the rightmost group represents the most noise. Furthermore, the left violinplot of each group contains the results from the controller with the inter-molecular controller (3.9), and the right with the quadratic controller (3.10). The upper subplot represents the simulations with the linear plant and the lower subplot with the non-linear plant.

C.2. Scenario Platoon 2: Disturbance Type I - Three Second Time Gap

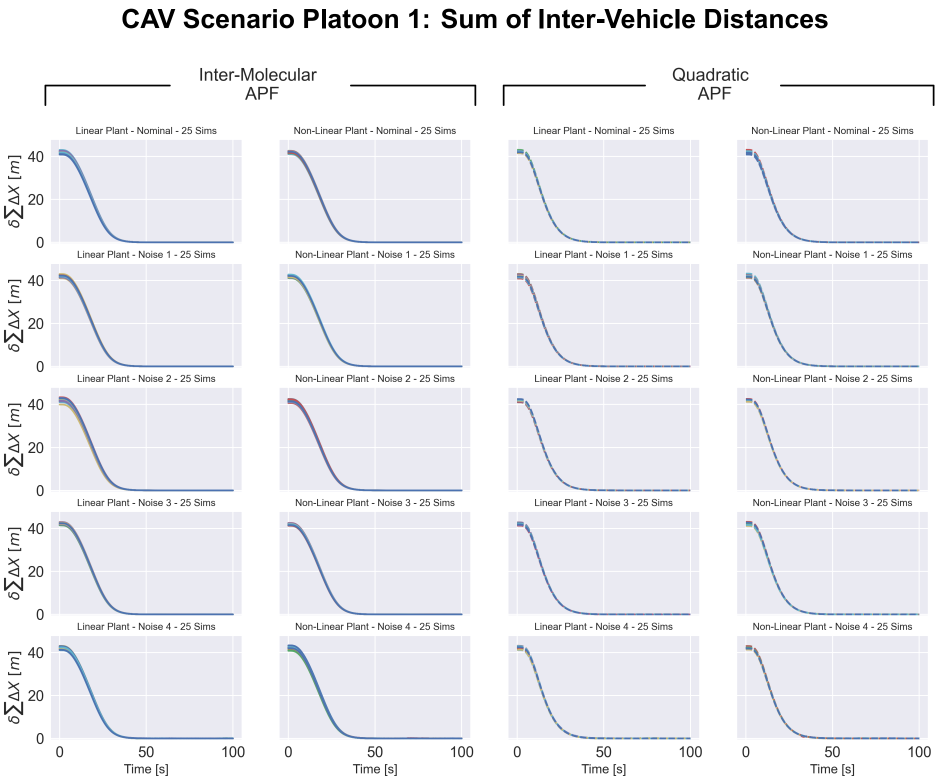

Figure C.7: Sum of the inter-vehicle distance for the platoon 2 scenario. The two left columns represent the simulations carried out with the the inter-molecular controller (3.9), and the right two columns with the quadratic controller (3.10), also indicated by the dashed lines. Each row represents a different noise level, where the first row contains no noise and the lower row represents the most. Lastly, columns one and three were simulated using the linear plant and columns two and four with the non-linear plant.

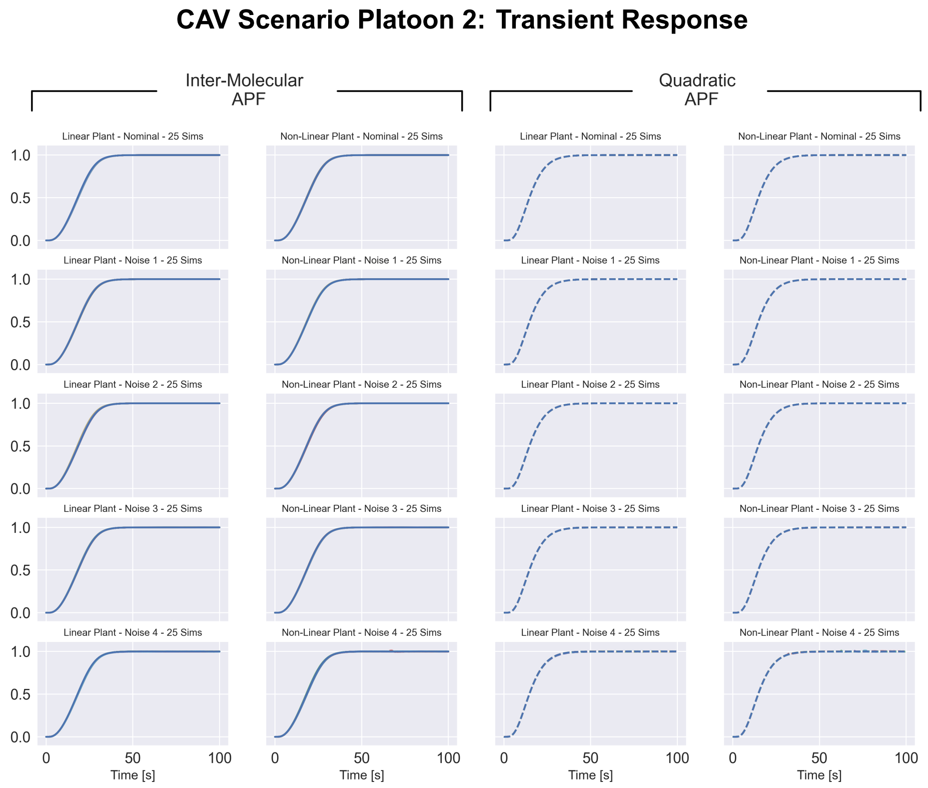
CAV Scenario Platoon 2: Transient Response

Figure C.8: Transient response of the sum of the inter-vehicle distance for the platoon 2 scenario. The two left columns represent the simulations carried out with the the inter-molecular controller (3.9), and the right two columns with the quadratic controller (3.10), also indicated by the dashed lines. Each row represents a different noise level, where the first row contains no noise and the lower row represents the most. Lastly, columns one and three were simulated using the linear plant and columns two and four with the non-linear plant.

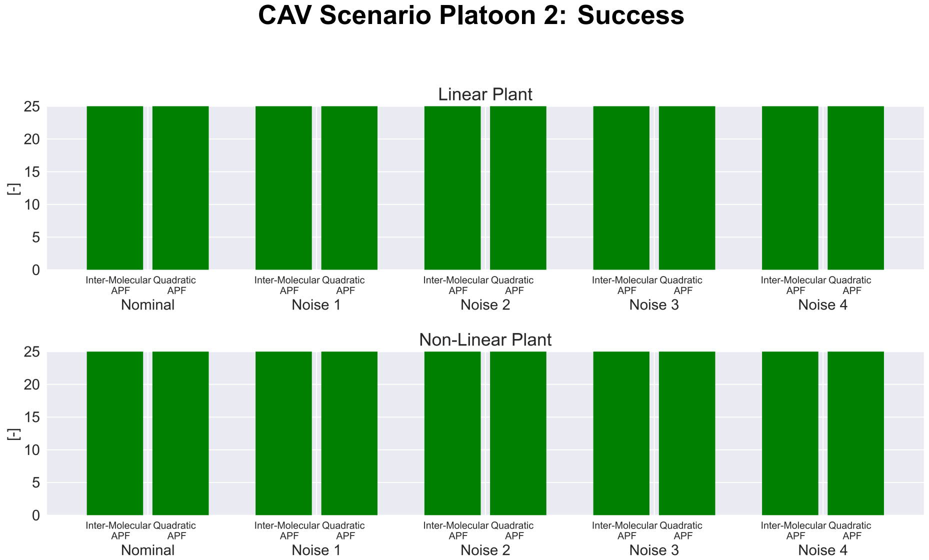
CAV Scenario Platoon 2: Success

Figure C.9: Visualization of the amount of success for the Platoon 2 scenario. Each group represents a different noise level; the left-most group represents no noise, and the rightmost group the most noise. The results in the upper subplot were gathered using a linear plant and the lower subplot with the non-linear plant. Lastly, the left column from each group represents the simulations carried out with the inter-molecular controller (3.9), and the right two columns with the quadratic controller (3.10). Lastly, the red areas indicate fail and the green success.

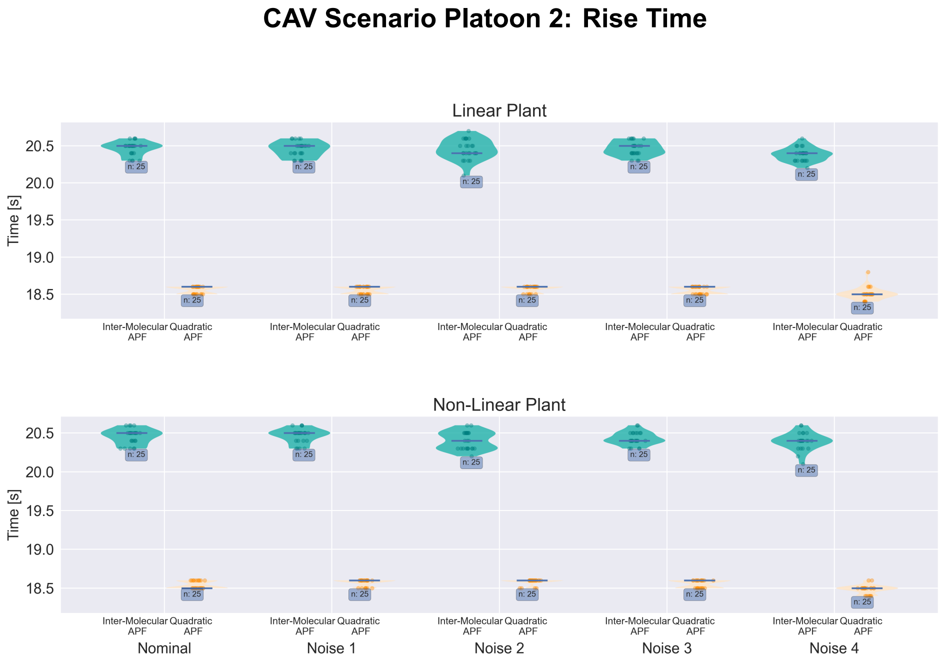

Figure C.10: Based on the transient response the Rise Time displayed. Multiple groups can be seen in subplot, where each group represents a different amount of measurement noise. The left-most group represents simulations without noise, and the rightmost group represents the most noise. Furthermore, the left violinplot of each group contains the results from the controller with the inter-molecular controller (3.9), and the right with the quadratic controller (3.10). The upper subplot represents the simulations with the linear plant and the lower subplot with the non-linear plant.

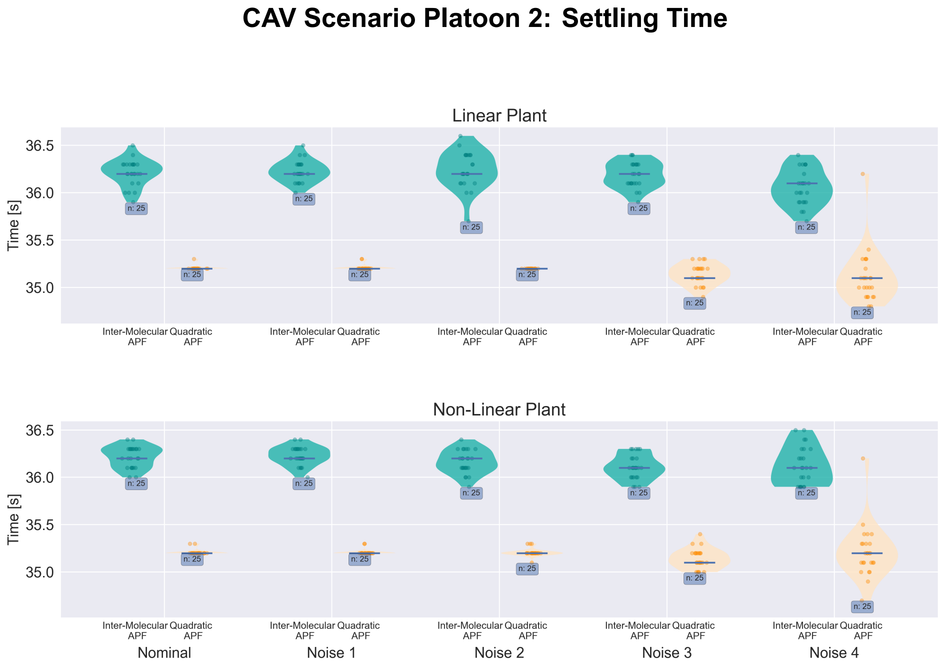

Figure C.11: Based on the transient response the Settling Time displayed. Multiple groups can be seen in subplot, where each group represents a different amount of measurement noise. The left-most group represents simulations without noise, and the rightmost group represents the most noise. Furthermore, the left violinplot of each group contains the results from the controller with the inter-molecular controller (3.9), and the right with the quadratic controller (3.10). The upper subplot represents the simulations with the linear plant and the lower subplot with the non-linear plant.

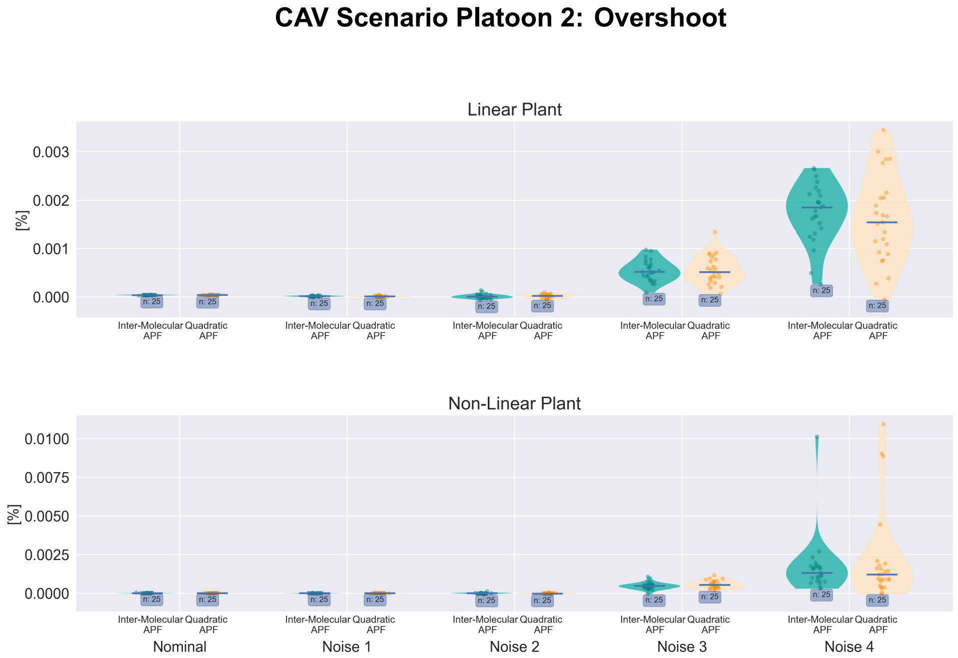

Figure C.12: Based on the transient response the Overshoot displayed. Multiple groups can be seen in subplot, where each group represents a different amount of measurement noise. The left-most group represents simulations without noise, and the rightmost group represents the most noise. Furthermore, the left violinplot of each group contains the results from the controller with the inter-molecular controller (3.9), and the right with the quadratic controller (3.10). The upper subplot represents the simulations with the linear plant and the lower subplot with the non-linear plant.

C.3. Scenario Platoon 3: Disturbance Type II - Three Second Time Gap

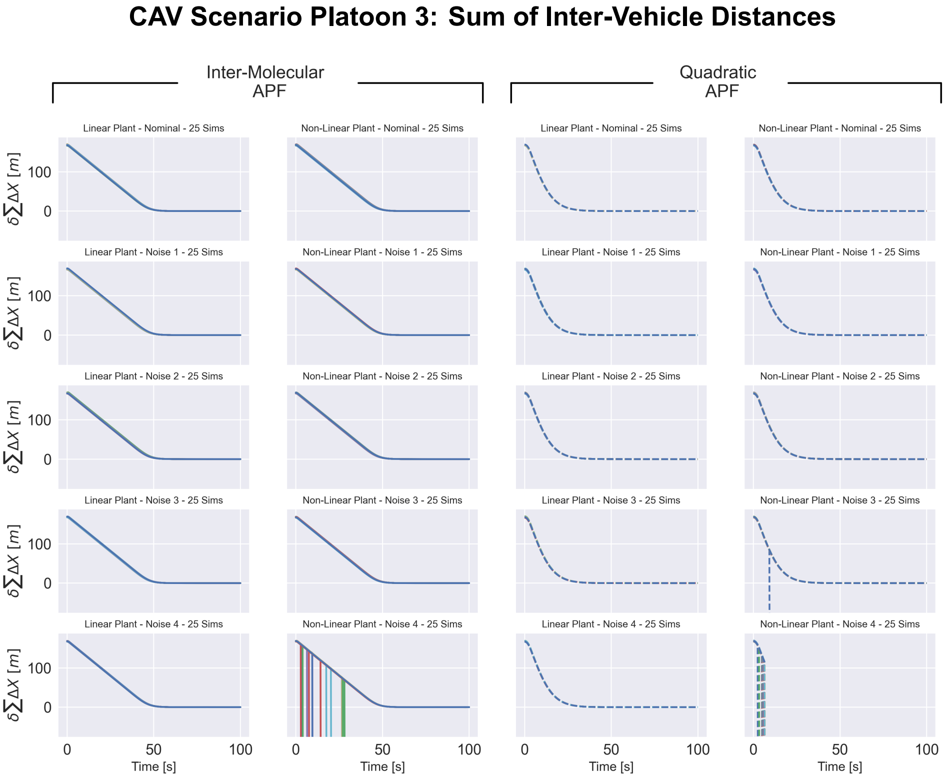

Figure C.13: Sum of the inter-vehicle distance for the platoon 3 scenario. The two left columns represent the simulations carried out with the the inter-molecular controller (3.9), and the right two columns with the quadratic controller (3.10), also indicated by the dashed lines. Each row represents a different noise level, where the first row contains no noise and the lower row represents the most. Lastly, columns one and three were simulated using the linear plant and columns two and four with the non-linear plant.

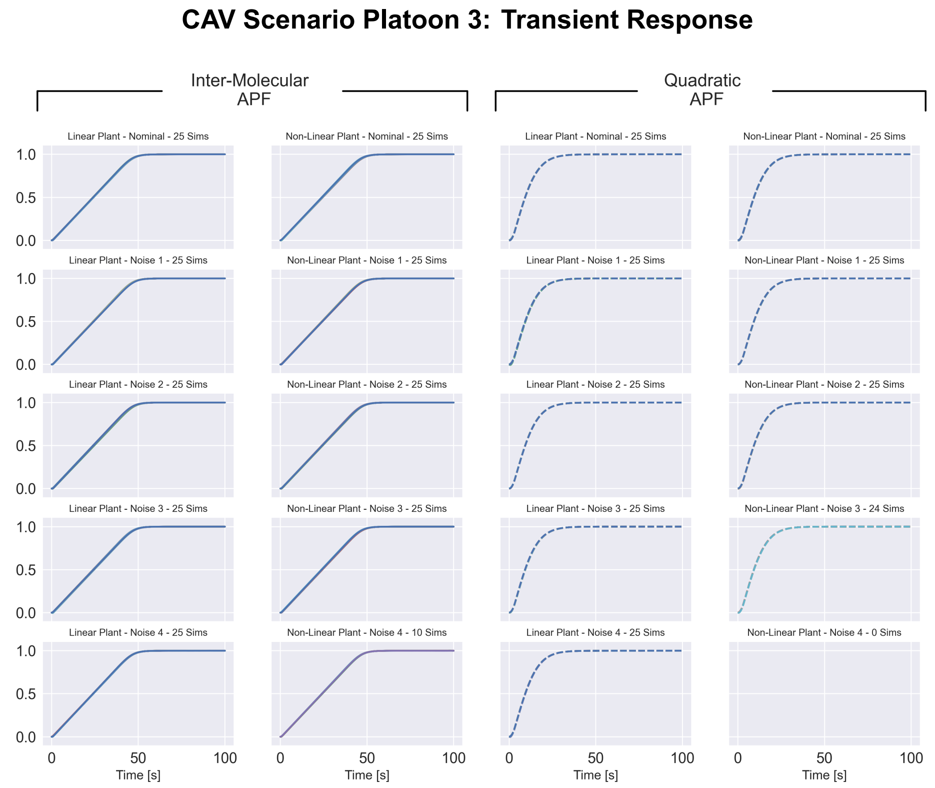

Figure C.14: Transient response of the sum of the inter-vehicle distance for the platoon 3 scenario. The two left columns represent the simulations carried out with the the inter-molecular controller (3.9), and the right two columns with the quadratic controller (3.10), also indicated by the dashed lines. Each row represents a different noise level, where the first row contains no noise and the lower row represents the most. Lastly, columns one and three were simulated using the linear plant and columns two and four with the non-linear plant.

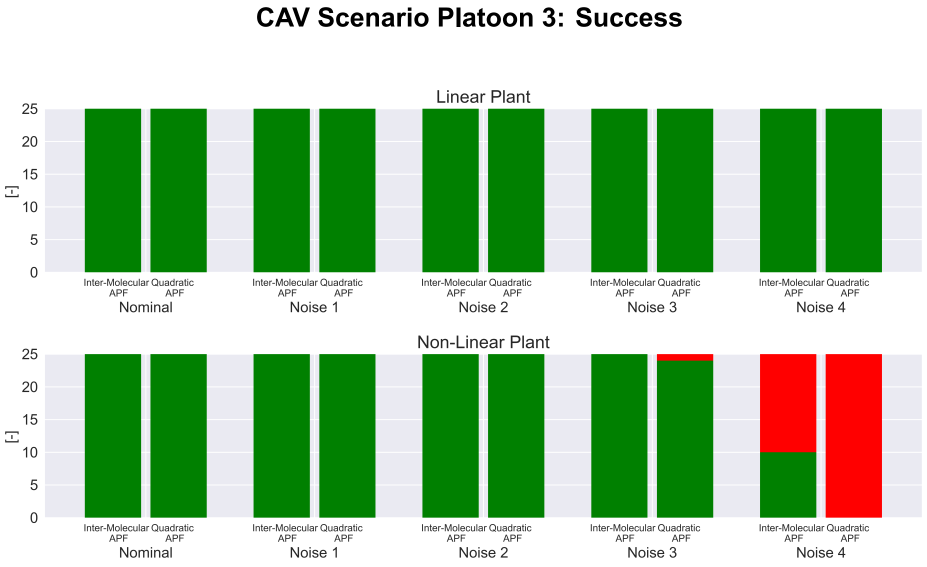

Figure C.15: Visualization of the amount of success for the Platoon 3 scenario. Each group represents a different noise level; the left-most group represents no noise, and the rightmost group the most noise. The results in the upper subplot were gathered using a linear plant and the lower subplot with the non-linear plant. Lastly, the left column from each group represents the simulations carried out with the inter-molecular controller (3.9), and the right two columns with the quadratic controller (3.10). Lastly, the red areas indicate fail and the green success

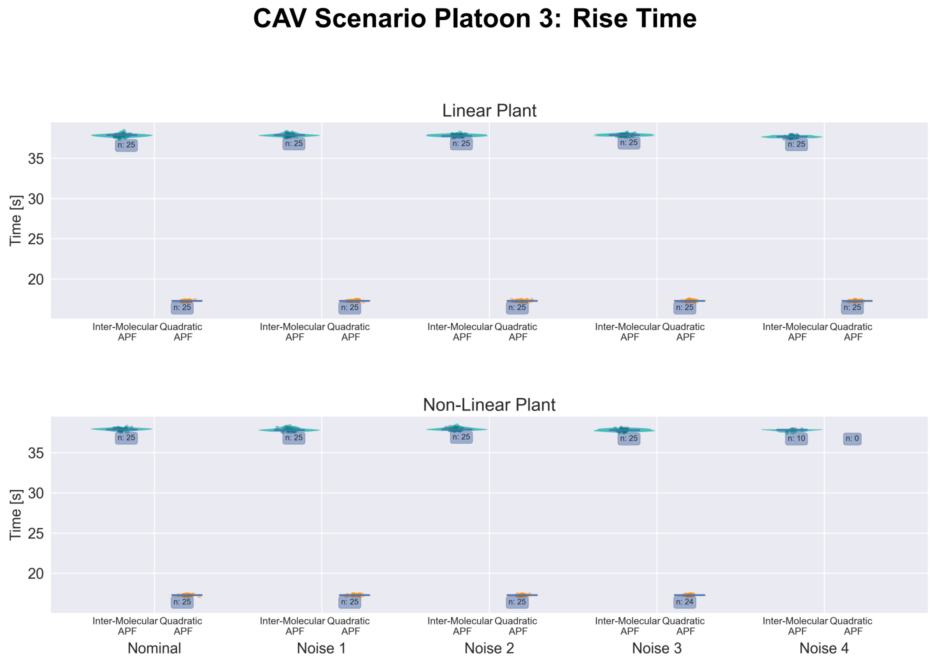
CAV Scenario Platoon 3: Rise Time

Linear Plant

Non-Linear Plant

Figure C.16: Based on the transient response the Rise Time displayed. Multiple groups can be seen in subplot, where each group represents a different amount of measurement noise. The left-most group represents simulations without noise, and the rightmost group represents the most noise. Furthermore, the left violinplot of each group contains the results from the controller with the inter-molecular controller (3.9), and the right with the quadratic controller (3.10). The upper subplot represents the simulations with the linear plant and the lower subplot with the non-linear plant.

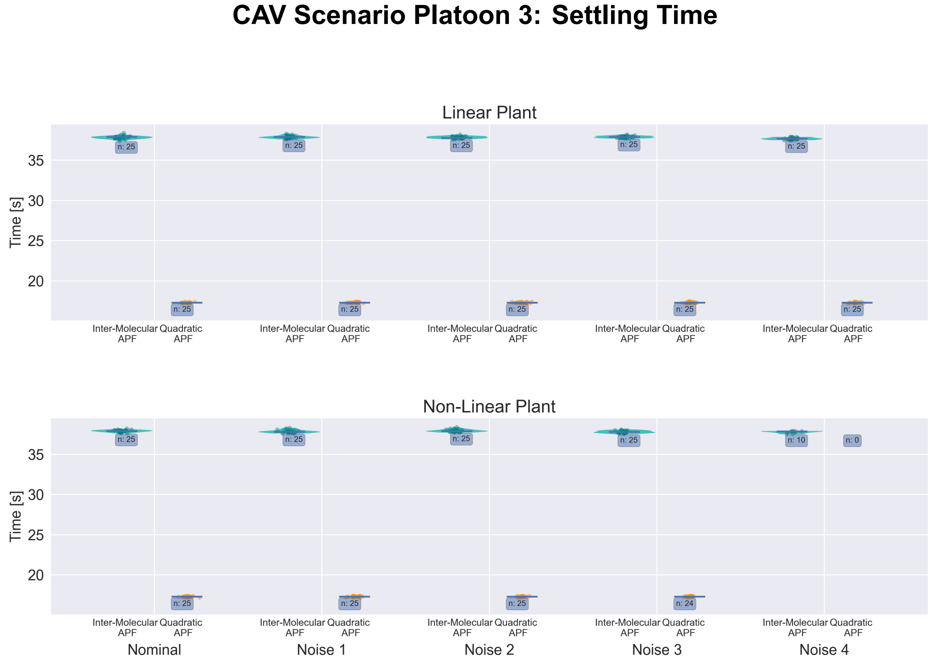
CAV Scenario Platoon 3: Settling Time

Linear Plant

Non-Linear Plant

Figure C.17: Based on the transient response the Settling Time displayed. Multiple groups can be seen in subplot, where each group represents a different amount of measurement noise. The left-most group represents simulations without noise, and the rightmost group represents the most noise. Furthermore, the left violinplot of each group contains the results from the controller with the inter-molecular controller (3.9), and the right with the quadratic controller (3.10). The upper subplot represents the simulations with the linear plant and the lower subplot with the non-linear plant.

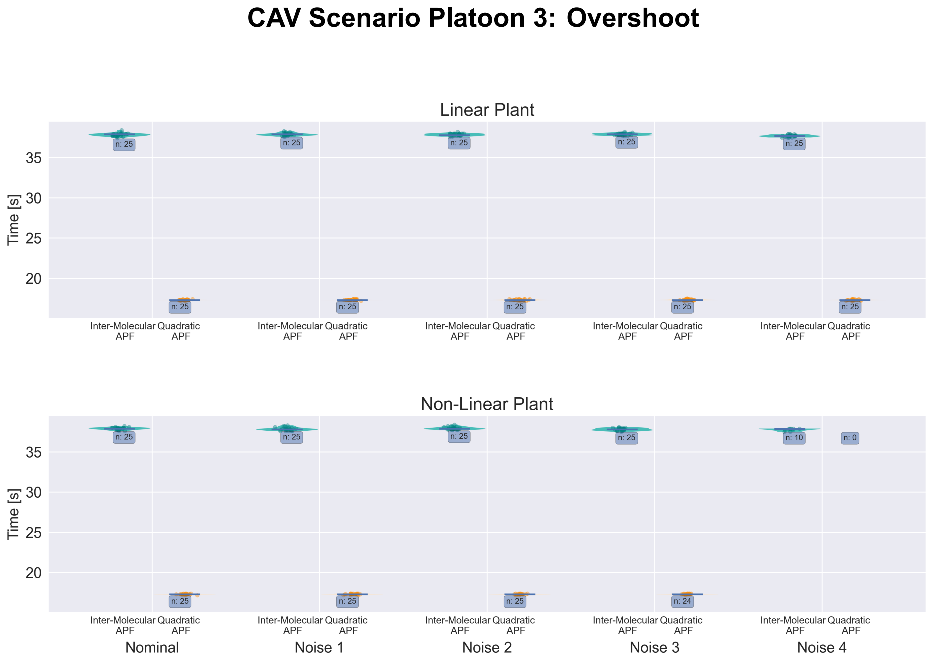

Figure C.18: Based on the transient response the Overshoot displayed. Multiple groups can be seen in subplot, where each group represents a different amount of measurement noise. The left-most group represents simulations without noise, and the rightmost group represents the most noise. Furthermore, the left violinplot of each group contains the results from the controller with the inter-molecular controller (3.9), and the right with the quadratic controller (3.10). The upper subplot represents the simulations with the linear plant and the lower subplot with the non-linear plant.

D

Compact Optimization Formulation

This appendix explains how the constraints of (2.17) can be rewritten to compact equivalent. This variation is used in the numerical implementation of this thesis. The constraints are rewritten to an inequality, $0 \leq g(\mathcal{U}_u)$ with g representing the constraints.

D.1. State Evolution

First, (2.17b), in combination with the LTI system, can be replaced by a matrix variant,

$$\bar{X} = Tx_0 + S\mathcal{U}_u, \tag{D.1}$$

with the prediction matrices $S \in \mathbb{R}^{(N)n \times Nm}$ and $T \in \mathbb{R}^{(N)n \times n}$,

$$S = \begin{bmatrix} 0 & 0 & 0 & \cdots & 0 \\ B & 0 & 0 & \cdots & 0 \\ AB & B & 0 & \cdots & 0 \\ \vdots & \vdots & \vdots & \ddots & 0 \\ A^{N-2}B & A^{N-3}B & A^{N-4}B & \cdots & B \end{bmatrix}, \tag{D.2}$$

$$T = \begin{bmatrix} I \\ A \\ A^2 \\ \vdots \\ A^{N-1} \end{bmatrix}. \tag{D.3}$$

D.2. State Constraints

Because v_x and γ are part of the state space vector x, the corresponding constraints (2.17f), (2.17g) will be combined by making use of the previous introduced matrices S and T. However, because $k = 0$ is not part of these constrains, the top matrix row is omitted,

$$S' = \begin{bmatrix} B & 0 & 0 & \cdots & 0 \\ AB & B & 0 & \cdots & 0 \\ \vdots & \vdots & \vdots & \ddots & 0 \\ A^{N-2}B & A^{N-3}B & A^{N-4}B & \cdots & B \end{bmatrix}, \tag{D.4}$$

$$T' = \begin{bmatrix} A \\ A^2 \\ \vdots \\ A^{N-1} \end{bmatrix}. \tag{D.5}$$

Furthermore, the limits can be formulated as a matrix as well,

$$M_{x,\max} = \mathbf{1}_N \otimes \begin{bmatrix} v_{x_{\max}} \end{bmatrix}, \tag{D.6}$$

$$M_{x,\min} = \mathbf{1}_N \otimes \begin{bmatrix} v_{x_{\min}} \end{bmatrix}, \tag{D.7}$$

where $\otimes$ is the kronecker product, and $\mathbf{1}_N$ is a column vector of size N, containing only ones. Because γ and v_x are the only two states that are constrained, they need to be isolated as $\bar{X}' = T'x_0 + S'\mathcal{U}_u$ calculates all states along the prediction horizon. The matrix F_1 extracts the required rows from the prediction matrices S', T',

$$F_1 = I_N \otimes \begin{bmatrix} 1 & 0 & 1 & 0 & 0 & 0 \end{bmatrix}. \tag{D.8}$$

By combining (D.4), (D.5), (D.6), (D.7), (D.8), a matrix variant of (2.17f) can be formulated into the desired inequalities,

$$0 \leq -(F_1 S'\mathcal{U}_u + F_1 T'x_0) + M_{x,\max} \tag{D.9a}$$

$$0 \leq (F_1 S'\mathcal{U}_u + F_1 T'x_0) - M_{x,\min}, \tag{D.9b}$$

which as well can be combined into one matrix inequality,

$$0 \leq Z_x \mathcal{U}_u + M_x, \tag{D.10}$$

where

$$Z_x = \begin{bmatrix} -F_1 S' \\ F_1 S' \end{bmatrix} \tag{D.11}$$

$$M_x = \begin{bmatrix} (-F_1 T'x_0 + M_{x,\max}) \\ -(-F_1 T'x_0 + M_{x,\min}) \end{bmatrix}. \tag{D.12}$$

D.3. Input Constraints

The input constraints from (2.17c) can be reformulated to the following inequalities as well,

$$0 \leq -u_k + u_{\max} \tag{D.13a}$$

$$0 \leq u_k - u_{\min}, \tag{D.13b}$$

which can be rewritten to a matrix form with the matrix input limits $M_{u,\max} \in \mathbb{R}^{Nm}$ $M_{u,\min} \in \mathbb{R}^{Nm}$, based on the horizon N,

$$0 \leq -I\mathcal{U}_u + M_{u,\max} \tag{D.14a}$$

$$0 \leq I\mathcal{U}_u - M_{u,\min}. \tag{D.14b}$$

where

$$M_{u,\max} = \mathbf{1}_N^\top \otimes u_{\max}, \tag{D.15}$$

$$M_{u,\min} = \mathbf{1}_N^\top \otimes u_{\min}. \tag{D.16}$$

Again (D.15), (D.16) can be combined with (D.14),

$$0 \leq Z_u \mathcal{U}_u + M_u, \tag{D.17}$$

where

$$Z_u = \begin{bmatrix} -I \\ I \end{bmatrix}, \tag{D.18}$$

$$M_u = \begin{bmatrix} M_{u,\max} \\ -M_{u,\min} \end{bmatrix}. \tag{D.19}$$

D.4. Input Rate Constraints

Similarly, the input rate constraints from (2.17d), (2.17e) can be reformulated,

$$0 \leq -u_{k+1} - u_k + \Delta u_{\max} \tag{D.20a}$$

$$0 \leq (u_{k+1} - u_k) - \Delta u_{\min}. \tag{D.20b}$$

In matrix form, with the matrix input rate of change limits $M_{\Delta u,\max} \in \mathbb{R}^{Nm}$,$M_{\Delta u,\min} \in \mathbb{R}^{Nm}$ based on N, with the matrix $\Delta U \in \mathbb{R}^{Nm \times Nm}$ which represents the difference calculation,

$$0 \leq -\Delta U\ \mathcal{U}_u + M_{\Delta u,\max} \tag{D.21a}$$

$$0 \leq \Delta U\ \mathcal{U}_u - M_{\Delta u,\min}, \tag{D.21b}$$

where

$$\Delta U = \begin{bmatrix} I & 0 & 0 & \cdots & 0 \\ -I & I & 0 & \cdots & 0 \\ 0 & -I & I & \ddots & \vdots \\ 0 & \ddots & \ddots & \ddots & \vdots \\ \vdots & \ddots & \ddots & \ddots & \vdots \\ 0 & \cdots & 0 & -I & I \end{bmatrix}, \tag{D.22}$$

$$M_{\Delta u,\max} = \mathbf{1}_N^\intercal \otimes \Delta u_{\max} + \begin{bmatrix} u(t-1) \\ 0 \\ \vdots \\ 0 \end{bmatrix}, \tag{D.23}$$

$$M_{\Delta u,\min} = \mathbf{1}_N^\intercal \otimes \Delta u_{\min} + \begin{bmatrix} u(t-1) \\ 0 \\ \vdots \\ 0 \end{bmatrix}, \tag{D.24}$$

with $u(t-1)$ being the input that was injected in the system during the previous timestep $k = -1$. Again (D.15), (D.16) can then be combined with (D.20),

$$0 \leq Z_{\Delta u} \mathcal{U}_u + M_{\Delta u}, \tag{D.25}$$

where

$$Z_{\Delta u} = \begin{bmatrix} -\Delta U \\ \Delta U \end{bmatrix}, \tag{D.26}$$

$$M_{\Delta u} = \begin{bmatrix} M_{\Delta u,\max} \\ -M_{\Delta u,\min} \end{bmatrix}. \tag{D.27}$$

D.5. Optimization Problem

All matrix constrains, (D.9), (D.17), (D.25), can be combined such that (2.17) can be rewritten more compactly,

$$\underset{\mathcal{U}_u}{\arg\min} \quad \mathbb{P}_N(x_0) : V_n = \sum_{k=0}^{N-1} l(x_k, u_k) \tag{D.28a}$$

$$\text{subject to} \quad 0 \leq Z\mathcal{U}_u + M, \tag{D.28b}$$

where

$$Z = \begin{bmatrix} Z_x \\ Z_u \\ Z_{\Delta_U} \end{bmatrix}, \tag{D.29}$$

$$M = \begin{bmatrix} M_x \\ M_u \\ M_{\Delta u} \end{bmatrix}. \tag{D.30}$$

Bibliography

[1] SAE, "Taxonomy and Definitions for Terms Related to Driving Automation Systems for On-Road Motor Vehicles J3016_202104," 2021. [Online]. Available: https://www-sae-org.tudelft.idm.oclc.org/standards/content/j3016_202104/.

[2] National Highway Traffic Safety Administration, "2014 Crash Data Key Findings," *TRAFFIC SAFETY FACTS*, no. November, pp. 1–2, 2015.

[3] S. Singh, "Critical reasons for crashes investigated in the National Motor Vehicle Crash Causation Survey," *National Highway Traffic Safety Administration*, no. February, 2015.

[4] J. D. Hill and L. N. Boyle, "Driver stress as influenced by driving maneuvers and roadway conditions," *Transportation Research Part F: Traffic Psychology and Behaviour*, vol. 10, no. 3, pp. 177–186, 2007, ISSN: 13698478. DOI: 10.1016/j.trf.2006.09.002.

[5] T. Zhang and A. H. Chan, "The association between driving anger and driving outcomes: A meta-analysis of evidence from the past twenty years," *Accident Analysis and Prevention*, vol. 90, pp. 50–62, 2016, ISSN: 00014575. DOI: 10.1016/j.aap.2016.02.009.

[6] Y. Fang, H. Min, X. Wu, W. Wang, X. Zhao, and G. Mao, "On-Ramp Merging Strategies of Connected and Automated Vehicles Considering Communication Delay," *IEEE Transactions on Intelligent Transportation Systems*, 2022, ISSN: 15580016. DOI: 10.1109/TITS.2022.3140219.

[7] E. Talavera, A. Díaz-Álvarez, F. Jiménez, and J. E. Naranjo, "Impact on Congestion and Fuel Consumption of a Cooperative Adaptive Cruise Control System with Lane-Level Position Estimation," *Energies 2018, Vol. 11, Page 194*, vol. 11, no. 1, p. 194, Jan. 2018, ISSN: 1996-1073. DOI: 10.3390/EN11010194. [Online]. Available: https://www.mdpi.com/1996-1073/11/1/194/htm%20https://www.mdpi.com/1996-1073/11/1/194.

[8] D. He, T. Qiu, and R. Luo, "Fuel efficiency-oriented platooning control of connected nonlinear vehicles: A distributed economic MPC approach," 2019. DOI: 10.1002/asjc.2049.

[9] W. Pan, Y. Xue, H. D. He, and W. Z. Lu, "Impacts of traffic congestion on fuel rate, dissipation and particle emission in a single lane based on Nasch Model," *Physica A: Statistical Mechanics and its Applications*, vol. 503, pp. 154–162, Aug. 2018, ISSN: 0378-4371. DOI: 10.1016/J.PHYSA.2018.02.199.

[10] UNTC, *7. d Paris Agreement*, 2015. [Online]. Available: https://treaties.un.org/pages/ViewDetails.aspx?src=TREATY&mtdsg_no=XXVII-7-d&chapter=27&clang=_en.

[11] U. Census Bureau, "Commuting in the United States: 2009," [Online]. Available: http://nhts.ornl.gov.

[12] Y. C. Lee and D. J. Bonfiglio, "What is stressful on the road? Analysis on aggression-inducing traffic situations through self-report," in *Proceedings of the Human Factors and Ergonomics Society*, 2013. DOI: 10.1177/1541931213571334.

[13] D. A. Hennessy and D. L. Wiesenthal, "Traffic congestion, driver stress, and driver aggression," *Aggressive Behavior*, vol. 25, no. 6, 1999, ISSN: 0096140X. DOI: 10.1002/(SICI)1098-2337(1999)25:6<409::AID-AB2>3.0.CO;2-0.

[14] MnDOT, *Connected and Automated Vehicles*. [Online]. Available: http://www.dot.state.mn.us/automated/.

[15] R. Wilson, *CES: Autonomous cars and the sensors to make them safe*, 2017. [Online]. Available: https://www.electronicsweekly.com/market-sectors/automotive-electronics/ces-autonomous-cars-sensors-make-safe-2017-01/.

[16] L. Hanrahan, *Here's how to ride Toronto's first self-driving shuttle bus*, Sep. 2021. [Online]. Available: https://dailyhive.com/toronto/how-to-ride-toronto-self-driving-shuttle-bus.

[17] M. Say, *Driverless shuttle bus trial runs in Birmingham*, Sep. 2021. [Online]. Available: https://www.ukauthority.com/articles/driverless-shuttle-bus-trial-runs-in-birmingham/.

[18] University of Bristol, *Heathrow pods - a new form of personal rapid transit*. [Online]. Available: http://www.bristol.ac.uk/research/impact/heathrow-personal-rapid-transport/.

[19] R. Van Hoek, J. Ploeg, and H. Nijmeijer, "Gap Closing for Cooperative Driving in Automated Vehicles using B-splines for Trajectory Planning," in *IEEE Intelligent Vehicles Symposium, Proceedings*, Institute of Electrical and Electronics Engineers Inc., 2020, pp. 370–375. DOI: 10.1109/IV47402.2020.9304732.

[20] J. Han, H. Shi, L. Chen, H. Li, and X. Wang, "The car-following model and its applications in the v2x environment: A historical review," *Future Internet*, vol. 14, no. 1, Jan. 2022, ISSN: 19995903. DOI: 10.3390/FI14010014.

[21] U. I. Atmaca, C. Maple, G. Epiphaniou, and A. T. Sheik, "Human Factors for Vehicle Platooning: A Review," *IET Conference Publications*, vol. 2021, no. CP786, 2021. DOI: 10.1049/ICP.2021.2429.

[22] H. Yang, Y. Chen, and J. Huang, "Long Distance Merge based on Vehicle-infrastructure Communication," in *Proceedings - 2020 Chinese Automation Congress, CAC 2020*, Institute of Electrical and Electronics Engineers Inc., Nov. 2020, pp. 5867–5872, ISBN: 9781728176871. DOI: 10.1109/CAC51589.2020.9326654.

[23] A. C. Eilbert, A. M. Chouinard, T. A. Tiernan, and S. B. Smith, "Performance comparisons of co-operative and adaptive cruise control testing," in *Proceedings of the Air and Waste Management Association's Annual Conference and Exhibition, AWMA*, vol. 2020-June, 2020.

[24] F. Liu, R. Pueboobpaphan, and B. Van Arem, "Assessment of traffic impact on future cooperative driving systems: Challenges and considerations," in *2009 International Conference on Ultra Modern Telecommunications and Workshops*, 2009, ISBN: 9781424439416. DOI: 10.1109/ICUMT.2009.5345339.

[25] J. Ligthart, E. Semsar-Kazerooni, J. Ploeg, M. Alirezaei, and H. Nijmeijer, "Controller Design for Cooperative Driving with Guaranteed Safe Behavior," in *2018 IEEE Conference on Control Technology and Applications, CCTA 2018*, Institute of Electrical and Electronics Engineers Inc., Oct. 2018, pp. 1460–1465, ISBN: 9781538676981. DOI: 10.1109/CCTA.2018.8511625.

[26] S. Badnava, N. Meskin, A. Gastli, *et al.*, "Platoon Transitional Maneuver Control System: A Review," *IEEE Access*, vol. 9, pp. 88 327–88 347, 2021, ISSN: 21693536. DOI: 10.1109/ACCESS.2021.3089615.

[27] A. Soni and H. Hu, "Formation control for a fleet of autonomous ground vehicles: A survey," *Robotics*, vol. 7, no. 4, Nov. 2018, ISSN: 22186581. DOI: 10.3390/ROBOTICS7040067.

[28] Z. Wang, G. Wu, and M. J. Barth, "A Review on Cooperative Adaptive Cruise Control (CACC) Systems: Architectures, Controls, and Applications," *IEEE Conference on Intelligent Transportation Systems, Proceedings, ITSC*, vol. 2018-Novem, pp. 2884–2891, Dec. 2018. DOI: 10.1109/ITSC.2018.8569947.

[29] A. Sie, "Comprehensive Predictive Control A New Autonomous Vehicle Control Strategy," Tech. Rep., 2022.

[30] W. Liu and Z. Li, "Comprehensive predictive control method for automated vehicles in dynamic traffic circumstances," *IET Intelligent Transport Systems*, vol. 12, no. 10, pp. 1455–1463, 2018, ISSN: 1751956X. DOI: 10.1049/iet-its.2018.5142. [Online]. Available: www.ietdl.org.

[31] S. M. LaValle, *Planning algorithms*. 2006, vol. 9780521862, pp. 1–826, ISBN: 9780511546877. DOI: 10.1017/CBO9780511546877.

[32] Z. Huang, Q. Wu, J. Ma, and S. Fan, “An APF and MPC combined collaborative driving controller using vehicular communication technologies,” *Chaos, Solitons and Fractals*, vol. 89, pp. 232–242, 2016, ISSN: 09600779. DOI: 10.1016/j.chaos.2015.11.009.

[33] J. Wang, J. Wu, X. Zheng, D. Ni, and K. Li, “Driving safety field theory modeling and its application in pre-collision warning system,” *Transportation Research Part C: Emerging Technologies*, vol. 72, pp. 306–324, Nov. 2016, ISSN: 0968090X. DOI: 10.1016/j.trc.2016.10.003.

[34] Z. Huang, D. Chu, C. Wu, and Y. He, “Path Planning and Cooperative Control for Automated Vehicle Platoon Using Hybrid Automata,” *IEEE Transactions on Intelligent Transportation Systems*, vol. 20, no. 3, pp. 959–974, Mar. 2019, ISSN: 15249050. DOI: 10.1109/TITS.2018.2841967.

[35] L. Li, J. Gan, X. Qu, W. Lu, P. Mao, and B. Ran, “A Dynamic Control Method for Cavs Platoon Based on the MPC Framework and Safety Potential Field Model,” *KSCE Journal of Civil Engineering*, vol. 25, no. 5, pp. 1874–1886, 2021, ISSN: 19763808. DOI: 10.1007/s12205-021-1585-5. [Online]. Available: www.springer.com/12205.

[36] M. Behrendt, *A discrete MPC scheme*, 2009. [Online]. Available: https://commons.wikimedia.org/w/index.php?curid=7963069.

[37] M. D. Rafal and W. F. Stevens, “Discrete dynamic optimization applied to on□line optimal control,” *AIChE Journal*, vol. 14, no. 1, pp. 85–91, 1968, ISSN: 15475905. DOI: 10.1002/aic.690140117.

[38] Ø. Hegrenæs, J. T. Gravdahl, and P. Tøndel, “Spacecraft attitude control using explicit model predictive control,” *Automatica*, vol. 41, no. 12, 2005, ISSN: 00051098. DOI: 10.1016/j.automatica.2005.06.015.

[39] P. Falcone, M. Tufo, F. Borrelli, J. Asgarit, and H. E. Tseng, “A linear time varying model predictive control approach to the integrated vehicle dynamics control problem in autonomous systems,” in *Proceedings of the IEEE Conference on Decision and Control*, 2007. DOI: 10.1109/CDC.2007.4434137.

[40] P. Falcone, F. Borrelli, J. Asgari, H. E. Tseng, and D. Hrovat, “Predictive active steering control for autonomous vehicle systems,” *IEEE Transactions on Control Systems Technology*, vol. 15, no. 3, 2007, ISSN: 10636536. DOI: 10.1109/TCST.2007.894653.

[41] C. Ocampo-Martinez, D. Barcelli, V. Puig, and A. Bemporad, “Hierarchical and decentralised model predictive control of drinking water networks: Application to Barcelona case study,” *IET Control Theory and Applications*, vol. 6, no. 1, pp. 62–71, 2012, ISSN: 17518644. DOI: 10.1049/iet-cta.2010.0737.

[42] T. Stastny and R. Siegwart, “Nonlinear Model Predictive Guidance for Fixed-wing UAVs Using Identified Control Augmented Dynamics,” in *2018 International Conference on Unmanned Aircraft Systems, ICUAS 2018*, 2018, pp. 432–442, ISBN: 9781538613535. DOI: 10.1109/ICUAS.2018.8453377.

[43] K. J. Astrom and Hagglund T., *PID Controllers, Theory, Design and Tuning*, 2nd Editio. Instrument Society of America, 1995.

[44] S. Grammatico, “Model Predictive Control - Lecture Slides (SC42125),” TU Delft, Tech. Rep., 2020.

[45] T. Shim, G. Adireddy, and H. Yuan, “Autonomous vehicle collision avoidance system using path planning and model-predictive-control-based active front steering and wheel torque control,” *Proceedings of the Institution of Mechanical Engineers, Part D: Journal of Automobile Engineering*, vol. 226, no. 6, pp. 767–778, 2012, ISSN: 09544070. DOI: 10.1177/0954407011430275.

[46] A. Carvalho, Y. Gao, A. Gray, H. E. Tseng, and F. Borrelli, “Predictive control of an autonomous ground vehicle using an iterative linearization approach,” in *IEEE Conference on Intelligent Transportation Systems, Proceedings, ITSC*, 2013, pp. 2335–2340, ISBN: 9781479929146. DOI: 10.1109/ITSC.2013.6728576.

[47] E. Kim, J. Kim, and M. Sunwoo, "Model predictive control strategy for smooth path tracking of autonomous vehicles with steering actuator dynamics," *International Journal of Automotive Technology*, vol. 15, no. 7, pp. 1155–1164, Nov. 2014, ISSN: 19763832. DOI: 10.1007/s12239-014-0120-9.

[48] H. Jiang, Z. Wang, Q. Chen, and J. Zhu, "Obstacle avoidance of autonomous vehicles with CQP-based model predictive control," in *2016 IEEE International Conference on Systems, Man, and Cybernetics, SMC 2016 - Conference Proceedings*, 2017, pp. 1668–1673, ISBN: 9781509018970. DOI: 10.1109/SMC.2016.7844477.

[49] M. Zhu, H. Chen, and G. Xiong, "A model predictive speed tracking control approach for autonomous ground vehicles," *Mechanical Systems and Signal Processing*, vol. 87, pp. 138–152, Mar. 2017, ISSN: 10961216. DOI: 10.1016/j.ymssp.2016.03.003.

[50] J. Yu, X. Pei, X. Guo, J. G. Lin, and M. Zhu, "Path tracking framework synthesizing robust model predictive control and stability control for autonomous vehicle," *Proceedings of the Institution of Mechanical Engineers, Part D: Journal of Automobile Engineering*, vol. 234, no. 9, pp. 2330–2341, Aug. 2020, ISSN: 09544070. DOI: 10.1177/0954407020914666.

[51] S. Yu, M. Hirche, Y. Huang, H. Chen, and F. Allgöwer, "Model predictive control for autonomous ground vehicles: a review," *Autonomous Intelligent Systems*, vol. 1, no. 1, Dec. 2021. DOI: 10.1007/s43684-021-00005-z.

[52] J. B. Rawlings, D. Angeli, and C. N. Bates, "Fundamentals of economic model predictive control," in *Proceedings of the IEEE Conference on Decision and Control*, 2012, pp. 3851–3861, ISBN: 9781467320641. DOI: 10.1109/CDC.2012.6425822.

[53] M. Ellis, H. Durand, and P. D. Christofides, "A tutorial review of economic model predictive control methods," *Journal of Process Control*, vol. 24, no. 8, pp. 1156–1178, Aug. 2014, ISSN: 0959-1524. DOI: 10.1016/J.JPROCONT.2014.03.010.

[54] M. J. Risbeck and J. B. Rawlings, "Economic Model Predictive Control for Time-Varying Cost and Peak Demand Charge Optimization," *IEEE Transactions on Automatic Control*, vol. 65, no. 7, pp. 2957–2968, 2020, ISSN: 15582523. DOI: 10.1109/TAC.2019.2939633.

[55] R. Halvgaard, N. K. Poulsen, H. Madsen, and J. B. Jørgensen, "Economic Model Predictive Control for building climate control in a Smart Grid," in *2012 IEEE PES Innovative Smart Grid Technologies, ISGT 2012*, 2012, ISBN: 9781457721588. DOI: 10.1109/ISGT.2012.6175631.

[56] J. Ma, J. Qin, T. Salsbury, and P. Xu, "Demand reduction in building energy systems based on economic model predictive control," *Chemical Engineering Science*, vol. 67, no. 1, pp. 92–100, Jan. 2012, ISSN: 0009-2509. DOI: 10.1016/J.CES.2011.07.052.

[57] R. Amrit, J. B. Rawlings, and L. T. Biegler, "Optimizing process economics online using model predictive control," *Computers and Chemical Engineering*, vol. 58, pp. 334–343, 2013, ISSN: 00981354. DOI: 10.1016/j.compchemeng.2013.07.015.

[58] D. Q. Rawlings J. B. Mayne and M. Diehl, *Model predictive control*. 2017, vol. 2017, ISBN: 2020942771. DOI: 10.1155/2012/240898.

[59] P. F. Lima, M. Trincavelli, M. Nilsson, J. Martensson, and B. Wahlberg, "Experimental evaluation of economic model predictive control for an autonomous truck," in *IEEE Intelligent Vehicles Symposium, Proceedings*, vol. 2016-Augus, 2016, pp. 710–715, ISBN: 9781509018215. DOI: 10.1109/IVS.2016.7535465.

[60] L. Lu, X. Song, D. He, and Q. Chen, "Stability and Fuel Economy of Nonlinear Vehicle Platoons: A Distributed Economic MPC Approach," *Chinese Control Conference, CCC*, vol. 2018-July, pp. 7678–7683, Oct. 2018, ISSN: 21612927. DOI: 10.23919/CHICC.2018.8483502.

[61] W. Liu and Z. Li, "Comprehensive Predictive Control Method for Automated Vehicles with Delays," *IEEE Access*, vol. 7, pp. 81 923–81 933, 2019, ISSN: 21693536. DOI: 10.1109/ACCESS.2019.2923762.

[62] W. Wang, W. Wang, J. Wan, D. Chu, Y. Xu, and L. Lu, "Potential field based path planning with predictive tracking control for autonomous vehicles," in *ICTIS 2019 - 5th International Conference on Transportation Information and Safety*, 2019, pp. 746–751, ISBN: 9781728104898. DOI: 10.1109/ICTIS.2019.8883841.

[63] E. N. Sabudin, R. Omar, and C. K. Che Ku Melor, “Potential field methods and their inherent approaches for path planning,” *ARPN Journal of Engineering and Applied Sciences*, vol. 11, no. 18, pp. 10 801–10 805, 2016, ISSN: 18196608.

[64] O. Khatib, “Real-time obstacle avoidance for manipulators and mobile robots,” in *Proceedings - IEEE International Conference on Robotics and Automation*, 1985, pp. 500–505, ISBN: 0818606150. DOI: `10.1109/ROBOT.1985.1087247`.

[65] R. Volpe and P. Khosla, “Manipulator Control with Superquadric Artificial Potential Functions: Theory and Experiments,” *IEEE Transactions on Systems, Man and Cybernetics*, vol. 20, no. 6, pp. 1423–1436, 1990, ISSN: 21682909. DOI: `10.1109/21.61211`.

[66] C. W. Warren, “Global path planning using artificial potential fields,” Publ by IEEE, 1989, pp. 316–321. DOI: `10.1109/robot.1989.100007`.

[67] M. T. Wolf and J. W. Burdick, “Artificial potential functions for highway driving with collision avoidance,” in *Proceedings - IEEE International Conference on Robotics and Automation*, 2008, pp. 3731–3736, ISBN: 9781424416479. DOI: `10.1109/ROBOT.2008.4543783`.

[68] Y. Rasekhipour, A. Khajepour, S. K. Chen, and B. Litkouhi, “A Potential Field-Based Model Predictive Path-Planning Controller for Autonomous Road Vehicles,” *IEEE Transactions on Intelligent Transportation Systems*, vol. 18, no. 5, 2017, ISSN: 15249050. DOI: `10.1109/TITS.2016.2604240`.

[69] L. Li, J. Gan, K. Zhou, X. Qu, and B. Ran, “A novel lane-changing model of connected and automated vehicles: Using the safety potential field theory,” *Physica A: Statistical Mechanics and its Applications*, vol. 559, p. 125 039, 2020, ISSN: 03784371. DOI: `10.1016/j.physa.2020.125039`. [Online]. Available: `https://doi.org/10.1016/j.physa.2020.125039`.

[70] ——, “A novel lane-changing model of connected and automated vehicles: Using the safety potential field theory,” *Physica A: Statistical Mechanics and its Applications*, vol. 559, Dec. 2020, ISSN: 03784371. DOI: `10.1016/J.PHYSA.2020.125039`.

[71] B. Lu, G. Li, H. Yu, *et al.*, “Adaptive Potential Field-Based Path Planning for Complex Autonomous Driving Scenarios,” *IEEE Access*, vol. 8, pp. 225 294–225 305, 2020, ISSN: 21693536. DOI: `10.1109/ACCESS.2020.3044909`.

[72] P. Hang, C. Lv, C. Huang, J. Cai, Z. Hu, and Y. Xing, “An Integrated Framework of Decision Making and Motion Planning for Autonomous Vehicles Considering Social Behaviors,” *IEEE Transactions on Vehicular Technology*, vol. 69, no. 12, pp. 14 458–14 469, 2020, ISSN: 19399359. DOI: `10.1109/TVT.2020.3040398`.

[73] H. Li, C. Wu, D. Chu, L. Lu, and K. Cheng, “Combined trajectory planning and tracking for autonomous vehicle considering driving styles,” *IEEE Access*, vol. 9, pp. 9453–9463, 2021, ISSN: 21693536. DOI: `10.1109/ACCESS.2021.3050005`.

[74] X. Yang, “Modeling of vehicle driving behavior in tunnel entrance zone based on artificial potential field theory,” *Proceedings of IEEE Asia-Pacific Conference on Image Processing, Electronics and Computers, IPEC 2021*, pp. 678–683, Apr. 2021. DOI: `10.1109/IPEC51340.2021.9421333`.

[75] U. Z. Abdul Hamid, H. Zamzuri, T. Yamada, M. A. Abdul Rahman, Y. Saito, and P. Raksincharoensak, “Modular design of artificial potential field and nonlinear model predictive control for a vehicle collision avoidance system with move blocking strategy,” *Proceedings of the Institution of Mechanical Engineers, Part D: Journal of Automobile Engineering*, vol. 232, no. 10, pp. 1353–1373, 2018, ISSN: 09544070. DOI: `10.1177/0954407017729057`.

[76] H. Wang, Y. Huang, A. Khajepour, Y. Zhang, Y. Rasekhipour, and D. Cao, “Crash Mitigation in Motion Planning for Autonomous Vehicles,” *IEEE Transactions on Intelligent Transportation Systems*, vol. 20, no. 9, pp. 3313–3323, 2019, ISSN: 15580016. DOI: `10.1109/TITS.2018.2873921`.

[77] C. Martínez and F. Jiménez, “Implementation of a potential field-based decision-making algorithm on autonomous vehicles for driving in complex environments,” *Sensors (Switzerland)*, vol. 19, no. 15, Aug. 2019, ISSN: 14248220. DOI: `10.3390/S19153318`.

[78] P. Wang, S. Gao, L. Li, B. Sun, and S. Cheng, “Obstacle avoidance path planning design for autonomous driving vehicles based on an improved artificial potential field algorithm,” *Energies*, vol. 12, no. 12, 2019, ISSN: 19961073. DOI: 10.3390/en12122342. [Online]. Available: www.mdpi.com/journal/energies.

[79] C. Li, X. Jiang, W. Wang, Q. Cheng, and Y. Shen, “A Simplified Car-following Model Based on the Artificial Potential Field,” in *Procedia Engineering*, vol. 137, No longer published by Elsevier, Jan. 2016, pp. 13–20. DOI: 10.1016/j.proeng.2016.01.229.

[80] P. Wu, F. Gao, and K. Li, “Humanlike Decision and Motion Planning for Expressway Lane Changing Based on Artificial Potential Field,” *IEEE Access*, vol. 10, pp. 4359–4373, 2022, ISSN: 21693536. DOI: 10.1109/ACCESS.2022.3141075.

[81] Y. Ma, P. Zhang, and B. Hu, “Active lane-changing model of vehicle in B-type weaving region based on potential energy field theory,” *Physica A: Statistical Mechanics and its Applications*, vol. 535, 2019, ISSN: 03784371. DOI: 10.1016/j.physa.2019.122291.

[82] Y. Jia, D. Qu, L. Han, L. Lin, and J. Hong, “Research on car-following model based on molecular dynamics,” *Advances in Mechanical Engineering*, vol. 13, no. 2, pp. 1–10, 2021, ISSN: 16878140. DOI: 10.1177/1687814021993003. [Online]. Available: https://us.sagepub.com/en-us/nam/open-access-at-sage.

[83] Y. Jia, D. Qu, H. Song, T. Wang, and Z. Zhao, “Car-following characteristics and model of connected autonomous vehicles based on safe potential field,” *Physica A: Statistical Mechanics and its Applications*, vol. 586, p. 126 502, 2022, ISSN: 03784371. DOI: 10.1016/j.physa.2021.126502. [Online]. Available: https://doi.org/10.1016/j.physa.2021.126502.

[84] J. Ji, A. Khajepour, W. W. Melek, and Y. Huang, “Path planning and tracking for vehicle collision avoidance based on model predictive control with multiconstraints,” *IEEE Transactions on Vehicular Technology*, vol. 66, no. 2, 2017, ISSN: 00189545. DOI: 10.1109/TVT.2016.2555853.

[85] S. Wang, Z. Li, B. Wang, J. Ma, and J. Yu, “Velocity Obstacle-Based Collision Avoidance and Motion Planning Framework for Connected and Automated Vehicles,” *Transportation Research Record: Journal of the Transportation Research Board*, vol. 2676, no. 5, pp. 748–766, Jan. 2022, ISSN: 0361-1981. DOI: 10.1177/03611981211070286. [Online]. Available: https://journals-sagepub-com.tudelft.idm.oclc.org/doi/10.1177/03611981211070286.

[86] Z. Elmi and M. Önder, “Path planning using model predictive controller based on potential field for autonomous vehicles,” in *Proceedings: IECON 2018 - 44th Annual Conference of the IEEE Industrial Electronics Society*, 2018, pp. 2613–2618, ISBN: 9781509066841. DOI: 10.1109/IECON.2018.8591282.

[87] Z. Zuo, X. Yang, Z. Zhang, and Y. Wang, “Lane-associated MPC path planning for autonomous vehicles,” in *Chinese Control Conference, CCC*, vol. 2019-July, 2019, pp. 6627–6632, ISBN: 9789881563972. DOI: 10.23919/ChiCC.2019.8866609.

[88] C. Ko, S. Han, M. Choi, and K. S. Kim, “Integrated path planning and tracking control of autonomous vehicle for collision avoidance based on model predictive control and potential field,” in *International Conference on Control, Automation and Systems*, vol. 2020-Octob, 2020, pp. 956–961, ISBN: 9788993215205. DOI: 10.23919/ICCAS50221.2020.9268369.

[89] S. Kato, S. Tsugawa, K. Tokuda, T. Matsui, and H. Fujii, “Vehicle Control Algorithms for Cooperative Driving with Automated Vehicles and Intervehicle Communications,” *IEEE Transactions on Intelligent Transportation Systems*, vol. 3, no. 3, pp. 155–160, Sep. 2002, ISSN: 15249050. DOI: 10.1109/TITS.2002.802929.

[90] B. Tian, G. Wang, Z. Xu, Y. Zhang, and X. Zhao, “Communication delay compensation for string stability of CACC system using LSTM prediction,” *Vehicular Communications*, vol. 29, Jun. 2021, ISSN: 22142096. DOI: 10.1016/J.VEHCOM.2021.100333.

[91] O. Pauca, A. Maxim, and C. F. Caruntu, “Control Architecture for Cooperative Autonomous Vehicles Driving in Platoons at Highway Speeds,” *IEEE Access*, vol. 9, pp. 153 472–153 490, 2021, ISSN: 21693536. DOI: 10.1109/ACCESS.2021.3128235.

[92] V. S. Dolk, J. Ploeg, and W. P. H. Heemels, "Event-Triggered Control for String-Stable Vehicle Platooning," *IEEE Transactions on Intelligent Transportation Systems*, vol. 18, no. 12, pp. 3486–3500, Dec. 2017, ISSN: 15249050. DOI: 10.1109/TITS.2017.2738446.

[93] Z. Wang, X. Chen, Y. Ouyang, and M. Li, "Emission Mitigation via Longitudinal Control of Intelligent Vehicles in a Congested Platoon," *Computer-Aided Civil and Infrastructure Engineering*, vol. 30, pp. 490–506, 2015. DOI: 10.1111/mice.12130.

[94] F. Ma, Y. Yang, J. Wang, *et al.*, "Predictive energy-saving optimization based on nonlinear model predictive control for cooperative connected vehicles platoon with V2V communication," *Energy*, vol. 189, Dec. 2019, ISSN: 03605442. DOI: 10.1016/j.energy.2019.116120.

[95] E. Semsar-Kazerooni, J. Verhaegh, J. Ploeg, and M. Alirezaei, "Cooperative adaptive cruise control: An artificial potential field approach," *IEEE Intelligent Vehicles Symposium, Proceedings*, vol. 2016-Augus, pp. 361–367, Aug. 2016. DOI: 10.1109/IVS.2016.7535411.

[96] S. E. Li, Y. Zheng, K. Li, and J. Wang, "An overview of vehicular platoon control under the four-component framework," in *IEEE Intelligent Vehicles Symposium, Proceedings*, vol. 2015-Augus, Institute of Electrical and Electronics Engineers Inc., Aug. 2015, pp. 286–291, ISBN: 9781467372664. DOI: 10.1109/IVS.2015.7225700.

[97] S. Shi and M. Lazar, "A recursively feasible distributed robust MPC algorithm for vehicle platooning," *IFAC-PapersOnLine*, vol. 51, no. 23, pp. 112–117, Jan. 2018, ISSN: 24058963. DOI: 10.1016/J.IFACOL.2018.12.020.

[98] ——, "On distributed model predictive control for vehicle platooning with a recursive feasibility guarantee," in *IFAC-PapersOnLine*, vol. 50, Elsevier B.V., Jul. 2017, pp. 7193–7198. DOI: 10.1016/j.ifacol.2017.08.607.

[99] O. E. Ganaoui-Mourlan, S. Camp, T. Hannagan, V. Arora, M. De Neuville, and V. A. Kousournas, "Path planning for autonomous platoon formation," *Sustainability (Switzerland)*, vol. 13, no. 9, May 2021, ISSN: 20711050. DOI: 10.3390/su13094668.

[100] X. Liu, G. Zhao, N. Masoud, and Q. Zhu, "Trajectory Planning for Connected and Automated Vehicles: Cruising, Lane Changing, and Platooning," *SAE International Journal of Connected and Automated Vehicles*, vol. 4, no. 4, 2021, ISSN: 2574075X. DOI: 10.4271/12-04-04-0025.

[101] L. Li, J. Gan, X. Qu, P. Mao, Z. Yi, and B. Ran, "A novel graph and safety potential field theory□based vehicle platoon formation and optimization method," *Applied Sciences (Switzerland)*, vol. 11, no. 3, pp. 1–22, Feb. 2021, ISSN: 20763417. DOI: 10.3390/APP11030958.

[102] R. Hao, M. Liu, W. Ma, B. van Arem, and M. Wang, "A flock-like two-dimensional cooperative vehicle formation model based on potential functions," *Transportmetrica B*, 2022, ISSN: 21680582. DOI: 10.1080/21680566.2022.2052998.

[103] R. Firoozi, X. Zhang, and F. Borrelli, "Formation and reconfiguration of tight multi-lane platoons," *Control Engineering Practice*, vol. 108, Mar. 2021, ISSN: 09670661. DOI: 10.1016/j.conengprac.2020.104714.

[104] L. Gao, D. Chu, Y. Cao, L. Lu, and C. Wu, "Multi-lane Convoy Control for Autonomous Vehicles based on Distributed Graph and Potential Field," in *2019 IEEE Intelligent Transportation Systems Conference, ITSC 2019*, Institute of Electrical and Electronics Engineers Inc., Oct. 2019, pp. 2463–2469, ISBN: 9781538670248. DOI: 10.1109/ITSC.2019.8917409.

[105] E. Semsar-Kazerooni, K. Elferink, J. Ploeg, and H. Nijmeijer, "Multi-objective platoon maneuvering using artificial potential fields," 1, vol. 50, Elsevier B.V., Jul. 2017, pp. 15 006–15 011. DOI: 10.1016/j.ifacol.2017.08.2570.

[106] R. Wu, L. Li, W. Lu, Y. Rui, and B. Ran, "Improving the safe operation of platoon lane changing for connected automated vehicles: A novel field-driven approach," *Applied Sciences (Switzerland)*, vol. 11, no. 16, Aug. 2021, ISSN: 20763417. DOI: 10.3390/app11167287.

[107] W. J. Scholte, P. W. Zegelaar, and H. Nijmeijer, "A control strategy for merging a single vehicle into a platoon at highway on-ramps," *Transportation Research Part C: Emerging Technologies*, vol. 136, Mar. 2022, ISSN: 0968090X. DOI: 10.1016/J.TRC.2021.103511.

[108] X. Chen and J. Martensson, “Optimization Based Merging Coordination of Connected and Automated Vehicles and Platoons,” *IEEE Conference on Intelligent Transportation Systems, Proceedings, ITSC*, vol. 2021-Septe, pp. 2547–2553, Sep. 2021. DOI: 10.1109/ITSC48978.2021.9564788.

[109] Z. Wang, Y. Bian, S. E. Shladover, G. Wu, S. E. Li, and M. J. Barth, *A Survey on Cooperative Longitudinal Motion Control of Multiple Connected and Automated Vehicles*, Mar. 2020. DOI: 10.1109/MITS.2019.2953562.

[110] T. Sturm, C. Krupitzer, M. Segata, and C. Becker, “A Taxonomy of Optimization Factors for Platooning,” *IEEE Transactions on Intelligent Transportation Systems*, vol. 22, no. 10, pp. 6097–6114, Oct. 2021, ISSN: 15580016. DOI: 10.1109/TITS.2020.2994537.

[111] V. Lesch, M. Breitbach, M. Segata, C. Becker, S. Kounev, and C. Krupitzer, “An Overview on Approaches for Coordination of Platoons,” *IEEE Transactions on Intelligent Transportation Systems*, 2021, ISSN: 15580016. DOI: 10.1109/TITS.2021.3115908.

[112] K. c. Chu, “Decentralized Control of High-Speed Vehicular Strings,” *https://doi.org/10.1287/trsc.8.4.361*, vol. 8, no. 4, pp. 361–384, Nov. 1974, ISSN: 00411655. DOI: 10.1287/TRSC.8.4.361. [Online]. Available: https://pubsonline.informs.org/doi/abs/10.1287/trsc.8.4.361.

[113] S. Feng, Y. Zhang, S. E. Li, Z. Cao, H. X. Liu, and L. Li, *String stability for vehicular platoon conarol: Definitions and analysis methods*, Jan. 2019. DOI: 10.1016/j.arcontrol.2019.03.001. [Online]. Available: https://doi.org/10.1016/j.arcontrol.2019.03.001.

[114] I. Karafyllis, D. Theodosis, and M. Papageorgiou, “Nonlinear adaptive cruise control of vehicular platoons,” *International Journal of Control*, 2021, ISSN: 13665820. DOI: 10.1080/00207179.2021.1982015.

[115] K. B. Devika and S. C. Subramanian, “Sliding Mode-Based Time-Headway Dynamics for Heavy Road Vehicle Platoon Control,” *2021 7th Indian Control Conference, ICC 2021 - Proceedings*, pp. 265–270, 2021. DOI: 10.1109/ICC54714.2021.9703151.

[116] R. Kianfar, P. Falcone, and J. Fredriksson, “A control matching model predictive control approach to string stable vehicle platooning,” *Control Engineering Practice*, vol. 45, pp. 163–173, 2015, ISSN: 09670661. DOI: 10.1016/j.conengprac.2015.09.011. [Online]. Available: http://dx.doi.org/10.1016/j.conengprac.2015.09.011.

[117] Y. Bian, Y. Zheng, W. Ren, S. E. Li, J. Wang, and K. Li, “Reducing time headway for platooning of connected vehicles via V2V communication,” *Transportation Research Part C: Emerging Technologies*, vol. 102, pp. 87–105, May 2019, ISSN: 0968090X. DOI: 10.1016/J.TRC.2019.03.002. [Online]. Available: https://doi.org/10.1016/j.trc.2019.03.002.

[118] J. Wang, S. Gong, and S. Peeta, “A real-time deployable model predictive control-based cooperative platooning approach for connected and autonomous vehicles,” *Transportation Research Part B*, vol. 128, pp. 271–301, 2019. DOI: 10.1016/j.trb.2019.08.002. [Online]. Available: https://doi.org/10.1016/j.trb.2019.08.002.

[119] W. B. Dunbar and D. S. Caveney, “Distributed receding horizon control of vehicle platoons: Stability and string stability,” *IEEE Transactions on Automatic Control*, vol. 57, no. 3, pp. 620–633, Mar. 2012, ISSN: 00189286. DOI: 10.1109/TAC.2011.2159651.

[120] Y. Zhu and F. Zhu, “Barrier-function-based distributed adaptive control of nonlinear CAVs with parametric uncertainty and full-state constraint,” *Transportation Research Part C: Emerging Technologies*, vol. 104, pp. 249–264, 2019, ISSN: 0968090X. DOI: 10.1016/j.trc.2019.05.002. [Online]. Available: https://doi.org/10.1016/j.trc.2019.05.002.

[121] K. B. Devika, G. Rohith, and S. C. Subramanian, “Potential Function-Based String Stable Controller for Heavy Road Vehicle Platoons,” *IEEE Access*, vol. 9, pp. 156 274–156 282, 2021, ISSN: 21693536. DOI: 10.1109/ACCESS.2021.3129191.

[122] Z. Liu, D. Liu, W. Yu, and S. Baldi, “A Cooperative Protocol for Vehicle Merging Using Bidimensional Artificial Potential Fields,” in *Lecture Notes in Networks and Systems*, vol. 429 LNNS, Springer Science and Business Media Deutschland GmbH, 2022, pp. 566–577, ISBN: 9783030976712. DOI: 10.1007/978-3-030-97672-9{_}51. [Online]. Available: https://link.springer.com/chapter/10.1007/978-3-030-97672-9_51.

[123] K. Hou, F. Zheng, X. Liu, and Z. Fan, “Dynamic Cooperative Vehicle Platoon Control Considering Longitudinal and Lane-changing Dynamics,” pp. 1–13, Jan. 2021. DOI: `10.48550/arxiv.2201.08553`. [Online]. Available: `https://arxiv.org/abs/2201.08553v1`.

[124] D. J. McCrone, E. Arasteh, and F. M. Jan, “An artificial potential field approach to simulate cooperative adaptive cruise controlled vehicles,” in *ASME 2017 Dynamic Systems and Control Conference, DSCC 2017*, vol. 1, American Society of Mechanical Engineers, 2017, ISBN: 9780791858271. DOI: `10.1115/DSCC2017-5020`.

[125] L. Segel, “Theoretical Prediction and Experimental Substantiation of the Response of the Automobile to Steering Control,” *Proceedings of the Institution of Mechanical Engineers: Automobile Division*, vol. 10, no. 1, 1956, ISSN: 0367-8822. DOI: `10.1243/pime{\_}auto{\_}1956{\_}000{\_}032{\_}02`.

[126] H. B. Pacejka, *Tire and Vehicle Dynamics*. 2006. DOI: `10.1016/B978-0-7506-6918-4.X5000-X`.

[127] R. A. DeCarlo, *Linear systems : a state variable approach with numerical implementation*. Englewood Cliffs N.J.: Prentice Hall, 1989, p. 495, ISBN: 9780135368145.

[128] H. YUKAWA, “On the Interaction of Elementary Particles. I,” *Proceedings of the Physico-Mathematical Society of Japan. 3rd Series*, vol. 17, pp. 48–57, 1935, ISSN: 0370-1239. DOI: `10.11429/PPMSJ1919.17.0{\_}48`.

[129] L. Zhao and Z. Liu, “Vehicle velocity and roll angle estimation with road and friction adaptation for four-wheel independent drive electric vehicle,” *Mathematical Problems in Engineering*, vol. 2014, 2014, ISSN: 15635147. DOI: `10.1155/2014/801628`.

[130] G. Franklin, J. D. Powell, and A. Emami-Naeini, *Feedback Control of Dynamic Systems(7th Edition)*. 2015.

[131] MATLAB, *stepinfo*. [Online]. Available: `https://nl.mathworks.com/help/ident/ref/lti.stepinfo.html`.

[132] F. Havlak and M. Campbell, “Discrete and continuous, probabilistic anticipation for autonomous robots in Urban environments,” *IEEE Transactions on Robotics*, vol. 30, no. 2, 2014, ISSN: 15523098. DOI: `10.1109/TRO.2013.2291620`.

[133] Q. Tran and J. Firl, “Modelling of traffic situations at urban intersections with probabilistic non-parametric regression,” in *IEEE Intelligent Vehicles Symposium, Proceedings*, 2013. DOI: `10.1109/IVS.2013.6629491`.

[134] R. Verma and D. Del Vecchio, “Semiautonomous multivehicle safety,” in *IEEE Robotics and Automation Magazine*, vol. 18, 2011. DOI: `10.1109/MRA.2011.942114`.

[135] S. Z. Yong, M. Zhu, and E. Frazzoli, “Generalized innovation and inference algorithms for hidden mode switched linear stochastic systems with unknown inputs,” in *Proceedings of the IEEE Conference on Decision and Control*, vol. 2015-February, 2014. DOI: `10.1109/CDC.2014.7039914`.

[136] Wegenwiki, *Redresseerstrook*. [Online]. Available: `https://www.wegenwiki.nl/Redresseerstrook`.

[137] citroen, *NIEUWE CITROËN C5 X EN C5 X PLUG-IN HYBRID*. [Online]. Available: `https://www.citroen.nl/modellen/c5x.html`.

[138] Queensland Goverment, *Stopping distances: speed and braking*, 2016. [Online]. Available: `https://www.qld.gov.au/transport/safety/road-safety/driving-safely/stopping-distances`.

[139] M. J. D. Powell, “A Direct Search Optimization Method That Models the Objective and Constraint Functions by Linear Interpolation,” in *Advances in Optimization and Numerical Analysis*, 1994. DOI: `10.1007/978-94-015-8330-5{\_}4`.

[140] ——, “A view of algorithms for optimization without derivatives,” *Mathematics Today-Bulletin of the Institute of …*, vol. 43, no. 5, pp. 1–12, 2007, ISSN: 1361-2042. [Online]. Available: `http://www.damtp.cam.ac.uk/user/na/NA_papers/NA2007_03.pdf`.

[141] B. d. Schutter, “Optimization for Systems and Control - Lecture Slides (SC42056),” Tech. Rep., 2020.

[142] J. Chen, P. Zhao, T. Mei, and H. Liang, “Lane change path planning based on piecewise bezier curve for autonomous vehicle,” in *Proceedings of 2013 IEEE International Conference on Vehicular Electronics and Safety, ICVES 2013*, 2013. DOI: `10.1109/ICVES.2013.6619595`.

[143] A. Runions and F. Samavati, “CINPACT-splines: A class of C∞ curves with compact support,” in *Lecture Notes in Computer Science (including subseries Lecture Notes in Artificial Intelligence and Lecture Notes in Bioinformatics)*, vol. 9213, 2015. DOI: `10.1007/978-3-319-22804-4{\_}27`.

[144] Mechanical Simulation, *CarSim*, 2022. [Online]. Available: `https://www.carsim.com/products/carsim/index.php`.